TWO-DIMENSIONAL TURBULENT JET ON A COMBINED WALL HAVING STEP CHANGES IN WALL CURVATURE

BY

YASUO NOGUCHI

THESIS SUBMITTED FOR THE DEGREE OF DOCTOR OF PHILOSOPHY

DEPARTMENT OF AERONAUTICAL AND MECHANICAL ENGINEERING
THE UNIVERSITY OF SALFORD

APRIL 1985

TO MY PARENTS

CONTENTS

Chapter 1 Introduction

Chapter 2 Experimental Apparatus

Chapter 3 Measurements

Chapter 4 Results and Discussions

LIST OF DIAGRAMS AND TABLES

Chapter 1

Figure

Chapter 2

Figure

Chapter 3

Figure

Chapter 4

Figure

Chapter 5

Figure

Table

ACKNOWLEDGEMENTS

The work was carried out in the Department of Aeronautical and Mechanical Engineering at the University of Salford under the supervision of Dr. R.A. Sawyer.

The author wishes to express his deepest gratitude to Dr. R.A. Sawyer for his invaluable advice, continuous guidance and supervision throughout this work. The author also gratefully acknowledges Dr. E.M. Laws for her invaluable advice during the final stage of the work.

The experimental work was carried out at the Aeronautical Laboratory in the Department. Many thanks are due to the staff of the Aeronautical, the Fluid Mechanics and the Thermo Dynamics Laboratories, the instrumentation the Design Office and the departmental work shop.

The author also gratefully acknowledges Professor P. Bradshaw of Imperial College of Science and Technology in London for offering the computer programs and for his encouragement. Considerable amount of time was saved by the offer of these programs. The computations were carried out at the University of Salford Computing Centre and at the University of Manchester Regional Computer Centre. The author wishes to thank the staff of both computer centres for their support and advice.

Thanks also to Mrs J.M. Bateson for her careful and neat typing and Mr and Mrs M.K. Ellery for their friendly help.

Finally, the author is indebted to his family for their continuous encouragement and financial support. A part of the financial support was also given by the Department of Aeronautical and Mechanical Engineering of the University of Salford.

SUMMARY

A study of a two-dimensional turbulent jet with a combination of two wall curvature parameters has been made. The wall consists of a plane, a logarithmic spiral and a plane surface. A large amount of attention has been paid to establish good two-dimensionality and to obtain best possible accuracy in the measurements with the hot-wire anemometer system. The development of the mean velocity components, the three normal stresses and the shear stress are presented. The effects of the sudden changes in curvature on the structure of the flow are observed. The corrections of the hot-wire's directional sensitivity are also evaluated and applied using third order correlations. The correlations on the plane and the curved surface show details of the large scale motions at the outer part of the jet. The dissipation measurements have also been made. These measurements enable the evaluation of the terms of the turbulent kinetic energy equation. In addition, an attempt has been made to calculate the development of the plane wall jet using the measured turbulent kinetic energy balance to evaluate the empirical functions in the governing equations. The measured values have been also used for the computation as the starting data.

Nomenclature

Ac	Angle between wire and instantaeous vector in eq. 3-16
a	King's law constant in eq. 2-1
a_1	Empirical function in eq. 5-4
B	Logarithmic law constants in eq. 5-14
Bc	Angle between instantaneous velocity vector and plane normal to wire containing wire and prongs
b	Slot thickness except King's law constant in eq. 2-1, hot-wires directional sensitivity factor in eq. 3-17 and correlation factor in eqs. 4-6 and 7
C	Calibration factor in eq. 3-1
C_f	Skin friction coefficient
C_{out}	Output signal from correlator in eq. 3-41
E	Entrainment constant in eq. 1-2
	Output voltage of C.T.A. in eq. 2-1
	Mean voltage from C.T.A. in eqs. 3-3 to 7
	Correction coefficient to $\overline{u'^2}$ in eq. 3-20
e	Instantaneous voltage = E + e'
e'	Fluctuating portion of e
e_{A+B}, e_{A-B}	Voltage equivalent to $(e'_A + e'_B)$ and $(e'_A - e'_B)$ respectively where A and B refer to channels of correlator
F	Correction coefficient to $\overline{v'^2}$ in eq. 3-21
	Frequency in eq. 3-42
f(r)	Logitudinal correlation in eq. 4-3
G	Correction coefficient to $\overline{u'v'}$ in eq. 3-22
	Empirical function in eq. 5-6
g(r)	Transverse correlation in eq. 4-4

H	Correction coefficient to $\overline{w'^2}$ in eq. 3-23
h	Hot-wire's directional sensitivity coefficient in eq.3-15
K	Surface curvature parameter in eq. 1-3, except logarithmic law constant in chapter 5
k	Turbulent kinetic energy = $\frac{1}{2}(\overline{u'^2} + \overline{v'^2} + \overline{w'^2})$, except Isentropic exponent in eq. 3-14 and hot-wire's directional sensitivity coefficient in eq. 3-15
L	Empirical function in eq. 5-5
L_f	Longitudinal integral scale in eq. 4-5
L_g	Transverse integral scale = $\int_0^\infty g(r)\, d(r)$
ℓ	Hot wire length in eq. 3-42
M, Mo	Momentum flux and slot momentum flux respectively in eq. 2-2
n	King's law constant in eq. 2-1
P_∞, P_s	Static pressures of surrouding fluid and on the surface
Po	Absolute pressure in eq. 3-14
p	Static pressure
Δp	Static pressure difference in eq. 3-14
$\overline{q^2}$	Twice the turbulent kinetic energy = $\overline{u'^2} + \overline{v'^2} + \overline{w'^2}$
q_e	Instantaneous effective velocity in eq. 3-18
q_e'	Fluctuating portion of q'_e
R	Local radius in eq. 3-14 and correlation coefficient in Chapters 3 and 4
R_s	Slot Reynolds number = $U_j\, b/\nu$
r	Separation in correlation
r'	Normalized separation in correlation = $\tau\, U/Y_{\frac{1}{2}}$ or $r/Y_{\frac{1}{2}}$
S_o	Initial surface arc length in eq. 1-4
s	Distance round surface in eq. 1-2 Measure along characteristic in eq. 5-11

T_o	Absolute temperature in eq. 3-14
U,V,W	Mean orthogonal velocity components in X, Y and Z direction
u,v,w	Instantaneous orthogonal velocity components
u',v',w'	Fluctuating portions of u,v,w
$\overline{u'^2},\overline{v'^2},\overline{w'^2}$	Mean squared values of u',v',w'
U_c	Velocity at calibration except convection velocity in eq. 4-11
U_{ce}	Effective cooling velocity which velocity component normal to wire in calibration condition
U_{CN}	Calibration velocity component normal to wire
Ue	Effective cooling velocity except free stream velocity in chapter 5
U_j	Initial slot velocity
U_N,U_T,U_{BN}	Velocity components normal, tangent and binormal to wire
U_τ	Skin friction velocity $= (\tau_w/\rho)^{\frac{1}{2}}$
X,Y,Z	Orthogonal coordinates (see fig. 1-2)
Ym	Distance between surface and maximum velocity (see fig. 4-1)
$Y_{mu},Y_{mv},Y_{mw},Y_{\overline{muv}}$	Distance between surface and maximum stresses $\overline{u'^2}$, $\overline{v'^2}$, $\overline{w'^2}$ and $\overline{u'v'}$ respectively (see fig. 4-1)
$Y_{\frac{1}{2}}$	Distance between surface and the point where mean velocity is half the maximum velocity (see fig. 4-1)
γ	Angle between characteristic and X axis
δ	Width of layer. Distance between points where $\tau = 0.05\tau_m$.
ε	Dissipation
θ	Surface inclination in eq. 1-4
	Momentum thickness in chapter 5
λ	Dissipation length scale in eq. 4-12
ν	Kinetic viscosity

ρ	Density
τ	Time delay in auto-correlation except shear stress = $-\rho\ \overline{u'v'}$ from eq. 5-9 τ for τ/ρ in chapter 5
τ^+, τ^-	τ on layer 1 and layer 2 respectively
τ_{tot}	Total shear stress = $\tau^+ + \tau^-$
τ_w	Wall shear stress
ψ	Angle between wire and axis though stem

Subscript

i, j	Indices
m	Denotes maximum value, except denotes 'measured' value in eqs. 3-20 to 33
1,2,3	Denote X, Y and Z directions
1,2,3,4,5	Denote positions shown in fig. 3-8 in chapter 3
α,β	Ingoing and outgoing characteristics

CHAPTER 1

INTRODUCTION

CHAPTER 1 INTRODUCTION

1-1 Purpose

The phenomenon a jet attaches to an adjacent curved surface is well known as 'Coanda' effect. This effect was patented by Coanda (1932); however, it had been observed and explained well before by others, for example, by Young (1800) and Reynolds (1870). Coanda's intentions were to exploit the effect to some practical applications rather than the details of the phenomenon. He applied the effect to enhance engine combustion chamber scavenging, to produce a nozzle with high thrust augmentation and to increase lift on wings. Since then, the Coanda effect has been exploited in many ways. In order to produce optimum designs to use potential benefits of the effect fully, the details of this phenomenon became important. Research work on Coanda effect has been extended in to many fields such as boundary layer on curved walls, wall jets on curved walls with or without moving streams, re-attachment of inclined jets to walls etc. These flows can be laminar or turbulent and can be two or three dimensional. Here we concentrate on two-dimensional turbulent wall jets.

A wall jet consists of inner and outer portions. The inner part of the jet is a wall shear layer which is often treated as a boundary layer. This portion is expected to be dominated by the wall effects. The outer portion can be linked to one half of a two-dimensional free jet. The matching of two layers is not simple because both turbulent regions interfere with each other. Also the shear stress in the wall jet is not a simple function of the local mean velocity gradient. This is apparent from the fact that the shear stress is not zero at the point where the velocity is maximum. The first experimental work on the simplest form of a wall jet, i.e. the wall jet on a plane surface, was carried out by Förthmann (1934). His work has been followed by many others. Plane wall jets in still air and in a moving stream with adverse pressure gradient can be self-preserving. Self-preserving forms are convenient for study, especially for test cases for computation, because the non-dimensional turbulent structures remain unchanged and independent of the initial conditions.

Meanwhile, there are large numbers of reports concerning curved wall jets. At first, many studies were made on wall jets over circular cylinders; these were soon followed by investigations on jets over logarithmic spiral surfaces. The later study was first made by Sawyer (1962). He showed that wall jets on logarithmic spiral surfaces could also establish self-preserving states exhibiting linear rates of growth. These experimental studies, which will be discussed later in this chapter, are sufficiently detailed to provide data for test cases for turbulent computations. However, there is no detailed study concerning other shapes of surface or the combination of surfaces. The practical use of the Coanda effect usually involves more complicated shapes of surface or a combination of surfaces rather than simply plane, circular or logarithmic spiral surfaces. On the other hand, trial and error methods are widely used to exploit the effect in engineering fields such as high lift devices on wings. Nevertheless these are studies to produce optimum designs, so that no serious attempts have been made to observe the detail of the structure. Therefore it is considered to be very useful to measure the details of structure of wall jets on more complicated shapes. However, these shapes should be simple enough to observe the structure under controlled conditions. The measurements should display mean flow quantities as well as turbulence quantities so that data can be used for computational purposes.

The present work concerned the combination of three sections of surfaces. The surface consists of plane, logarithmic spiral and plane surface to obtain the effects of step changes in the curvature parameter on the jet and its turbulence structure. The following measurements have been made to observe the jet in detail.

1) Mean flow quantities.
2) Turbulence quantities.

In order to achieve better accuracy in these quantities, some extra care should be taken. These are:

a) Flow two-dimensionality.
b) Accuracy of equipment and techniques.

Some qualitative measurements have also been required to observe turbulence structures. These are

3) Correlations.
4) Turbulent kinetic energy balance.

1-2 Surfaces

It is assumed that the wall friction can be neglected, then the jet momentum flux is conserved. In this type of flow, the non-dimensional entrainment rate is a function of the curvature ratio $Y_{\frac{1}{2}}/R$ where $Y_{\frac{1}{2}}$ is the jet width at the point where the velocity is one half of the maximum velocity of the jet U_m, and R is the local radius of the curvature. Entrainment theory was first performed by Head (1960). The relations can be written as:

$$U^2m \; Y\tfrac{1}{2} = \text{Const.}, \qquad (1\text{-}1)$$

and

$$\frac{1}{U^2m} \frac{d}{dS} (Um \; Y\tfrac{1}{2}) = E(\frac{Y\frac{1}{2}}{R}), \qquad (1\text{-}2)$$

where S is the distance round the surface and E is the entrainment constant. Self-preserving jets, therefore, have relations

$$Y\tfrac{1}{2} \propto S$$

$$Um \propto S^a$$

and

$$R \propto S$$

where a is slightly smaller than $-\frac{1}{2}$. Thus the jets over the surface which has the relation

$$S/R = K = \text{Const.} \qquad (1\text{-}3)$$

can be self-preserving. These have been confirmed by Sawyer (1962), Giles, Hays and Sawyer (1966) and Guitton and Newman (1977), with the linear growth rates of jet width and velocity profiles independent of S. These surfaces are conveniently expressed in the form

$$S = So.e^{\theta/K} \qquad (1\text{-}4)$$

where So is the initial surface arc length and θ is the surface inclination to an appropriate datum. This is the logarithmic spiral surface.

The wall arrangement is shown in Fig. 1-1 which consists of three surfaces. The first surface has the curvature parameter K = 0, i.e. a plane surface 13ins (330.2mm) long. The length of the first surface has been chosen to give a jet of the correct thickness at the end of this surface so as to achieve a constant $Y\frac{1}{2}/R$ jet on the second surface, after the transition region where the structure of the jet responds to the curvature change. The second surface with $K = 1.0$ and 9.62 in (244.3mm) long. The final part of the surface is again a plane surface with $K = 0$ and 26.4 ins (670mm)long . The co-ordinate system is shown in fig. 1-2. X is in the streamwise direction, Y is in the direction normal to the surface and Z is in the direction normal to the streamwise direction and parallel to the surface. The logarithmic spiral surface parameters $K = 1.0$ and $S_0 = 2.0$ ins. (50.8mm) have been chosen. The details of the wall and slot arrangements will be shown in the later chapter. The distance round the curved surface S has a rather complicated definition because of the surface combination. The curved surface starts at $X = 13$ in (330.2mm) where the local radius of curvature, i.e. initial radius S_0,is 2 ins. (50.8mm). Since $S/R = K = 1.0$ thus $S = R$ by definition, S at the start of the curved surface i.e. at $X = 13$in. (330.2mm) is 2in (50.8mm). Therefore on the curved surface

$$S = X - (13 - 2) \text{ ins}$$

or

$$S = X - (330.2 - 50.8) \text{ mm.}$$

The slot width has been set at $b = \frac{1}{4}$ ins (6.35mm).
The slot Reynolds number $Rs = 2.5 \times 10^4$ has been used throughout the experiments.

1-3 Previous work

There are large numbers of experimental studies of turbulent wall jets. These reports have been recently reviewed and summarised by Launder and Rodi (1981) and they include various types of wall jets. They discussed six different types of wall jets. These are plane wall jets in still air, in a moving stream with adverse pressure gradient, in a moving stream without pressure gradient, wall jets on circular cylinders, on logarithmic spiral surfaces and three-dimensional wall jets. In the present experiment the jet is on the plane and the logarithmic spiral surfaces in still air. Therefore the literature on these two and also jets on circular cylinders is relevant to this study.

The plane wall jet in still air which is, in the present experiments, established on the first plane surface. Therefore the already known results on plane wall jets are very useful to exhibit general credibility in comparison with the present data. The very first solutions for both laminar and turbulent, radial and plane wall jets were obtained by Glauert (1956) and Bakke (1957). In those early days, research work was mainly centred on the growth rates of jets and the maximum velocity decays. These studies were soon followed by detailed measurements of turbulence quantities. Launder and Rodi insisted that before looking at these qunatities two-dimensionality should be checked. From the criteria which have been set by them, the measurements of Förthmann (1934), Bradshaw and Gee (1960), Patel (1962), Tailland (1967, 1970), Guitton (1964, 1970) and Verhof (1970) are acceptable. The growth rates of jet width are linear in these measurements and in good agreement. Tailland has measured three different slot Reynolds numbers. His data indicates a slight decrease in the rate of growth with increase in Reynolds number. Also there is a shift in the rate of growth with Reynolds number change. These tendencies are also seen in the decay of the maximum velocity. The range of streamwise direction in these measurements vary from X/b = 3 to 1459 and Reynolds numbers from $Re_s = 0.61 \times 10^4$ to 3.1×10^4. The non-dimensionalized velocity profiles are in very good agreement. These well established results may be used to check the general credibility of the present measurements. However, there are considerable variations in turbulence quantities. If the flows are self-preserving, therefore, they should be independent of the past history of the flow. Although the flows seemed to be self-preserving, in each case the scatter is large. The variation in non-dimensionalized $\overline{u'^2}$ is relatively small. However, for example, the maximum normalized turbulent kinetic energy measured by Tailland is 45% higher than that measured by Guitton. This is attributed mainly by the scatter in $\overline{v'^2}$. Therefore previous results are useful to check the turbulence quantities generally. However, the large scatter within the results makes for more uncertainty than is the case when comparing mean quantities.

The previous experiments on wall jets on curved surfaces can be divided into two parts. The first is wall jets over circular cylinders and the second is jets over logarithmic spiral surfaces. Since Nakaguchi's (1961) and Newman's (1961) first detailed measurements on the jets over circular cylinders, there have been many reports on both concave and convex surfaces. Here we only look at the experiments on convex surfaces. Two-dimensionality is again the major problem. The surface curvature generates stronger secondary vortices near the side walls than for flow with zero curvature. Fekete (1963) undertook Newman's original work and re-designed the apparatus to achieve better quality flow. His interest was mainly on mean quantities. Detailed measurements were made to predict the growth rate of the jet. However, only longitudinal turbulent intensity was measured. Guitton (1964) has pointed out the differences between plane wall jets and curved wall jets. They are:

1) The velocity profiles of curved wall jets are fuller.
2) Curved wall jets grow more rapidly and decay more quickly than plane wall jets.

3) The turbulence intesities and mixing are higher in curved wall jets.

One of the most extensive studies has probably been made by Alcaraz, Charnay and Mathieu (1977). They measured the jet on a large radius cylinder. Their work has provided all the important Reynolds stresses and triple correlations. Turbulence energy dissipation rates have also been measured. These extensive measurements made it possible to evaluate all the terms in the conservation equation for the turbulent kinetic energy except for the pressure diffusion term which was obtained by differences. Because of the very small slot width to radius of curvature ratio $b/R = 0.0031$, the data at $X/b = 30$ probably provides details of the turbulence structure close to that of a wall jet on a plane surface. At that station the effect of the surface curvature is thought to be minimal. The jet over a circular cylinder is not self-preserving; therefore, the development of the jet can also be seen.

Wall jets over logarithimic spiral surfaces have been extensively studied by three groups of researchers. The first detailed measurements have been made by Sawyer (1962) and Giles, Hays and Sawyer (1966). These were followed by Guitton (1970) and Guitton and Newman (1977). Kanemoto (1974) also made experimental work on this subject. All the reports have provided the measurements on various curvature parameters K. The growth rates are linear in all the cases except the steepest curvature $K = 1.25$. This indicates the flows are closely self-preserving. The mean quantities agree reasonably well. Kanemoto has measured only the longitudinal turbulent intensity and the data have been plotted on a very small scale. Therefore not much information can be obtained from the turbulent intensity data. The difference between the turbulence quantities measured by Giles et al. and Guitton and

Newman is large. It is particularly noticeable in the $\overline{v'^2}$ profiles and the outer part of the $\overline{u'^2}$ and $\overline{u'v'}$ profiles. Guitton and Newman have suggested that there are three possible explanations for the discrepancy between the results. These are three-dimensional flow effects, the use of rather bulky X-wire probes and the use of unlinearized anemometer systems in the measurements of Giles et al. Guitton has paid a large amount of attention to achieve two-dimensionality in his work. He has also used single wire probes for the Reynolds stress measurements to avoid the interference between wires which can not be avoided with X-wire probes. These probes have been used in conjunction with a linearized hot-wire anemometer system. Therefore the turbulence quantities reported by Guitton and Newman may be trusted most. They have measured all the three normal stresses, the Reynolds shear stress $\overline{u'v'}$, the surface pressure distribution, the intermittency distribution and the skin friction. These data may be useful for computational procedures for complex turbulent flows.

There is a brief report on the measurement of the jet on combined surfaces which has been made by Simpson (1970). The surface consisted of plane, logarithmic spiral and plane surfaces which is identical to the present arrangement in the streamwise geometry. The aspect ratio of the rig was not large and there were severe three dimensional effects. The work was done as a final year undergraduate project so that he was unable to provide reliable turbulence quantities. Therefore only the mean quantities can be used for a reference purpose. Sawyer (1973) made a brief report on the prediction method for this jet arrangement.

The contribution of large eddy motions is expected to be significant in the outer part of the jet. The turbulence structure of this region is thought to have some relation to that of free turbulent jets. Since the early study by Townsend (1956), the existence of coherent structures in the mixing region of turbulent flows has been continually discussed. He considered that the large scale motion, which contributed most to the correlations with large separations, was determined by pairs of large but weak energy containing eddies in the wake behind a circular cylinder. This theory has been extended further in many ways. Bradshaw, Ferriss and Johnson (1964) presented extensive correlation measurements in a round free jet. They concluded that the large scale motion appeared to be mixing-jet type motion. This motion was discussed first by Grant (1958) with his comprehensive correlation measurements in a wake flow and a boundary layer. The contributions of coherent structures to turbulent transport of momentum, heat or mass and aerodynamic noise can be significant. Recent developments in flow visualisation, conditional sampling and data processing techniques have resulted in a clearer understanding of the structures. Research work on the coherent structures in shear flows has been reviewed by Davis and Yule (1975). Since the discovery of strong two-dimensionality in these structures by Crow and Champagne (1971) and Brown and Roshko (1974) in turbulent mixing layers, there is a controversy about the form of these structures. The controversy, which is whether the large scale motions are effectively two-dimensional (or axisymmetric) or purely three-dimensional has still to be resolved. Bradshaw (1981) has summarised this controversy.

Finally, the accuracy and reliability of measurements is very important in the present experiments, because one of the purposes is to establish mean and turbulence quantities with the present wall arrangement; therefore, some reports on hot-wire measurement have been studied. The development and improvement of constant temperature anemometer systems with hot-wire probes have allowed better accuracy in turbulence measurements. However, there are some other important problems with the hot-wire measurements which have been discussed by Hinze (1975). The simplest problems may be the fluid temperature change and dust deposition on the wire. The principle of this method is based on the thermal loss of heated wires, so that the changes in fluid temperature and heat transfer rate caused by dust accumulation are serious. Although with the improvements made by manufacturers to the systems and probes to achieve little interference to the flow, better frequency response, high signal-to-noise ratio etc., these difficulties should carefully be removed. The biggest problem of all is the directional sensitivity of the hot-wire probes. The effect of high intensity turbulence on the response of the probes is large. These problems and their counter measures will be discussed in a later chapter. An extensive coverage of fundamental principles in hot-wire anemometry has been given by Perry (1982).

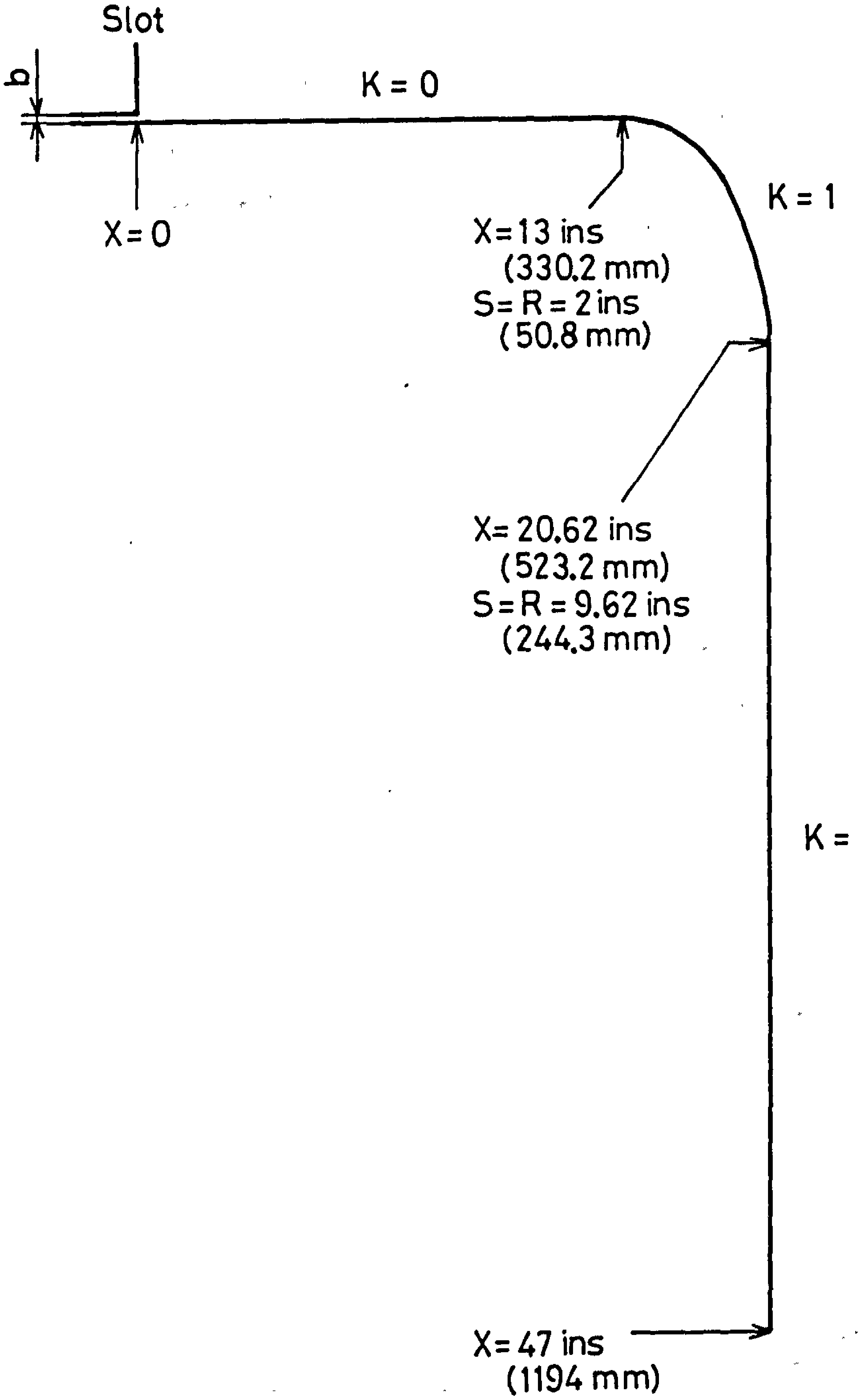

FIG. 1-1 WALL ARRANGEMENT

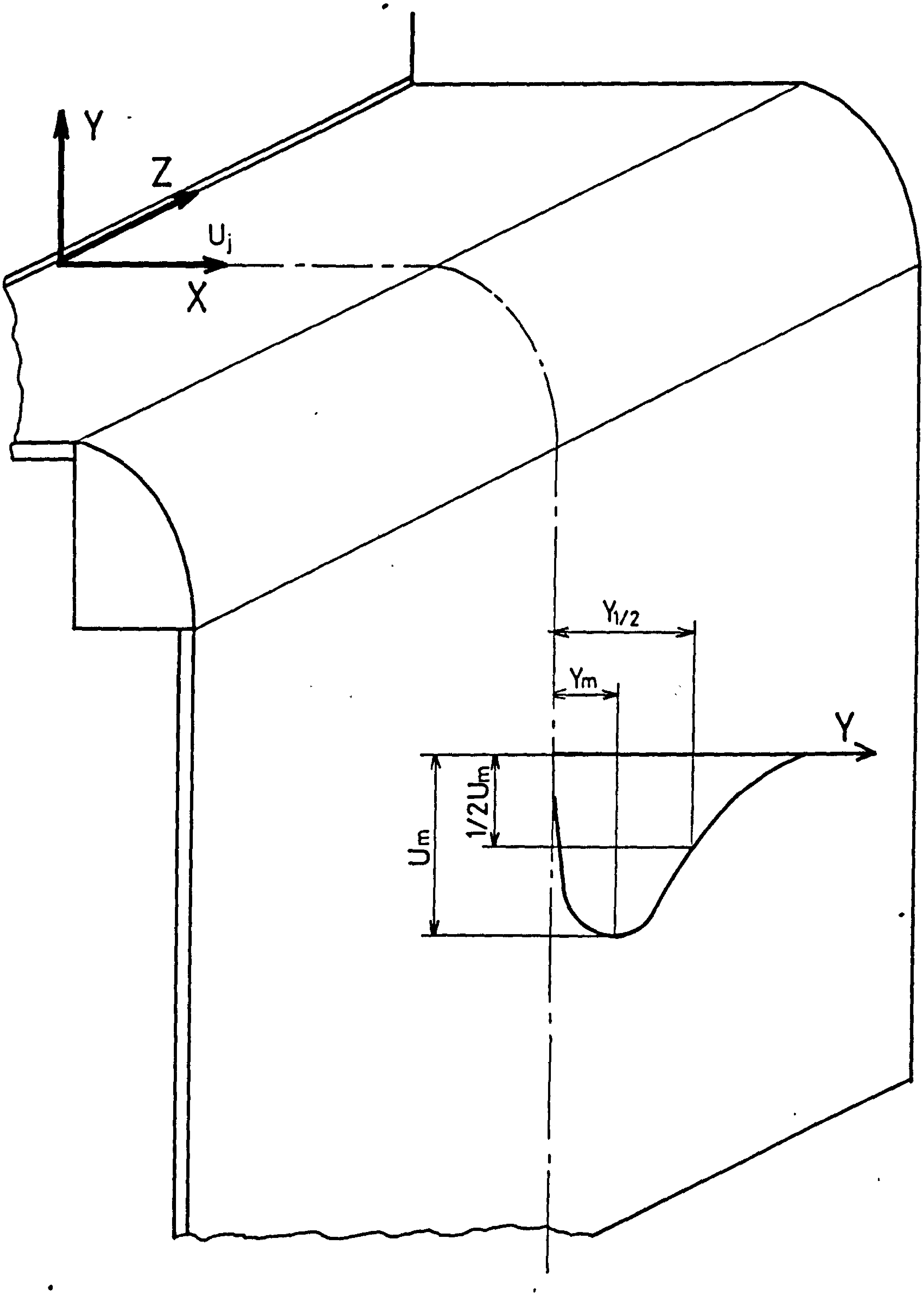

FIG. 1-2 COORDINATE SYSTEM AND SYMBOLS

CHAPTER 2

EXPERIMENTAL APPARATUS

CHAPTER 2 EXPERIMENTAL APPARATUS

2-1 Test rig

2-1-1 Construction

The rig is installed on the upper deck of the Aeronautical laboratory of the University of Salford. The general layout is shown in figs. 2-1 and 2-2. The rig was made in the workshop of the department of Aeronautical and Mechanical Engineering.

The centrifgual blower is driven by a 10 H.P. induction motor. The ductings which follow were made from 18 s.w.g. metal sheet and flexible hoses. A heat exchanger is installed just after the blower, and this is followed by an electrostatic filter. The heat exchanger is fed by Churchill type 0J/CTCHG Chiller and Churchill type CTCV Chiller thermocircular water coolers. The heat extraction rates are 4500 B.T.U/hour at 20°C water and 1000 B.T.U./hour at 20°C respectively. The cooling water contains Ethylene glycol and methanol as antifreeze agents.

The cooled and cleaned air is then supplied to the expansion and settling chambers by a flexible hose. There are a series of screens and honeycomb cells in the chambers. The final contraction ratio is 13.3:1.

The air intake arrangements are shown in fig. 2-3. Air is supplied from either outside the building or from the laboratory to the air intake chamber, which is located on the lower floor in the laboratory. In the chamber, large dust particles are separated. The air is roughly cleaned by means of fabric filters and supplied to the blower via a flexible hose.

The slot velocity is controlled by a valve which is installed just before the blower. The jet temperature is measured by a thermometer at the slot.

2-1-2 Wall arrangement

The wall arrangement is shown in fig. 2-4. The wall consists of three sections. A plane wall K = 0 from X = 0 (at the slot) to X = 13in.(330.2mm). A logarithmic spiral wall with K = 1 from X = 13in. to X = 20.62in. (523.7mm). This is followed by a further length of plane wall to X = 47 in. (1194mm).

Both parts of the plane surfaces are made from ½in. thick aluminium alloy. The logarithmic part of the surface has been carefully machined from an aluminium alloy block. The width of the walls is 44.5in. (1130mm).

The static pressure tappings are of 0.0938in. (2.38mm) diameter and are drilled in the surfaces on its centre. The locations are shown in fig. 2-5.

The side walls are made of ¼in. (6.35mm) thick perspex and bolted on the surfaces. The heights of the side walls are 225mm on the first part of the plane surface and 560mm on the second part of the plane surface. The distance between the walls is adjustable between 530mm and 1000mm. After a series of tests, which are described in a later chapter, in order to obtain the greatest span of flow consistent with the best uniformity of the slot width and uniform velocity along the slot, 925mm was chosen.

The slot width can be adjusted by moving the upper part of the slot by means of two sets of bolts and nuts. After adjustment, the upper part and its casing are screwed together so that there is no air leak from the joint. The slot arrangement is shown in fig. 2-6.

The wall and slot assembly are mounted on an angle iron frame and bolted together. In order to adjust the slot width accurately, three bolts are mounted on the frame underneath the lower surface of the slot, i.e. the lower surface of the ½in. thick aluminium alloy wall. Tightening or loosening the bolts moves the wall slightly, thus controlling the flatness of the wall accurately, The slot width was adjusted to ¼in. (6.35mm). The slot aspect ratio is, therefore, 146.

2-2 Constant Temperature Anemometer (C.T.A.)

2-2-1 Principle of C.T.A.

The principle of C.T.A. is based on the thermal heat loss from an electrically heated fine wire. The heat loss mainly depends on velocity, pressure and temperature of the flow. If only the velocity of the flow changes, then the heat loss of the wire is a measure of the velocity of the flow.

The block diagram is shown in fig. 2-7 which consists of a Wheatstone bridge and a servo amplifier. An increase in the flow velocity will cause a decrease in temperature of the wire. The resultant resistance change brings the bridge unbalance thus an error voltage is produced. When the error voltage is fed to the servo amplifier input, the output voltage of the servo amplifier is applied to the bridge top thus maintaining the original wire temperature.

Therefore the balanced bridge voltage is directly proportional to the change in wire resistance and varies with the velocity.

Detailed determination of velocity, turbulence intensity are described in Chapter 3.

2-2-2 Instruments

DISA type 55M01 main units were used in conjunction with type 55M10 standard bridges. The signals were then fed to type 55D10 linearizers.

The principle of the operation of a hot-wire is an application of the King's Law voltage-velocity relationship. It has the form

$$E^2 = a + bU^n \tag{2-1}$$

where E is the output signal from a C.T.A., U is the flow velocity, a,b and n are constants. When the turbulence intensity is high, the non-linearized signal may produce an excessive error. In the case of wall jet measurements, the use of linearizers was recommended by Guitton (1970).

The linearizers were followed by either DISA type 55D25 auxiliary units or D26 signal conditioners. These were used to eliminate noise from the signals by means of low-pass and high-pass filters.

The signals were fed to appropriate instruments depending on the quantity to be measured.

Mean values of signals were measured by DISA type 55D30 D.C. volt meters. The mean squared value of a signal was measured by a type 55D35 R.M.S. volt meter in conjunction with a type D30 D.C. volt meter.

After some measurements, the type D35 R.M.S. volt meter was found inaccurate. Calibrations were made with a sine wave generator and A.C. Volt meters. Comparisons with turbulence processor were also made. After re-adjustment, the squared output was found to be more accurate than the square root output. All the measurements were, therefore, made with the squared output.

Maximum damping of superimposed AC signal or rapid fluctuations of the D.C. signal of type D30 D.C. volt meter was 10 seconds. This was found to be too short for the measurements in intermittent regions. Additional 6μF capacitors were connected parallel to the 10 sec. damping capacitor in the instrument to increase the damping. The number of capacitors depended on the requirement of damping.

Auto-correlations were carried out with the DISA type 55D70 analog correlator in conjunction with a type 55D75 time delay unit, a type 52B01 sweep drive unit and a Bryans type 2500 X-Y recorder. The Analog correlator had become over heated after a few hours of operation so that an extra cooling fan was installed.

For higher order correlations, a DISA type 52B25 turbulence processor and a type 55A06 random signal indicator and correlator were used. The later instrument was also used for dissipation measurements.

A Telequipment type D61 Oscilloscope, a Farnell type L30-5 stabilised power supply and a Feedback type T.W.G. 300 test wave form generator were also used for tests, signal monitoring and calibrations.

These instruments are shown in fig.2-8.

2-2-3 Probes and Probe Supports

A DISA type 55P01 straight and a P02 45^{0} slanting single wire probes were used for mean velocity and turbulent intensity measurements. These probes are shown in fig. 2-9. The probes consist of 5 μm - diameter and 3mm long platinum plated tungsten wires. Both ends of the wire are copper and gold plated to a diameter of approximately 30 μm to provide a sensitive wire length of 1.25 mm. The plating accurately defines the sensing length and reduces the amount of heat loss by the prongs. Also wider spacing between the prongs makes less interference to the flow field at the sensitive part of the wire.

Damaged probes are repaired using a gold-plated replacement wire magazine with the DISA type 55A13 spot welding equipment. Extreme care and concentration are required to spot weld a wire on to prongs compared with the non-gold-plated wire replacements. Despite a lack of experience with this technique the limited availability of the spare wires meant that spot welding had to be undertaken at times.

These probes are supported by a DISA type 55H20 probe support with a type 55H153 and a 140 mounting tube and guide tube respectively. These are shown in fig. 2-10.

For longitudinal Auto-correlations and dissipation measurements, a DISA type 55A22 straight single wire probe was used. The probe consists of 5 μm diameter platinum plated tungsten wire whose length is approximately 1.2mm. This is chosen because these measurements are qualitative rather than quantitative so that they require less accuracy. The probe is also easy to repair.

The probe was supported by either DISA type 55A20 or 42 support with holders to fix the support to the guide tube. These are shown in fig. 2-10.

Other correlations including third order correlations ($\overline{u'v'^2}$ and $\overline{u'w'^2}$) were measured by a DISA type 55A32 X-wire probe. The wires are perpendicular to each other. The dimensions of the wires are the same as type 55A22 probe. The probe was supported by a type 55A30 probe support and holders to fix it to the guide tube. These are shown in fig. 2-11.

The probes are connected to the anemometer bridge unit with 5m coaxial cables.

2-2-4 Calibration Unit

Several kinds of calibration devices were studied. A 75 H.P. motor driven open circuit tunnel was considered. The velocity range and turbulent intensity were acceptable, however, temperature of the air rose considerably. The air flow from the rig was also considered. The air cleanliness and temperature control were the best of all. Nevertheless, in order to obtain the required flow velocity range and low turbulent intensity, a newly designed chamber and a duct had to be constructed. These were not found to be practical. Finally, a DISA type 55D41 miniature wind tunnel was chosen in conjunction with a 55D42 variable transformer and an Advance Volstat sine wave output. These are shown in fig. 2-12.

The tunnel had been designed to calibrate DISA type 55A series probes. A special adaptor was, therefore, designed and manufactured to calibrate type 55P01 and 02 probes. This was used with the type 55A67 adaptor section.

2-3 Manometers

A Tecquipment multi-probe manometer filled with paraffin of specific gravity equal to 0.776 (at 20°C) was used for the static pressure measurement. The manometer could be inclined to give a suitable range of pressure. The maximum range of pressure which could be measured on this manometer was 1050mm paraffin gauge.

Three Airflow Developments 10in. manometers were used to measure static pressure differences. These were filled with Airflow Developments manometer fluid of specific gravity equal to 0.784 (at 20°C) and 0.787 (at 16°C).

One was used to measure static pressure differences between inlet section and working section to determine the calibrating velocity in the DISA calibration tunnel.

The other two were connected to the rig to measure static pressure difference between two different area sections to determine the initial slot velocity. One was placed near the instruments to monitor the slot velocity while the measurements were in progress. Another one was placed near the valve to control and adjust the slot velocity.

2-4 Traversing devices

2-4-1 Traversing mechanism

A DISA type 55E40 traversing mechanism was employed for the Y direction traverse, except for the Z direction traverse of the longitudinal turbulence correlations R_{11} $(0{:}0,0,r_3)$. These measurements were carried out with a DISA type 52C01 stepper motor to traverse electronically which was controlled by the type 52B01 sweep drive unit.

The resolution of this mechanism is 0.1mm with the gear ratio of 1:1. A modification has been carried out to extend the maximum traversing length from 100mm to 340mm which had been limited by the length of the guide tube.

2-4-2 Traversing frame

The traversing frame to traverse the DISA traversing mechanism for X and Z directions was designed by the design office and manufactured in the work shop of the Department of Aeronautical and Mechanical Engineering. The frame consists of the Z direction guide rail, the Traverse mechanism mount, the X direction guide rail and the main frame. The whole assembly is shown in fig. 2-13.

The mounting on the Z direction guide rail to which the DISA traverse mechanism is fixed, can be slid in the Z direction and can be fixed in a desired position by a locking screw. The Z direction guide rail itself is on the X direction guide rail and can be slid to a desired position. This is also fixed by locking screws. The Z direction guide rail can be rotated so that the angle of the probe axis is adjustable relative to the surface.

In order to avoid excessive vibration from the floor, the whole assembly is mounted on rubber strips.

2-4-3 Probe positioning device

Once the probe is positioned at the appropriate angle and located in the X and Z directions, it may be traversed in Y direction to an accuracy of 0.1mm by the DISA traversing mechanism. However, the accurate initial distance between the surface and the wire is also required. This was measured by a hand made device and a scale.

The device consists of a small microscope of magnitude of 30X and a stand. The microscope has a small light and batteries to obtain a clear view. The batteries have been replaced by larger capacity ones and are fixed in the stand. A cross wire has been installed next to the field lens.

At first the focus is set to the maximum distance to avoid an accidental contact with the wire. The distance between the surface and the point of focus is measured by means of the adjustable length scale, which is brought into view. The length of the scale is adjusted, to set the top of the scale at the centre of the cross. Then, the length of the scale is measured by a micrometer. When the wire is set at the centre of the cross, the distance between the surface and the wire is the measurement shown on the scale. The device is shown on fig. 2-14.

2-5 Two-dimensionality improvements

2-5-1 Spanwise total pressure distribution

The total pressure distribution at X = 300mm at Y = Ym are shown in fig. 2-15. It can be seen that there is considerable scatter at X = 300mm and non-uniformity at the slot.

The slot width was carefully adjusted by the three bolts to adjust the flatness of the lower slot and the two sets of bolts and nuts used to move the upper slot. The width of ¼in (6.35mm) was maintained within 0.001in (0.0254mm) over the central 700mm of the slot.

Even after the adjustment, slight non-uniformity of the slot total pressure distribution was found. This was thought to be caused by non-uniform velocity distribution in the settling chamber. Some different mesh size screens were inserted in different positions to improve flow uniformity. The final arrangement was made after a series of tests.

Fig. 2-15 also shows the improved total pressure distribution at X = 300mm at Y = Ym. It is clearly shown that the spanwise velocity distribution has been considerably improved.

2-5-2 Flow visualization

Flow visualization tests were mainly made in conjunction with a smoke generator. This type of flow visualization was particularly useful in observing the flow at the corners of the rig where entrainment flow could be separated from the side walls etc. Large secondary flows at the downstream parts of the wall could also be seen. The device is portable and easy to use so a number of tests were made while the two-dimensionality improvement tests were in progress. These tests are described in a later section. No photos have been taken with this method.

Other flow visualisation tests were made to see the secondary flow vortices near the side walls. Some preliminary tests were carried out to obtain the best photos.

The first test was to evaluate the colour effect of the dyes on the photo. Yellow, red and black dyes were tested. The dye was mixed with clean paraffin and painted on the surface with a brush. Immdediately after, the rig was run until the paraffin dried out. Polaroid photos were taken to see the contrast of the pattern. Two 100 W lights were used. The thickness of the mixture of dye and paraffin was also tested. The powder colour full black was found to be the best on the photo.

The photo is shown in fig. 2-16. A large vortex is clearly seen at the corner of the side wall and the surface.

2-5-3 Momentum Flux

Launder and Rodi (1981) recommended that two-dimensionality should be judged by close satisfaction of the two-dimensional momentum integral equation. They also commented that the near uniformity of the flow at different spanwise locations was, on its own, not regarded as strong evidence of two-dimensionality. For this purpose, the momentum flux ratio M/Mo was calculated at the various X stations.

$$\frac{M}{Mo} = \frac{1}{U_j^2 b} \int_o^\infty U^2 dy = \left(\frac{Um}{U_j}\right)^2 \frac{Y_{\frac{1}{2}}}{b} \int_o^\infty \left(\frac{U}{Um}\right)^2 dy/Y_{\frac{1}{2}} . \qquad (2\text{-}2)$$

Ten different modifications were tested. The sketches of these modifications are shown in fig. 2-17.

At first, three tests were made which concentrated on the first part of plane surface.

(1) A higher wall on the slot casing to reduce separation effect.

(2) Higher side walls to reduce separation effects.

(3) Extra side walls to cut off boundary layer developments on the side walls.

These tests showed approximately 7% improvement in momentum flux at X = 300mm. This demonstrated the possible improvements in two-dimensionality. Further tests were carried out.

(4) The joints between the surface and the side walls were not smooth, so that these were carefully smoothed.

The result was however surprisingly worse.

(5) The secondary vortex cut off plates were installed.

The plates were fixed at $Y = 2 \cdot Y_{\frac{1}{2}}$ and the width was $Y_{\frac{1}{2}}$. The plates made only slight improvement at X = 300mm, however at further downstream stages showed impressive improvement.

(6) (5) was tested with higher walls.

There was no effect on the momentum flux.

(7) Even higher side walls were tested.

The result showed remarkable change for the worse.

(8) The higher wall on the slot was removed and triangle panels were fixed to reduce vortex effects induced by the corners of the high walls and original side walls.

The result was even worse.

(9) The vortex cut off plates were removed from (8).

The momentum flux recovered and slightly better than (5).

Some further tests were carried out with modification (9).

The final arrangement consisted of two sets of wings and extended side walls. The M/Mo versus some X stations graph with no modification, (6), (9) and the final arrangement are shown in fig. 2-18. The values of Mo is not exactly U_j^2 x b because of the boundary layers on the upper and lower surfaces of the slot. Therefore the values of M/Mo should be regarded with this fact.

2-5-4 Spanwise velocity profiles

Near uniformity of the flow at different spanwise locations gives some kind of evidence for two-dimensionality, althought it is not regarded as strong evidence.

Spanwise velocity profiles were measured at X = 300mm at Z = +150, 0 and - 150mm. X = 600mm at Z = +125, 0 and - 125mm. These are shown in fig. 2-19(A) and 2-19(B) respectively. These measurements were made after the two-dimensional improvements which have been described in section 2-5-3.

At X = 300mm, it can be seen that the mean velocity is within 1.6% even at the edge of the jet. At X = 600mm, the profiles are less uniform than those at X = 300mm. The mean velocity varies approximately 5% at half-width of the jet. This is thought to be caused by the secondary vortices because these vortices are developed rapidly on the curved surface as has been shown in the flow visualization photos.

FIG. 2-1 DUCTING ARRANGEMENT

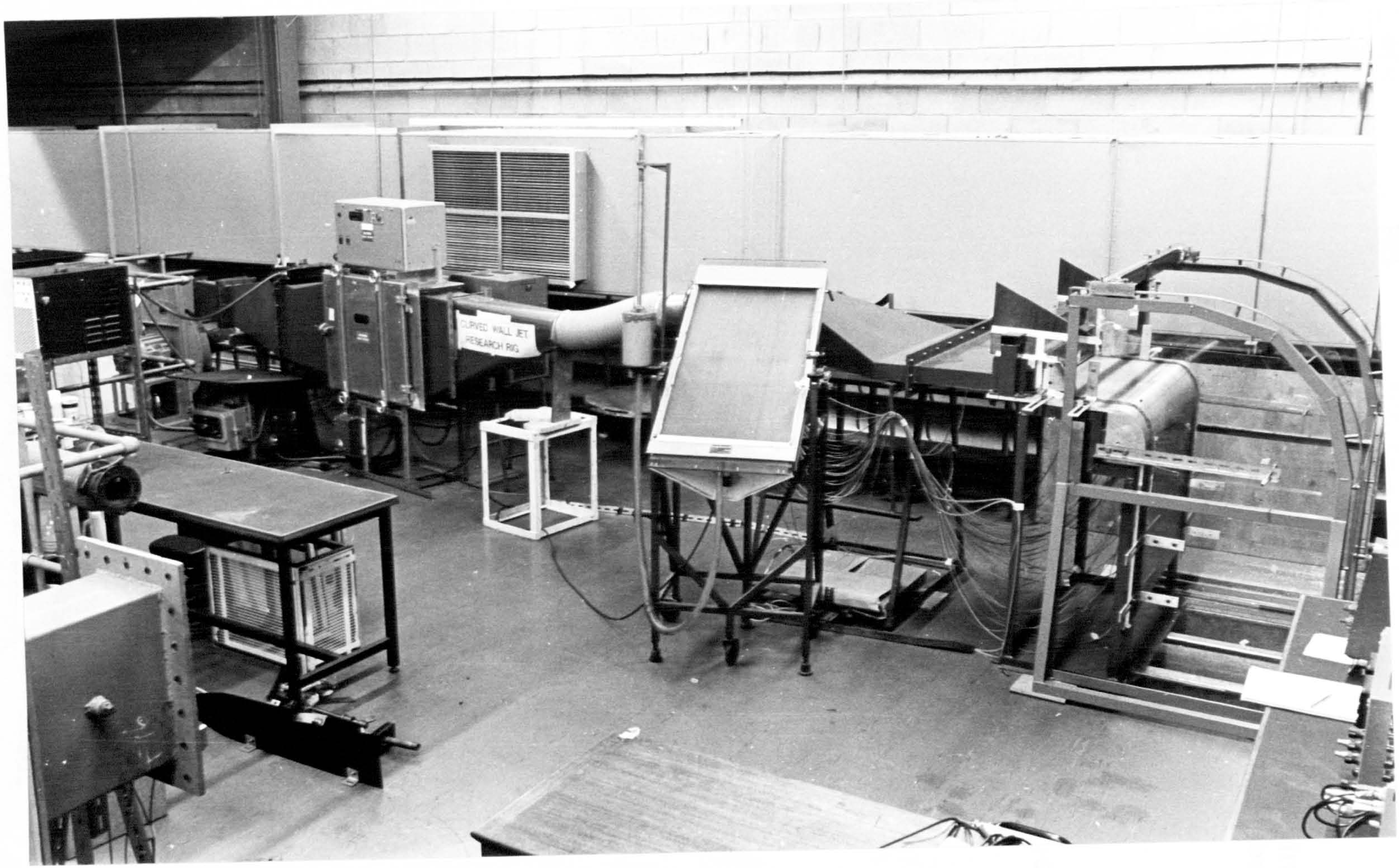

FIG. 2-2 DUCTING ARRANGEMENT

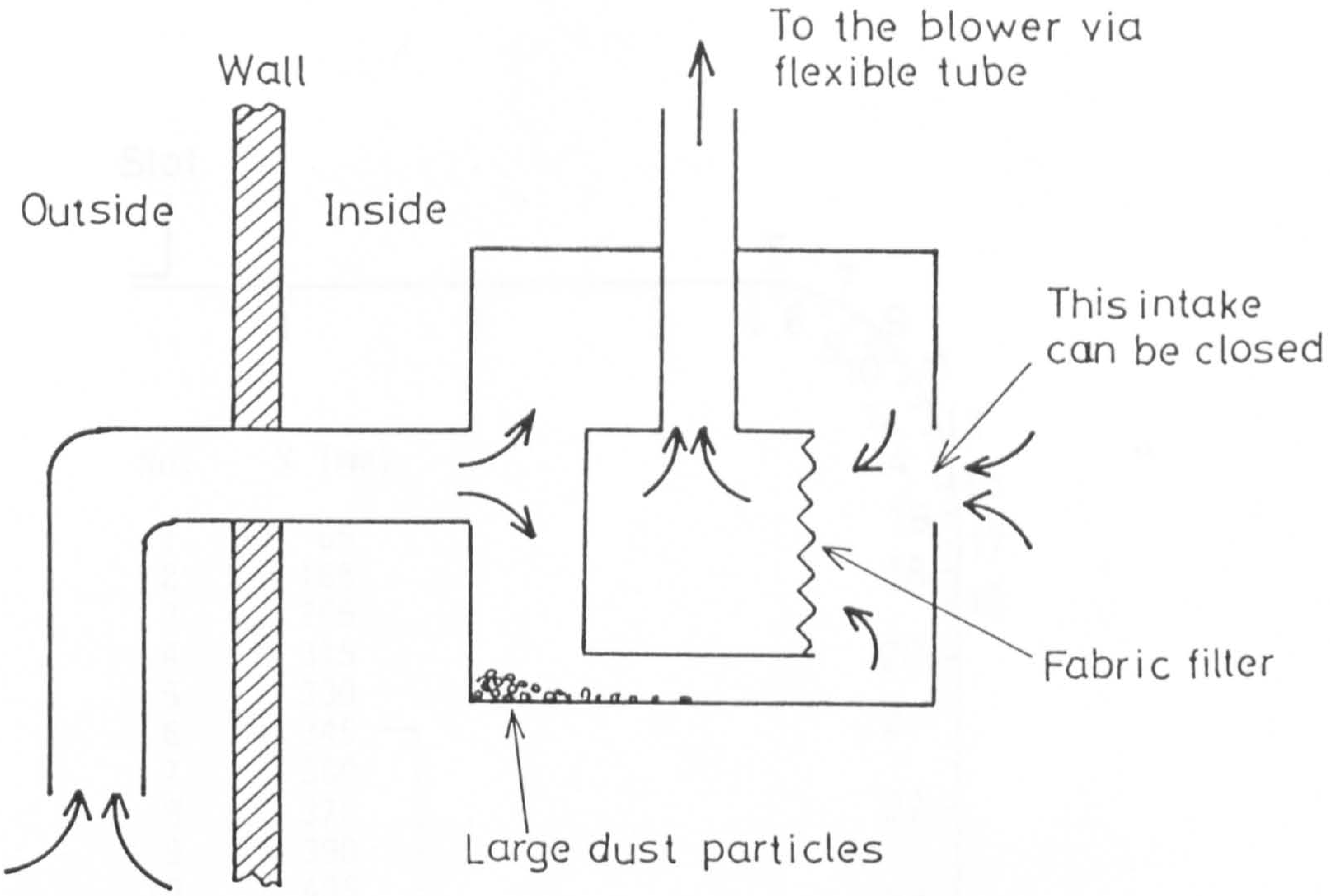

FIG. 2-3 AIR INTAKE ARRANGEMENT

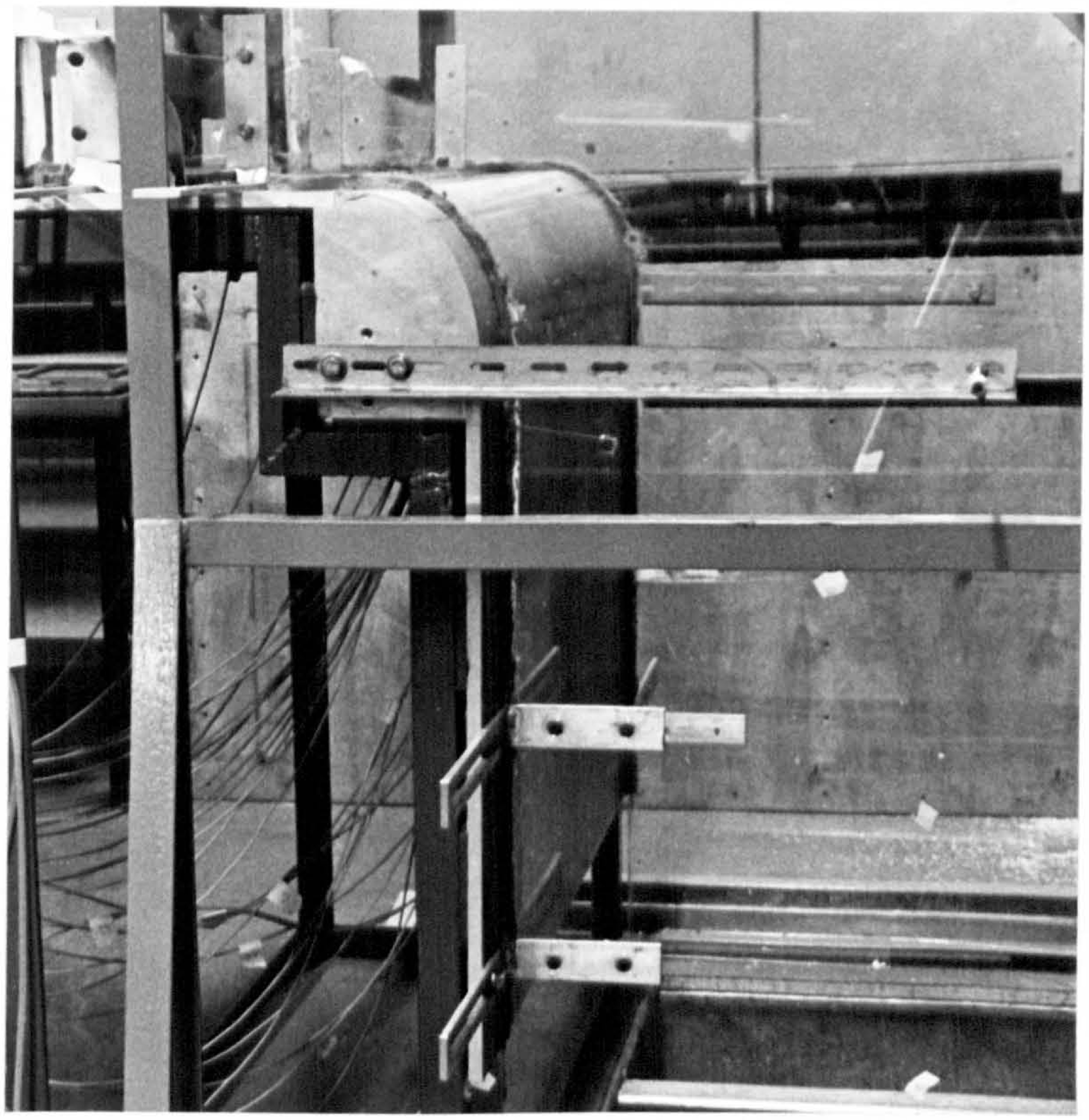

FIG. 2-4 SURFACE

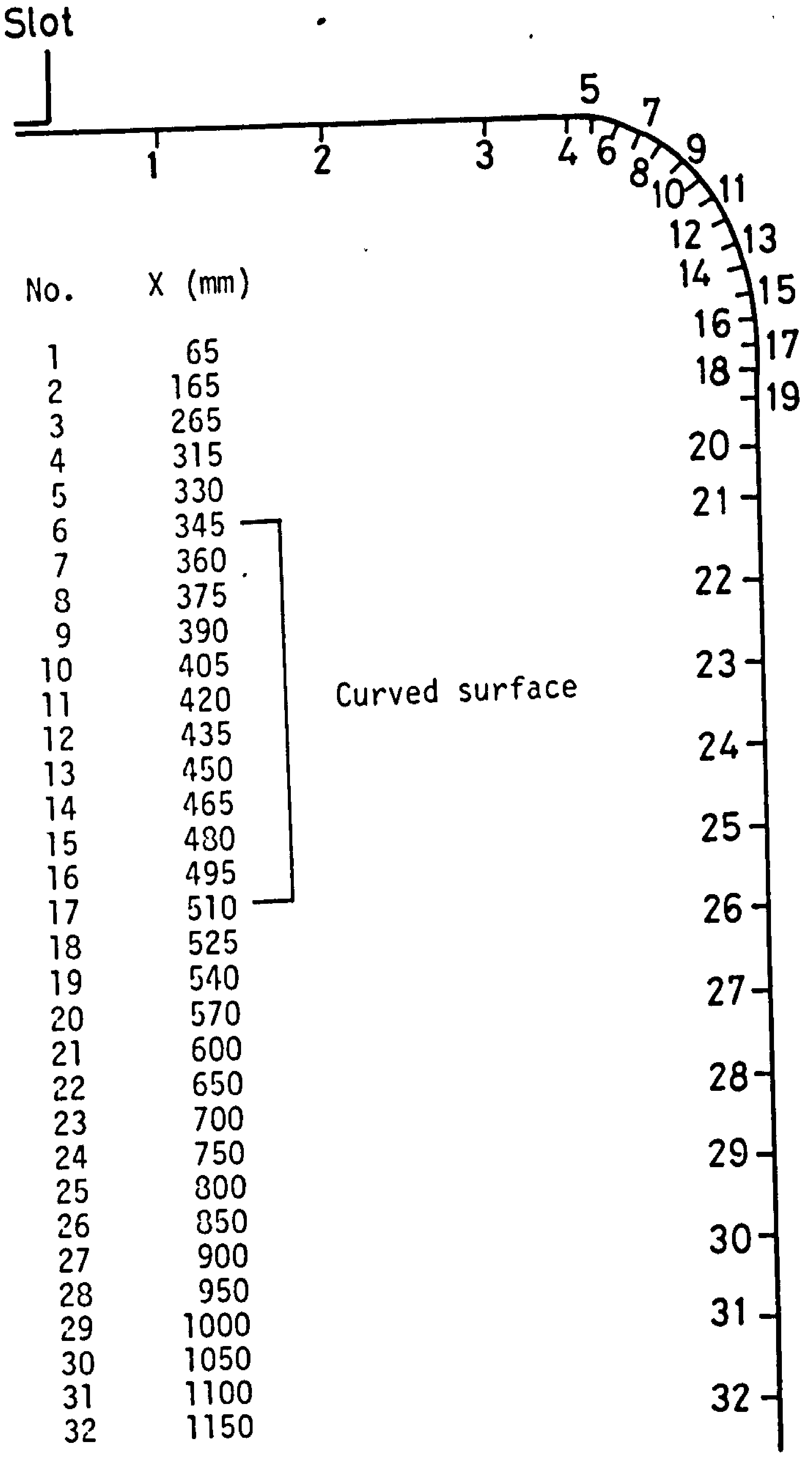

No.	X (mm)	
1	65	
2	165	
3	265	
4	315	
5	330	
6	345	Curved surface
7	360	
8	375	
9	390	
10	405	
11	420	
12	435	
13	450	
14	465	
15	480	
16	495	
17	510	
18	525	
19	540	
20	570	
21	600	
22	650	
23	700	
24	750	
25	800	
26	850	
27	900	
28	950	
29	1000	
30	1050	
31	1100	
32	1150	

FIG. 2-5 SURFACE AND STATIC TAPPINGS

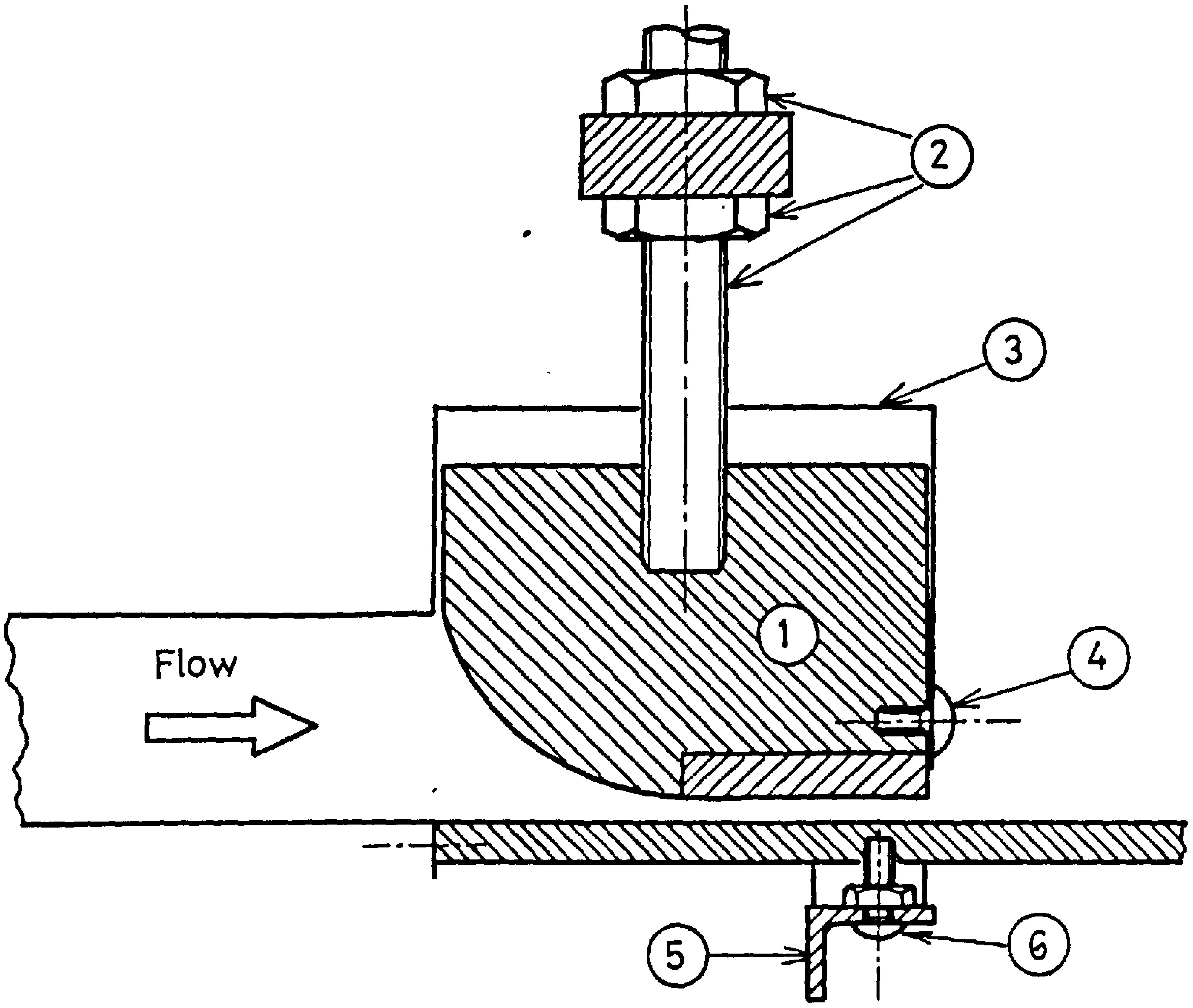

FIG. 2-6 SECTION VIEW OF SLOT ASSEMBLY

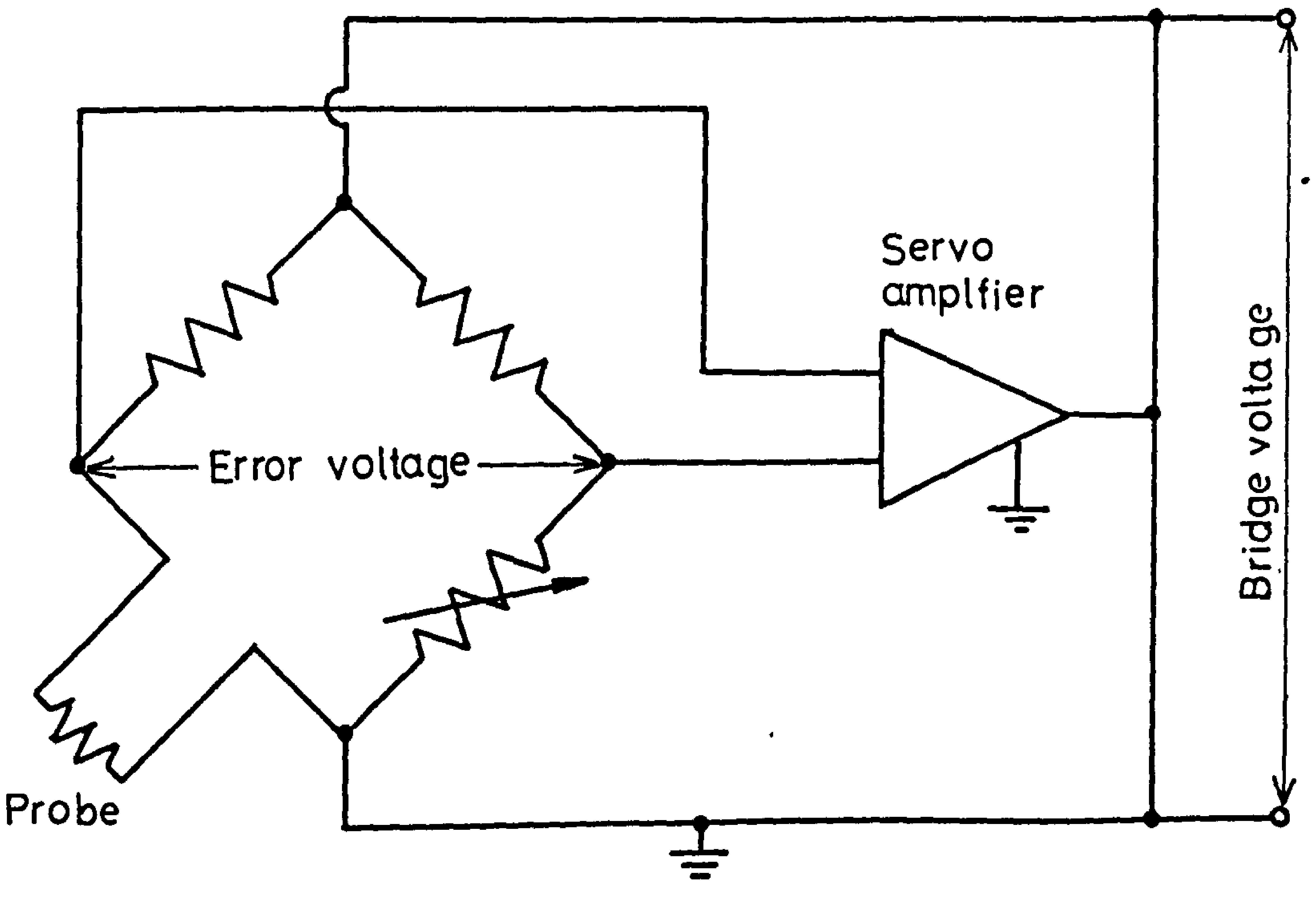

FIG. 2-7 PRINCIPLE OF C.T.A.

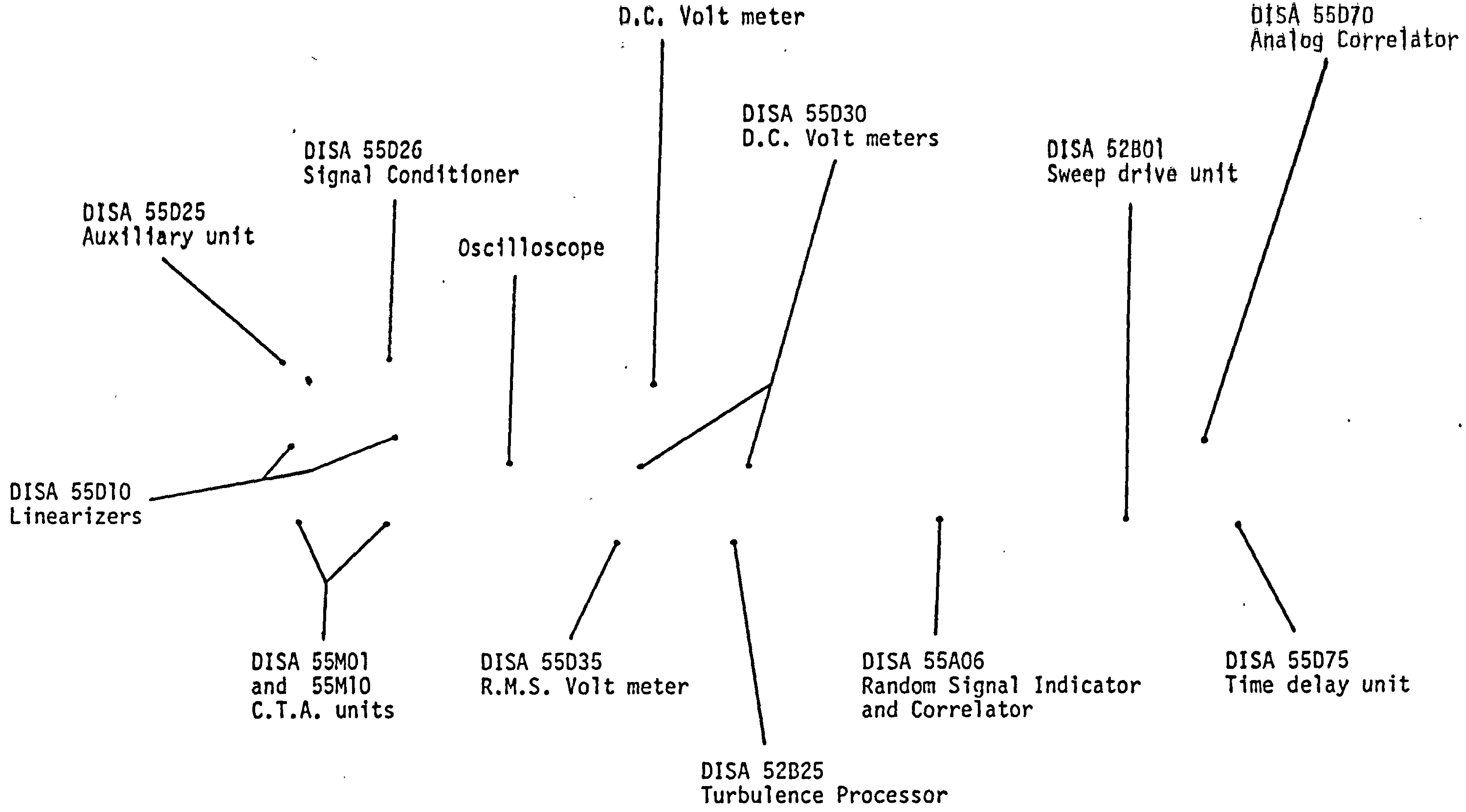
D.C. Volt meter
DISA 55D70
Analog Correlator
DISA 55D30
D.C. Volt meters
DISA 52B01
Sweep drive unit
DISA 55D26
Signal Conditioner
DISA 55D25
Auxiliary unit
Oscilloscope
DISA 55D10
Linearizers
DISA 55M01
and 55M10
C.T.A. units
DISA 55D35
R.M.S. Volt meter
DISA 55A06
Random Signal Indicator
and Correlator
DISA 55D75
Time delay unit
DISA 52B25
Turbulence Processor

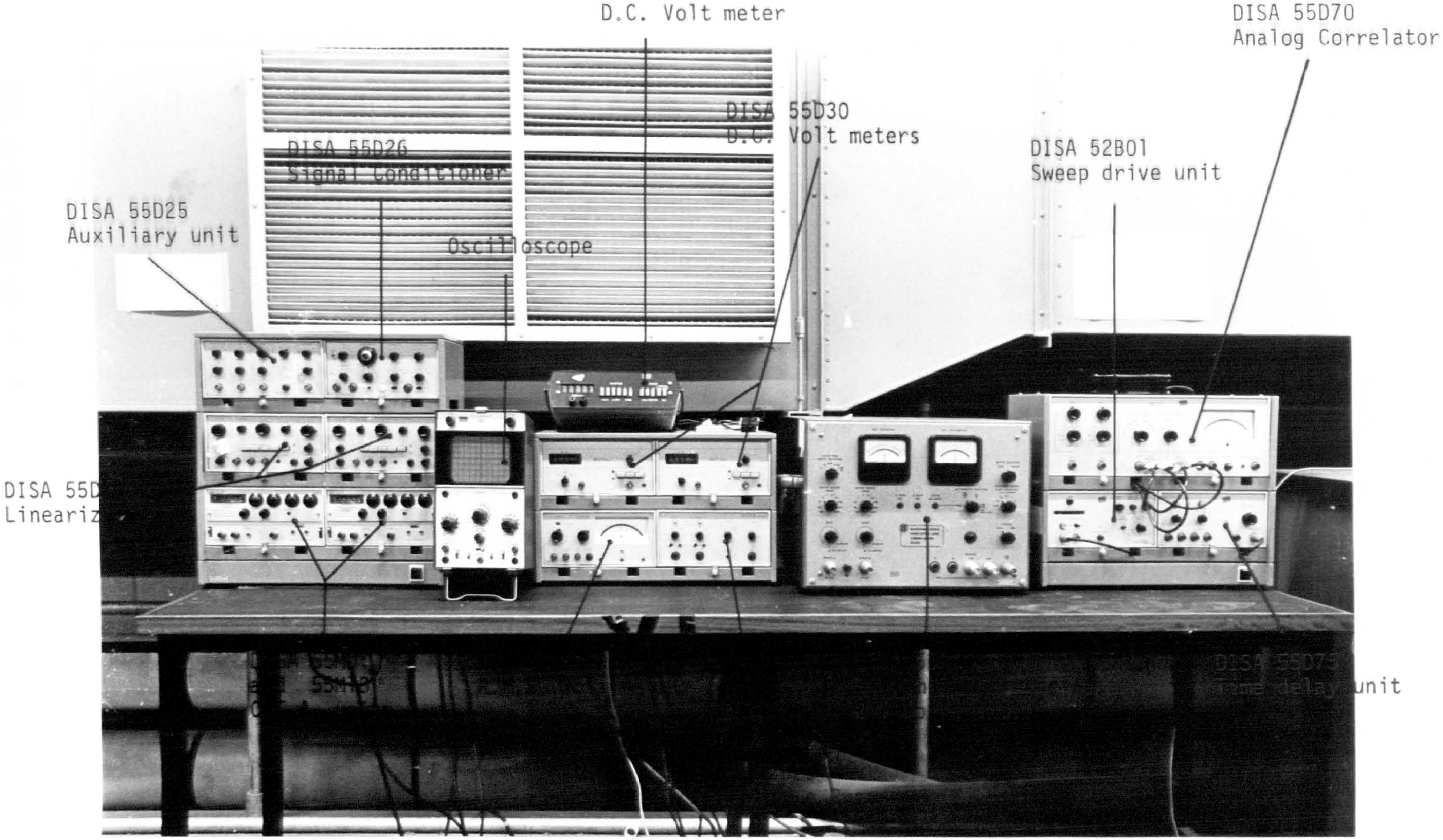

FIG. 2-8 INSTRUMENTS

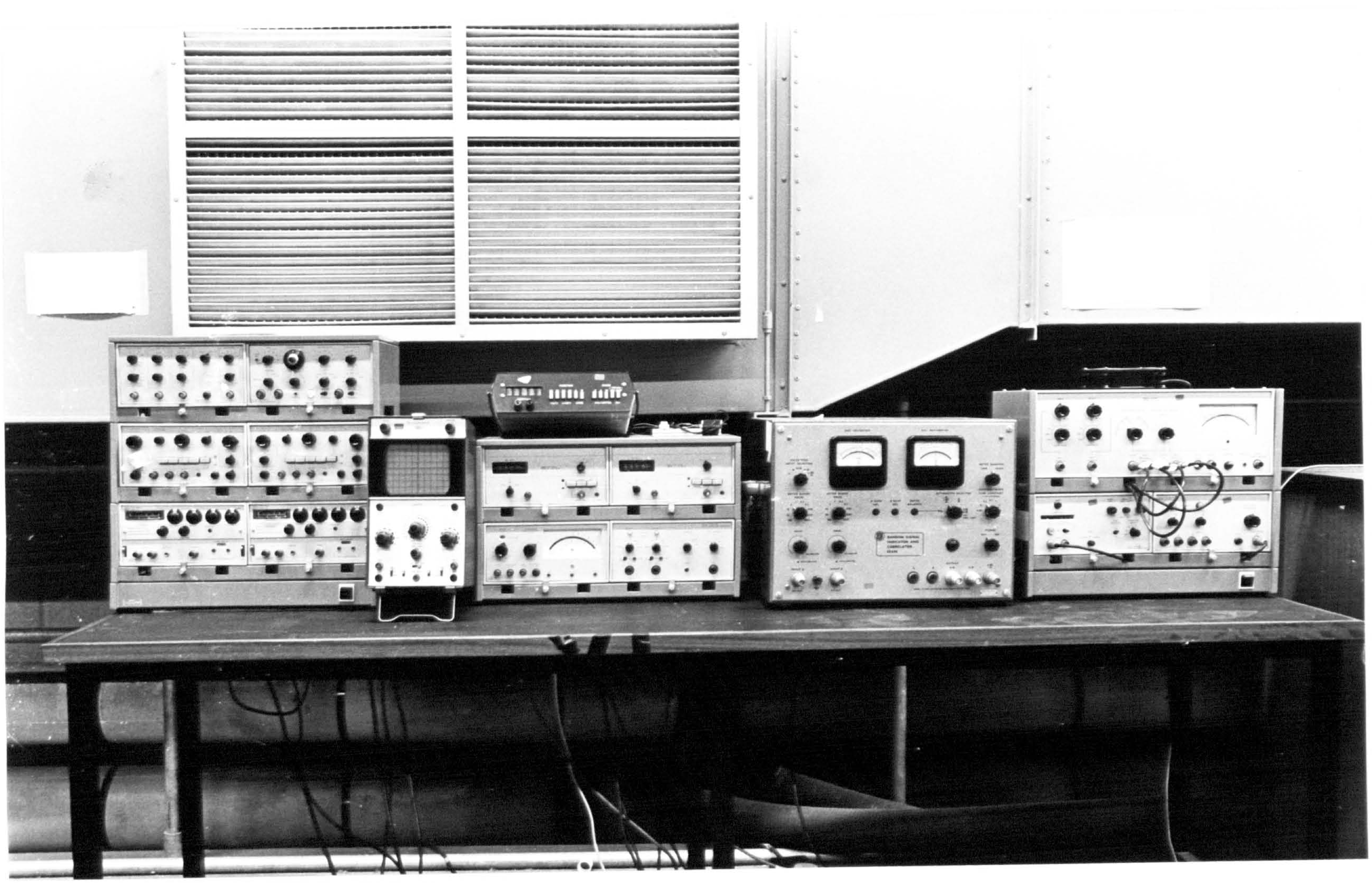

FIG. 2-8 INSTRUMENTS

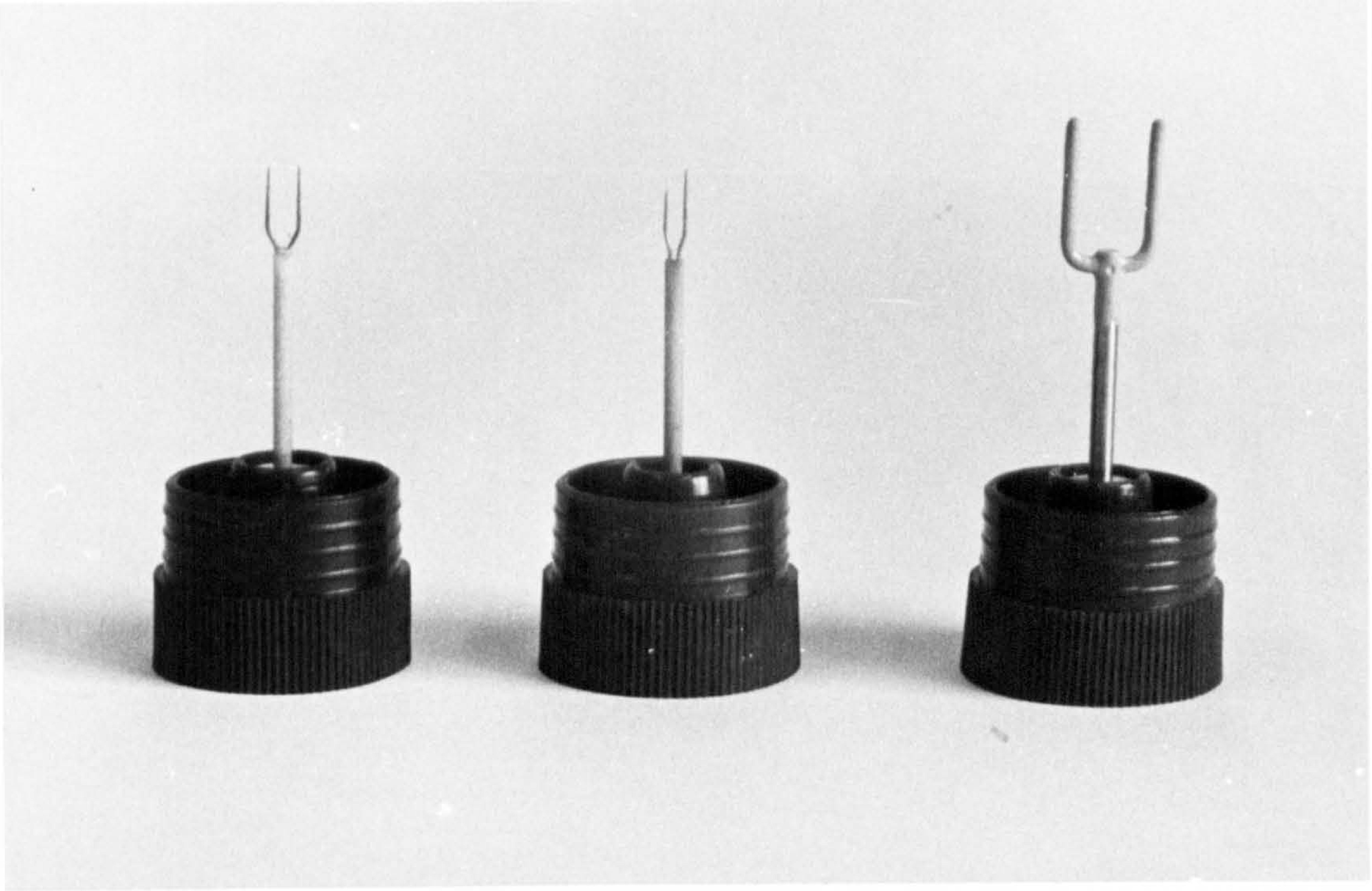

FIG. 2-9 GOLD-PLATED HOT-WIRE PROBES AND REPLACEMENT WIRE MAGAZINE

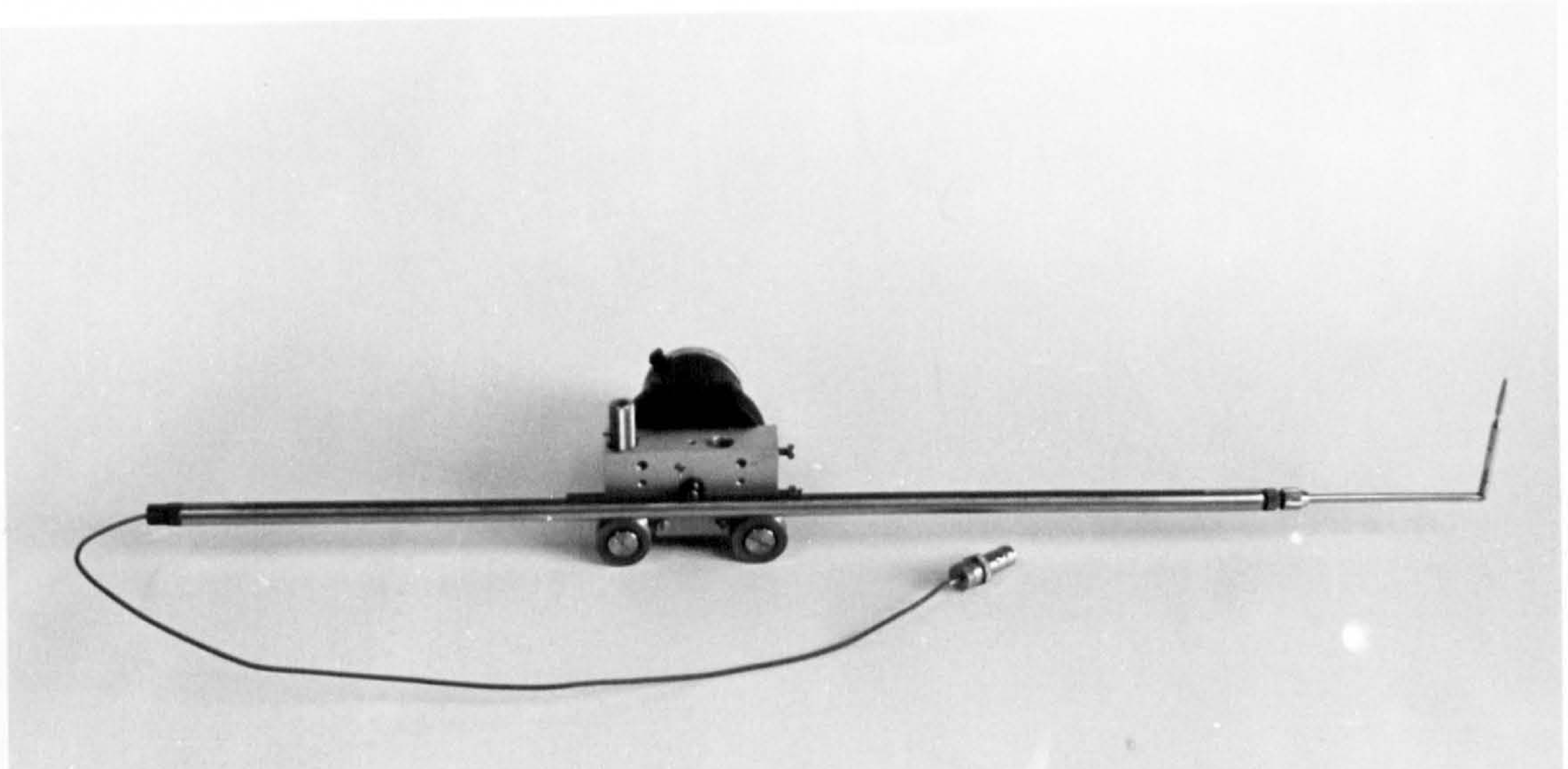

FIG. 2-10 PROBE SUPPORT

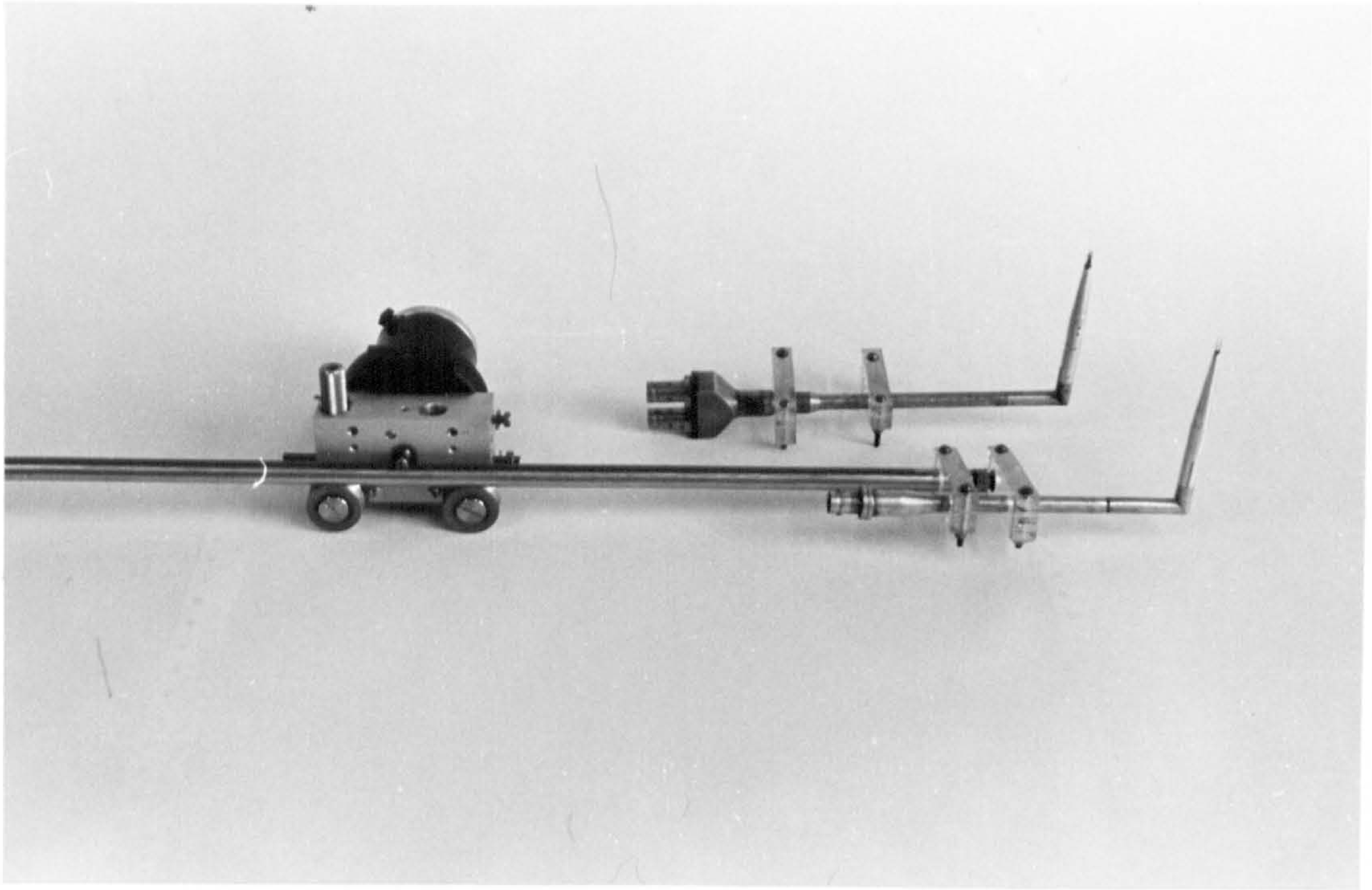

FIG. 2-11 SINGLE WIRE, X-WIRE PROBES AND THEIR SUPPORTS

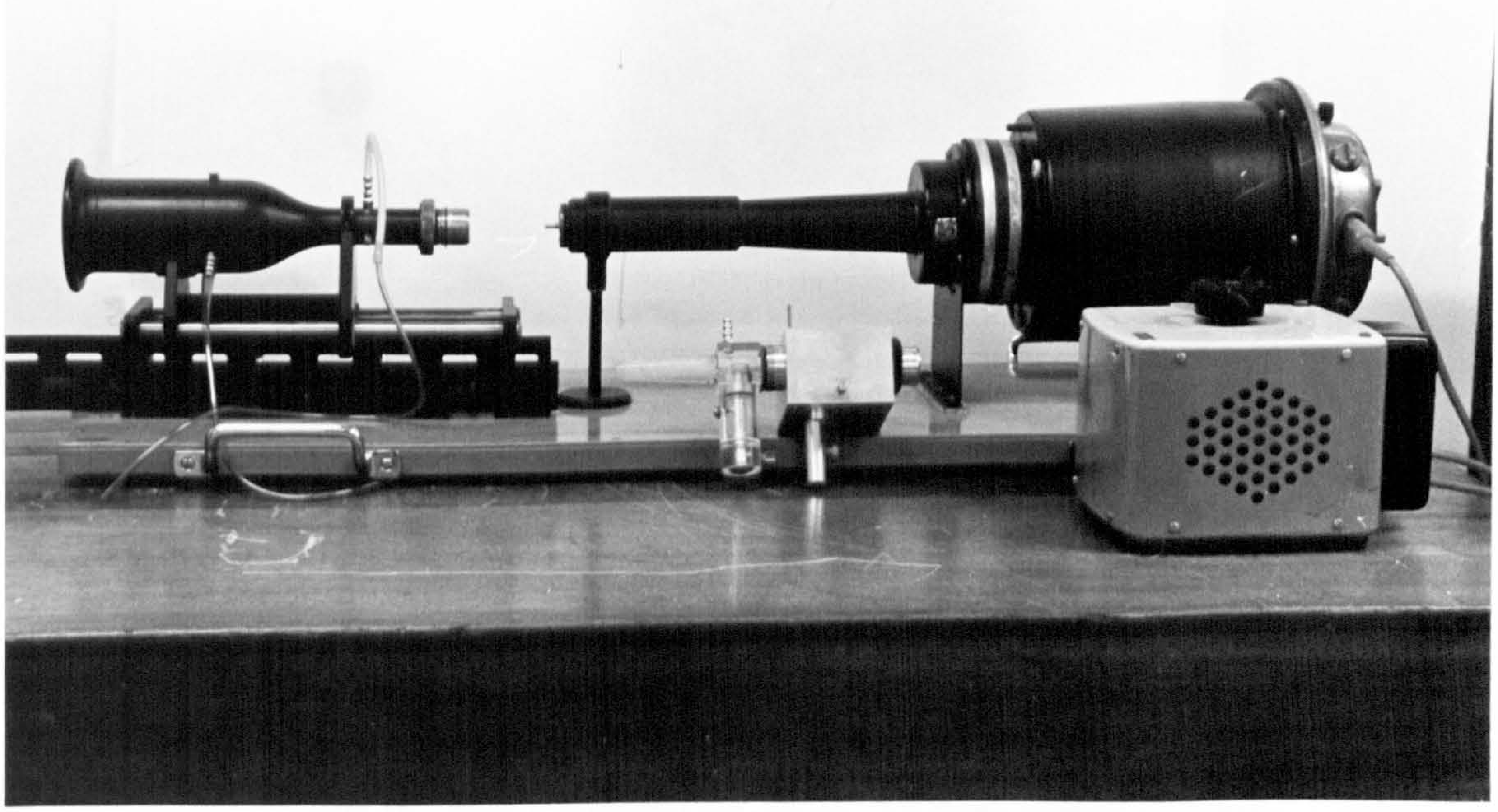

FIG. 2-12 CALIBRATION UNIT AND ADAPTERS

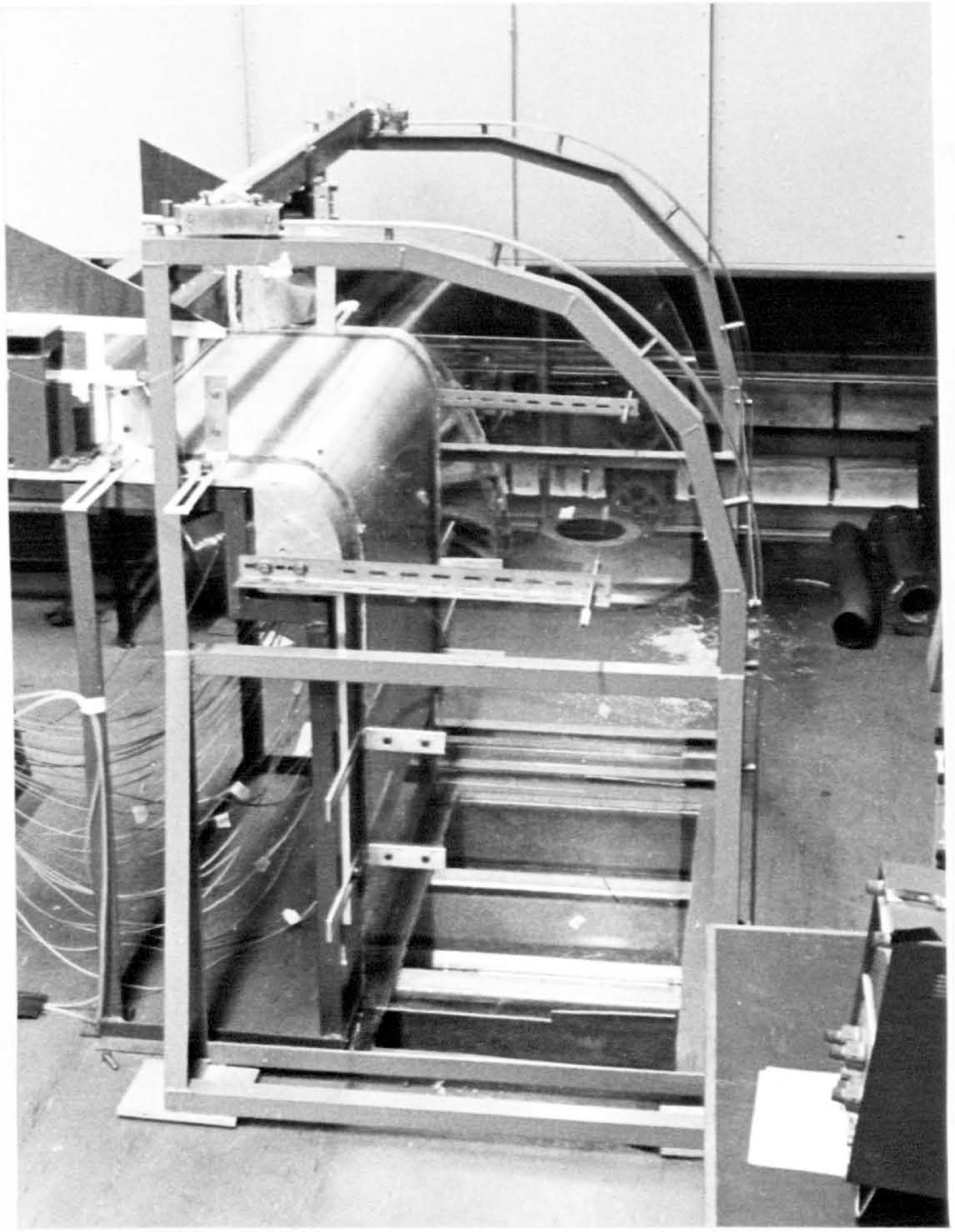

FIG. 2-13 TRAVERSING FRAME

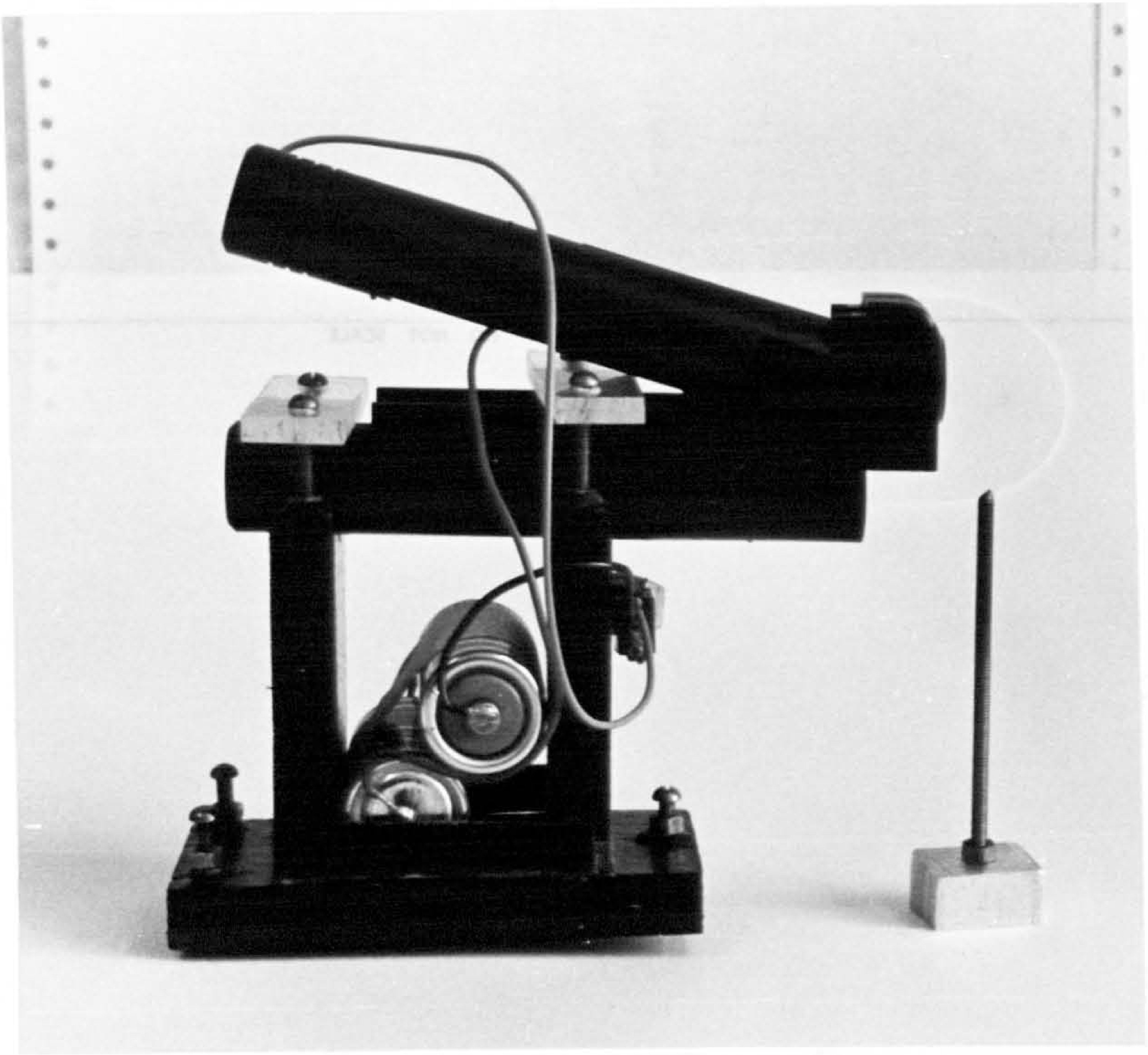

FIG. 2-14 PROBE POSITIONING DEVICE

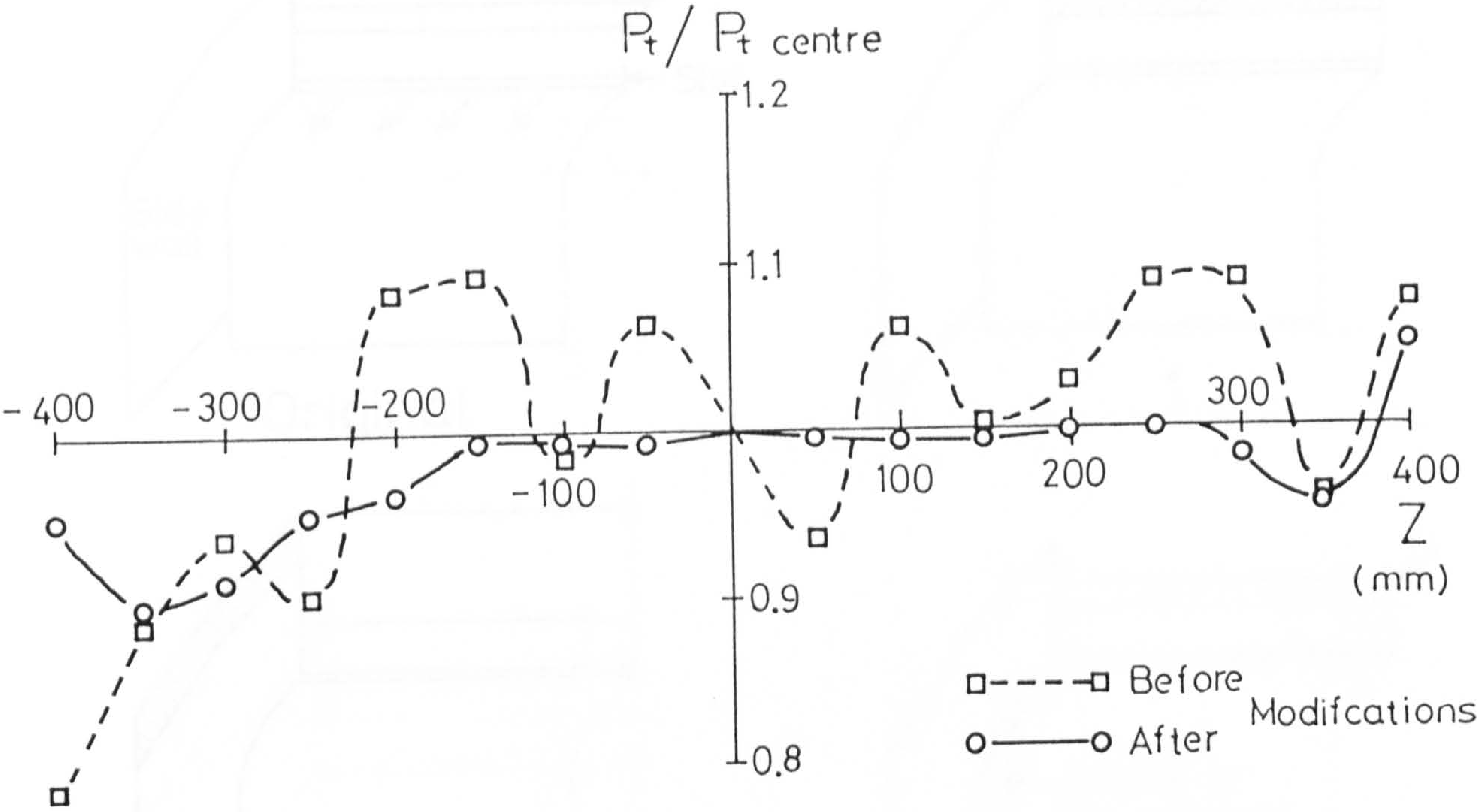

FIG. 2-15 SPANWISE TOTAL PRESSURE DISTRIBUTION AT X=300mm

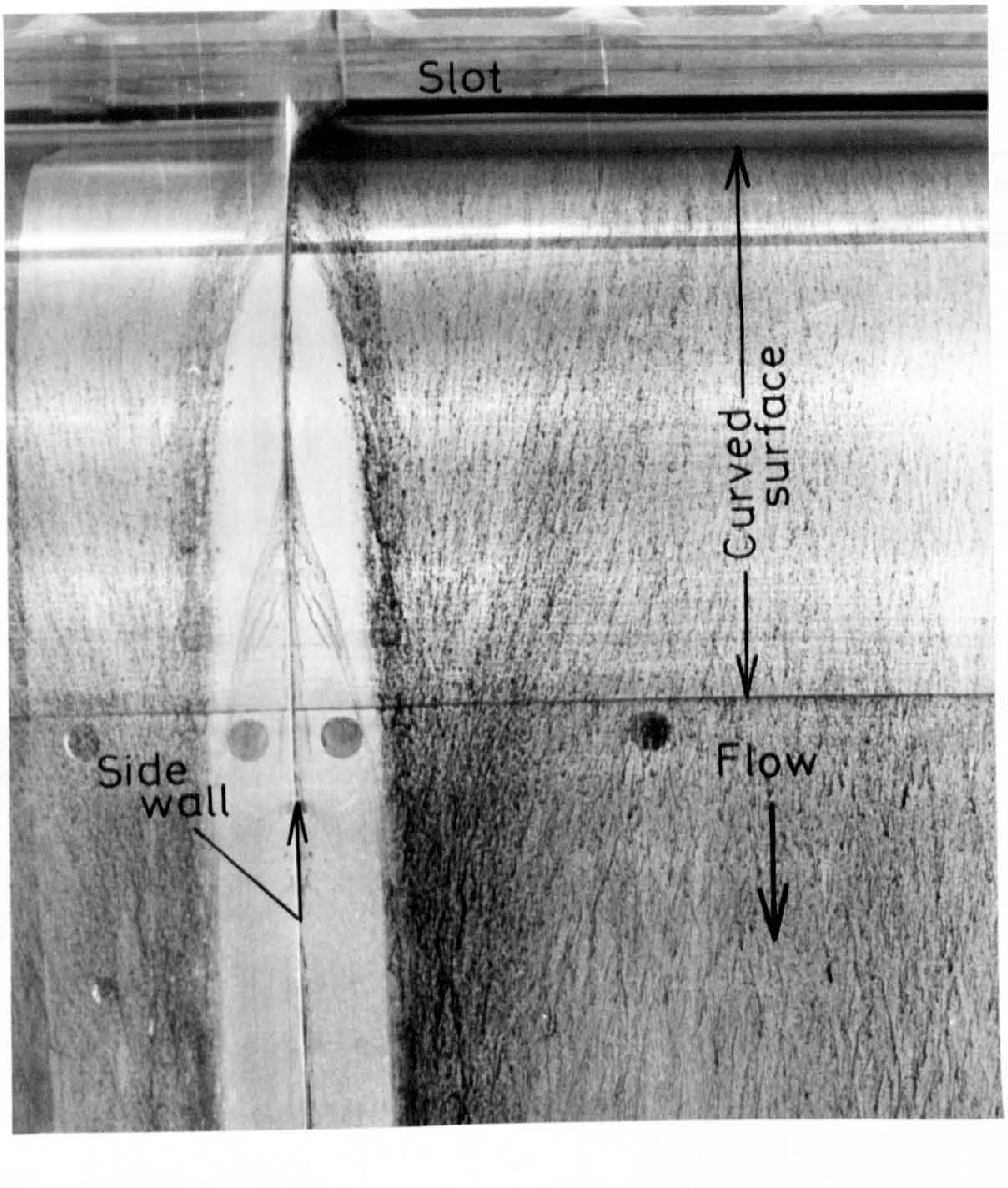

FIG. 2-16 FLOW-VISUALIZATION, SECONDARY VORTEX NEAR A SIDE WALL

FIG. 2-17 MODIFICATIONS TO IMPROVE TWO-DIMENSIONALITY

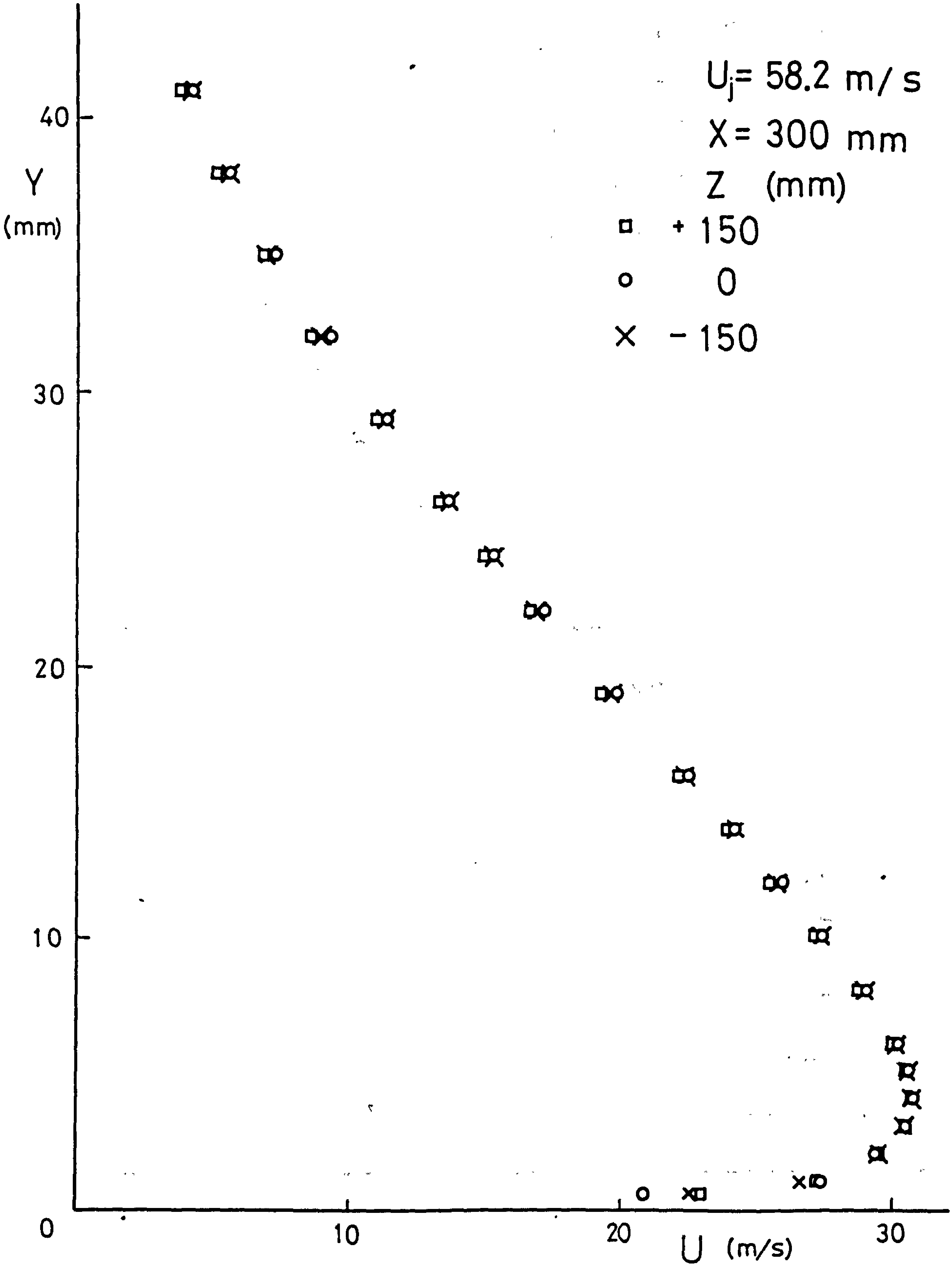

FIG. 2-19(A) SPANWISE VELOCITY DISTRIBUTION AT X=300mm

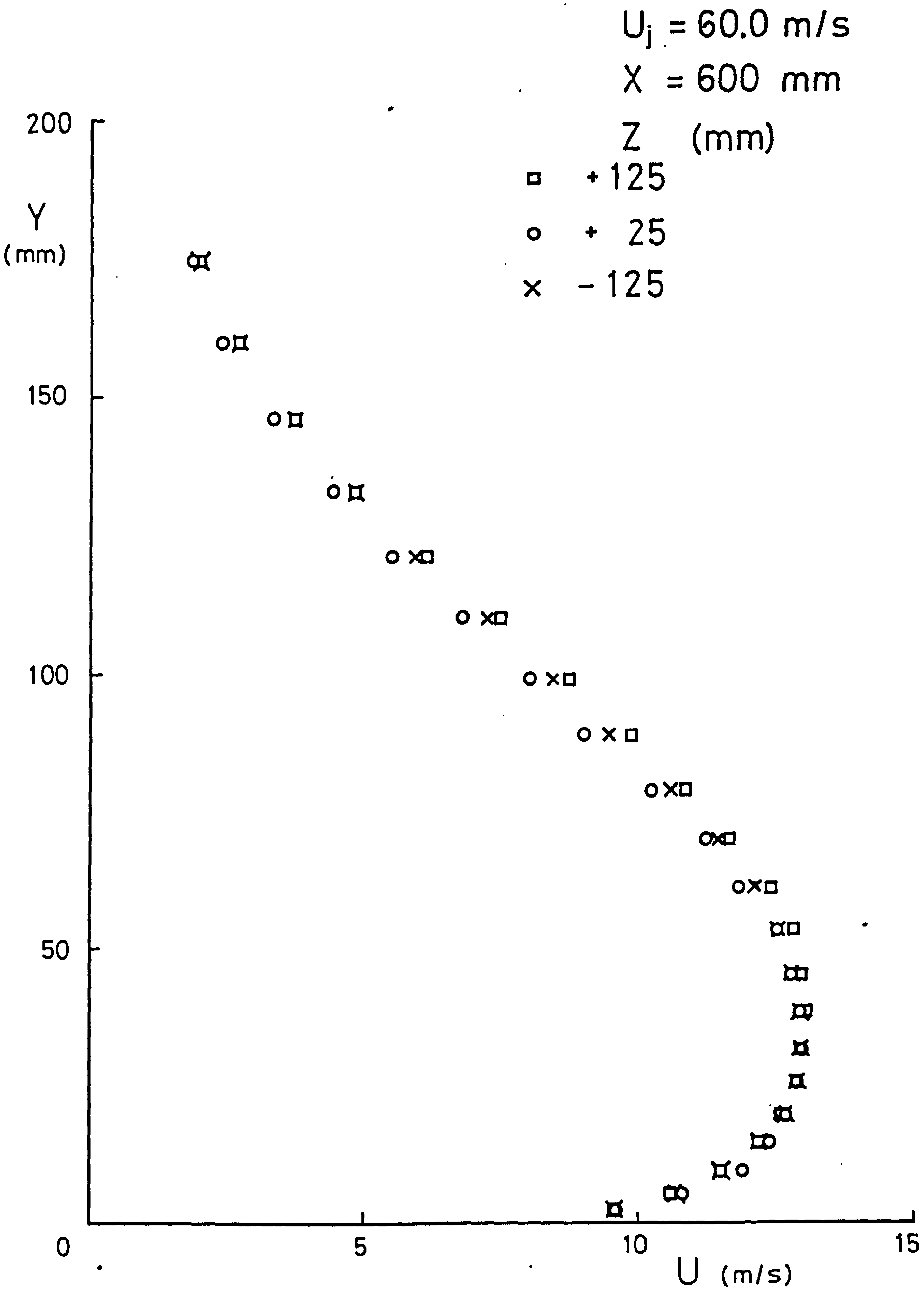

FIG. 2-19(B) SPANWISE VELOCITY DISTRIBUTION AT X=600mm

CHAPTER 3

MEASUREMENTS

CHAPTER 3 MEASUREMENTS

3-1 Hot-wire measurement and its problems

At the very first stage of the research work, mean velocity measurements by total head tube were considered. There is a divergence of opinion about the use of hot-wires for mean velocity meausrements because of the calibration drift caused by such as dust accumulation on the wire or flow temperature change. These problems are discussed later in this chapter.

Fekete (1963) made a comparison between velocity profiles taken by hot-wires and by total-static probes on a two-dimensional wall jet on the outside of a circular cylinder. This showed considerable discrepancy. After a further test, he concluded that velocity measurements with hot-wire in highly curved flows were likely to be more accurate than those measured by total-static tubes.

Hot-wires were used, therefore, for all velocity measurements.

3-1-1 Operation procedure and adjustments

Operations of the hot-wire anemometer and other instruments were made under the instructions of the manufacturer's user's manuals. Some extra care was taken to obtain better accuracy.

'The wire was placed under a microscope and its condition such as straightness, weldings and cleanliness were examined. If it found to be unacceptable, the wire was cleaned or replaced. The cleaning procedure is described in the next section.

The wire resistance was measured at room temperature by the anemometer after balancing out the cable and support resistances. The overheat ratio was chosen to maintain the wire at an air temperature difference of approximately 250°C.

The anemometer's frequency response adjustment was made by means of a square wave test. This test was repeated only when a cleaned or new wire was introduced.

In a highly intermittent flow, both D.C. and R.M.S. Voltmeters had to be set at long time constants. In order to obtain the time response of these meters, some tests were made. An example of D.C. Volt meter time response is shown in fig. 3-1. In this example, 1 D.C. Voltage was supplied to the meter and the time and the readings were taken with the damping rate No. 3 plus one capacitor.

3-1-2 Temperature effect

One of the parameters which effects hot-wire measurement is temperature. Temperature change or fluctuation, therefore, causes significant error. Bradshaw (1971) showed the effect of fluid temperature in his book. In air, 1°C temperature change may produce an error of 2% in mean velocity. Thus, it is important to keep the jet temperature constant throughout the run. Since the decision to use DISA calibration unit, it is also important to keep the jet temperature equal to the room temperature. The air temperature of the working section of the calibration tunnel is approximately equal to the room temperature. The advantage which results from the adjustment to keep the jet temperature equal to the room temperature has less effect from the temperature fluctuation. Because the temperature difference between jet and entrainment flow is small, there is hardly any temperature fluctuation.

In order to make the above conditions possible, some modifictions to the test rig were made.

Originally, the rig was fitted with a small heat exchanger. The device consisted of several brass tubes in a 4in. diameter duct. The tubes were parallel to the flow direction. This comparatively small area duct made flow velocity very high. This caused a significant flow resistance and also required low cooling water temperature because of the low heat transfer rate. The lower cooling water caused a thermal contraction which led to water leakage. Therefore, an entirely new ducting fitted with a car radiator was designed.

Even after the new arrangement was introduced, it was found to be difficult to keep jet temperature low enough, especially on sunny days. The reason thought to be likely was the construction of the laboratory. The deck, where the rig was placed, had a kind of prefabricated construction. This was built after the laboratory itself had been built. Therefore, when the air conditioning system was designed there was no allowance for an upper deck. As a result of this fact, the upper deck is usually 2°C warmer than the lower floor. Also on a sunny day, there is an extra heat from the tinned roof in the laboratory where there is no ceiling resulting even higher temperature on the upper deck.

As it was mentioned above, the temperature on the lower floor was constantly lower than the upper deck. On the other hand, the outdoor temperature was sometimes found even lower than the lower floor. The decision was made to carry out another modification. The air intake was placed on the lower floor and air could be taken either from the lower floor or outdoor. This was dependent on the temperature difference between upper deck, lower floor and outdoor. Another small water cooler was also added in the system.

These series of improvements made for satisfactorily result except a very hot sunny day in summer. In this case, experiments had to be carried out during the night before dawn.

All the measurements were taken after at least 15 minutes warm up run to stabilize the flow temperature.

3-1-3 Dust effect

Dust accumulation on the wire can cause large changes in probe calibration and the frequency response. Some detailed investigations were carried out by Morrow (1972) and Martinez-val, Jimenez & Rebollo (1982).

A change in probe calibration without a change in cold resistance is usually caused by a thin layer of dirt on the wire. Large particles on the wire are easily detected by microscope. Relatively large dust, say larger than 5 μm, can also easily be removed from the flow by means of fabric filters.

Smaller particles or fume are, on the other hand, very difficult to detect and remove. Even after the temperature problem had been solved, there was a considerable calibration drift. The drift was as much as 10% only after 30 min. exposure in the flow and varied day by day. An example of calibrations is shown in fig. 3-2. These calibrations were made just before and after the wire was exposed in the jet.

Several causes were considered.

(1) Jet temperature change - this was solved.
(2) C.T.A. cable resistance out of balance - this was found negligible.
(3) Atmospheric pressure change - this was negligible.
(4) C.T.A. or linearizer fault - tests were made to compare other systems and found no difference.
(5) Lack of instruments warm up - a comparison was made with 30 min. and 4 hours warm ups and found no difference.
(6) Cold resistance change for some reason - there was negligible change in cold resistance.
(7) Probe failure for some reason - tests were made with some various probes and no difference found.
(8) Electrical connection failure - all connectors and cables were cleaned and checked. There was no failure.

As the result of these considerations, only wire contamination could cause such a large calibration drift. The probe was cleaned and recalibrated. The results on fig. 3-3 show clear evidence of wire contamination.

The best way of cleaning a wire may be to immerse it in an ultrasonic solvent bath. This method is very effective for the most types of probes. Nevertheless, the gold-plated wire probes are physically weaker than the others because of its wider spacing between prongs. These types of probes could be damaged while in the bath. Wyatt (1953) applied a technique, soaking the wire in a solvent liquid and vibrating the container by means of a loud speaker. This method could remove 80 to 90% of the dust on the wire. Since the present tests required only to detect the cause of the drift, a simpler technique was chosen. This was suggested by Lim (1980). The probe was soaked in a container filled with trichloroethylene for several hours.

All the ducts were cleaned and filters were replaced with new Vokes Air Filters Ltd. Multi-vee fabric air filters. However, the result showed the same amount of calibration drift.

Finally, the decision was made to install an electrostatic filter. The new ducting was designed and made in the work shop. A Sturtevant Unicell type 12W 24H electrostatic filter was installed just downstream of the heat exchanger. According to the catalogue, it is able to remove over 95% of atmospheric dirt and other debris smaller than 5μm compared with 50 to 75% with fabric filters. The efficiencies depend on the dust particle size and flow velocity.

The tests showed remarkable achievement on the calibration drift. The probe was exposed in the jet over three hours, which was needed to measure turbulence intensity normal to the flow direction, the drift of calibration found to be negligible.

3-2 Mean velocity and turbulence intensity

Mean velocities and turbulence intensities in all X, Y and Z directions were taken at following X stations. X = 200 and 300mm on the first plane surface, X = 350, 400, 450 and 500 mm on the logarithmic spiral surface, and X = 550, 600, 700, 850 and 950mm on the second plane surface. Z = 25.0mm for all stations to avoid the interference of the static tappings which were positioned on the centre of the surface. Fig. 3-4 shows the measured stations on the surface.

3-2-1 Instrumentation

No X-wire probe was used for the measurements. Jerome, Guitton and Patel (1971) studied the thermal wake interference between wires. In a high turbulence intensity flow, the use of X-wire probe may cause significant error. In the present work, the jet is indeed a high turbulence intensity flow. Accordingly, the measurements were made with a straight and a 45° slanting single wire probes.

Fig. 3-5 shows the circuit of amemomemtry system. The error which may arise from fluctuating signals due to the non-linearity is conveniently removed by linearizer. The signal has a relationship

$$E = Uce/C \qquad (3\text{-}1)$$

where E is the output signal from the C.T.A. system, Uce is the effective cooling velocity which velocity component is normal to the wire in a calibration condition and C is the calibration factor.

If the velocity in the calibation tunnel is Uc , the calibration factor is

$$C = Uce/E = Uc \sin \psi/E \tag{3-2}$$

where ψ is the angle of the wire to the flow, 90^o for straight wire probe and 45^o for slanting wire probe.

In linearized operations the following positions and values are defined. The positions are shown in fig. 3-6.

$$U_{c1} = C_1 E_1 \tag{3-3}$$

$$U_{c2} = C_2 E_2 / \sin \psi \tag{3-4}$$

$$U_{c3} = C_3 E_3 / \sin \psi \tag{3-5}$$

$$U_{c4} = C_4 E_4 / \sin \psi \tag{3-6}$$

$$U_{c5} = C_5 E_5 / \sin \psi \tag{3-7}$$

where subscripts C refer to calibration conditions and numbers denote the positions.

The determination of mean velocities and turbulence intensities are from the equations

$$U = U_{c1} \tag{3-8}$$

$$V = \frac{U_{c3} - U_{c2}}{2 \cot\psi} \tag{3-9}$$

$$\overline{u'^2} = \frac{U_{c1}}{E_1} \cdot \overline{e_1'^2} = C^2.\overline{e_1'^2} \tag{3-10}$$

$$\overline{v'^2} = \frac{\left(\frac{U_{c3}}{E_3}\right)^2 \cdot \overline{e_3'^2} + \left(\frac{U_{c2}}{E_2}\right)^2 \cdot \overline{e'^2} - 2\overline{u'^2}}{2 \cot \psi} \tag{3-11}$$

$$\overline{u'v'} = \frac{\left(\frac{U_{c3}}{E_3}\right)^2 \cdot \overline{e_3'^2} - \left(\frac{U_{c2}}{E_2}\right)^2 \cdot \overline{e_2'^2}}{4 \cot \psi} \tag{3-12}$$

$$\overline{w'^2} = \frac{\left(\frac{U_{c5}}{E_5}\right)^2 \cdot \overline{e_5'^2} + \left(\frac{U_{c4}}{E_4}\right)^2 \cdot \overline{e_4'^2} - 2\,\overline{u'^2}}{2 \cot \psi} \tag{3-13}$$

where small letters denote fluctuating portion of the signal.

The signal from the linearizer was fed to the signal conditioner in which low-pass filter was set 50 kHZ to cut off high frequency noise. This was followed by the R.M.S. Volt meter where $\overline{e'^2}$ was measured. The mean value of the signal E was measured by the DC. volt meter.

The time constants for DC. and RMS. volt meters depended on the X stations. High frequency response adjustment was made in the calibration tunnel. Usually, two of the slanting wire probe measurements of a velocity component, i.e. E_2, E_3, $\overline{e_2'^2}$ and $\overline{e_3'^2}$ or E_4, E_5, $\overline{e_4'^2}$ and $\overline{e_5'^2}$, were made at the same run to reduce possible error. This was done by rotating the probe 90° in its probe axis and the Y traverse was repeated.

3-2-2 Calibration

The calibrations of gold-plated wire probes were carried out in the DISA calibration tunnel with DISA adaptor section and a purpose made adapter section. The flow velocity in the working section, whose direction is parallel to the probe axis, was calculated from a reading of the static pressure difference ΔPs between nozzle inlet and the working section. The working section is located at the throat of the nozzle, which is the highest velocity region in the tunnel. The velocity U is calculated by the formula

$$U^2 = \frac{2k}{k-1} . R . To \left[1 - (1 - \frac{\Delta p}{Po})^{\frac{k-1}{k}}\right] \qquad (3\text{-}14)$$

where k is the isentropic exponent of the air and R is the gas constant, the values used being $k = 1.4$ and $R = 287$ (J/kg ^{o}k). To and Po are absolute temperature and pressure respectively. The temperature in the working section varies with the velocity of the flow in the section. However, even with the maximum flow velocity for the experiments, the difference between the flow and room temperature was found to be negligible.

After the probe was set in position, the variable transformer was adjusted to obtain the intended flow velocity. The pressure difference Δp was measured by a manometer which could be inclined if necessary. The Δp(i.e. velocity)was kept constant. We call this the "maximum velocity" for convenience. The linearizer output E was adjusted to 10 V. Then, the velocity was reduced to half the maximum velocity. If the linearizer output was not 5 V, this is an indication of signal non-linearity so that the exponent of the linearizer was re-adjusted. This procedure was repeated until the linearizer output became 10 V at the maximum velocity and 5 V when the half maximum velocity was applied. This looked somewhat more complicated and time consuming than the procedure described in the instruction manual of of the DISA unit. However, once the approximate value of exponent was discovered, the above procedure was simpler and quicker.

The probe was next rotated 90° and the maximum velocity was applied. If the linearizer output departed from 10 V, this was the indication of the probe misalignment. The probe axis angle to the flow direction was checked and the whole procedure was repeated. This check was especially important for the slanting wire probe calibration because probe misalignment could cause significant error.

The example of a calibration is shown in fig. 3-7(A). This shows smoothly linearized signal with the flow velocity. The calibrations were made just before and after the measurements. Usually, it took one and a half hours for a Y direction traverse. This meant it took approximately one and a half hours for straight wire probe and three hours for slanting wire probe between calibrations. If the discrepancy between the calibrations was found unacceptable, the experiment was repeated.

Calibrations for fluctuating velocity components were made prior to the measurements. These calibrations were carried out in Lim's (1980) rig in the same laboratory. The rig was constructed to investigate pipe flows in various upstream profiles produced by screens of different shapes. Nevertheless, it is known that in fully developed pipe flow, the shear stress is proportional to the radial distance from the centre of the pipe. This is expressed by the equation

$$\frac{\overline{u'v'}}{U_\tau^2} = \frac{r}{R}$$

where U_τ is the wall friction velocity, r is the distance from the centre of the pipe and R is the radius of the pipe which is 4.06in (51.5mm) for this rig. In order to obtain fully-developed flow, the screens were removed after the contraction section of the rig. The measurements were made at 80 pipe diameters downstream from the contraction with a DISA type 55P02 slanted wire probe. The anemometer system and the procedures were the same as those described for shear stress measurements.

The probe was positioned at the centre of the pipe with the probe axis parallel to the flow direction. After measurements at several r stations the probe was rotated 90 degrees and the measurements were repeated. The measurements were made with Reynolds numbers between 1.0×10^5 and 2.0×10^5. A typical calibration is shown in fig. 3-7(B). The values of the wall friction velocities were taken from Lim's measurements. The measured values are approximately 10% lower than the values of $\overline{u'v'}/U_\tau^2 = r/R$ and almost linear. However, when the values are corrected for the hot-wire's directional sensitivity and high intensity turbulence, the difference becomes only 2.5%. The correction factor used is that which has been calculated by Guitton (1968).

3-3 Corrections for hot-wire's directional sensitivity

3-3-1 Introduction

There may be two sources of measurement error in a hot-wire measurement. First, for a wire of finite length, the axial flow component develops a boundary layer along the wire giving a change in the rate of heat transfer. This is the so-called longitudinal cooling effect. Second, the effect caused by the wake of the upstream prong. This is called prong interference. The latter effect was extensively studied by Gilmore (1967). He found a DISA miniature hot-wire probe type 55A25 suffer from prong interference effects. However, Guitton (1974) found even with the older type probes, the latter effect could be neglected when calculating the former effect.

The two effects could be combined together for the point of view of directional sensitivity of a hot-wire. This can be expressed by the equation

$$Ue^2 = U_N^2 + k^2U_T^2 + h^2U_{BN}^2 \tag{3-15}$$

where Ue is effective cooling velocity, U_N, U_T and U_{BN} are velocity components normal, tangent and binormal to the wire respectively. k and h are directional sensitivity coefficients. The experiments of Champagne, Sleicher and Wehrmann (1967) indicated k is primarily a function of the aspect ratio of the wire. For gold-plated DISA type 55F11 probe which is similar to the type 55P01 probe, k = 0.2 and h = 1.04 were taken by Jørgensen (1971). He also took values for non-gold plated probe, which was k = 0.32 and h = 1.08. The error resulting for the flow field by neglecting directional sensitivity could be considerable. This was shown by Acrivlellis . (1978). For the present calculations k = 0.2 and h = 1.05 were chosen. The value was also chosen by Guitton (1968).

There are several methods to evaluate the velocity components U_N, U_T and U_{BN}. In general, so-called conventional methods expand the square root signal in a series. Another way is to rotate probes in the direction of a flow axis and measure squared signals at several positions. This new approach was first described by Rodi (1975). Acrivlellis (1977) presented time averaged velocity vectors and the turbulence quantities of the flow field in streamline based co-ordinates. He represented the improved method soon after (1978). However, the validity of this method is subject to some limitations. Bartenwerfer (1979) pointed out some remarks on Acrivlellis's method. These methods also require greater number of measurements at a position. The present experiments required all three velocity components at over 240 points. Thus new methods are not practical.

In the conventional method, on the other hand, as discussed by Heskestad (1965), Champagne and Sleicher (1967), Rose (1962) and Guitton (1974), higher order correlations were not negligible. Guitton (1968, 1974) provided corrections to turbulence stresses which were measured in a two-dimensional mean flow of high turbulence intensity by means of a linearized hot-wire anemometer including higher order correlations. The present study followed his method to correct directional sensitivity effects on the hot-wire probes.

3-3-2 Theory

The flow considered is two-dimensional and has a single dominant direction. The coordinate system is shown in fig.3-8. The wire is positioned in the X-Y plane for simplification, however, it may be positioned arbitrarily. The equation 3-15 can be re-written

$$\mathrm{Uce} = U_{CN}(1 + k^2\cot^2 \mathrm{Ac})^{\frac{1}{2}}\,(1 + b \sin^2 \mathrm{Bc}) \qquad (3\text{-}16)$$

where Uce is the effective cooling velocity in a calibration condition,

U_{CN} is the calibration velocity component normal to the wire, Ac is the angle between the wire and instantaneous velocity vector and Bc is the angle between instantaneous velocity vector and the plane normal to the wire containing the wire and prongs. b is defined as

$$b = \tfrac{1}{2}(h^2 - 1) \qquad (3\text{-}17)$$

The relationship between signal and velocity is defined by equations 3-1 and 3-2. The time dependent signal is given by

$$\frac{e'}{E} = \frac{dqe}{U} \qquad (3\text{-}18)$$

where qe is the instantaneous effective normal velocity component which is a function of orthogonal velocity components and the wire orientation. The equation 3-18 is now written as

$$\frac{e'}{E} = \frac{dqe}{U} = \frac{dqe}{U_{CN}\,(1 + k^2\ \mathrm{Cot\ Ac})^{\frac{1}{2}}\,(1 + b\ \sin^2 \mathrm{Bc})} \qquad (3\text{-}19)$$

where Ac and Bc are obtainable when V = W = 0. It is now possible to evaluate dqe by carrying out a series expansion. The details of expansion are shown in Guitton's original work.

It is convenient to express the corrected values in terms of coefficients. These are defined by

$$\text{Coefficient} = \frac{\text{Corrected value}}{\text{Measured value}}$$

E, F, G and H represent the coefficients for $\overline{u'^2}$, $\overline{v'^2}$, $\overline{u'v}$ and $\overline{w'^2}$ respectively. These are

$$E = 1 + \frac{V^2}{U_{c1}^2} - \frac{V^2\overline{v'^2}}{\overline{u'^2_m}\,U^2} - \frac{2V\,\overline{u'v'}}{U_{c1}\overline{u'^2_m}} - \frac{4bV\,\overline{u'v'}}{\overline{u'^2_m}\,U}$$

$$- (1 + 2b)\frac{\overline{u'v'^2}}{\overline{u'^2_m}U_{c1}} + \frac{\overline{u'^2v'^2}}{\overline{u'^2_m}\,U_{c1}} + \frac{\overline{u'^2v'^2}}{\overline{u'^2_m}\,U^2} - \tfrac{1}{4}\left(\frac{\overline{v'^4} - (\overline{v'^2})^2}{U^2\,\overline{u'^2_m}}\right)$$

(3-20)

$$F = \frac{1}{1-\dfrac{2k^2}{\sin^2\psi}} - \frac{(1 + 2b)}{\mathrm{Cos}^2\cdot\psi}\,\frac{\overline{u'w'^2}}{\overline{v'^2_m}\,U_{c3}}\left(1 + \mathrm{Cot}\,\psi\,\frac{V}{U_{c2}}\right) - (E - 1)\,\frac{\overline{u'^2_m}}{\overline{v'^2_m}}$$

$$+ \frac{1}{\sin^2\psi}\,\frac{\overline{v'w'^2}\,V}{\overline{v'^2_m}\,U^2} + \frac{1\quad\overline{u'^2w'^2}}{\mathrm{Cos}^2\psi\,\overline{v'^2_m}\,U^2} +$$

$$\frac{\overline{v'^2w'^2}}{\mathrm{Sin}^2\psi\overline{v'^2_m}\,U^2} - \frac{1}{\mathrm{Sin}^2 2\psi}\left(\frac{\overline{w'^4} - (\overline{w'^2})^2}{\overline{v'^2_m}\quad U^2}\right)$$

(3-21) .

$$G = \frac{1}{1-\dfrac{k^2}{\mathrm{Sin}^2\psi}} - \frac{(1 + 2b)}{2\,\mathrm{Sin}^2\psi}\left(1 + \mathrm{Cot}\psi\,\frac{V}{U}\right)\frac{\overline{v'w'^2}}{U_{c3}}\cdot\overline{u'v'}_m +$$

$$\frac{1}{2\mathrm{Sin}^2\psi}\,\frac{\overline{u\,w'^2}}{\overline{u'v'}_m}\,\frac{V}{U^2} + \frac{1}{\mathrm{Sin}^2\,\psi}\,\frac{\overline{u'v'w'^2}}{\overline{u'v'}_m U^2}$$

(3-22)

$$H = \frac{1}{1 - \frac{k^2}{\mathrm{Sin}^2\psi}} - \frac{(E - 1)}{\mathrm{Cot}^2\psi}\,\frac{\overline{u'^2}}{\overline{w'^2}_m} - \frac{1}{\mathrm{Cos}^2\psi}\,\frac{\overline{u'v'^2}}{U\,\overline{w'^2}_m} +$$

$$\frac{1}{\mathrm{Cos}^2\psi}\,\frac{\overline{u'^2v'^2}}{U^2\overline{w'^2}_m} + \frac{1}{\mathrm{Sin}^2\psi}\,\frac{\overline{v'^2w'^2}}{U^2\,\overline{w'^2}_m} - \frac{1}{4\mathrm{Sin}^2\psi\,\mathrm{Cos}^2\psi} -$$

$$\left(\frac{\overline{v'^4} - (\overline{v'^2})^2}{U^2\,\overline{w'^2}_m}\right) \qquad (3\text{-}23)$$

where subscript m denotes measured value. That is the value calculated from 3-10 to 3-13 without incorporating any correction terms. The wire inclination ψ is 45°. The value H is based on the assumption $V = 0$ because of the complexity of the equation.

There still are values which are difficult to obtain in practice. Some approximations are introduced.

$$\frac{\overline{u'^4}}{(\overline{u'^2})^2} = \frac{\overline{v'^4}}{(\overline{v'^2})^2} = \frac{\overline{w'^4}}{(\overline{w'^2})^2} = 3 \qquad (3\text{-}24)$$

$$\frac{\overline{u'^2v'^2}}{\overline{u'^2}.\overline{v'^2}} = 2 \qquad (3\text{-}25)$$

$$\overline{v'^2w'^2} = \overline{v'^2}\cdot\overline{w'^2} \qquad (3\text{-}26)$$

$$\overline{u'^2 w'^2} = \overline{u'^2} \,.\, \overline{w'^2} \qquad (3\text{-}27)$$

$$\overline{u'v'w'^2} = \overline{u'v'} \,.\, \overline{w'^2} \qquad (3\text{-}28)$$

$$\overline{v'w'^2} = \overline{u'w'^2} \; (\overline{v'^2}/\overline{u'^2})^{\frac{1}{2}} \qquad (3\text{-}29)$$

The justifications of these approximations are also presented in Guitton's original work.

From these assumptions, equations 3-20 to 3-23 can be reduced to forms applicable to the present arrangement where b = 0.05, k = 0.2 and $\psi = 45^{o}$.

$$E = 1 + \frac{V^2}{U_{cl}^2} - \frac{V^2\,\overline{v^{\ 2}}}{\overline{u'^2_m}\,U^2} - \frac{2V\,\overline{u'v'}}{\overline{u'^2}\,U_{cl}} - \frac{0.2\,V\,\overline{u'v'}}{\overline{u'^2_m}\quad U}$$

$$- 1.1\frac{\overline{u'v'^2}}{\overline{u'^2_m}\,U_{cl}} + \frac{2\,\overline{v'^2_m}}{U^2} - \tfrac{1}{2}\,\frac{(\overline{v'^2})^2}{\overline{u'^2_m}\quad U^2} \qquad (3\text{-}30)$$

$$F = 1.19 - 2.2\left(1 + \frac{V}{U_{c2}}\right)\frac{\overline{u'w'^2}}{\overline{v'^2_m}\,U_{c3}} - (E - 1)\,\frac{\overline{u'^2_m}}{\overline{v'^2_m}}$$

$$+ \frac{2V\,\overline{u'w'^2}}{(\overline{u'^2_m})^{\frac{1}{2}}\;(\overline{v'^2_m})^{\frac{1}{2}}\;U^2} + \frac{2\,\overline{u'^2_m}\,.\,\overline{w'^2_m}}{\overline{v'^2_m}\quad U^2}$$

$$+ \frac{2\,\overline{w'^2_m}}{U^2} - \frac{2(\overline{w'^2_m})^2}{\overline{v'^2_m}\;U^2} \qquad (3\text{-}31)$$

$$G = 1.09 - 1.1 \left(1 + \frac{V}{U}\right) \frac{\overline{u'w'^2} \; . \; (\overline{v'^2_m})^{\frac{1}{2}}}{\overline{u'v'}_m \; (\overline{u'^2_m})^{\frac{1}{2}} \; U_{c3}}$$

$$+ \frac{V \; . \; \overline{u'w'^2}}{\overline{u'v'}_m U^2} \quad + \frac{2 \, \overline{w'^2_m}}{U^2} \qquad (3\text{-}32)$$

$$H = 1.19 + (E - .1) \frac{\overline{u'^2}}{\overline{w'^2_m}} - \frac{2 \, \overline{u'v'^2}}{\overline{w'^2_m} \; U} + \frac{2 \, \overline{u'^2_m} \; . \; \overline{v'^2_m}}{\overline{w'^2_m} \quad U^2}$$

$$+ \frac{2 \, \overline{v'^2_m}}{U^2} - \frac{2(\overline{v'^2_m})^2}{\overline{w'^2_m} \, U^2} \qquad (3\text{-}33)$$

The final form of the equations now requires third order correlations $\overline{u'v'^2}$ and $\overline{u'w'^2}$. These quantities were measured at X = 300, 550 and 700 mm.

3-3-3 Instrumentation

An x-wire probe was used for the measurements. The block diagram is shown in fig. 3-9. Two sets of anemometer systems were used which consisted of main anemometer units, linearizers and electronic filters. The signals from the systems were fed to the correlator. This instrument was used simply as an addition and subtraction device. The signals from the instrument output e_{A+B}

and e_{A-B} were v' and u' respectively. It must be mentioned that both wire calibration lines have to be identical and this was assured by adjusting the linearizers.

The u' signal was squared by the R.M.S. volt meter which had the output of instantaneous value of the squared input signal. Finally, both u' and v'^2 signals were fed into the turbulence processor. The function of this instrument was set "A·B" which multiplied two input signals. D.C. mode was selected because the signal v'^2 had a D.C. component. The output of the turbulence processor was measured by D.C. volt meter. The time constant was selected at an appropriate value for the measurement.

3-3-4 Calibration

Calibrations were made with the original DISA calibration unit. The procedure was similar to the gold-plated wire probe calibration which was described in 3-2-2. However, unlike the gold-plated wire probe calibration, it was necessary to compensate for the increased cable resistance introduced by the built in probe support. Each calibration, the shorting probe was mounted in the unit support and cable resistance was balanced out by adjusting the anemometer's potentiometer. The same resistance balancing out procedure with the probe support was made for the measurements. High frequency response adjustment was not possible in the calibration tunnel because of the same reason. This was done in a 7.5 H.P. motor driven tunnel whose velocity range could be conveniently controlled for the adjustments. As it was mentioned in 3-3-3, the output signals from the linearizers were adjusted to give the same level at the maximum velocity.

3-4 Correlations

3-4-1 Types of correlations

Details of the turbulence structure may be provided by correlations. The measurement errors are less sensitive for the correlation coefficient than turbulence intensity measurements. Most of the previous work is mainly on grid generated turbulence, wakes, boundary layers and circular jets.

Grant (1958) studied wakes, boundary layer and grid generated turbulence extensively. Townsend (1970) carried out further work with Grant's results and some predictions were made. These works may be useful for general interpretation of the correlations.

For convenience we define the correlation coefficients in the form of:-

$$R_{ij}(\tau:r_1,r_2,r_3) = \frac{\overline{u_i'(0:0,0,0)\quad u_j'(\tau:r_1,r_2,r_3)}}{\sqrt{\overline{u_i'^2(0:0,0,0)}}\ \sqrt{\overline{u_j'^2(\tau:r_1,r_2,r_3)}}} \qquad (3\text{-}34).$$

where i and j denote the velocity components. 1, 2 and 3 represent u, v and w components respectively. τ is the time delay and r is the separation between two wires.

For the present experimental arrangement, there is considerable difficulties with the space separation in X direction. Because, on the curved surface, the curvature ratio changes every millimeter. This may give a considerable change in turbulence characteristics. There is also difficulty with traversing the probe in X direction.

When the probe is traversed in X direction, Y must be changed to keep constant $Y/Y_{\frac{1}{2}}$ value and the probe angle also adjusted to keep the same inclination to the surface.

One solution is to use auto-correlations. If we assume the flow is locally isotropic and the turbulence intensity not extreme the relation

$$\frac{\partial}{\partial t} = -U \frac{\partial}{\partial X} \qquad (3\text{-}35)$$

known as Taylor's hypothesis holds. According to this theory, we can put

$$r_1 = U \cdot \tau \qquad (3\text{-}36)$$

where U is local mean velocity. Therefore, auto-correlations were taken instead of r_1 separation. Measured calibrations were

R_{11} (τ: 0, 0, 0)

R_{22} (τ: 0, 0, 0)

R_{33} (τ: 0, 0, 0)

R_{12} (τ: 0, 0, 0)

at $Y = Y_{\frac{1}{2}}$ and $0.7Y_{\frac{1}{2}}$ at X = 300 and 550 mm.

R_{11} (0: 0, 0, r_3)

at $Y = Y_{\frac{1}{2}}$ at X = 300 and 550 mm.

3-4-2 Instrumentation

The auto-correlations were made using a single wire probe or a X-wire probe. Two sets of the anemometer systems were used. For $R_{11}(\tau:0,0,0)$ correlations, only one system was needed. For R_{22} and R_{33} correlations, signals from the systems were fed to the first correlator. This instrument was used as an addition and subtraction device. The output from e_{A-B} was either v' or w' depending on the probe orientation. For R_{12} correlation, the turbulence processor was used for the multiplication of the outputs e_{A-B} and e_{A+B} i.e. v' and u' from the first correlator. Now, the signal was fed to the time delay unit to filter the signal and to avoid overloading the second correlator. Then, the signal was fed to the second correlator. After amplification of the two identical signals, they were fed to the time delay unit again. This time the signals were sampled and converted in pulses. This is because the auto-correlation does not require the use of whole analog signals. It is simpler to sample the signal for the desired time delay. The two outputs from this unit carry a sample of the original signal and a sample of delayed signal. The time delay was controlled by the sweep drive unit. The output from the sweep drive unit is proportional to the time delay. The sweep speed and time integral range of the correlator were calculated using the information given in the instruction manual for the DISA T.C.A. system. The time delay range was decided after preliminary tests. The signals were back into the second correlator again where correlation coefficient was proportional to the output of this device. The output signal was fed to a X-Y recorder Y axis input and also was monitored with a D.C. volt meter. The X-Y recorder X axis was controlled by the sweep drive unit. Therefore, the record chart now represents a time delay τ versus correlation coefficient R curve. The calibration of the X-Y recorder was made prior to the measurement with a stabilized D.C. voltage generator. The circuit diagram is shown in fig. 3-10.

For $R_{11}(0:0,0,r_3)$ correlation, the time delay unit was removed from the system. For this measurement, two single wire probes were used. One probe was fixed at a point and the other was traversed in Z direction by a stepper motor which was controlled by the sweep drive unit. This unit also drove the X-Y recorder. Therefore the output from the sweep drive unit was proportional to r_3. It was impossible to bring the two wires to exactly the same position at the same time. In order to normalize the correlation, on the other hand, an adjustment to balance two signals in the correlator was needed. This was made first with one wire at $r_3 = 0$ then the other at the same position. This adjustment should produce maximum correlation coefficient $R = 1.0$ if the wires at the the same point. The same adjustment was made with the space-time correlation. $R_{11}(0:0,0,r_3)$ correlation arrangement is shown in fig. 3-11.

The space-time correlations were made also with two single wire probes. The signals from the anemometer systems were fed to the time delay unit. The rest of the signal process system was identical to the auto-correlation arrangement.

3-4-3 Calibration

The calibrations concentrated on the linearization and, in the case where two anemometer systems were involved, to make two signals identical at the maximum velocity. The correlations were normalised so that the calculation of calibration factors were not required.

3-5 Dissipation

3-5-1 Theory

To explain the magnitude of the nature and mechanics of turbulence, the turbulent kinetic energy balance equation is one clear indicator. This equation,for the jet flow considered, may be reduced to the approximate relation.

$$\tfrac{1}{2}U\frac{\partial\overline{q^2}}{\partial x} + \tfrac{1}{2}V\frac{\partial\overline{q^2}}{\partial y} + \overline{u'v'}\frac{\partial U}{\partial y} + \frac{\partial}{\partial y}\overline{v'\left(\frac{p}{\rho} + \frac{q^2}{2}\right)} - \varepsilon = 0 \qquad (3\text{-}37)$$

where the first and second terms are called Convection, the third is Production, the fourth is Diffusion and the last is Dissipation. All the terms can be measured experimentally. However the diffusion term is difficult to measure because of the pressure fluctuation term. Usually this term is obtained by difference. Therefore the measurement of dissipation term is required.

The dissipation of turbulence per unit mass is given by

$$\varepsilon = \nu\,\overline{\left(\frac{\partial u_i}{\partial x_j} + \frac{\partial u_j}{\partial x_i}\right)\frac{\partial u_j}{\partial x_i}} \qquad (3\text{-}38)$$

This equation still requires very complicated measurements. Nevertheless, for local isotropic flow, this may be reduced to:-

$$\varepsilon = 15\nu\overline{\left(\frac{\partial u}{\partial x}\right)^2} \qquad (3\text{-}39)$$

This simple expression was justified even in a two-dimensional channel flow except for the region very close to the wall. This was briefly discussed by Hinze (1975).

The equation 3-39 is still far from easy to measure. Once again it is assumed the local flow is isotropic and Taylor's hypothesis equation 3-29 is introduced. Townsend (1956) used this method at the very first stages of turbulent research work. The equation 3-29 is reformed to

$$-\frac{\partial}{\partial x} = \frac{1}{U}\frac{\partial}{\partial t}$$

Hence $$\overline{\left(\frac{\partial u}{\partial x}\right)^2} = \frac{1}{U^2}\overline{\left(\frac{\partial u}{\partial t}\right)^2} \qquad (3\text{-}40)$$

DISA type 55A06 Random Signal indicator and correlator has a differentiator. It can provide the time derivative of the input signal multiplied by a selective time constant τ. The output from the instrument,Cout,is given by the form

$$\text{Cout} = \tau^2\sqrt{\overline{\left(\frac{\partial u}{\partial t}\right)^2}}$$

Therefore equation 3-40 can be expressed

$$\overline{\left(\frac{\partial u}{\partial x}\right)^2} = \frac{1}{U^2}\,\frac{1}{\tau^2}\left[\tau\sqrt{\overline{\left(\frac{\partial u}{\partial t}\right)^2}}\,\right]^2$$

$$= \frac{1}{U^2}\,\frac{1}{\tau^2}\,(\text{Cout})^2 \qquad (3\text{-}41)$$

Cout was measured at X = 300 and 550mm at Y = $Y_{\frac{1}{2}}$.

3-5-2 Instrumentation

A single wire probe was used for this measurement. The single channel anemometer system output was fed to the random signal indicator/correlator. The output signal was read on the built in meter.

Prior to the measurements, the calibration of the correlators were made by means of a wave generator and an oscilloscope. The triangle wave i.e. constant derivative signal from the wave generator was fed to the correlators. The derivative of the signal was calculated from the reading of the oscilloscope and compared with the reading of the correlator. Various frequency signals were tested. Only one of the three correlators was found usable. The instrument which was found to be most accurate still produced approximately 10% error. However, the accuracy of the calibration was concerned, it was thought to be acceptable.

Another concern for the accuracy was the filtering of the input signal. The derivative of the input signal was entirely dependent on the filtering of the signal. In general, the higher frequency signal obviously produces the higher level of derivative. For the present measurements, we assumed that the smallest eddy which could be detected by the hot-wire probe was decided by the wire dimension. Therefore, the low-pass filter was adjusted to cut off the higher frequency than the calculated frequency F. This frequency F represented the smallest measurable eddy size. The calculation form was given by

$$F = U/\ell \qquad (3\text{-}42)$$

where U is local mean velocity and ℓ is the wire length. The low-pass filter was set on 25 kHZ for X = 300mm and 10 kHZ for X = 550mm measurements. The arrangement for the measurement of dissipation is shown in fig. 3-12.

3-5-3 Calibration

The calibrations were made with the original DISA calibration unit. The procedure was similar to the higher turbulence correction measurement. It was described in section 3-3-4. It was also necessary to compensate the cable resistance because of the use of built in probe support of the calibration unit.

3-6 Experimental procedure - General

The summary of the Chapter 3 can be made with the description of the check list. This was made to reduce simple mistakes. Some simple mistakes had been made earlier before the check list was introduced. For example, the rig was operated while the electrostatic filter was left inoperative. The consequence was not only the calibration drift but also dust contamination on the probe. This could lead wire cleaning or worst case, wire replacement.

The experiments were carried out in accordance with the list. The procedure could vary with experiments. The general procedure was as follows.

3-6-1 Before experiment

(1) The electrostatic and fabric filter were inspected. If the

amount of dust collected in the filters was excessive, the filters were cleaned.

(2) The instruments were switched on for warm up for at least 30 minutes.

(3) The traverse device was set in position and at the current angle.

(4) The surface was wiped and cleaned.

(5) The connection between the static tappings and the multi-tube manometer was checked.

(6) Three single tube manometers zero level adjustments were made.

(7) Atmospheric pressure and temperature were measured.

(8) Static pressure difference Δp which decides the initial slot velocity was calculated.

(9) All the instruments were adjusted adequately.

3-6-2 Calibration

(1) Screens of the calibration tunnel were inspected. If necessary they were cleaned.

(2) The inlet of the tunnel was cleaned.

(3) For gold-plated probes, the probe axis was carefully adjusted to parallel to the flow direction.

(4) For non-gold-plated probes, cable resistance balance out was made.

3-6-3 Before starting the rig

(1) Probe was set in position and distance between the probe and the surface was measured.

(2) For non-gold-plated probes, cable resistance balance out was made.

(3) Water coolers were turned on.

(4) Electro static filter was turned on.

3-6-4 Before meter reading

(1) Warm up run for at least 15 min.

(2) Jet temperature was checked and if necessary cooling water temperature was readjusted.

(3) Jet initial slot velocity was checked and if necessary readjusted.

(4) Air or water leak was inspected especially around the slot assembly.

3-6-5 During measurements

(1) When probe was traversed to a position, readings were taken after the specified time for the meter damping rate.

(2) Frequent checks were made for jet temperature, slot velocity and air or water leak.

3-6-6 After measurements

(1) Last measurement was made with Y at Umax position. The anemometer's mean and R.M.S. output was compared with the readings already taken. If large discrepancy was found, the experiment was stopped and repeated.

(2) Calibration was made.

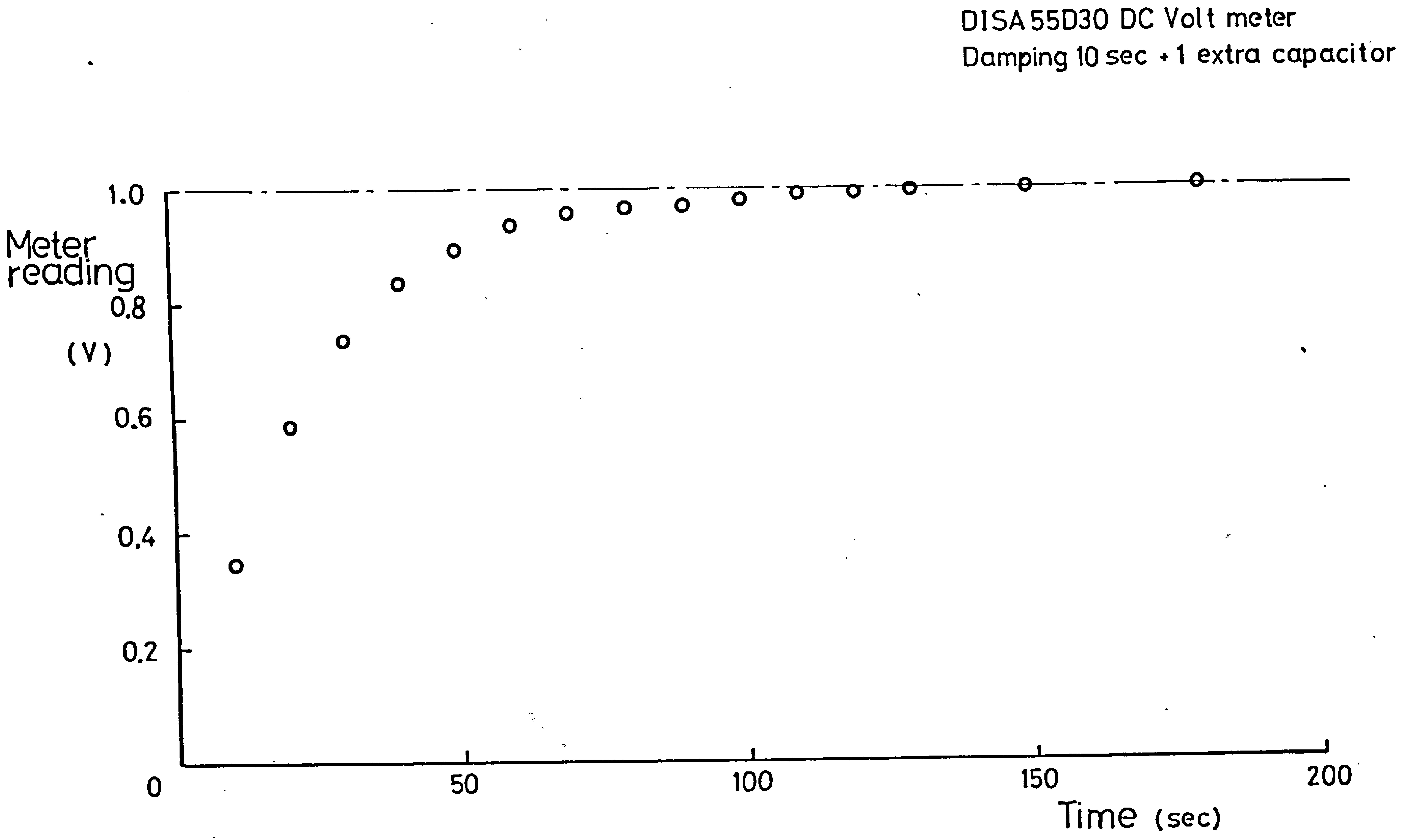

FIG. 3-1 D.C. VOLT METER TIME RESPONSE

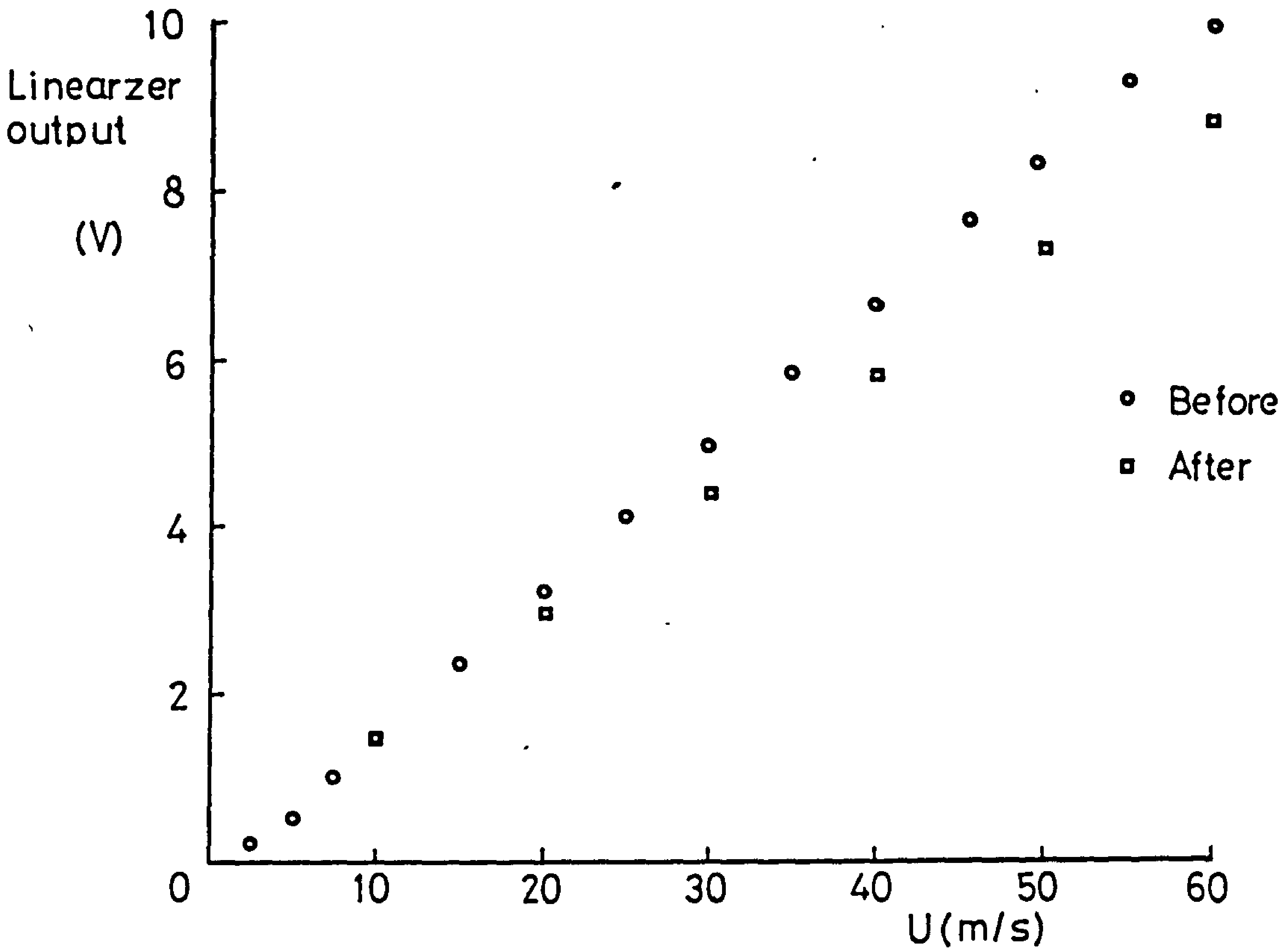

FIG. 3-2 DUST EFFECT ON CALIBRATION

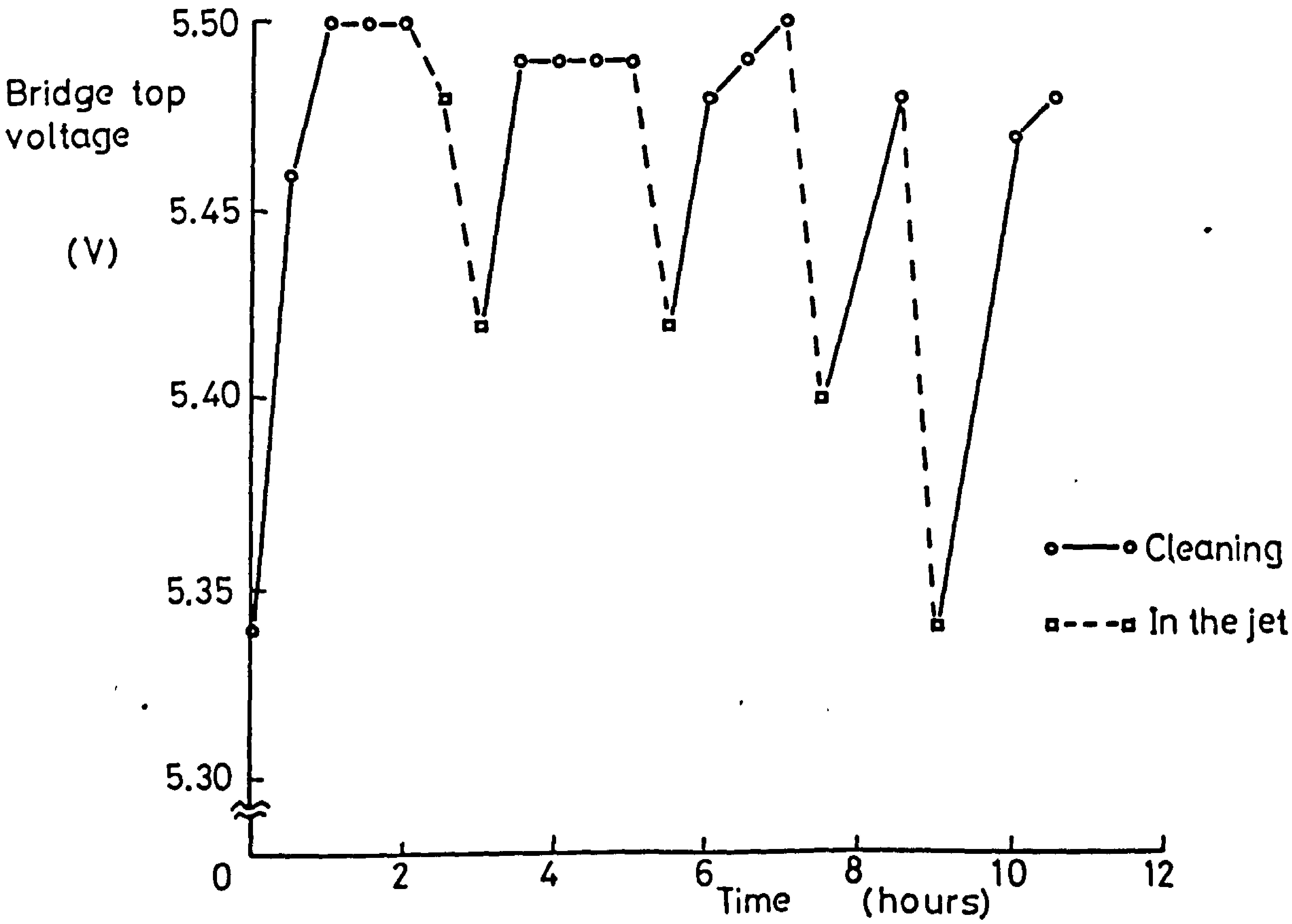

FIG. 3-3 CLEANING EFFECT ON C.T.A. OUTPUT

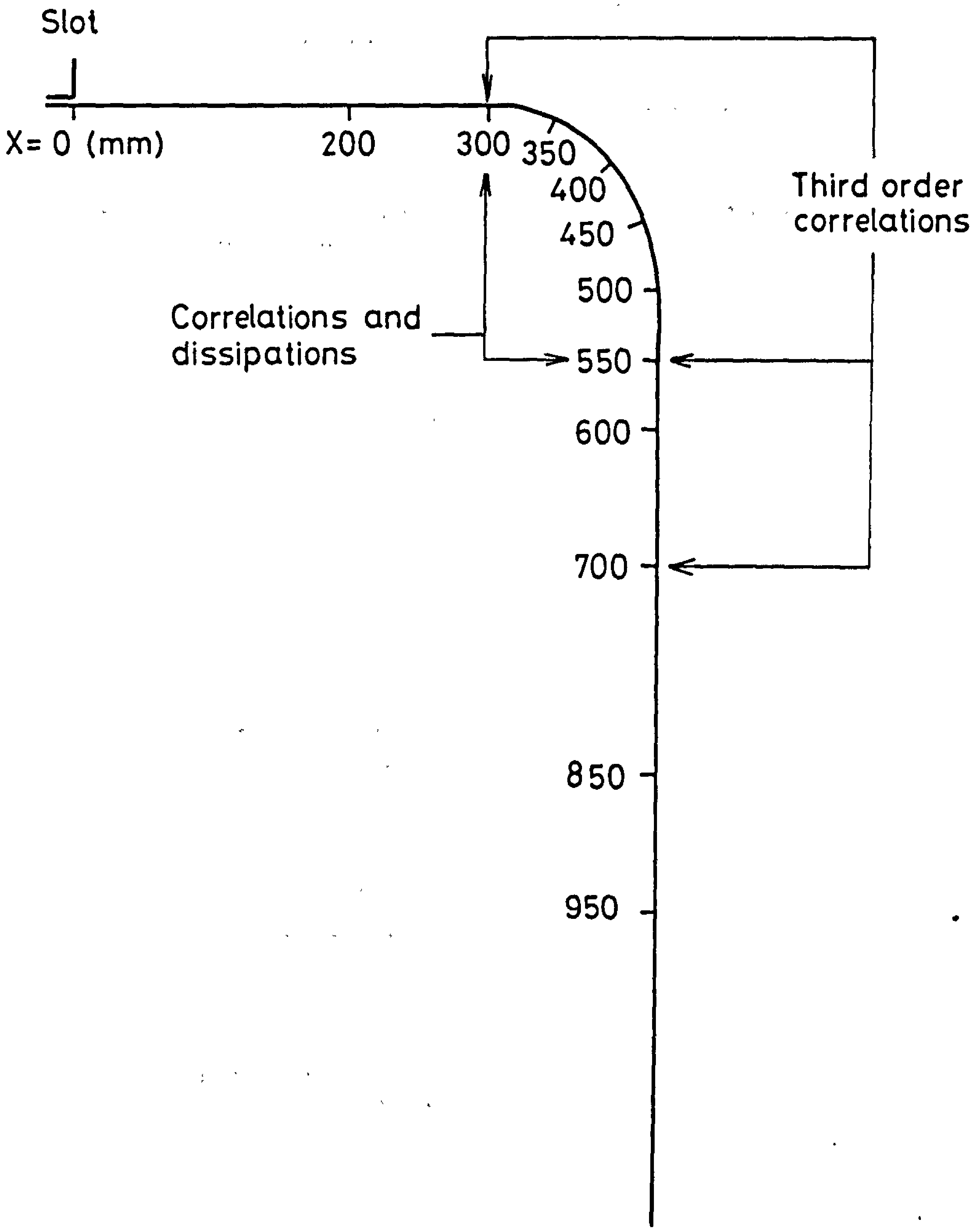

FIG. 3-4 MEASURED STATIONS

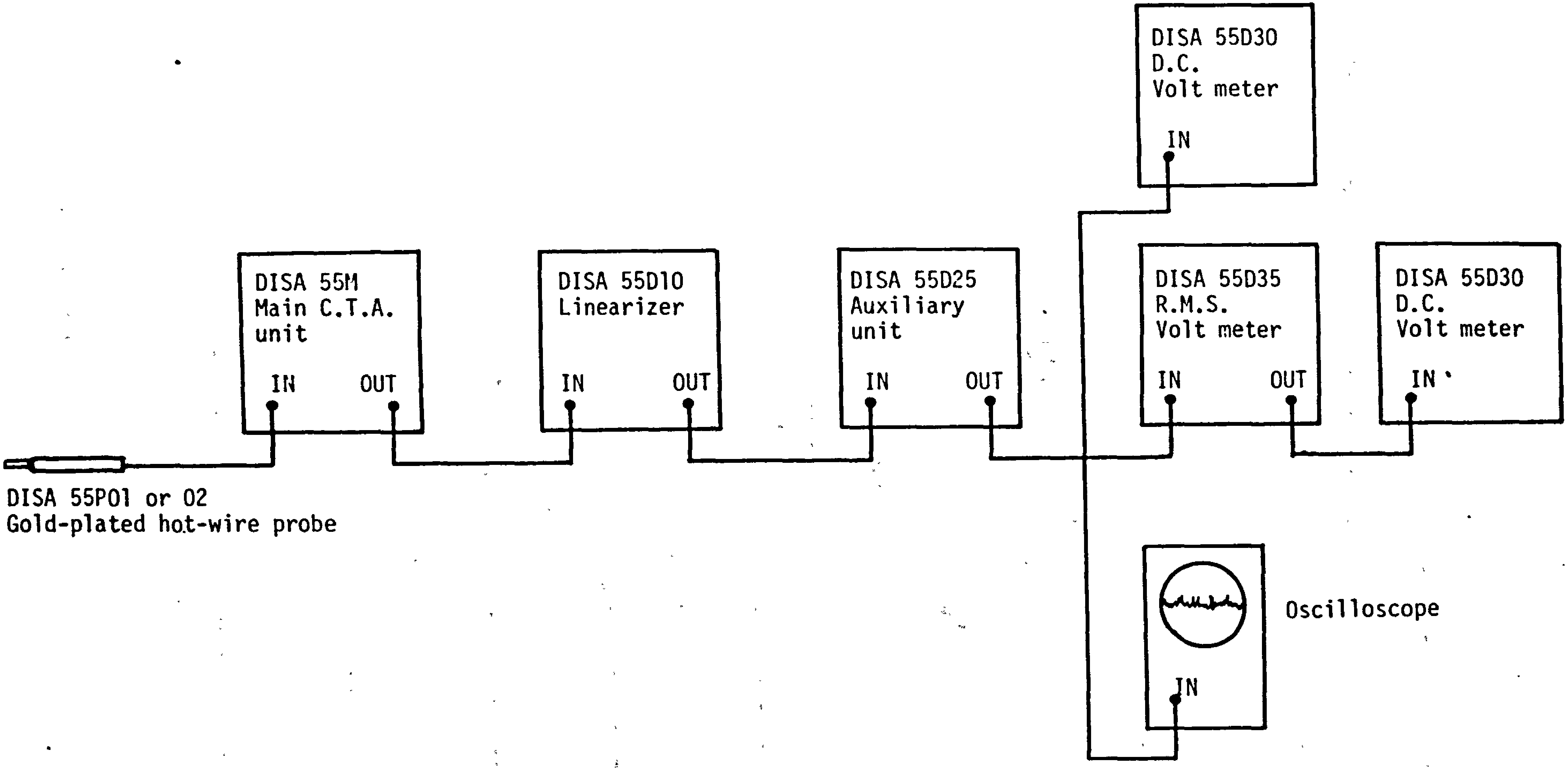

FIG. 3-5 INSTRUMENTATION, MEAN AND TURBULENCE QUANTITIES

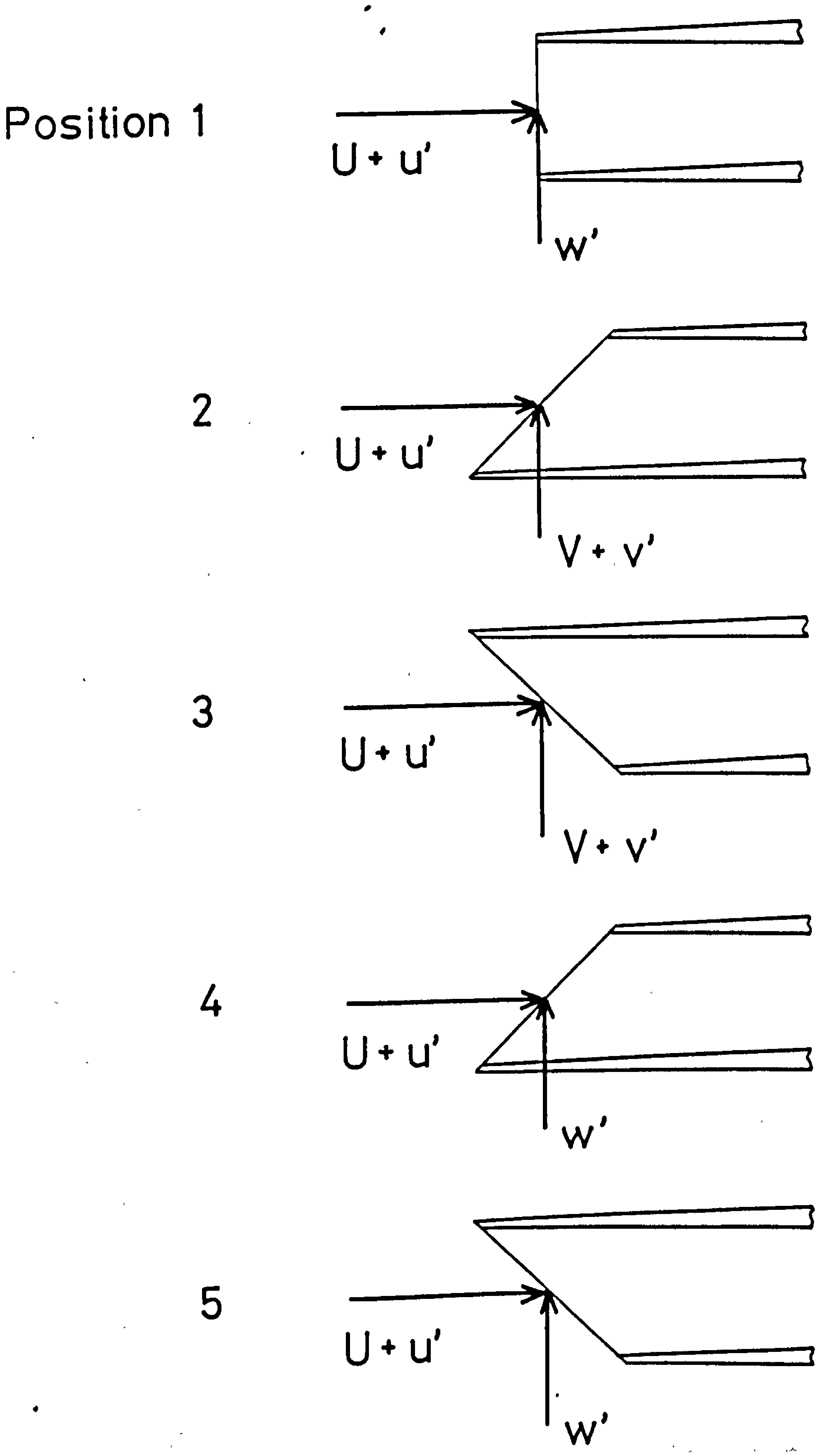

FIG. 3-6 WIRE POSITIONS

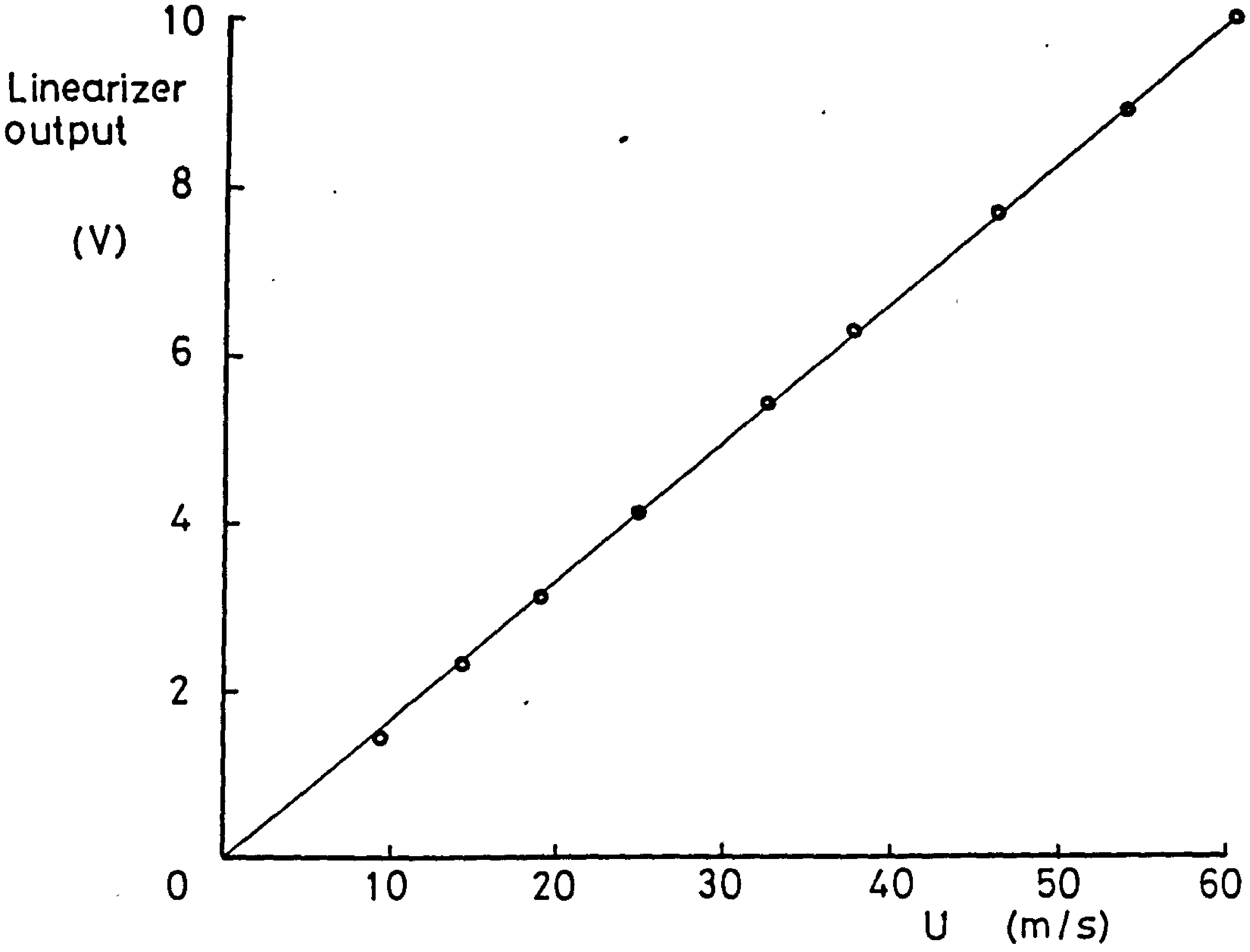

FIG. 3-7(A) TYPICAL CALIBRATION, MEAN VELOCITY

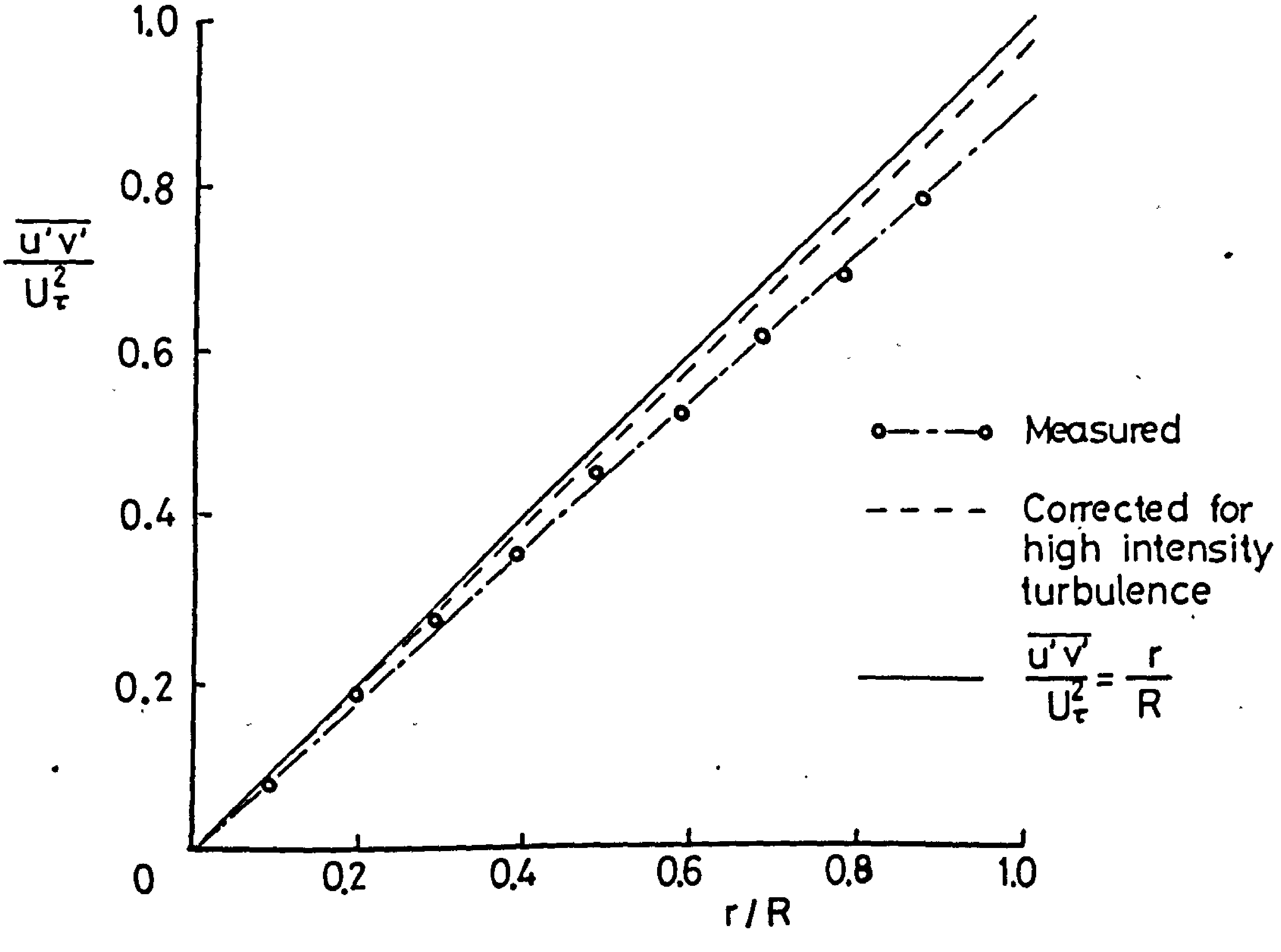

FIG. 3-7(B) TYPICAL CALIBRATION, TURBULENCE

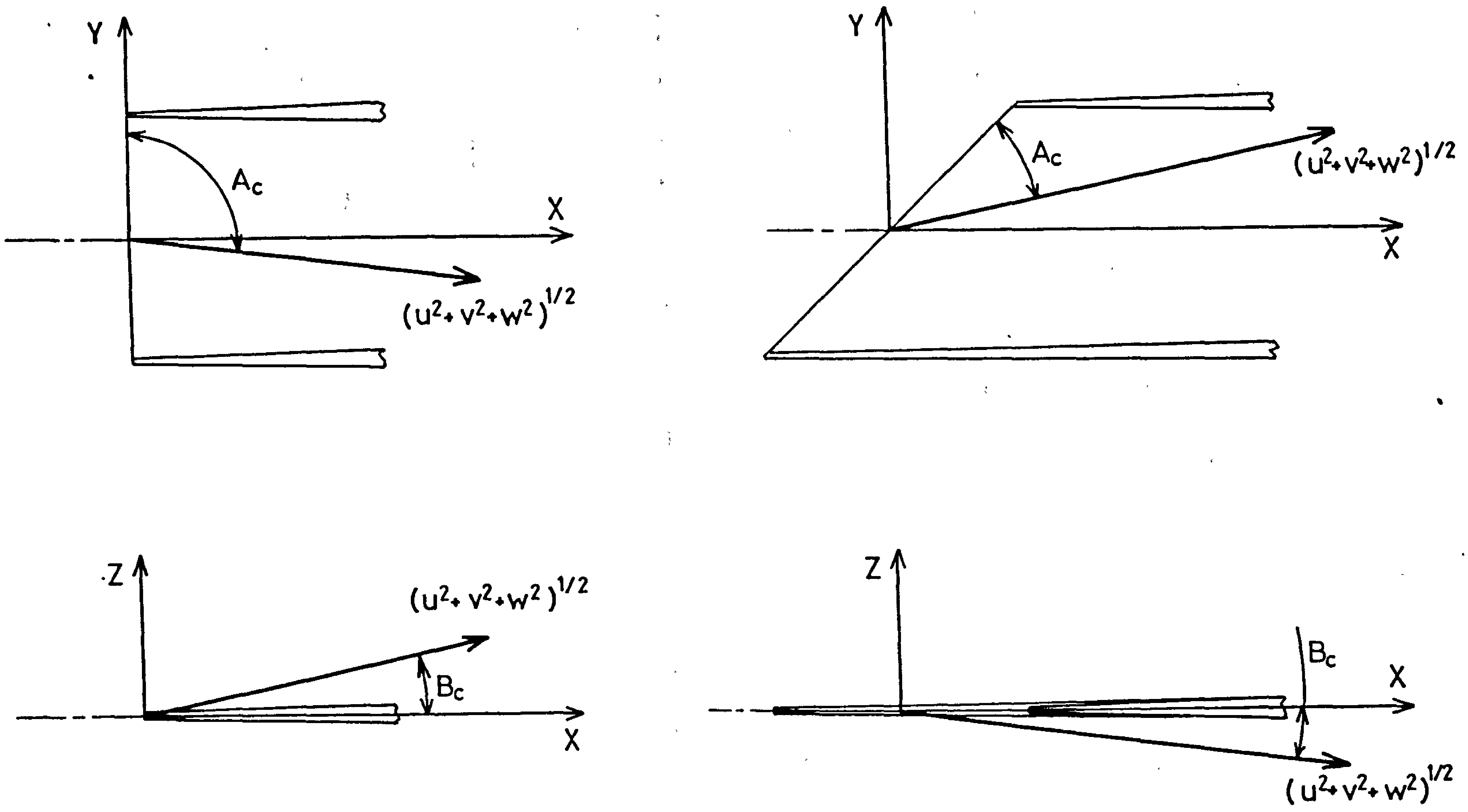

Straight wire probe

Slanted wire probe

FIG. 3-8 COORDINATE SYSTEM FOR HOT-WIRE'S DIRECTIONAL SENSITIVITY

FIG. 3-9 INSTRUMENTATION, TRIPLE VELOCITY CORRELATION

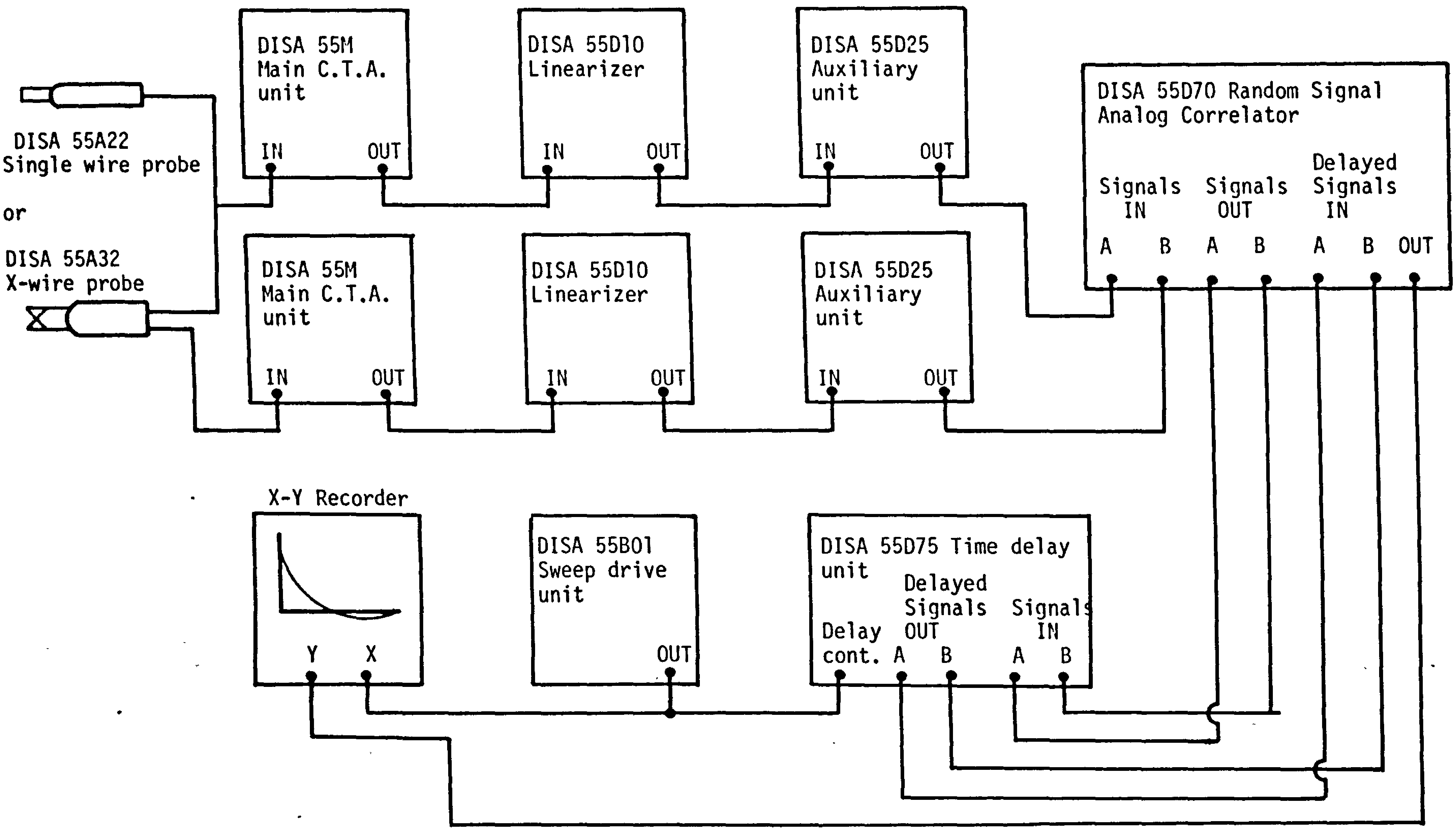

FIG. 3-10 INSTRUMENTATION, AUTO-CORRELATION

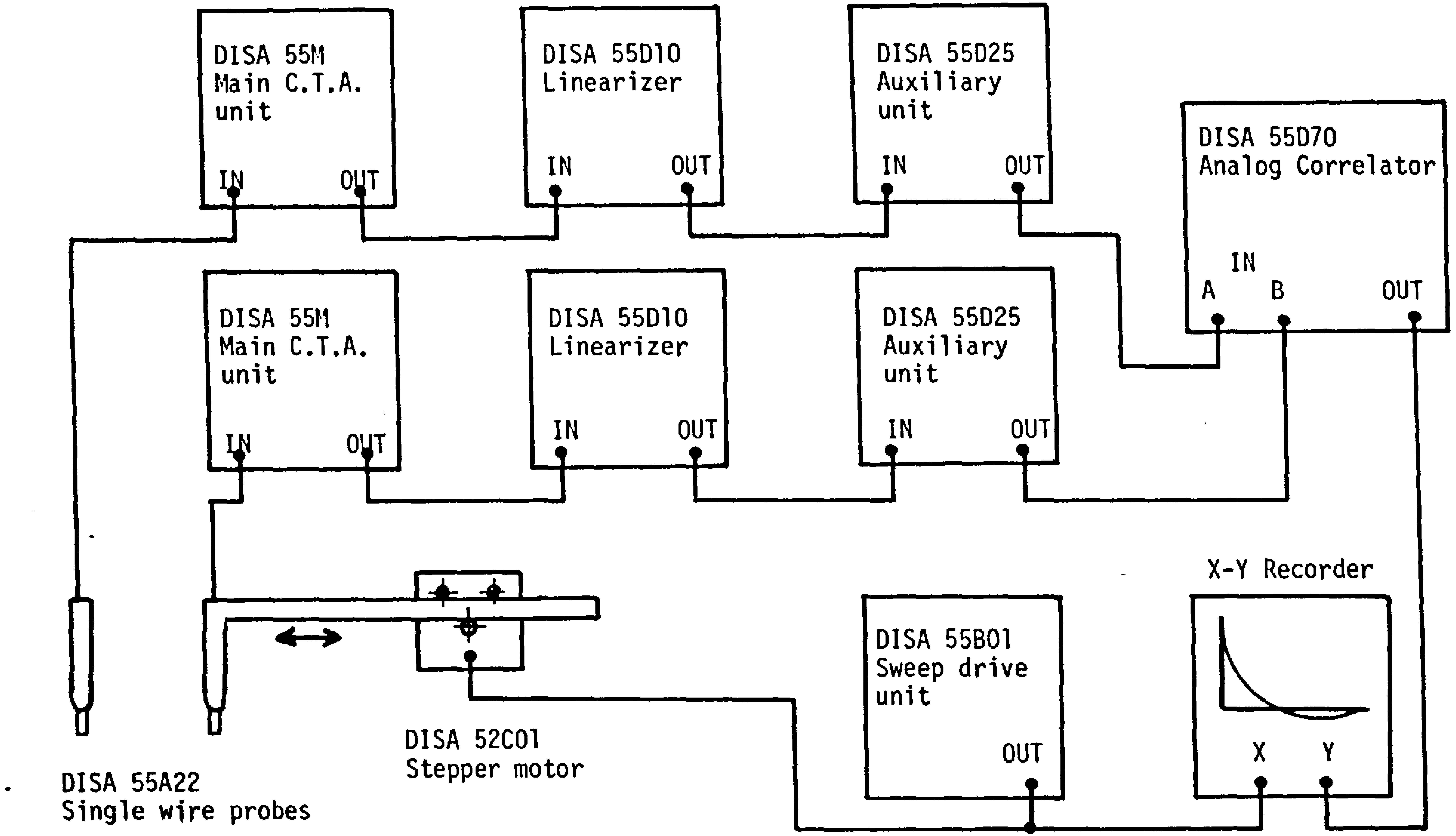

FIG. 3-11 INSTRUMENTATION, $R_{11}(0{:}0,0,r_3)$ CORRELATION

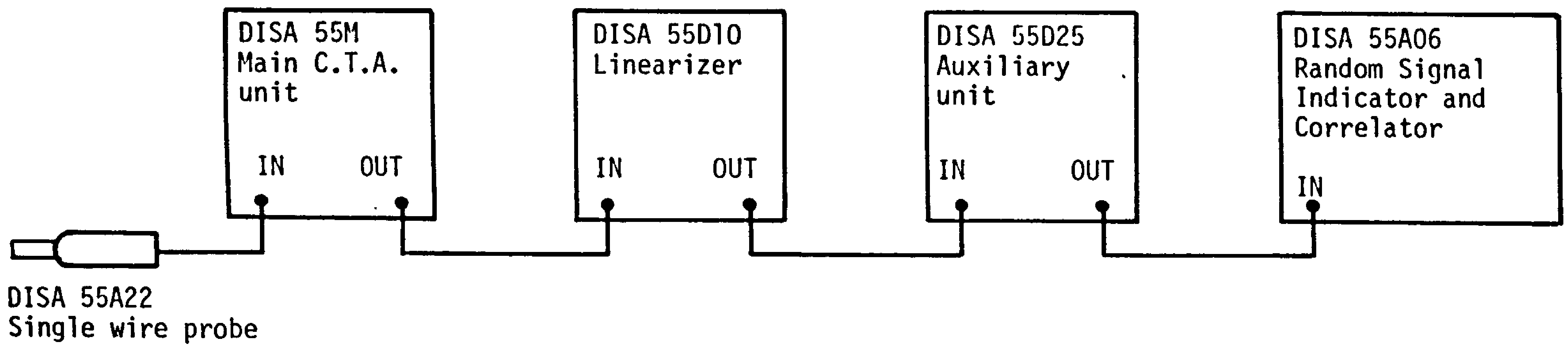

FIG. 3-12 INSTRUMENTATION, DISSIPATION

CHAPTER 4

RESULTS AND DISCUSSIONS

CHAPTER 4 RESULTS AND DISCUSSIONS

4-1 Mean velocity components

4-1-1 Velocity profiles

On the first plane surface, the velocity profiles have been measured at X = 200 and 300 mm. The profiles have been non-dimensionalized using the maximum mean velocty Um and half-width $Y_{\frac{1}{2}}$ at each station. The flow situation and definition of symbols are shown in fig. 4-1. The notations for turbulence intensity profile are the same for other Reynolds stresses. For example the maximum $\overline{v'^2}$ is written as $\overline{v'^2_m}$ and the distance between the position where $\overline{v'^2_m}$ and the surface is written as Y_{mv}.

Some preliminary measurements showed that the velocity profiles measured at the stations closer to the slot than X = 200 mm varied with X. This indicates that the velocity profiles do not reach an equilibrium state or become fully developed until X = 200 or X/b = 31.5.

The profiles measured at X = 200 and 300 mm are in good agreement. A comparison with profiles measured by other researchers is made. A large number of studies concerning plane wall jets have been published. The various sets of velocity profiles are in good agreement. The profile measured by Guitton (1977) is shown in fig. 4-2 with the profile taken at X = 300 mm. These profiles are also in very good agreement.

At X = 350 mm, which is the first measured station on the curved surface, the velocity profile differs from the profile on the plane surface. The distance between the maximum velocity position across the jet and the surface, Y_m, decreases slightly. The profile is thinner than the profile on theplane surface.

The measured stations on the curved surface are X = 350, 400, 450 and 500 mm. From X = 400 to 500 mm, the profiles this time become fuller and Y_m increases slightly. From X = 500 to 700 mm the shapes of the velocity profiles and Y_m remain unchanged. The second part of the plane surface begins at X = 523.7 mm. so the shapes of the velocity profiles and values of Y_m are indications that the flow settles into another equilibrium state. However, at X = 850 and 950 mm, the shapes of the profiles become slightly fuller and Y_m decreases slightly. The velocity profiles are shown in figs. 4-3(A), (B), (C) and (D). The comparison between the velocity profile on logarithmic spiral surface (in this and following comparisons, curvature parameter k = 1 for logarithmic spiral sirface) measured by Guitton and the profiles at X = 450, 550 and 950 mm is shown in fig. 4-4.

4-1-2 Growth rate of jet and maximum velocity decay

The growth rate of half-width $Y_{\frac{1}{2}}$ is plotted versus X on fig. 4-5. The same data which is non-dimensionalized by slot width b is re-plotted in fig. 4-6.

On the plane surface, the growth rate is linear. The comparison with the data measured by Förthmann (1934); Patel (1962), Tailland (1967, 1970) and Guitton (1970) is shown in Fig. 4-7. The three data sets produced by Tailland for different Reynolds numbers indicate there is a shift of the virtual origin. Here the results for Reynolds Number Re = 2.5 x 10^4 closest to the present Reynolds number Re = 2.54 x 10^4 are chosen. Launder and Rodi (1981) concluded that the growth rate of half-width on the plane wall jet falls within the range

$$\frac{dY_{\frac{1}{2}}}{dx} = 0.073 \pm 0.002 \qquad (4\text{-}1)$$

The present experiment shows the rate is 0.069. The value is slightly out of range, however, the present experiments are not only for the study of the plane wall jet and the plane surface extends only as far as X/b = 52.0. The measurements on the plane surface were made between X/b = 31.5 and 47.2 so that a small error in $Y_{\frac{1}{2}}$ could lead a large error in the rate of growth.

At the very first station on the curved surface, i.e. X = 350 mm, the growth of the jet remains unchanged from the growth at X = 300mm. This is followed by a rapid accelerating growth rate until at the end of the curved surface. The local growth rate $dY_{\frac{1}{2}}/dx$ is approximately 0.39. The growth rate $Y_{\frac{1}{2}}/S$ is approximately 0.32 where S is the distance round the surface from the virtual origin of the curvature. The study of the jet on a logarithmic spiral surface by Guitton (1977) showed the local growth rate and growth rate to be 0.3 and 0.267 respectively.

From the end of the curved surface, the growth rate gradually decreases. The rate falls close to that on the first plane surface, and it nearly settles to a straight line.

The decay of maximum velocity Um versus X is shown in fig. 4-8. Fig. 4-9 is non dimensionalised form of the decay of max. velocity. In this fig. the velocities are squared.

On the plane surface, the decay is compared with the results taken by others which are shown in fig. 4-10. Although the rate of decay is slightly higher than the others, it is clearly linear and in reasonable agreement.

As was seen in the growth rate of jet width, there is a sudden change on the curved surface. This time the maximum velocity increases at X = 350mm. Then this is followed by a steady decay rate on the curved surface. When the flow reaches the second plane surface, the rate of decay slowly decreases. Again it does not settle to a straight line.

4-1-3 Discussions of 4-1

On the first plane surface, the jet is, when only the mean velocity components are concerned, in the equilibrium state, although the surface extends only as far as X/b = 52.0. The velocity profiles, the growth rate of jet width and the max. velocity decay are in good agreement with the results of Föthmann, Patel, Tailland and Guitton.

This equilibrium state is broken by a sudden change of the surface curvature. The flow soon settles into linear rates of growth of jet width and maximum velocity decay. The levels of the rates are higher than the rates on the plane surface. However, the velocity profiles keep changing their shapes on the curved surface. The sudden change at

X = 350mm in the velocity profile, growth rate of jet width and maximum velocity decay, may be described by the surface pressure change. The pressure is shown in fig. 4-11 where the surface pressure P_s is non-dimensionalized as $(P_\infty - P_s)/\rho U_m^2$. The sudden drop of the pressure at X = 350mm is clearly shown. This drop produces the static pressure drop across the jet thus accelerates the flow. This pressure change settles soon to a nearly equilibrium state on the curved surface. Therefore the growth rate of jet and maximum velocity decay maintain the linear rates. The surface pressure starts increasing from approximately X = 500mm which is just upstream of the end of the curved surface. The rate of pressure rise is not as rapid as that in the first change at the beginning of the curved surface.

On the second plane surface, the rates of the growth of jet width and the maximum velocity decay gradually decrease. However, unlike on the curved surface, these rates do not settle in to a new equilibrium type. This is also true for the surface pressure distribution and velocity profiles on the end of the curved surface to the second plane surface.

The very first study concerning this type of combined surfaces was carried out by Simpson (1970). He reported that the velocity profiles settled in a new shape and the rate of growth of jet width was linear on the second plane surface. However, his measurements were made by total head and static tubes and did not concern the V component. Also his rig had the slot aspect ratio of 72 compared with 146 for the present rig. Therefore his report should be treated with some caution.

The reason for this non-equilibrium ending of the jet is not clear. However, it may be caused by a lack of two-dimensionality or the second part of plane surface is not long enough for a new equilibrium state to be developed. No further study was made concerning this matter, since the extent of the rig is limited and the local flow velocities in these regions are difficult to measure with acceptable accuracy.

4-2 Fluctuating velocity components

4-2-1 Longitudinal turbulence component $\overline{u'^2}$

The longitudinal turbulent intensity profiles are shown in figs. 4-12(A), (B), (C) and (D). The turbulent intensities have been non-dimensionalised by the maximum velocity Um. Fig. 4-12(A) clearly shows two profiles on the plane surface at X = 200 and 300mm are in good agreement. These profiles are compared with the profiles measured by Tailland, Wilson and Goldstein and Guitton in Fig. 4-13. The circles represent measured values and squares represent the values which are corrected for high intensity turbulence with the response of the hot-wire. The level of the turbulent intensity is similar to the measurements of Wilson and Goldstein. The shape of the profile is in reasonable agreement with Guitton's data. The level of the intensity, however, is approximately 19% and 23% higher than the measurement of Guitton when the correction is not and is applied respectively.

At X = 350mm, there is a sudden change in both the level and the shape of the turbulent intensity profile. In order to see the levels of the intensity against X, the maximum value of turbulent intensities $\overline{u'^2_m}$ and their positions at each station are plotted against X in fig. 4-14.

There is a sudden decrease in the level of the turbulence at X = 350mm. This is followed by a rapid increase in the level which stops at X = 550mm. Then, the level gradually decreases. At X = 550mm the maximum turbulence level is 2.5 times higher than the maximum level on the plane surface. This maximum turbulence level is also 50% higher than the turbulence level measured on the logarithmic spiral surface by Guitton and 64% higher when correction is applied. The distance between the maximum value $\overline{u'^2_m}$ and the surface which is Y_{mu} becomes closer to the surface on the curved surface. This movement is also observed for the jet on a circular cylinder. After X = 550mm i.e. on the second plane surface, the Y_{mu} become larger. There are increases in turbulence intensities close to the surface i.e. $Y/Y_{\frac{1}{2}} < 0.1$. These are seen in figs. 4-12(A), (B), (C) and (D), however, this tendency is not clear at X = 550 and 600mm.

4-2-2 Lateral turbulence component $\overline{v'^2}$

The lateral turbulent intensity profiles are shown in figs. 4-15 (A), (B), (C) and (D). Fig. 4-15(A) clearly shows the profiles taken on the plane surface at X = 200 and 300mm are in good agreement. The comparison with the profiles measured by others is shown in fig. 4-16. There is more variation of $\overline{v'^2}$ in the reported profiles than the longitudinal turbulence intensity. The measurements made by Tailland show considerably higher levels of $\overline{v'^2}$ component so that the measurement made by Alcaraz who is from the same laboratory is presented instead. Large variations both in levels and the shape of the profiles are seen in the fig. The profile of the present measurement is similar to Guitton's measurement:however the levels of the turbulence are 27% and 57%, when corrected, higher than his measurements. On the other hand the level of the measured profile is almost the same as Wilson and Goldstein's measurements. The level of the corrected values is similar to the measurement of Alcaraz.

The maximum values $\overline{v'^2_m}$ and their positions are plotted against X. This is shown in fig. 4-17. The figure shows a sudden increase in the level of turbulence intensity at the beginning of the curved surface i.e. X = 350mm. $\overline{v'^2_m}$ reaches maximum at X = 550mm. The level is 4.6 times higher than the level of the plane surface. The levels are 25% and 68%, when corrected, higher than the level measured by Guitton on the logarithmic spiral surface. The level of $\overline{v'^2_m}$ gradually decreases from X = 550mm towards the end of the surface. The values of Y_{mv} change with similar manner as Y_{mu}.

4-2-3 Lateral turbulence component $\overline{w'^2}$

The lateral turbulent intensity $\overline{w'^2}$ varies with X. The profiles are shown in figs. 4-18(A), (B), (C) and (D). On the plane surface the profiles at X = 200 and 300 mm agree reasonably well in the outer part of the jet. $\overline{w'^2_m}$ and their positions are plotted against X in fig. 4-19. The tendency which has been observed in $\overline{u'^2_m}$ and $\overline{v'^2_m}$ is also seen in the case of $\overline{w'^2_m}$. The maximum $\overline{w'^2_m}$ is seen at X = 550mm and 3.4 times higher than on the plane surface. The levels are also 70% and 230%, when corrected, higher than the measurements made by Guitton on the log. spiral surface.

4-2-4 Turbulent shear stress $\overline{u'v'}$

The profiles of turbulent shear stress are shown in figs. 4-20(A), (B), (C) and (D). Once again the two profiles taken on the plane surface are in good agreement. The comparison with the profiles measured by others is shown in fig. 4-21. The shape of the profile is similar to the profile measured by Tailland. The level is 5% lower and 10%, when corrected, higher than the level measured by Guitton.

The maximum values $\overline{u'v'}_m$ and their positions are plotted against X in fig. 4-22. The result is also very similar to the figs. for $\overline{u'^2_m}$, $\overline{v'^2_m}$ and $\overline{w'^2_m}$. The maximum $\overline{u'v'_m}$ is at X = 550mm. The levels are 30% and 67%, when corrected, higher than the measurements on the log. spiral surface by Guitton. The position where $\overline{u'v'} = 0$ is also shown in fig. 4-22. The position becomes closer to the surface for X = 350 to 450mm. This tendency can also be observed for the jet on a circular cylinder. The position becomes closest from the surface at X = 450mm where is still the middle of the curved surface. The position moves away from the surface from X = 450 to 600mm. This is followed by a very slow inward movement towards the end of the second plane surface.

4-2-5 Turbulent kinetic energy k

The turbulent kinetic energy k is defined by the equation

$$k = \tfrac{1}{2}(\overline{u'^2} + \overline{v'^2} + \overline{w'^2}) \qquad (4\text{-}2)$$

i.e. the half the sum of the normal stresses.

On the plane surface, the profiles taken at X = 200 and 300mm agree reasonably well. The profile is shown in fig. 4-23 with the profiles measured by Alcaraz, Wilson and Guitton. The profile is similar to Guitton's measurement however the levels are 8% and 28%, when corrected, higher than his profile.

The maximum values km and their positions are plotted against X in fig. 4-24. The shape of this figure is similar to the shapes which have been observed in the cases of $\overline{u'^2_m}$, $\overline{v'^2_m}$, $\overline{w'^2_m}$ and $\overline{u'v'_m}$. On the curved surface from X = 400 to 550mm, there is a rapid increase in the level of k which reaches its maximum value at X = 550mm. The maximum level is 3.2 times higher than on the plane surface and 42% and 83%, when corrected, higher than the level measured by Guitton on the log. spiral surface. A comparison is made with the corrected k profiles on the plane, curved and second plane surfaces and the profiles on the plane and log. spiral surfaces measured by Guitton. This is shown in fig. 4-25. The figure shows that the profiles are in good agreement, however, the levels are higher than the Guitton's data.

4-2-6 Discussion of 4-2

The similarity of the profiles of the non-dimensionalised normal stresses $\overline{u'^2}$, $\overline{v'^2}$ and $\overline{w'^2}$ and the shear stress $\overline{u'v'}$ distributions at X = 200 and 300mm on the plane surface clearly indicates the flow is self-preserving. This confirms the results from the mean velocity components which have been discussed in the former section. The levels of the stresses on the plane surface, except the uncorrected shear stress are all higher than the stresses measured by Guitton. However, the comparisons with the measurements made by

Tailland, Wilson, Wilson and Goldstein, and Alcaraz are in reasonably good agreement.

The first measured station on the curved surface at X = 350mm, there are sudden changes in the turbulence intensities as well as the profiles. The decrease in $\overline{u'^2_m}$ can also be explained by the static pressure changes. The drop of the static pressure across the jet causes the flow to accelerate thus reducing the longitudinal turbulent level. This acceleration affects only the longitudinal turbulent intensity because the direction of the mean flow is most affected by the static pressure change. The level of the other stresses i.e. $\overline{v'^2}$, $\overline{w'^2}$ and $\overline{u'v'}$ start increasing at X = 350mm.

The stresses reach their maximum values at X = 550mm. The levels of the stresses vary 2.5 times for the case of $\overline{u'^2}$ to 4.6 times for the case of $\overline{v'^2}$ higher than the levels on the plane surface. From X = 550mm the levels of the stresses decrease to the final measured station X = 950mm where the levels are still falling. Therefore, unlike the results of mean velocity components, the flow does not reach the equilibrium state on the curved surface. On the second plane surface, both mean velocity components and fluctuating velocity components indicate that the flow does not reach the equilibrium stage.

The positions of the maximum stresses in the profiles become closer to the surface when the curved surface begins. The positions reach closest to the surface at the end of the curved surface, i.e. X = 550mm. On the second plane surface, the positions gradually move towards the outside of the jet. The positions vary with the components.

In the profiles of $\overline{u'^2}$ and $\overline{w'^2}$ across the jet, there is a clear sign of increase in the levels of the stresses in the region close to the surface. In boundary layer the intensities of $\overline{u'^2}$ and $\overline{w'^2}$ components increase in the area close to the surface. Therefore the increase in the level of $\overline{u'^2}$ and $\overline{w'^2}$ very close to the surface can be explained by this fact. The positions of the lowest turbulence intensities just outside of the increase which has been explained above may be the interfaces between outer and inner portions of the jet. It may be mentioned that the size of the increase in $\overline{w'^2}$ component near the surface is larger than the $\overline{u'^2}$ component. This may be caused by an extra effect by vortices similar to Görtler vortices whose axis are parallel to the streamwise direction.

The magnitude of increase in $\overline{v'^2}$ and $\overline{w'^2}$ compared with $\overline{u'^2}$ due to curvature is shown in fig. 4-26. The maximum ratios in each station $(\overline{u'^2} / \overline{v'^2})_m$ and $(\overline{u'^2} / \overline{w'^2})_m$ are plotted against X. $(\overline{u'^2} / \overline{v'^2})_m$ and $(\overline{u'^2} / \overline{w'^2})_m$ are the maximum value of $\overline{u'^2} / \overline{v'^2}$ and $\overline{u'^2} / \overline{w'^2}$ in the outer part of the jet. Because the region close to the surface the $\overline{v'^2}$ component is restricted by the presence of the solid boundary thus the level of the intensity becomes lower as it approaches the surface. The $\overline{u'^2}$ component is, on the other hand, higher near the surface as it is seen in the case of boundary layer. Therefore, the ratio $\overline{u'^2} / \overline{v'^2}$ has the highest value in the region very close to the surface. The profiles of the ratio are shown in fig. 4-27. The intensities $\overline{u'^2}$ and $\overline{v'^2}$ are corrected for high intensity turbulence.

In fig. 4-26 a sudden increase in the level of the $\overline{v'^2}$ component at the beginning of the curved surface is clearly seen. The ratio reaches the minimum value at X = 400, then gradually increases towards the end of the surface. The level of the ratio is compared with Guitton's data in fig. 4-27. The level of the ratio on the plane surface differs from his result. This is because of the higher level of measured $\overline{v'^2}$ component compared with his measurement. However, at X = 550mm the level of the ratio agrees well with the measurement on the logarithmic spiral surface by Guitton.

The ratio of the turbulent shear stress and the turbulent kinetic energy $\overline{u'v'}/k$ across the jet is shown in fig. 4-28. The values are also corrected for high intensity turbulence. Guitton reported that the ratio is insensitive to curvature within the accuracy of the measurements. However, the present measurements show that the ratio varies with X except on the plane surface.

4-3 Corrections for hot-wire's directional sensitivity

The high intensity turbulence effects on the response of hot-wires have been discussed in the former chapter. The necessity of measurements of higher order correlations has been pointed out in the chapter. The measurements of $\overline{u'v'^2}$ and $\overline{u'w'^2}$ were made on the plane surface at X = 300mm, at the end of the curved surface at X = 550mm and on the second plane surface at X = 700mm. The measured values have been calculated with the other measured velocity components. The final form of the corrections are expressed by the coefficients

$$\text{Coefficient} = \frac{\text{Corrected value}}{\text{Measured value}}$$

where E, F, G and H represent the correction coefficients for $\overline{u'^2}$, $\overline{v'^2}$, $\overline{u'v'}$ and $\overline{w'^2}$ respectively.

The results are shown in figs. 4-29(A), (B), (C) and (D). All the coefficients are large at the outer part of the jet except in the case of F. These coefficients at the outer part of the jet are suspect because the flow is intermittent and the intensities become large so that it is necessary to include even higher order correlations. Generally the coefficients at X = 300mm are the smallest and at X = 550mm are the largest. At X = 700mm, the coefficients fall between those two.

The corrections for $\overline{u'^2}$ are relatively small. The coefficients at X = 550mm almost coincide the coefficients at X = 700mm. The corrections for $\overline{v'^2}$ are large especially at X = 550mm. It is plausible that the intensity of $\overline{v'^2}$ increases on the curved surface, thus the values of F at X = 550mm are much higher than at X = 300 or 700mm. This tendency is also observed for the corrections for $\overline{u'v'}$. The values of G at X = 550mm are much higher than the other two measured stations. The corrections for $\overline{w'^2}$ is the largest. The coefficients at X = 300 and 700mm do not differ much. The calculations of H is based on the assumption V = 0 because of the complexity of the calculation. Therefore, the corrections for $\overline{w'^2}$ should be regarded with some uncertainties.

The coefficients E, F and H at X = 300mm on the plane surface have similar profiles to the results made by Guitton on the plane wall jet, although the levels are much higher than his results. The coefficients G have different shapes from Guitton's result. On the curved and second plane surfaces, the coefficients across the jet have similar profiles to the results made by Guitton. The higher levels of coefficients may be due to the higher levels of measured turbulent stresses than the values measured by Guitton.

The corrected and uncorrected turbulent stresses across the jet are shown in figs. 4-30 to 33. The squares represent corrected values and triangles represent uncorrected values.

4-4 Correlations

All the auto-correlations have been non-dimensionalized by local mean velocity U and half-width Y½. $R_{11}(0;\ 0,0,r_3)$ correlations have been non-dimensionalized by Y½. There are some arguments about the use of U when normalizing auto-correlations. These will be discussed later. The abscissas in the correlograms τ.U/Y½ or r/Y½ will be written r' for convenience. The ordinates are written R_{ij}.

4-4-1 On the plane surface

$R_{11}(\tau;0,0,0)_{1.0 \text{ and } 0.7}$ correlations on the plane surface at X = 300mm are shown in fig. 4-34(A). The solid line and broken line represent the correlations taken at Y/Y½ = 1.0 and 0.7 respectively. Also the subscripts 1.0 and 0.7, e.g. $R_{11}(\tau:0,0,0)_{1.0}$, indicate the positions Y/Y½ where the measurements have been made. The two correlations are in reasonable agreement. The most notable point is that the correlations have negative values. In isotropic, homogeneous and most inhomogeneous flows, there are no negative values in $R_{11}(\tau:0,0,0)$ or $R_{11}(0:r_1,0,0)$ correlations, althought there is no mathematical reason why these should be all positive. The curves change sign at r' = 2.1 and 2.6 and the minimum values are approximately R_{11} = -0.05 and - 0.06 at Y/Y½ = 1.0 and 0.7 respectively.

$R_{22}(\tau:0,0,0)_{1.0 \text{ and } 0.7}$ correlations are shown in fig. 4-34(C).

The correlations at $Y/Y\frac{1}{2} = 1.0$ and 0.7 are in good agreement. The values also become negative at $r' = 1.0$. The minimum value is approximately $R_{22} = -0.06$.

$R_{33}(\tau{:}0,0,0)_{1.0 \text{ and } 0.7}$ correlations are shown in fig. 4-34(D). The correlations are again in reasonable agreement. The $R_{33}(\tau)$ correlations are also in reasonable agreement with $R_{22}(\tau)$ correlations.

The transverse correlation, $R_{11}(0{:}0,0,r_3)_{1.0}$ is measured at $Y/Y\frac{1}{2} = 1.0$ and this is shown in fig. 4-34(B). The correlation becomes negative at $r' = 0.55$ and has a large negative loop. The minimum value reaches $R_{11} = -0.15$.

The shear stress correlations $R_{12}(\tau{:}0,0,0)_{1.0 \text{ and } 0.7}$ are shown in fig. 4-35(A). Two correlations are almost identical. The value of correlation becomes negative at $r' = 0.6$ and the minimum value is $R_{12} = -0.03$.

In isotropic turbulence, the correlation can be divided by longitudinal and transverse correlations. The longitudinal correlation $f(r)$ has the velocity components parallel to the separation r of hot-wires. In the case of auto-correlation, the separation is parallel to the mean flow direction, i.e. approximately X direction. When the velocity components are at right angle to the separation, it is the transverse correlation $g(r)$. In the initial isotropic turbulence, the longitudinal correlation has the form

$$f(r) = e^{-r/L_f} \tag{4-3}$$

and the transverse correlation has the form

$$g(r) = (1 - \frac{1}{2}\frac{r}{L_f})\, e^{-r/L_f} \qquad (4\text{-}4)$$

where L_f is the longitudinal integral length scale. This scale is defined by

$$L_f = \int_0^\infty f(r)\, dr \qquad (4\text{-}5)$$

The correlations which have been presented show that the flow is far from isotropic. For example, the $R_{11}(\tau{:}0,0,0)_{1.0}$ correlation, which is the longitudinal correlation, has negative values. However the longitudinal correlation form 4-3 does not have negative values. Therefore it is not possible to fit the measured correlations into the isotropic correlation forms. Attempts have been made to fit the measured correlations into the modified forms which have two more constants. The forms are

$$f(r) = a \; e^{-r/L_f} - b \qquad (4\text{-}6)$$

for the longitudinal correlations and

$$g(r) = a\,(1 - \frac{1}{2}\frac{r}{L_f})e^{-r/L_f} - b \qquad (4\text{-}7)$$

for the transverse correlations. a and b are the constants. These approximations are well fitted to the measured correlations except at the region of small values of r' where only small eddies contribute to the correlations. The small eddies do not contribute much to the kinetic energy therefore it is more important to fit the curves at large values of r'. The results are shown in table 4-1. The table also present the values of r' where $R_{ij} = 0$ and $R_{ij} = \text{min.}$, the measured integral scales and their non-dimensionalized values.

The integral scales from the auto-correlations, however, are in doubt when they are compared with the scales obtained from space correlations. Because the normalization of r' is based on the Taylor's "frozen" flow hypothesis and the validity of this hypothesis is on the assumpations that the flow is locally isotropic and that the turbulent intensities are not high. The turbulence flow pattern may be convected by convection velocity Uc instead of local mean velocity U. Wygnanski and Fiedler (1969), for example, successfully obtained convection velocities which made the difference between auto-correlations and space correlations very small. Some problems arise, however, from this theory. There are two or more ways to define convection velocities. The small-scale motion may be convected faster than the large-scale motion and so convection velocities may depend on the size of the eddies. The relative comparisons between auto-correlations are not affected by these facts. However the comparison between auto-correlations and the $R_{11}(0;0,0,r_3)$ correlations should be treated with some allowances. The convection velocity at $Y/Y\frac{1}{2} = 1.0$ has been obtained for a reference purpose.

The space-time correlations are shown in fig. 4-36. The separations are 5, 10, 15, 20 and 30mm from the X = 300mm station. The last station is therefore at the very end of the plane surface. The iso-correlation curves are obtained from this figure which is shown in fig. 4-37. If the pattern of turbulence is of the "frozen" type, this figure should consist of straight lines. The average convection velocities can be defined from the conditions

$$\frac{\partial R}{\partial r} = 0 \qquad (4\text{-}8)$$

$$\frac{\partial R}{\partial \tau} = 0 \qquad (4\text{-}9)$$

where R is the correlation coefficient, r is the separation, and τ is the time delay. Two convection velocities tend to the same value in this figure. Therefore the convection velocity which represents all sizes of eddies and time averaged is Uc = 17.3 m/s. This is approximately 12% higher than the local mean flow velocity.

This value has been compared with the calculated value. Wygnanski and Fiedler (1970) calculated the convection velocity from a transformation from temporal to spatial derivatives. This is given by:

$$\overline{\left(\frac{\partial u'}{\partial t}\right)^2} \Big/ \overline{\left(\frac{\partial u'}{\partial x}\right)^2} = U^2 \left(1 + \frac{\overline{u'^2}}{U^2} + 2\,\frac{\overline{v'^2}}{U^2} + \frac{\overline{w'^2}}{U^2}\right) \qquad (4\text{-}10)$$

The equation is based on the assumptions of isotropy and the independence of the large and small scale eddies. The above equation defines the convection velocity as

$$U_c^2 = U^2 + \overline{u'^2} + 2\overline{v'^2} + \overline{w'^2} \qquad (4\text{-}11)$$

The calculated convection velocity is U_c = 18.1 m/s which is only 4.6% higher than the measured one. Because of the uncertainties in the definition of the convection velocity, this difference is considered to be relatively small.

If it is assumed that the turbulence pattern is convected by the convection velocity, the itegral length scale is L_f = 9.69mm and non-dimensionalized, the scale is $L_f/Y_{\frac{1}{2}}$ = 0.431 compared with the values 8.68mm and 0.386 respectively when obtained from the local mean velocity. The ratio of longitudinal and transverse scales is L_f/L_g = 4.85 compared with 4.34. Such a large value in the ratio is caused by the large negative loop in the $R_{11}(0{:}0,0,r_3)$ correlation.

The negative values in $R_{11}(\tau{:}0,0,0)$, $R_{22}(\tau{:}0,0,0)$, $R_{33}(\tau{:}0,0,0)$ and $R_{11}(0;0,0,r_3)$ correlations may be explained by mixing jet type large scale motion which has been suggested by Grant (1958). The strong negative loops in $R_{11}(0{:}0,0,r_3)$ and $R_{33}(\tau,0,0,0)$ can be caused by an array of large eddies whose axis in the Y-direction. However, from this theory, it is difficult to explain why the $R_{11}(0{:}0,0,r_3)$ negative loop is more noticeable than the $R_{11}(\tau{:}0,0,0)$ one. The minimum value in $R_{11}(0{:}0,0,r_3)$ is twice the value of $R_{11}(\tau{:}0,0,0)$ correlation. Bradshaw, Ferriss and Johnson (1964) considered that this difference, in correlations in the mixing layer in the round jet, was caused by the Y-direction velocity component rather than the Z-direction velocity component. This Y-direction motion was thought to be a mixing-jet type motion which is in the X-Y plane. From the discussion in the former section it is appropriate to expect a similarity with the plane wall jet and the free jet. Therefore we consider that the outer portion of the jet on the plane surface has a similar structure to the free jet and follow their approach.

If the mixing jet type motion does exist in the outer portion of the jet, it is expected that $R_{11}(0{:}0,0,r_3)$ should have a more moticeable negative loop than that of $R_{11}(\tau{:}0,0,0)$.

When the mixing jet arrives at the measured point, it has a u' velocity component different from the one outside the mixing jet The negative loop in the correlation which has the separation in the Z-direction is stronger if the mixing jet has a finite width. Because the correlations are time averaged values, the $R_{11}(\tau:0,0,0)$ correlations cannot clearly show the motion since it has random frequencies and sizes, unlike the correlations $R_{11}(0:0,0,r_3)$ which correlates the u' velocity components between inside and outside of a finite width motion. Another support for this is the $R_{11}(0:0,0,r_3)$ correlation which has no sign of periodicity. If there is an array of eddies with the axis in the Y-direction, the correlation should have a kind of periodicity. There are also no signs of periodicity in the $R_{11}(\tau:0,0,0)$, $R_{22}(\tau:0,0,0)$ and $R_{33}(\tau:0,0,0)$. However, because of the slow recovery of the negative values in the correlations with large τ and the scatter of the signals, it is not certain whether there are periodicities or not. The similar magnitudes of the negative values in $R_{11}(\tau:0,0,0)$ and $R_{22}(\tau:0,0,0)$ correlations indicate a strong connection between them which cannot be explained by the array of eddies with axis in the Y-direction. Because in the case of the above eddies there should be no connection between u' and v' components, while on the other hand there should be connections between $R_{33}(\tau:0,0,0)$ and $R_{11}(0:0,0,r_3)$, of which there is no sign.

There are approximately the same level of negative values at $Y/Y_{\frac{1}{2}} = 1.0$ and 0.7 in the $R_{11}(\tau:0,0,0)$, $R_{22}(\tau:0,0,0)$ and $R_{33}(\tau:0,0,0)$ correlations. However, the positions of the minimum values vary except for the $R_{22}(\tau:0,0,0)$ correlations. The positions of the minimum correlations take a larger value of τ at $Y/Y_{\frac{1}{2}} = 0.7$ than at 1.0. This may be evidence that although the strength of the mixing jets is the same at both points, at $Y/Y_{\frac{1}{2}} = 1.0$ the position is relatively outside of the mixing jets region because the minimum correlations appear at smaller values of τ than is the case at $Y/Y_{\frac{1}{2}} = 0.7$. Therefore the distance between the boundaries of a mixing

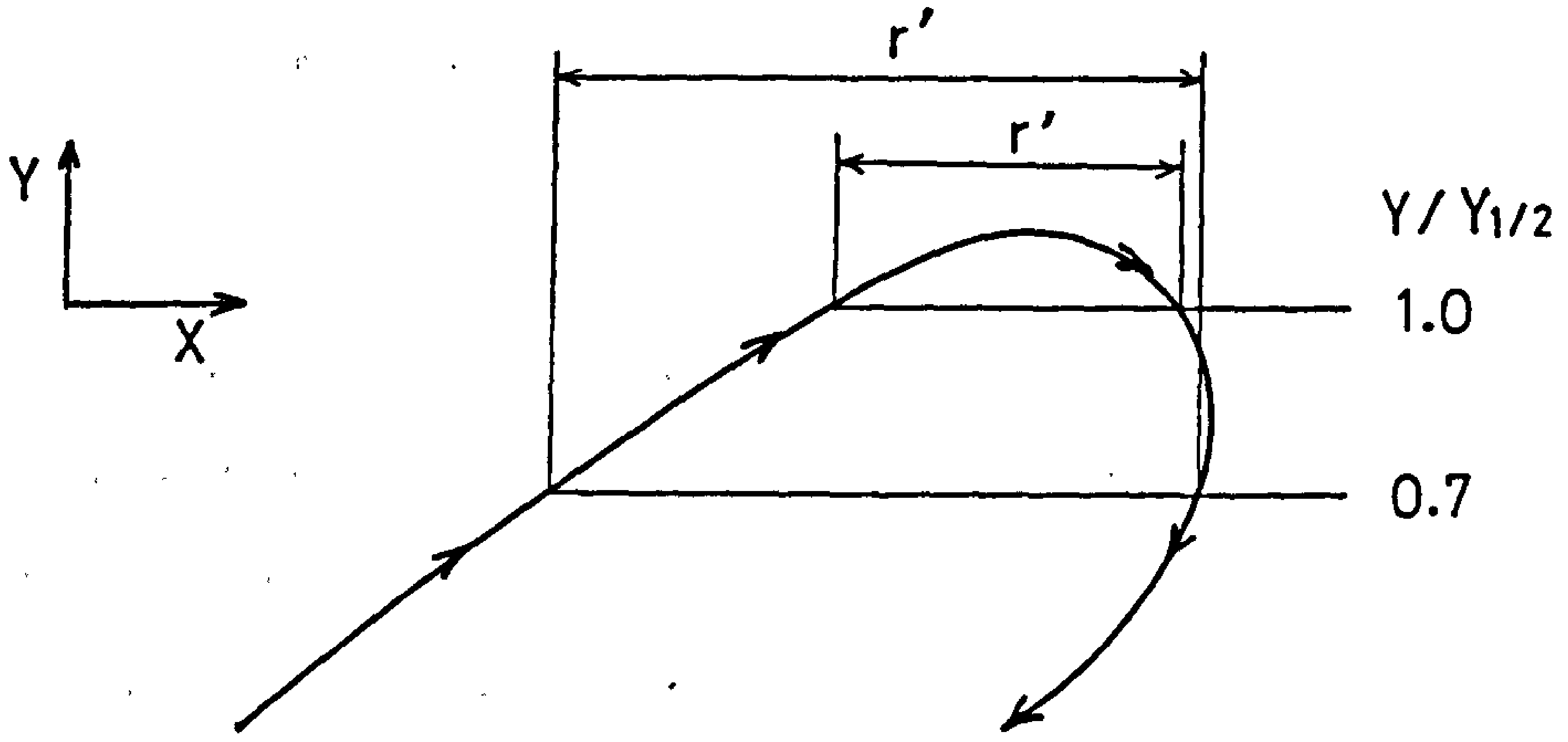

jet in a X-direction is smaller at $Y/Y_{\frac{1}{2}} = 1.0$ (see sketch). The correlations measured at $Y/Y_{\frac{1}{2}} = 1.0$ and 0.7 show only slight differences. If the mixing jet type motion is large in size or relatively weak in strength then the difference between the correlations is expected to be large. Another fact is that from the similarity between $R_{22}(\tau:0,0,0)$ and $R_{33}(\tau:0,0,0)$ correlations there is a kind of homogeneity in X - Y plane. Therefore the author's view is that although there is evidence for the existence of a mixing jet type motion, it is not as strong or as clear as the motion in the free jet. It is very difficult to obtain sufficient data to see the details of such structures from statistical measurements unless the motion is very strong.

The $R_{12}(\tau:0,0,0)$ correlations are almost identical. This confirms the homogeneity of the flow. The integral scale of this correlation is approximately 2.18(mm). The ratios are 0.250 and 0.276 of the integral scale of $R_{11}(\tau:0,0,0)_{1.0 \text{ and } 0.7}$ respectively. From this and the correlogram it is thought that the frequency ranges in the shear stress spectra are narrower than those of normal stresses spectra.

4-4-2 On the curved surface

$R_{11}(\tau:0,0,0)_{1.0 \text{ and } 0.7}$ correlations on the curved surface at X = 550mm are shown in fig. 4-38(A). Two curves which have been measured at $Y/Y\frac{1}{2}$ = 1.0 and 0.7 differ at large r'. The correlations have negative values and change sign at r' = 0.90 and 1.15. The minimum values are R_{ij} = -0.09 and - 0.06.

$R_{22}(\tau:0,0,0)_{1.0 \text{ and } 0.7}$ correlations are shown in fig. 4-38(C). There is a clear difference between the correlations measured at $Y/Y\frac{1}{2}$ = 1.0 and 0.7. The correlations change sign at r' = 0.75 and 0.83.

The minimum values are R_{ij} = -0.10 and - 0.06.

$R_{33}(\tau:0,0,0)_{1.0 \text{ and } 0.7}$ correlations, on the other hand, are in good agreement except at very large r'. The correlations change sign at r' = 0.65 and the minimum value is R_{ij} = -0.06. These are shown in fig. 6-38(D).

The transverse correlation $R_{11}(0:0,0,r_3)_{1.0}$ is shown in fig. 6-38(B). The curve changes sign at r' = 0.4 and the minimum value is R_{ij} = -0.11.

The shear stress correlations $R_{12}(\tau:0,0,0)_{1.0 \text{ and } 0.7}$ are shown in fig. 6-35(B). The correlations are in reasonable agreement. The curves change sign at r' = 0.18. The minimum values are R_{ij} = -0.01 and - 0.02.

The space-time correlations are shown in fig. 4-39. From this figure iso-correlation curves are plotted which are shown in fig. 4-40. The separations between the hot-wires are 10, 20, 35, 50 and 80 mm. Therefore the positions are not actually on the curved surface. The convection velocity at $Y/Y\frac{1}{2} = 1.0$ is obtained by the same method as has been described before. The measured and calculated convection velocities are $U_c = 8.4$ and 9.5 m/s respectively. The calculated value is 13% higher than the measured value. This figure is large even when the accuracies and difficulties of the definition and the measurement are taken into account. This may be the departure from the assumption which is required by the equation 4-10 to calculate the convection velocity.

The correlations indicate that the flow is further from isotropic than the flow on the plane surface. Therefore, again the equations 4-6 and 4-7 have been used to approximate the measured correlations. The results are shown in table 4-1.

The integral length scales are $L_f = 12.9$ and 15.4mm at $Y/Y\frac{1}{2} = 1.0$ and 0.7 respectively when calculated from the local mean velocity. The non-dimensionalized scales are $L_f/Y\frac{1}{2} = 0.137$ and 0.164. These figures become $L_f = 14.6$ and $L_f/Y\frac{1}{2} = 0.155$ at $Y/Y\frac{1}{2} = 1.0$ when calculated from the convection velocity. The ratio of longitudinal and transverse scales is $L_f/L_g = 1.60$ and 1.83 when calculated from local mean velocity and convection velocity respectively.

The negative loops in the correlations $R_{11}(\tau{:}0,0,0)$, $R_{22}(\tau{:}0,0,0)$, $R_{33}(\tau{:}0,0,0)$ and $R_{11}(0{:}0,0,r_3)$ can also be explained by the mixing jet type motion. The support for this is the similar levels of negative values in $R_{11}(\tau:0,0,0)_{1.0}$, $R_{22}(\tau:0,0,0)_{1.0}$. It suggests, therefore, a strong relation between the correlations. This relation can only be explained by the mixing jet motion. Because if there is an array of eddies with axis in Y-direction, there should be a relation between the $R_{33}(\tau:0,0,0)$ and $R_{11}(0:0,0,r_3)$ correlations. The level of the negative loop in $R_{33}(\tau:0,0,0)_{1.0}$ correlation is clearly lower than that of the $R_{11}(0:0,0,r_3)$ correlation. The negative loop in $R_{11}(0:0,0,r_3)_{1.0}$ correlation is less noticeable than the correlation on the plane surface. This may be the indication either that the strength of the mixing jets become weaker or that the variation of the width of the mixing jets in Z-direction become wider. The former suggestion is the more difficult to justify because the level of the negative loops in the correlations become larger than the correlations on the plane surface. One another support for the existence of mixing jet type motion is that there seem to be periodicities in $R_{22}(\tau:0,0,0)_{1.0 \text{ and } 0.7}$ correlations. Because of the extreme intermittency of the flow, it is very difficult to obtain smooth correlation curves at large r'. Therefore there is no definite sign of periodicities; however, from the profiles of the correlations $R_{22}(\tau:0,0,0)_{1.0 \text{ and } 0.7}$ it is likely that the correlations have periodicities. If there are periodicities in $R_{22}(\tau:0,0,0)$ correlations, it may be strong support for the existence of an array of eddies with axis in the Z-direction introduced by the mixing jets motion.

The positions, i.e. values of r', of minimum values in the correlations at $Y/Y\frac{1}{2} = 0.7$ are larger than the r' in the correlations at $Y/Y\frac{1}{2} = 1.0$. This trend is clearer than the corresponding trend on the plane surface. This indicates that the size of the motion relative to the half-wdith $Y\frac{1}{2}$ become smaller at X = 550mm than X = 300mm , because the differences between the values of r' at minimum correlations measured

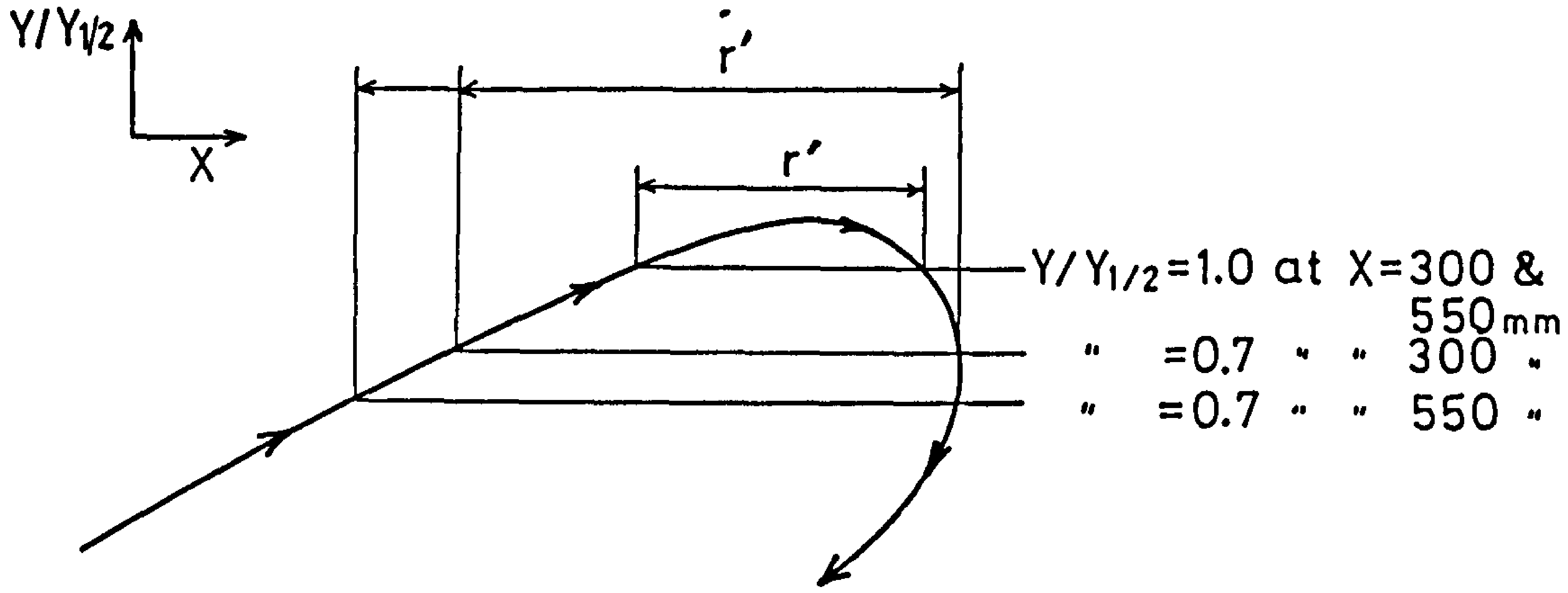

at Y/Y½ = 1.0 and 0.7 are larger on the curved surface, as shown in the sketch. This will be discussed in the later section.

The integral scales of $R_{12}(\tau:0,0,0)_{1.0 \text{ and } 0.7}$ correlations are again much smaller than the scale of $R_{11}(\tau:0,0,0)_{1.0 \text{ and } 0.7}$ correlations. The ratios are 0.210 and 0.138 respectively. The two correlations differ slightly.

4-4-3 Comparisons of correlations on the plane and the curved surfaces

There are obvious structure changes in the flows on the plane and curved surfaces. First of all, on the plane surface, there is a kind of homogenity in the X - Y plane, however, on the curved surface, there is no sign of homogenity in the correlations. This fact on the curved surface has been confirmed by the difference between measured and calculated convection velocities. The measured correlations show an increase in the longitudinal integral length scale L_f on the curved surface. However the non-dimensional scale L_f/Y½ decreases. This tendency is also clearly seen from the values of r' where the correlation curves change sign to negative.

The ratios, i.e. the integral scales on the plane surface are divided by those on the curved surface, are 0.673 and 0.510 at $Y/Y_{\frac{1}{2}} = 1.0$ and 0.7 respectively. The non-dimensional scale ratios are 2.82 and 2.13. The integral length scale represents the large scale motion therefore it is appropriate to seek a reason from the largest scale eddies in the flow. The increase in integral scales with dimension at X = 550mm shows the large scale motions are greater in size. The decrease in non-dimensional scale, on the other hand, shows the scales relative to the jet width $Y_{\frac{1}{2}}$ are smaller. Therefore the largest scale eddies, or possibly the mixing jet type motions which contribute mainly to the correlations, become relatively smaller on the curved surface for some reason.

The dissipation length scales λ at $Y/Y_{\frac{1}{2}} = 1.0$ at X = 300 and X = 550mm are 1.42 and 2.26mm respectively. These scales are calculated from the corrected turbulence energy balances which will be discussed in the later section. Because of the uncertainty of the filtering of the signals, the corrected values are used here. The dissipation length is defined as

$$\frac{1}{\lambda_2} = \frac{1}{\overline{u'^2}}\left(\overline{\frac{\partial u'}{\partial x}^{2}}\right)^{2} \qquad (4\text{-}12)$$

The dissipation is defined as

$$\varepsilon = 15\nu\,\overline{\frac{\partial u'}{\partial x}^{2}} \qquad (4\text{-}13)$$

From the values of the corrected dissipation curves, the dissipation scales have been calculated. The non-dimensional dissipation scales

$\lambda/Y\frac{1}{2}$ are 0.0631 and 0.0240 at X = 300 and 550mm respectively. The ratios, i.e. the scales on the plane surface divided by the scales on the curved surface, are 0.628 and 2.63 when dimensioned and when made non-dimensioned respectively. These values are very similar to the values for the integral length scales. It may be suggested that the range of the eddy sizes on both surfaces are, when non-dimensionalized, approximately the same. On the other hand the non-dimensionalized eddy sizes, which mainly contribute to the correlations, become smaller on the curved surface.

This is only true for the longitudinal correlations. The lateral integral scales L_g from $R_{11}(0:0,0,r_3)$ correlations at $Y/Y\frac{1}{2} = 1.0$ are 2.0 and 8.0mm on the plane surface and the curved surface respectively. The non-dimensionalized values are 0.089 and 0.085. Though the former value is 5% larger, from considerations of the accuracy of the measurements this may be negligible. This indicates that the size of the eddies in Z-direction become larger on the curved surface but the non-dimensionalized sizes are the same. If we assume that there are mixing-jets on both plane and curved surfaces, the non-dimensional length in the X-direction becomes smaller on the curved surface, which may be because of the surface curvature change. However, the length in the Z-direction remains unchanged. This tendency is clearly seen in the ratios L_f/L_g, which are 4.34 and 1.61 on the plane and curved surfaces respectively.

The integral scales from $R_{22}(\tau:0,0,0)_{1.0 \text{ and } 0.7}$ and $R_{33}(\tau:0,0,0)_{1.0 \text{ and } 0.7}$ correlations on the plane surface are very small. In fact the scales of $R_{22}(\tau:0,0,0)_{0.7}$ and $R_{33}(\tau:0,0,0)_{0.7}$ are negative because of the large negative loops in the correlations.

The accuracy of these scales is not likely to be very good because the values are so small. On the other hand the integral scales from the same correlations on the curved surface are large compared with the scales on the plane surface. The ratios, i.e. L are divided by longitudical scale L_f, of the scales of $R_{22}(\tau:0,0,0)_{1.0}$ and $R_{33}(\tau:0,0,0)_{1.0}$ are 0.57 and 0.63 respectively. The ratios at $Y/Y_{\frac{1}{2}} = 0.7$ are 0.24 and 0.14. Once again the values measured at $Y/Y_{\frac{1}{2}} = 0.7$ are likely to be inaccurate. $R_{22}(\tau:0,0,0)_{1.0}$ and $R_{33}(\tau:0,0,0)_{1.0}$ correlations change sign at $r' = 0.7$, compared with $r' = 0.9$ on the curved surface. These values are 1.0 and 2.0 on the plane surface. From these facts, it is clear that on the curved surface, the v' and w' motions are stronger when compared with u' motion. This can be explaned by the inclinations of the mixing-jets. On the plane surface, the u' motion is much stronger than the v' motion. If we assume that a mixing-jet is inclined in the X-Y plane, the steeper inclination causes the stronger u' motion. Therefore the inclinations of the mixing-jets may be steeper on the plane surface than the curved surface (see sketch). There is also a considerable

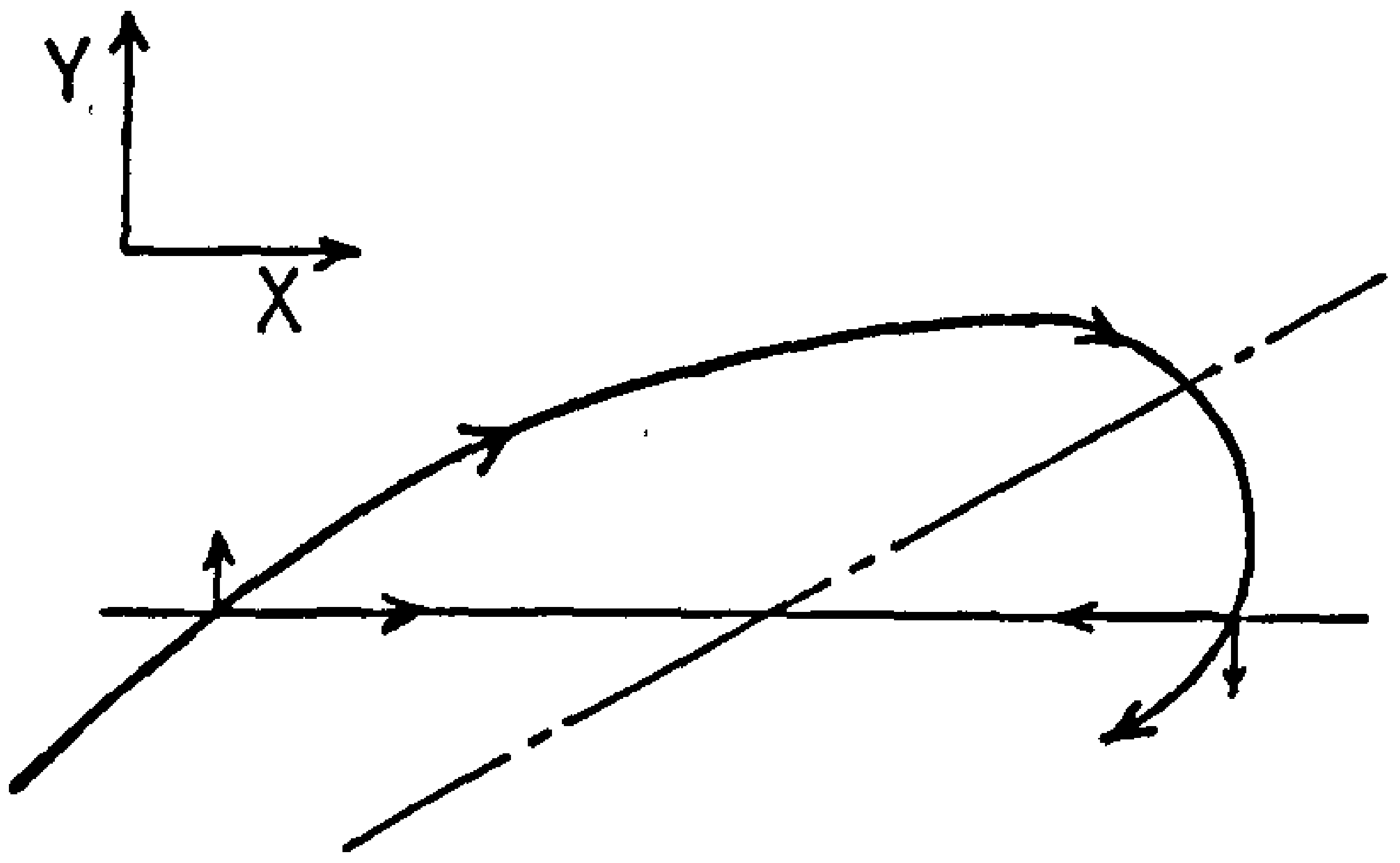

X = 300mm

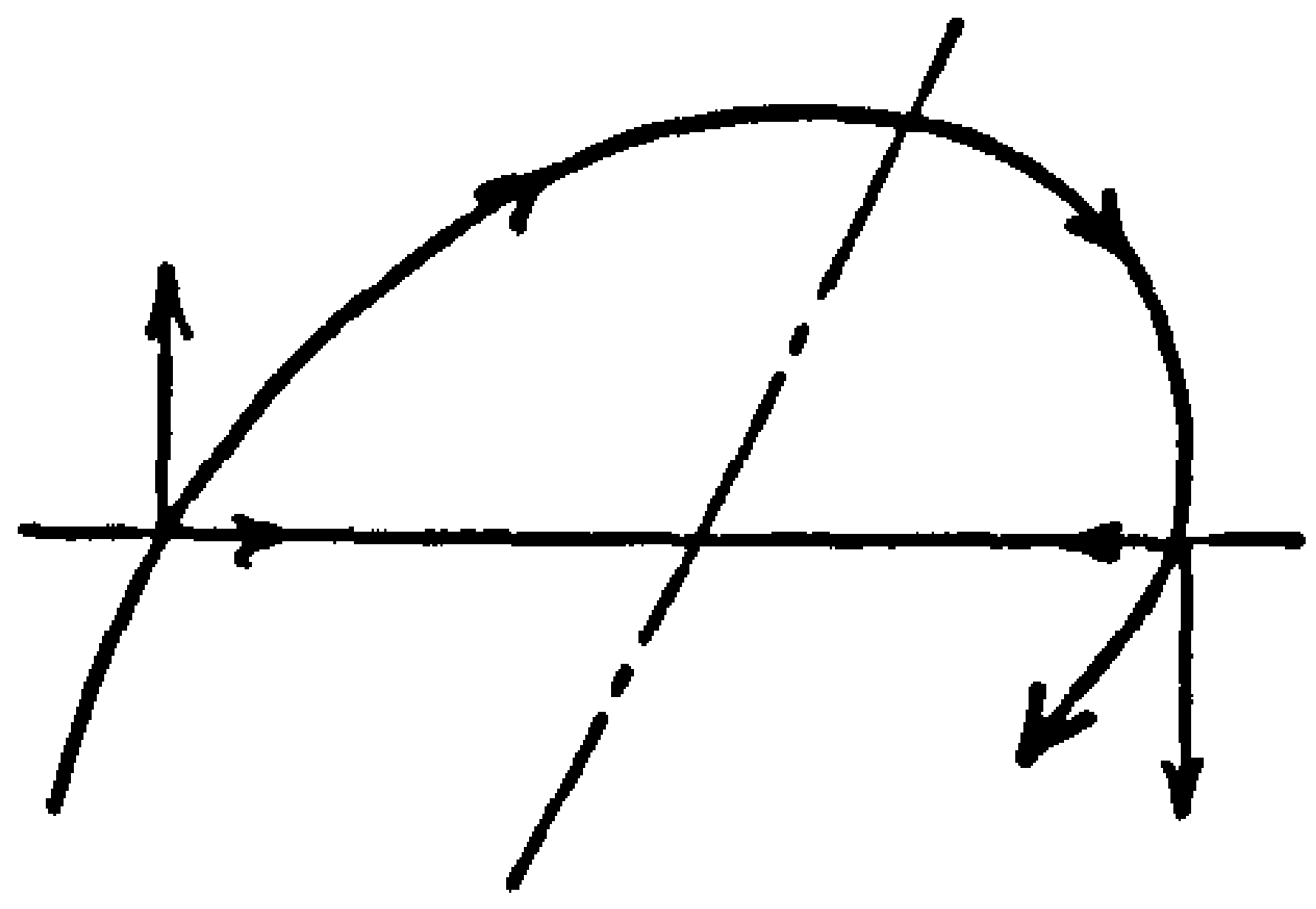

X = 550mm

increase in turbulent intensity in Y-direction i.e. $\overline{v'^2}$. This is another reason for the increase in the integral scales of $R'_{22}(\tau:0,0,0)$ on the curved surface.

From the correlations we may conclude that there are evidences of the existence of the mixing-jets type motions. The jets are inclined in X-Y plane and the angle is larger on the plane surface. The sizes of the jets in the X-direction are larger on the curved surface. However, the non-dimensional sizes i.e. relative to the half-width $Y_{\frac{1}{2}}$, become smaller on the curved surface. The width of the jets in the Z-direction is also larger on the curved surface. Nevertheless, the non-dimensional sizes remain unchanged.

4-5 Turbulent kinetic energy balances

4-5-1 Theory

From the measurement of dissipation and other turbulent intensities which were described earlier, all the terms of the turbulent kinetic energy balance equation can be calculated except for the diffusion term. Hinze (1974) described the details of the theory. The present investigation follows his approach. The conservation equation for turbulent energy is given by equation (3-37). The terms of this equation are

$$\text{Advection} = -\left(\tfrac{1}{2}U\frac{\partial \overline{q^2}}{\partial x} + \tfrac{1}{2}V\frac{\partial \overline{q^2}}{\partial Y}\right)\left(\frac{Y_{\frac{1}{2}}}{U_m^3}\right) \qquad (4\text{-}14)$$

$$\text{Production} = -\overline{u'v'}\left(\frac{\partial U}{\partial Y}\right)\left(\frac{Y_{\frac{1}{2}}}{U_m^3}\right) \qquad (4\text{-}15)$$

$$\text{Dissipation} = -15\nu\overline{\left(\frac{\partial u}{\partial x}\right)^2}\left(\frac{Y_{\frac{1}{2}}}{U_m^3}\right) \qquad (4\text{-}16)$$

$$\text{Diffusion} = -(\text{Advection} + \text{Production} + \text{Dissipation})$$

where $\overline{q'^2}$ is the sum of the normal stresses i.e. twice the turbulent kinetic energy. The terms are non-dimensioned by the half-width $Y_{\frac{1}{2}}$ and the maximum velocity U_m. The dissipation term is based on the assumption for the Taylor's "frozen" flow which was described in Chapter 3.

4-5-2 Results and discussions

The measured turbulent energy balances at X = 300mm on the plane surface and X = 550mm on the curved surface are shown in figs. 4-41(A) and (B). Positive value in the figures means a gain in energy and negative value means a loss of energy.

The magnitude of the dissipation term depends on the filtering of the signal, which has been described in the previous chapter. A change in the magnitude of the dissipation leads to corresponding changes in the level and profile of the diffusion curve since the diffusion term is obtained by difference. Because of the uncertainty in the measurement of the dissipation, allowances with respect to accuracy have to be made. However, the accuracy of the diffusion can be assessed, in part, from the requirement that the net diffusion of turbulent energy across the jet has to be zero. The two terms i.e. the diffusion and dissipation terms, have been obtained by suitably scaling the measured dissipation to satisfy the requirement for the diffusion. The resulting energy balances are shown in fig. 42(A) and (B). The scaling factors of the dissipation term at X = 300 and 550mm are 2.3 and 1.2 respectively. The difference between the two factors shows that on the plane surface, the contribution to the dissipation by the eddies, which are smaller than the hot-wire length, are greater than those on the curved surface. Because the signals from the eddies smaller than the hot-wire length have been cut off by the low-pass filtering effect of the hot-wire. Therefore on the plane surface the 'filter' could cut off more signals from the eddies which contribute to the dissipation.

On the plane surface at X = 300mm, the production term is the main contributor to the gain of turbulent energy. This term is largest near the position of maximum shear stress. The main contribution to the loss of energy is given by the dissipation. The diffusion term contributes to the loss at $0.2 < Y/Y_{\frac{1}{2}} < 1.0$. The loss of energy by diffusion does not completely counter balance the production, nevertheless it is the main contributor to balance the production. At both the inner and outer regions of the jet, the diffusion changes sign to negative. The advection term also changes sign to negative at $Y/Y_{\frac{1}{2}} = 1.0$. The magnitude of the negative is, however, very small. The dissipation becomes greater near the surface $Y/Y_{\frac{1}{2}} < 0.1$. It can be seen in the boundary layer in which dissipation and production dominate the energy balance near the surface. These two terms balance each other. In the present flow, the production term has not been measured close enough to observe this tendency because of the dimensions of the hot-wires. However, the advection and the diffusion terms seem to approach zero at $Y/Y_{\frac{1}{2}} < 0.1$. The production term obviously becomes larger when approaching the surface, because the term $\partial U/\partial Y$ becomes negative and very large at $Y/Y_{\frac{1}{2}} < 0.1$ and $\overline{u'v'}$ becomes also negative and larger (negative) when approaching the surface. Thus the production term should become large at $Y/Y_{\frac{1}{2}} < 0.1$.

On the other hand, in the outer part of the jet, i.e. for

$Y/Y_{\frac{1}{2}} > 0.1$, the balance of kinetic energy becomes very close to the energy balance for a free jet, e.g. see Bradbury (1965). In the free jet, the dissipation contributes to the loss of energy. The diffusion changes sign twice and the production dominates the gain of energy. The advection has its positive (gain) peak relatively close to the inner part of the jet. Therefore it may be said that the plane wall jet consists of a wall shear layer which is often treated as a boundary layer and one half of a free jet.

Alcaraz, Charnay and Mathieu (1977) measured the terms of the turbulent energy balance equation for the wall jet over a large radius cylinder. The levels of the terms increase in the streamwise direction. However, the profiles at X/b = 30 may provide the balance terms for the plane wall jet because the position corresponding to only 7^{o} of arc so that the effects of curvature can be considered as being small. This is demonstrated by the level of the maximum shear stress at X/b = 30, which is similar to that on the plane surface. The levels of the production and the advection terms are almost the same levels as the terms on the plane surface. Their measurement for the dissipation is, however, very small so that the net diffusion is not zero. If the dissipation term is multiplied by a constant to adjust the net diffusion across the jet to be zero, the whole survey balance is in very good agreement with the present results. The present results are also in good agreement with those measured by Kobayashi and Fujisawa (1983) on a plane jet.

On the curved surface at X = 550mm, there are some differences from as well as similarities to the plane surface. Although the terms have been non-dimensioned by $Y_{\frac{1}{2}}$ and U_m, the magnitude of the turbulent energy balance is approximately ten times larger. The profiles of the individual terms are quite similar to the profiles on the plane surface. The production term is also greatest near the position of the maximum shear. This term changes sign to negative (loss) at $Y/Y_{\frac{1}{2}}$; nevertheless, the magnitude of the loss is very small. This is caused by the larger difference between the maximum velocity position and the position where $\overline{u'v'} = 0$. The dissipation is distributed over the whole jet and its graph less undulating than that for the plane surface. The most noticeable difference is the advection. This term is the main contribution at the middle to inner part of the jet. The turbulence diffusion term no longer changes sign to positive at the inner portion of the jet. This term does change sign, however, to positive at $Y/Y_{\frac{1}{2}} = 0.9$. Therefore, there is a transfer of energy by turbulence diffusion from the inner part of the jet toward the outer part. The dissipation and the production terms increase their levels when approaching the surface. Because of the higher level of the advection term, however, the balance at inner part of the jet differs from the balance in the boundary layer. This is also true for the outer part of the jet. The balance is no longer similar to the free jet. From these facts it is now clear that the profiles of the energy balance on the curved surface are in reasonable agreement with the profiles on the plane surface. The magnitudes of the advection term and production term are responsible for the differences between two balances.

The lateral advection is very much smaller than the longitudinal advection on both surfaces. The magnitudes of the advection and production terms increase in the downstream direction until X = 550mm, then decrease further downstream. This tendency is very similar to that of the turbulent stress distributions in the X direction. The rate of increase in the adveotion is much larger than the rate in the production. Thus the maximums of the advection and the production are almost equal at X = 450mm and X = 950mm and between the two stations the advection is much larger than the production. Therefore at X = 550mm, the kinetic energy transport is more important than the energy produced by the mean velocity gradient.

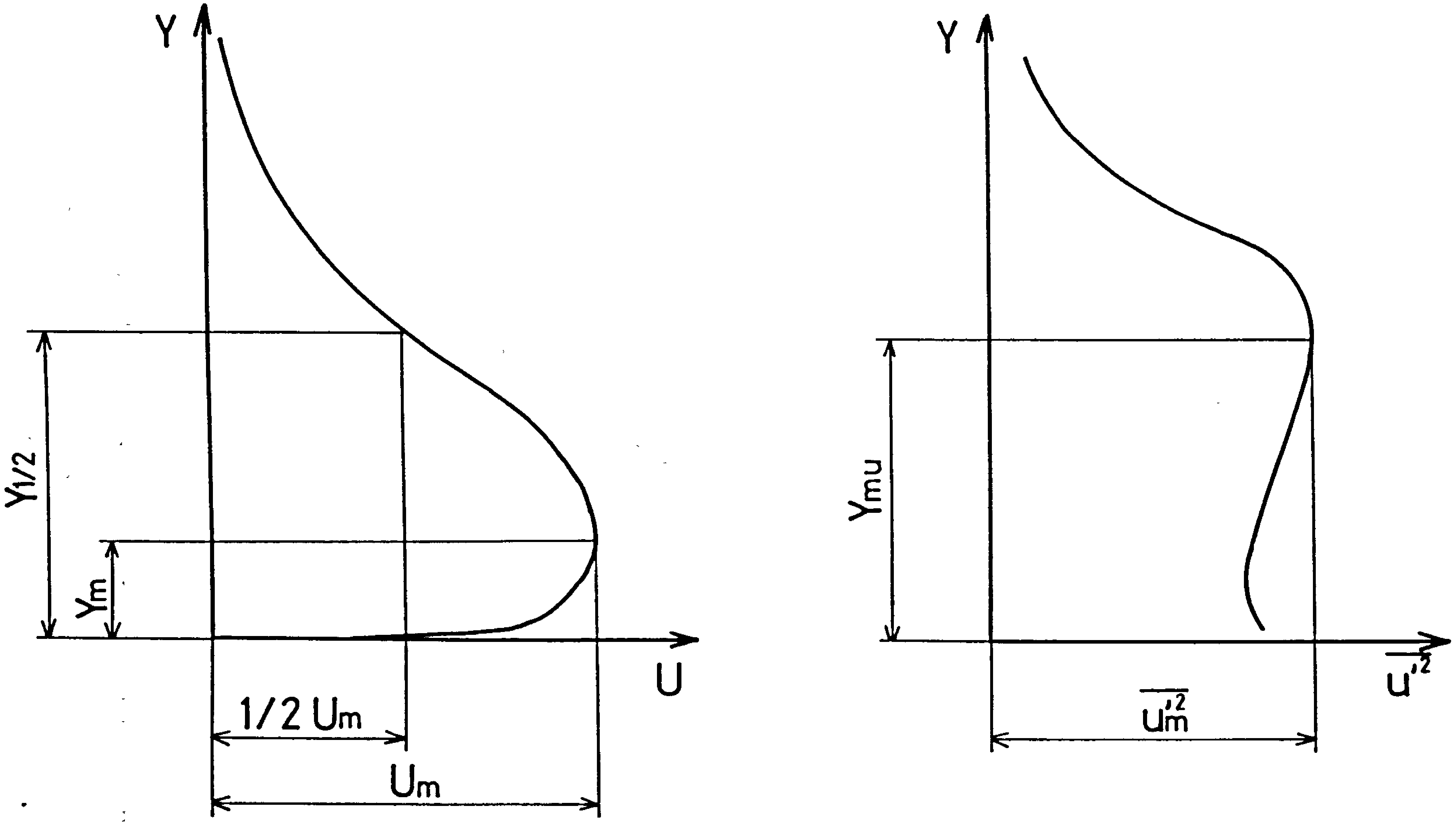

FIG. 4-1 FLOW SITUATION AND DEFINITION OF SYMBOLS

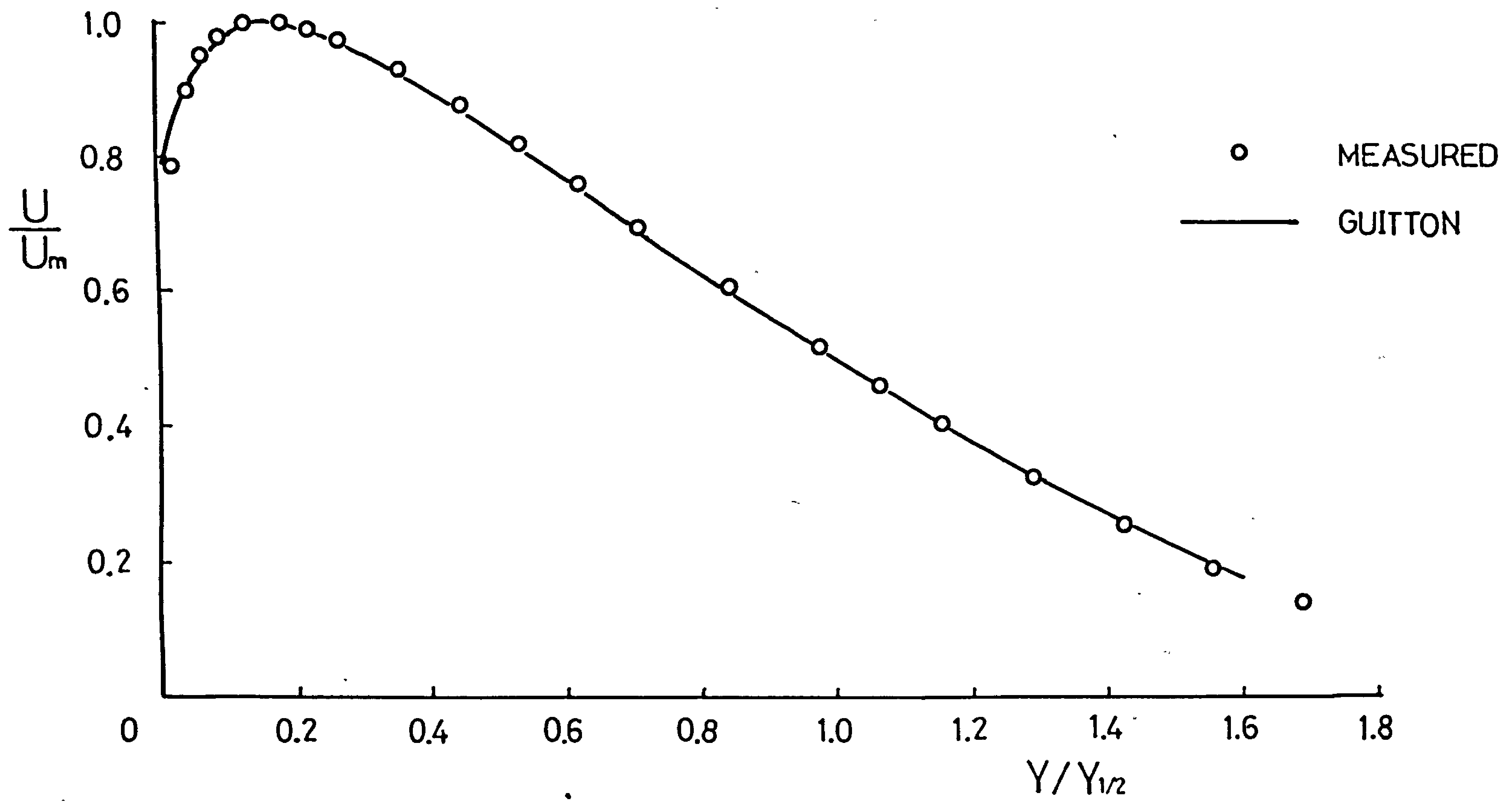

FIG. 4-2 VELOCITY PROFILES FOR PLANE WALL JETS

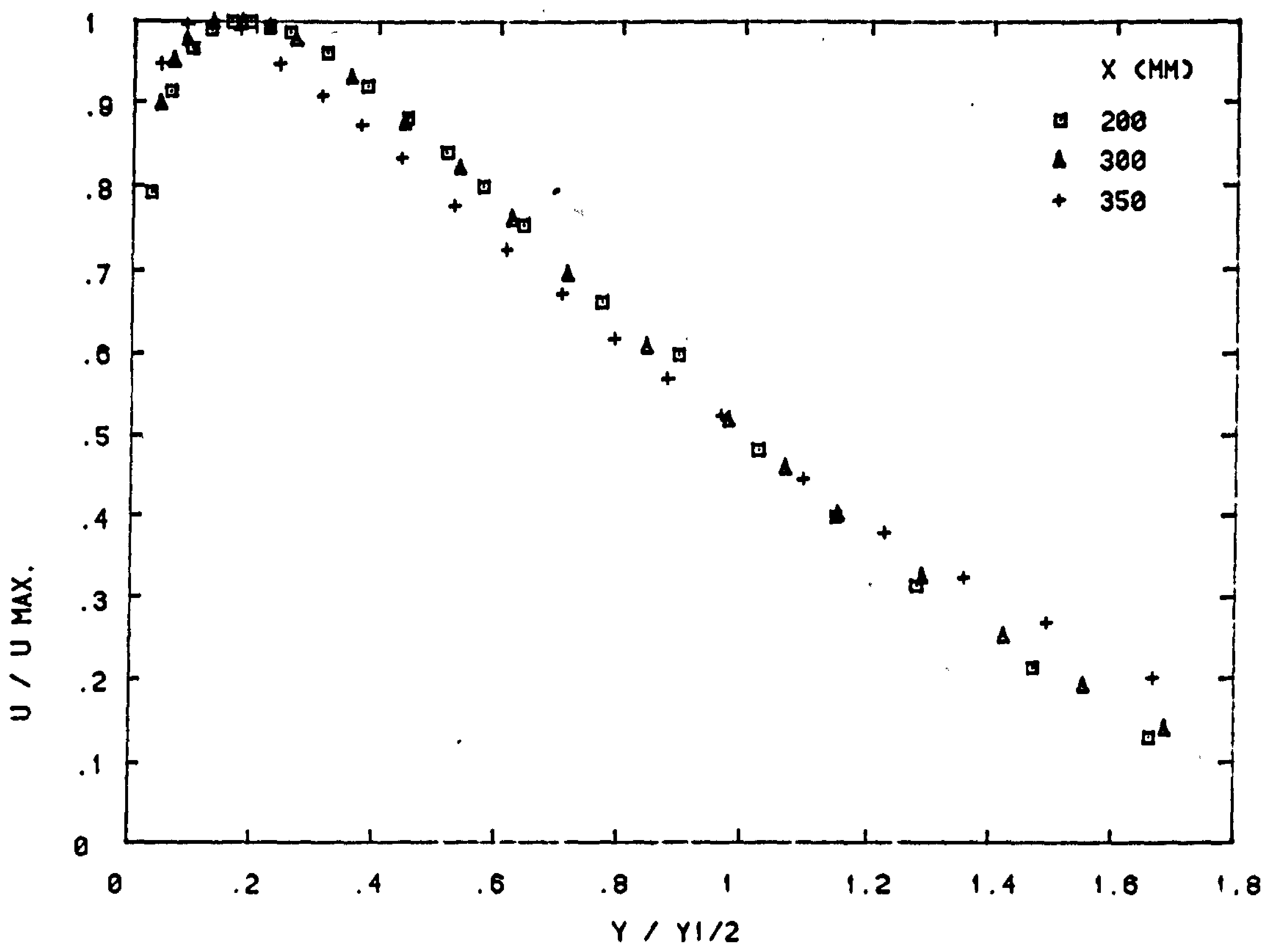

FIG. 4-3(A) VELOCITY PROFILES ACROSS THE JET

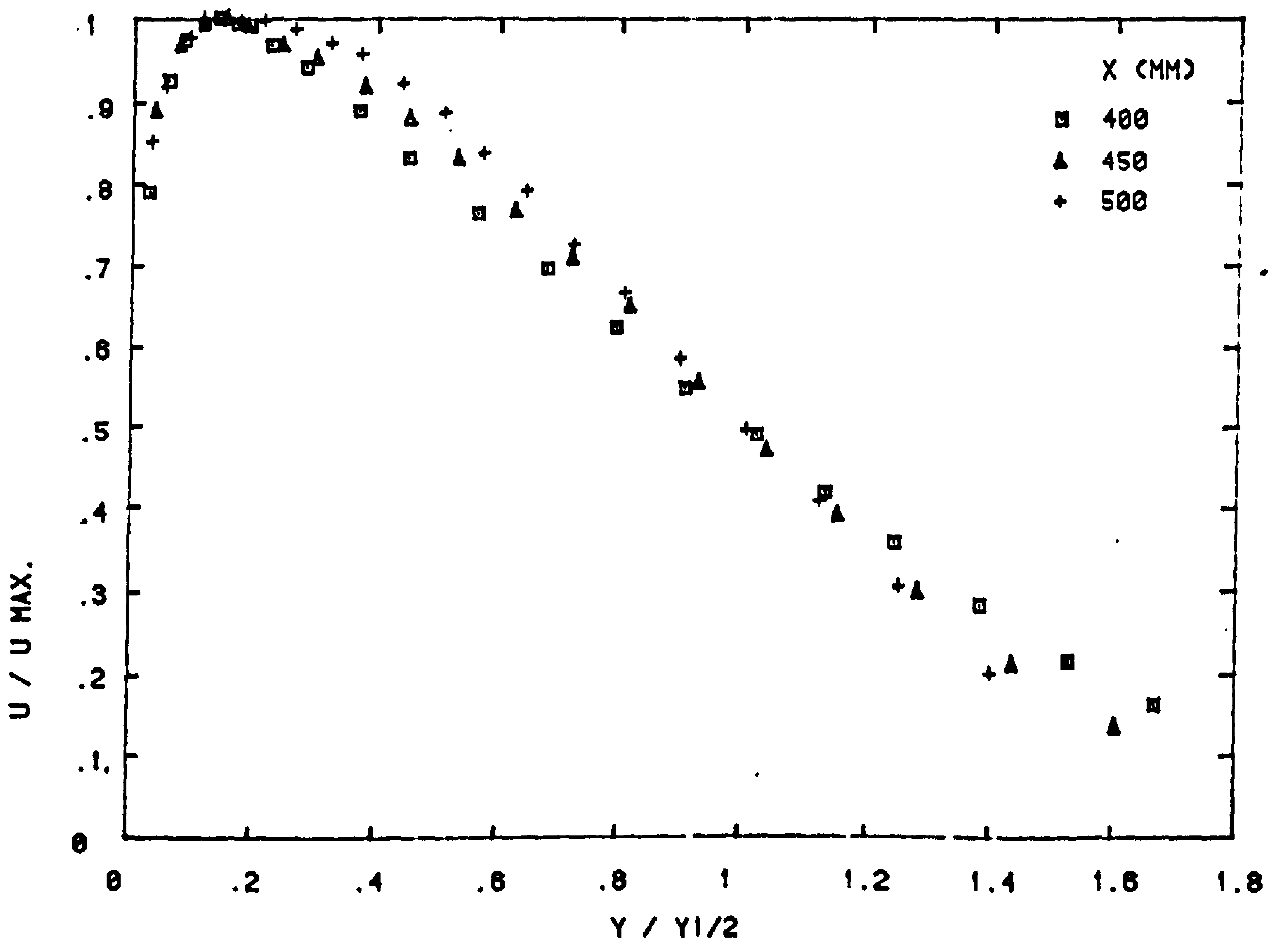

FIG. 4-3(B) VELOCITY PROFILES ACROSS THE JET

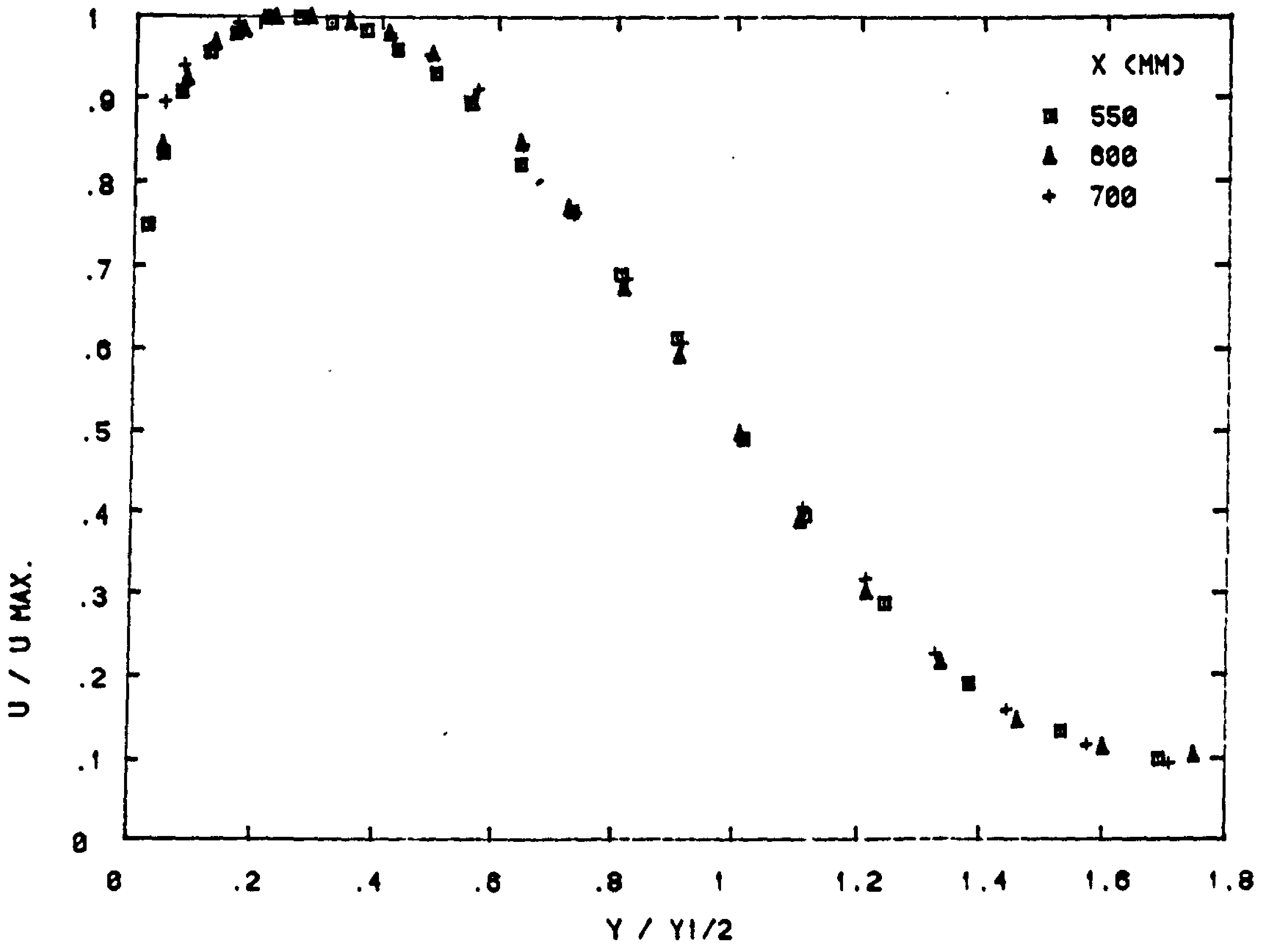

FIG. 4-3(C) VELOCITY PROFILES ACROSS THE JET

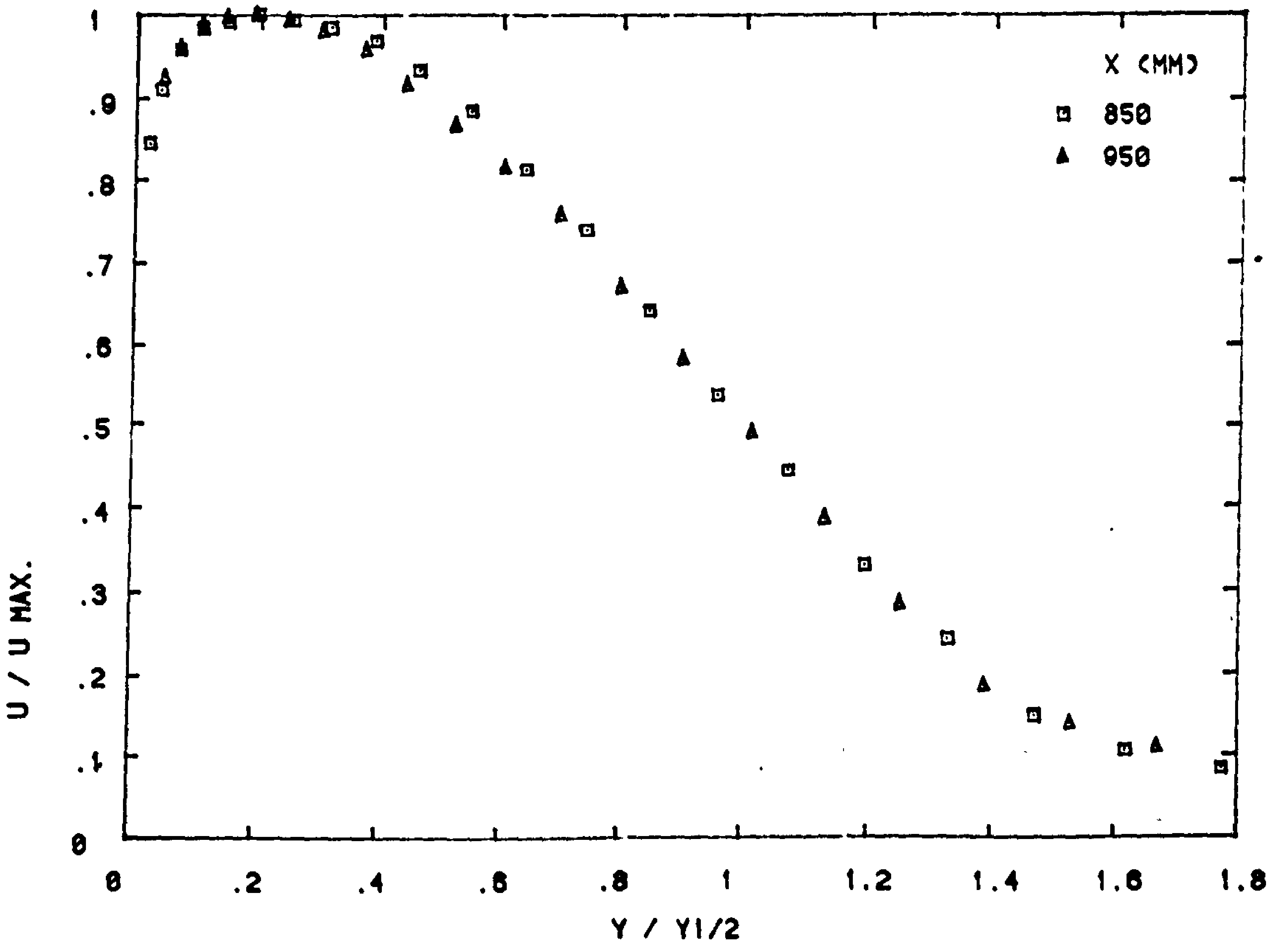

FIG. 4-3(D) VELOCITY PROFILES ACROSS THE JET

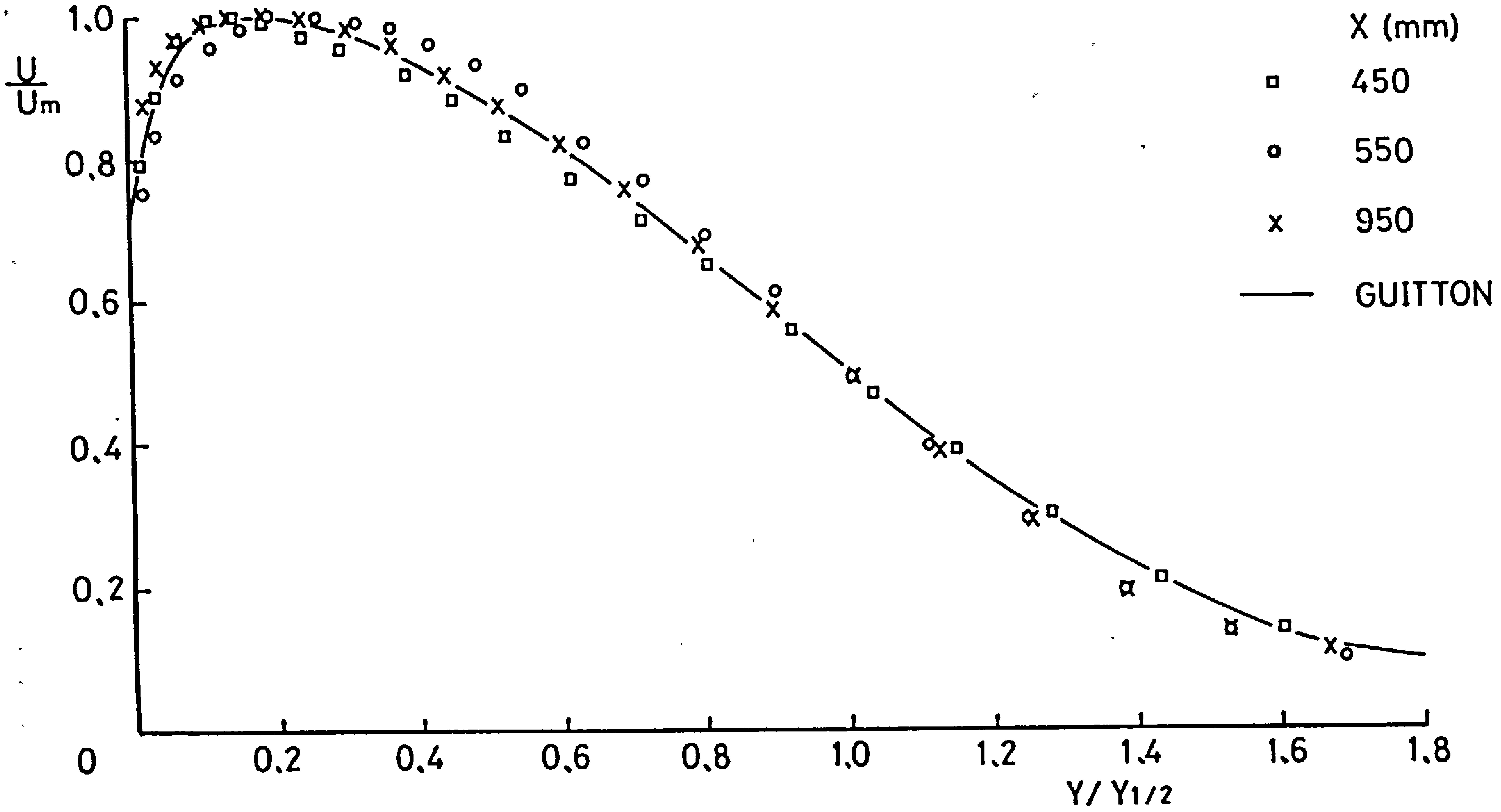

FIG. 4-4 VELOCITY PROFILES FOR CURVED WALL JETS

FIG. 4-5 GROWTH OF JET WIDTH

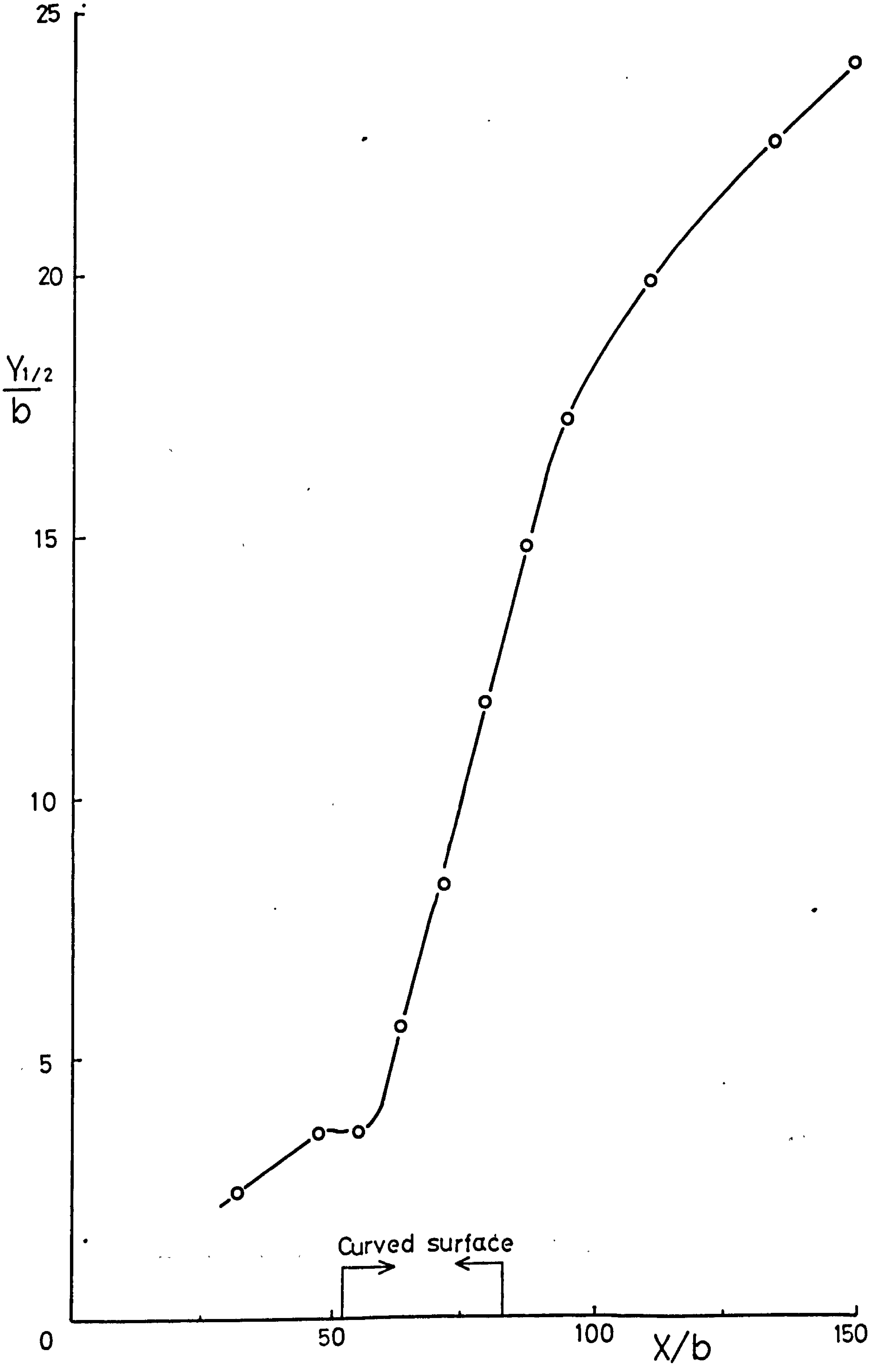

FIG. 4-6 NORMALIZED GROWTH OF JET WIDTH

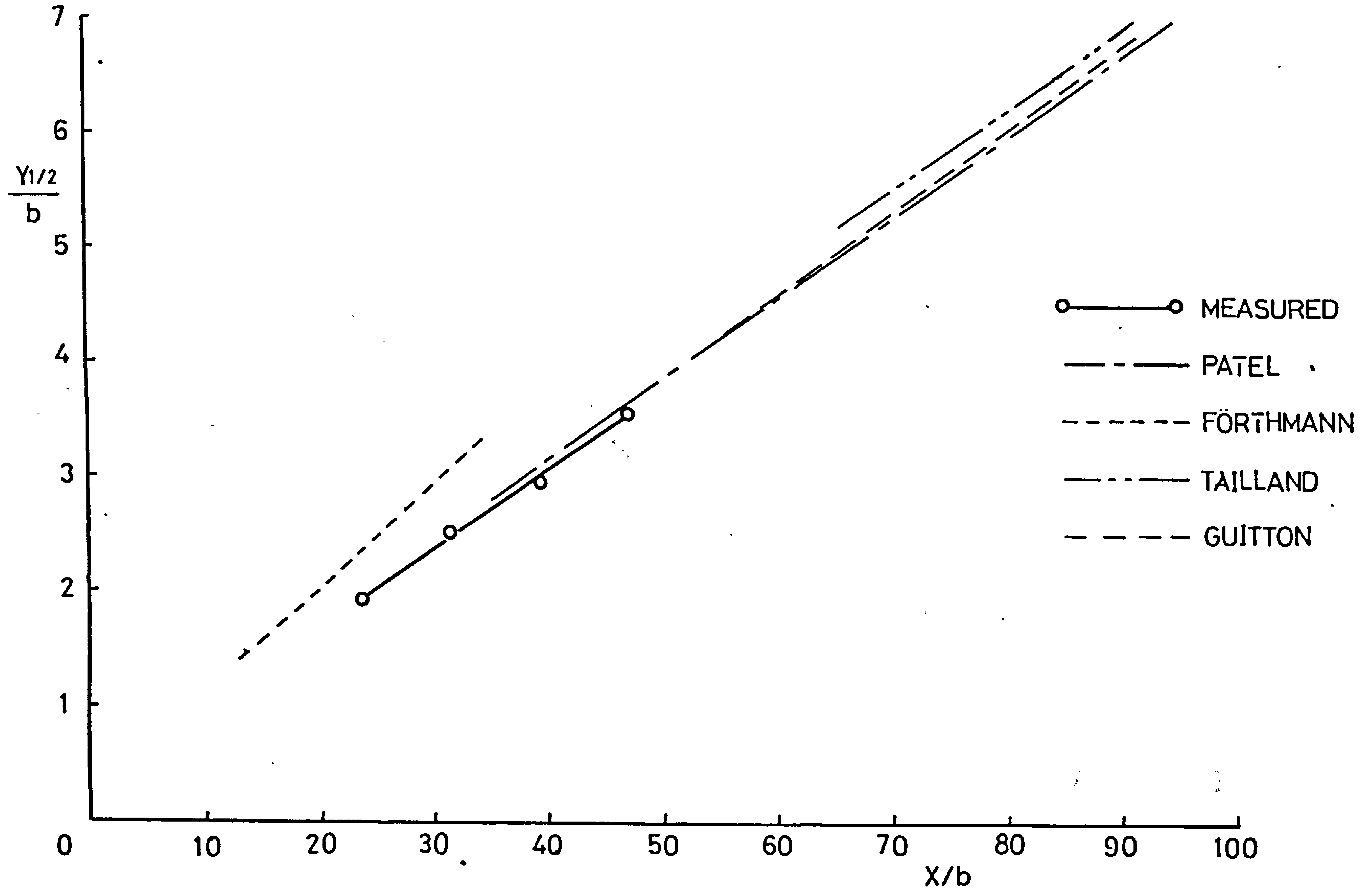

FIG. 4-7 NORMALIZED GROWTH OF JET WIDTH FOR PLANE WALL JETS

FIG. 4-8 MAXIMUM VELOCITY DECAY

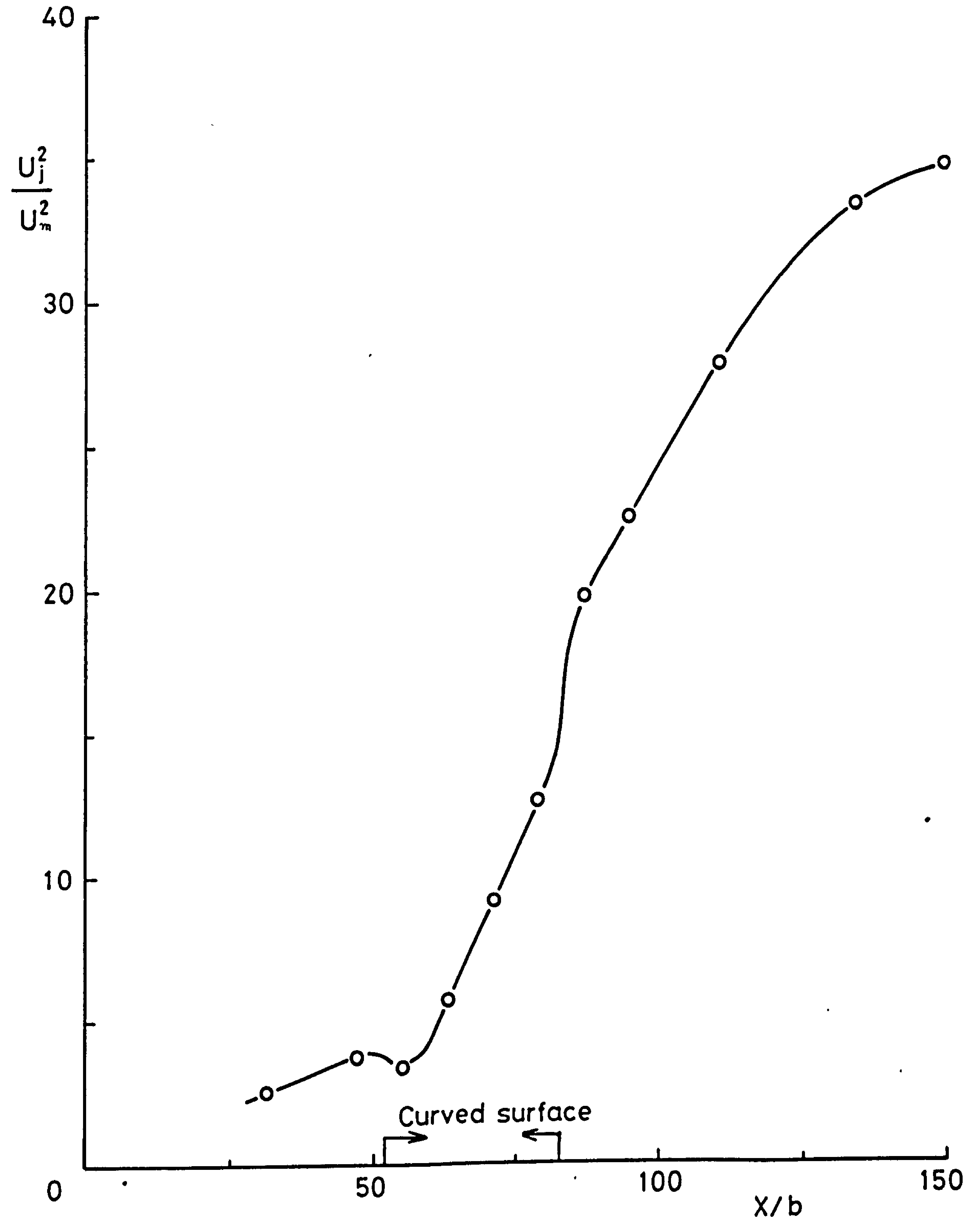

FIG. 4-9 NORMALIZED MAXIMUM VELOCITY DECAY

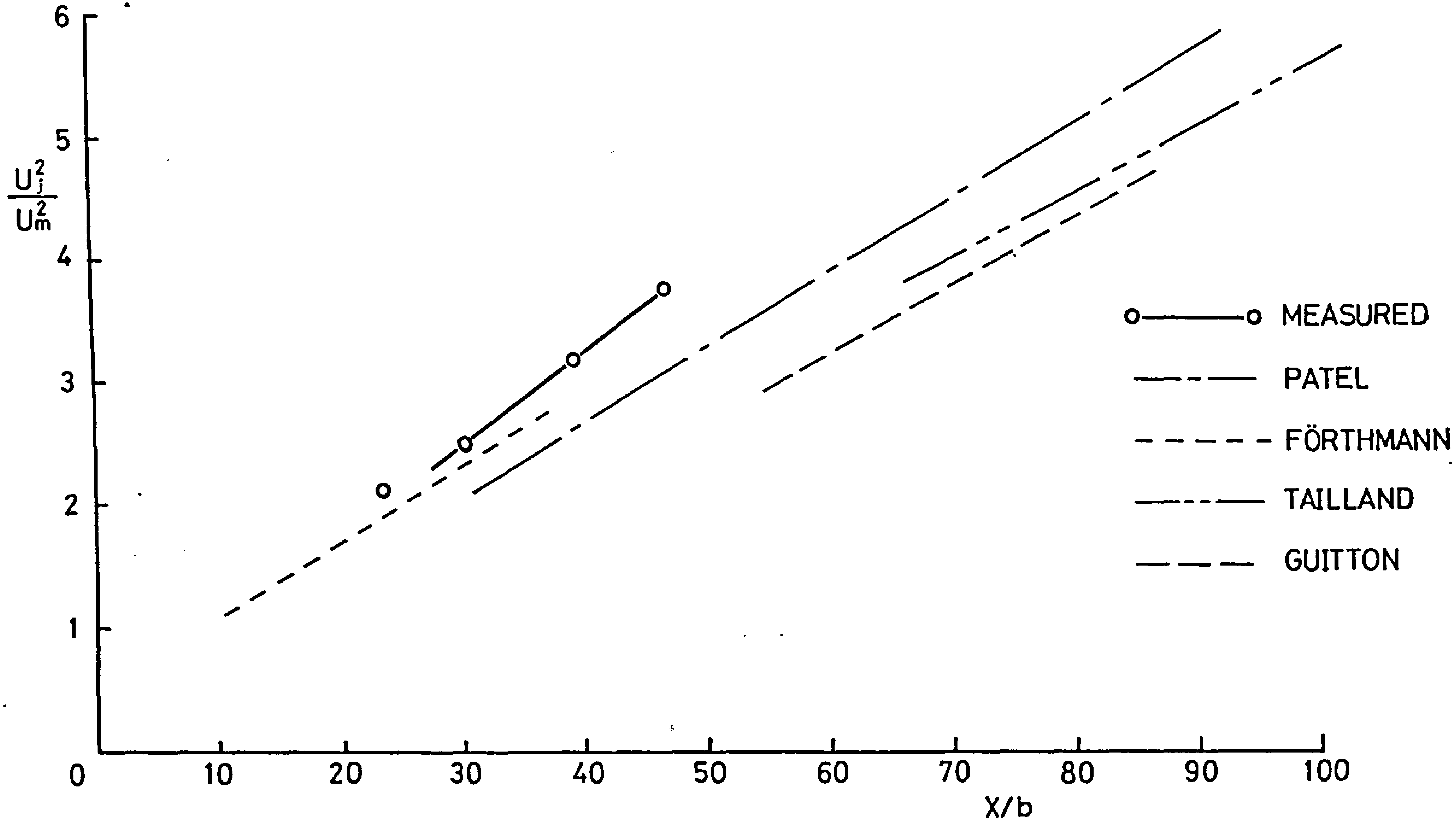

FIG. 4-10 NORMALIZED MAXIMUM VELOCITY DECAY FOR PLANE WALL JETS

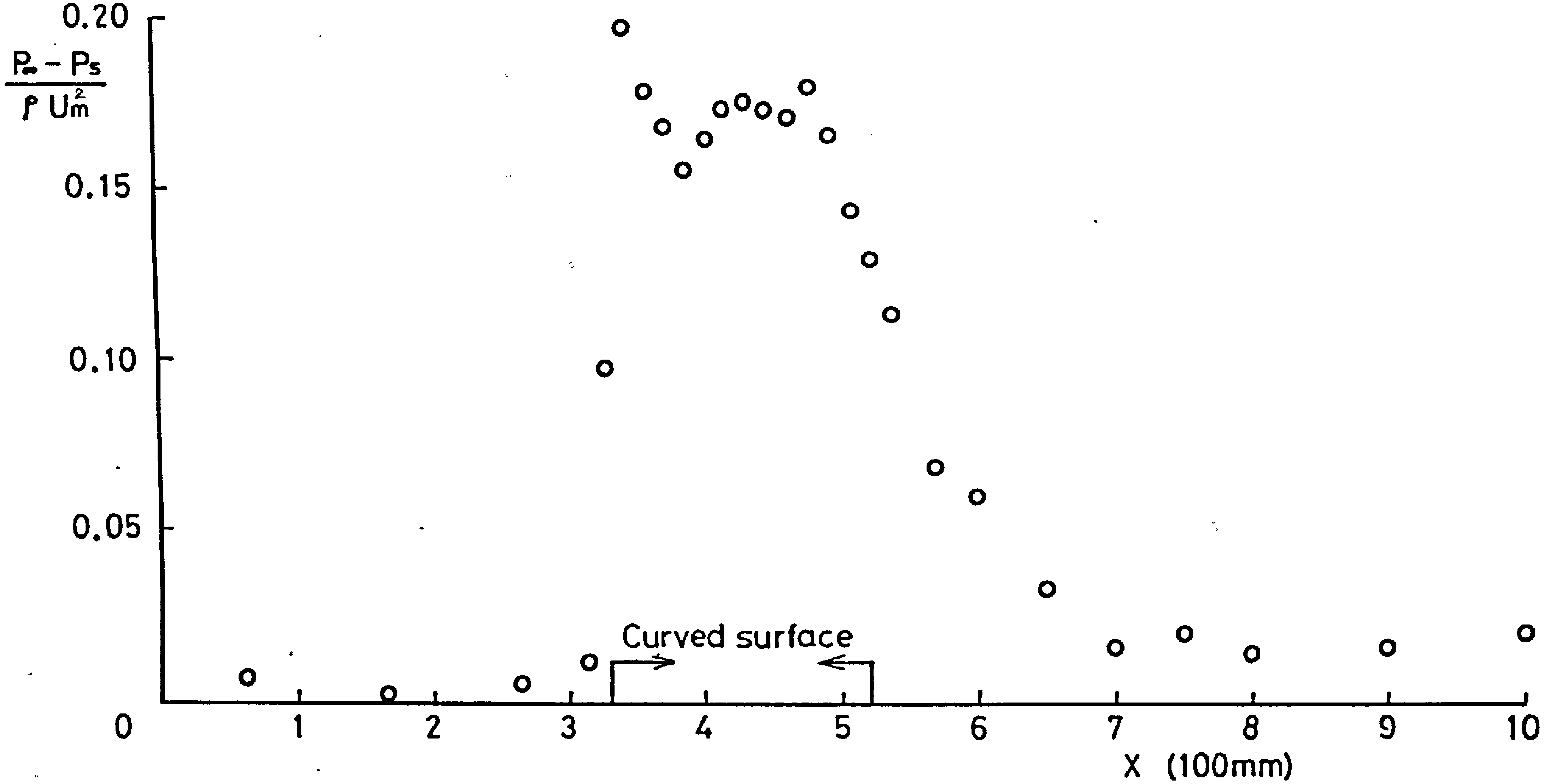

FIG. 4-11 STATIC PRESSURE DISTRIBUTION

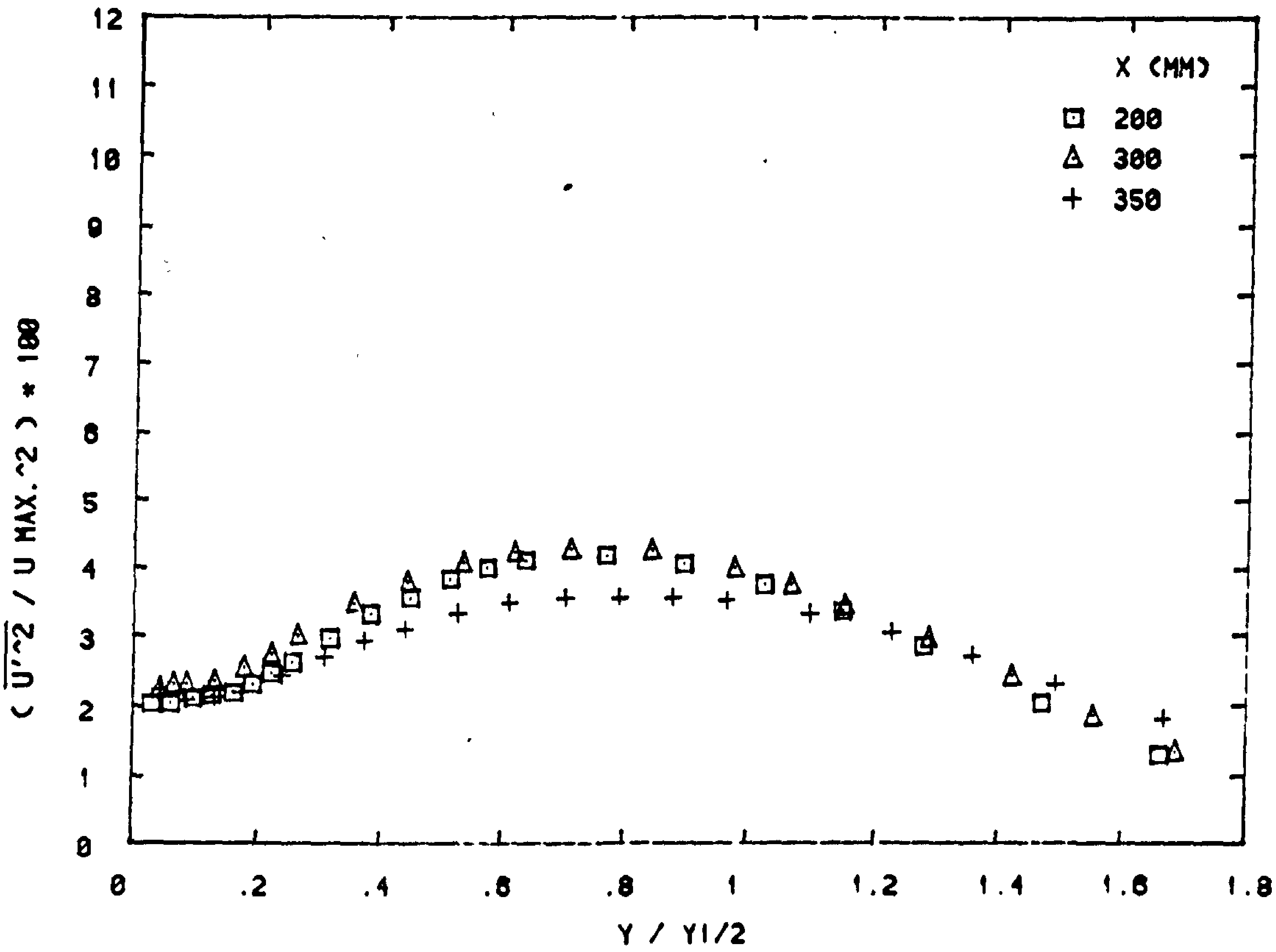

FIG. 4-12(A) TURBULENCE INTENSITY $\overline{u'^2}$ ACROSS THE JET

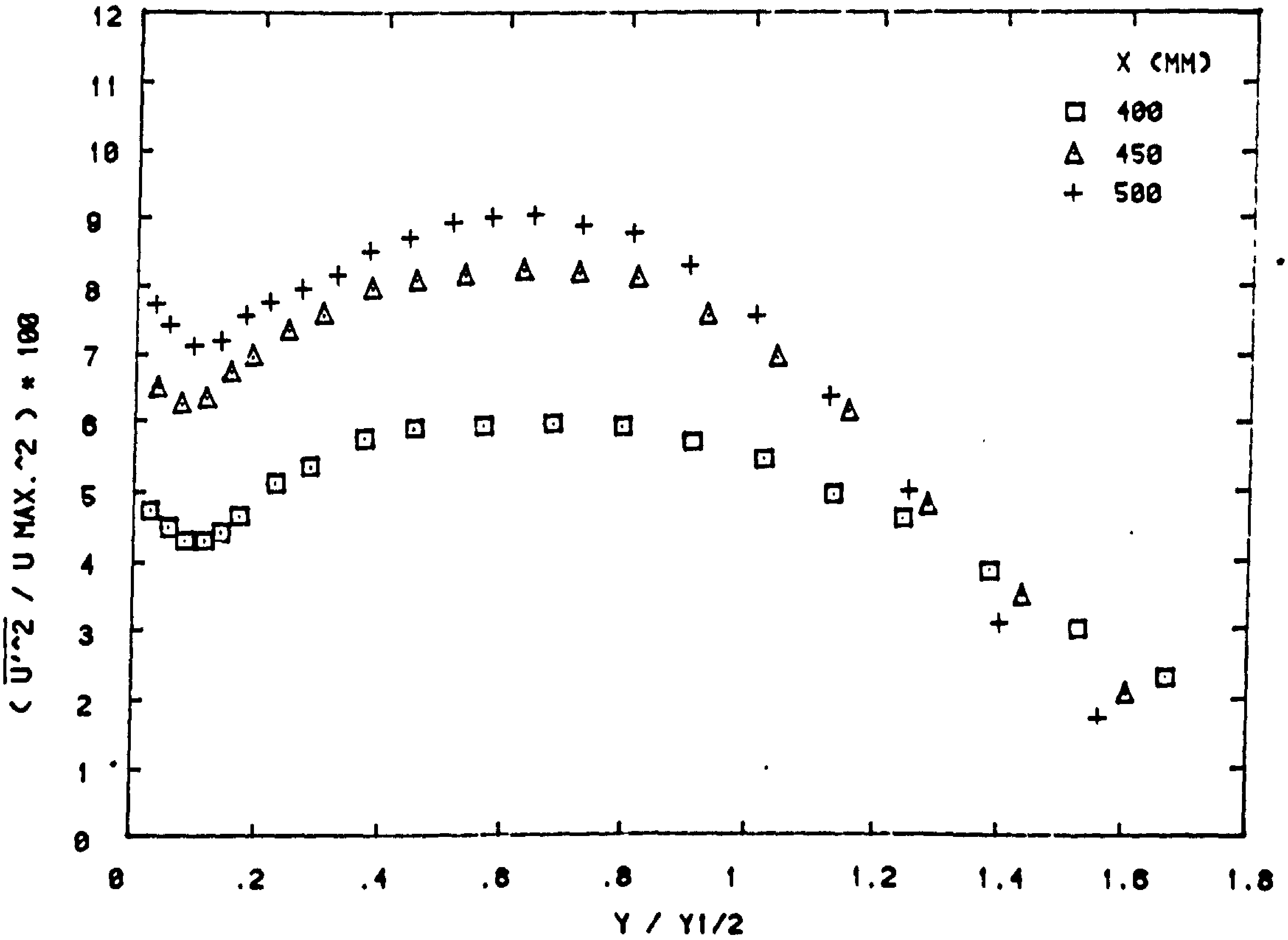

FIG. 4-12(B) TURBULENCE INTENSITY $\overline{u'^2}$ ACROSS THE JET

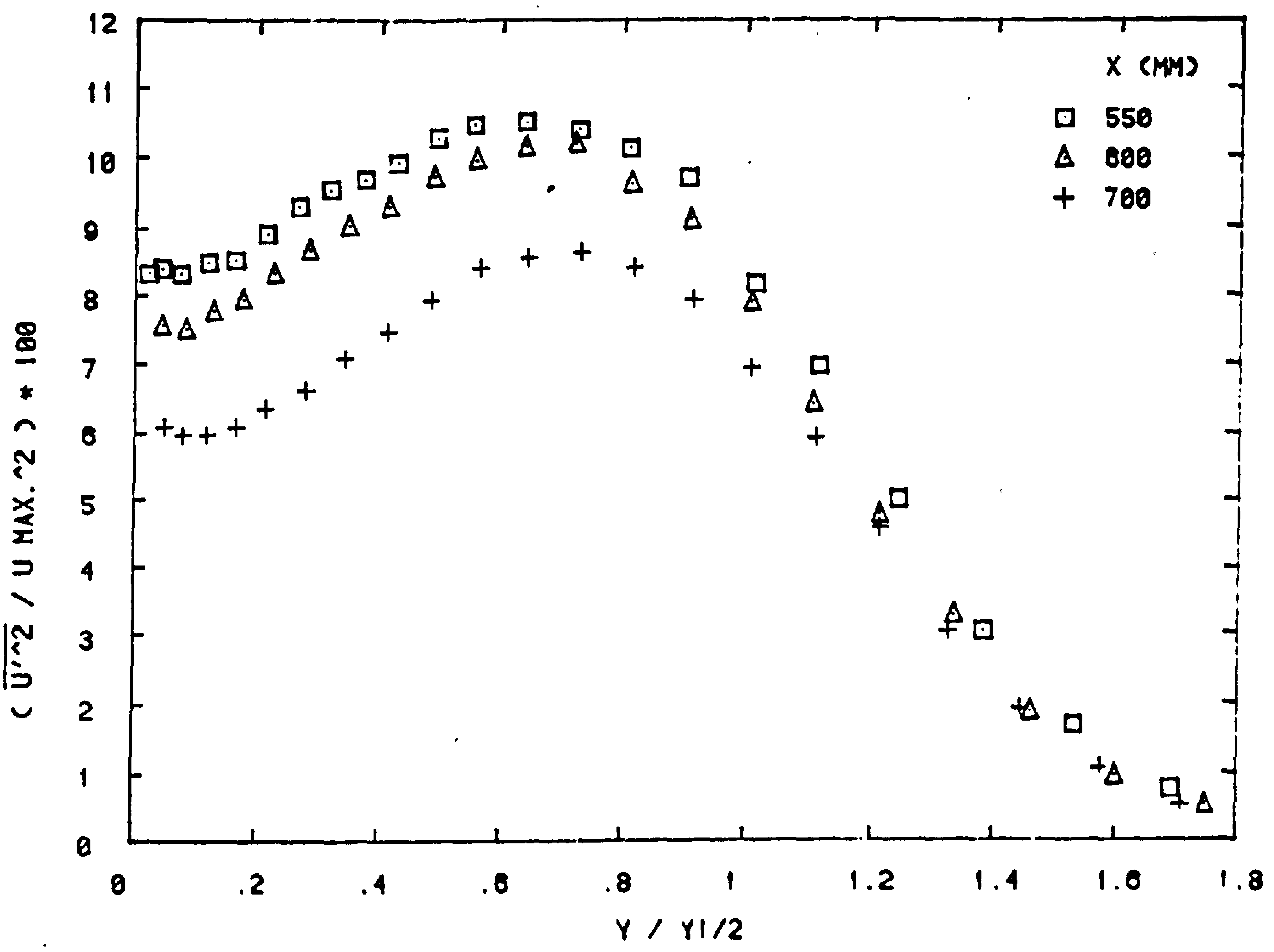

FIG. 4-12(C) TURBULENCE INTENSITY $\overline{u'^2}$ ACROSS THE JET

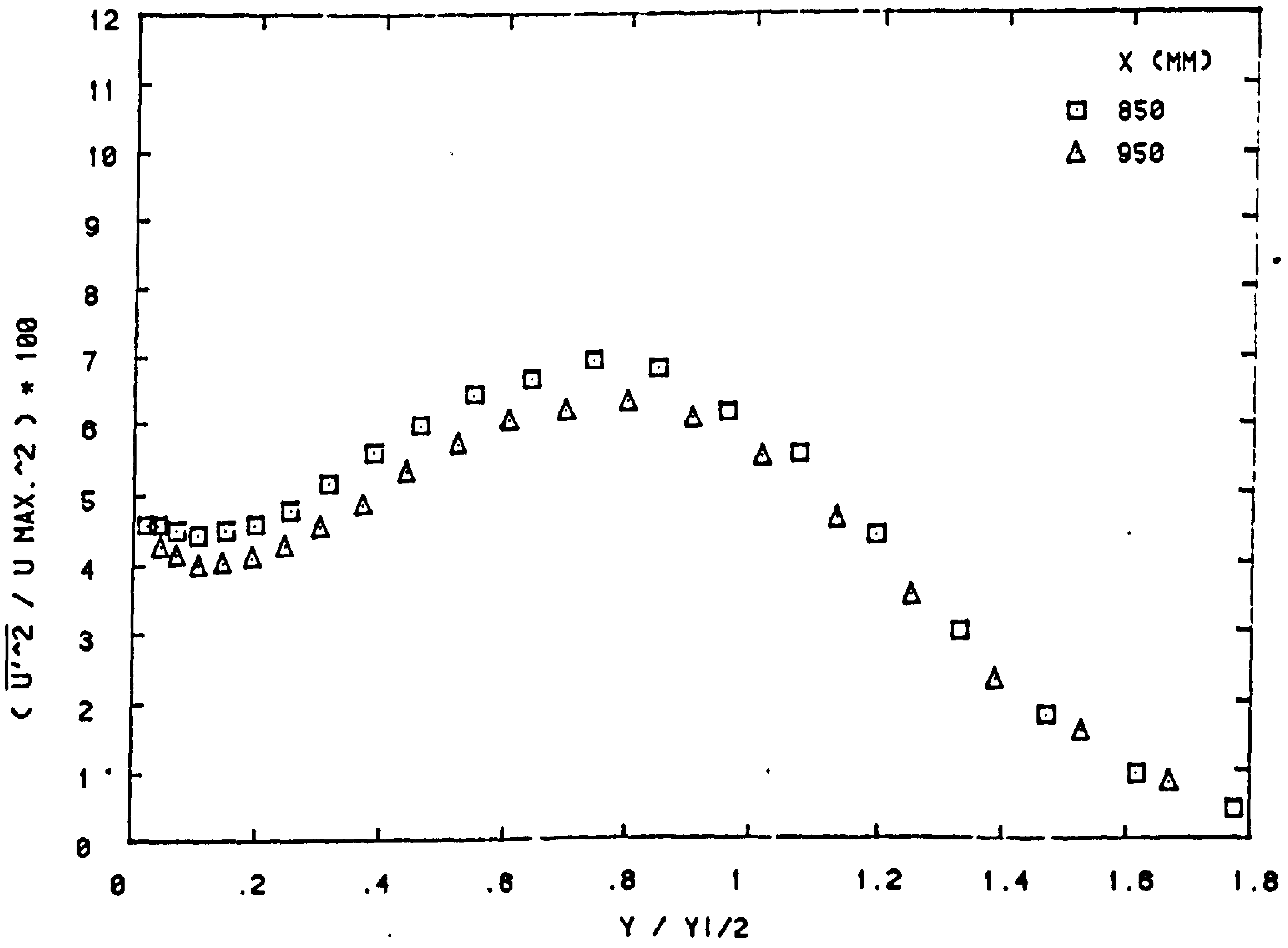

FIG. 4-12(D) TURBULENCE INTENSITY $\overline{u'^2}$ ACROSS THE JET

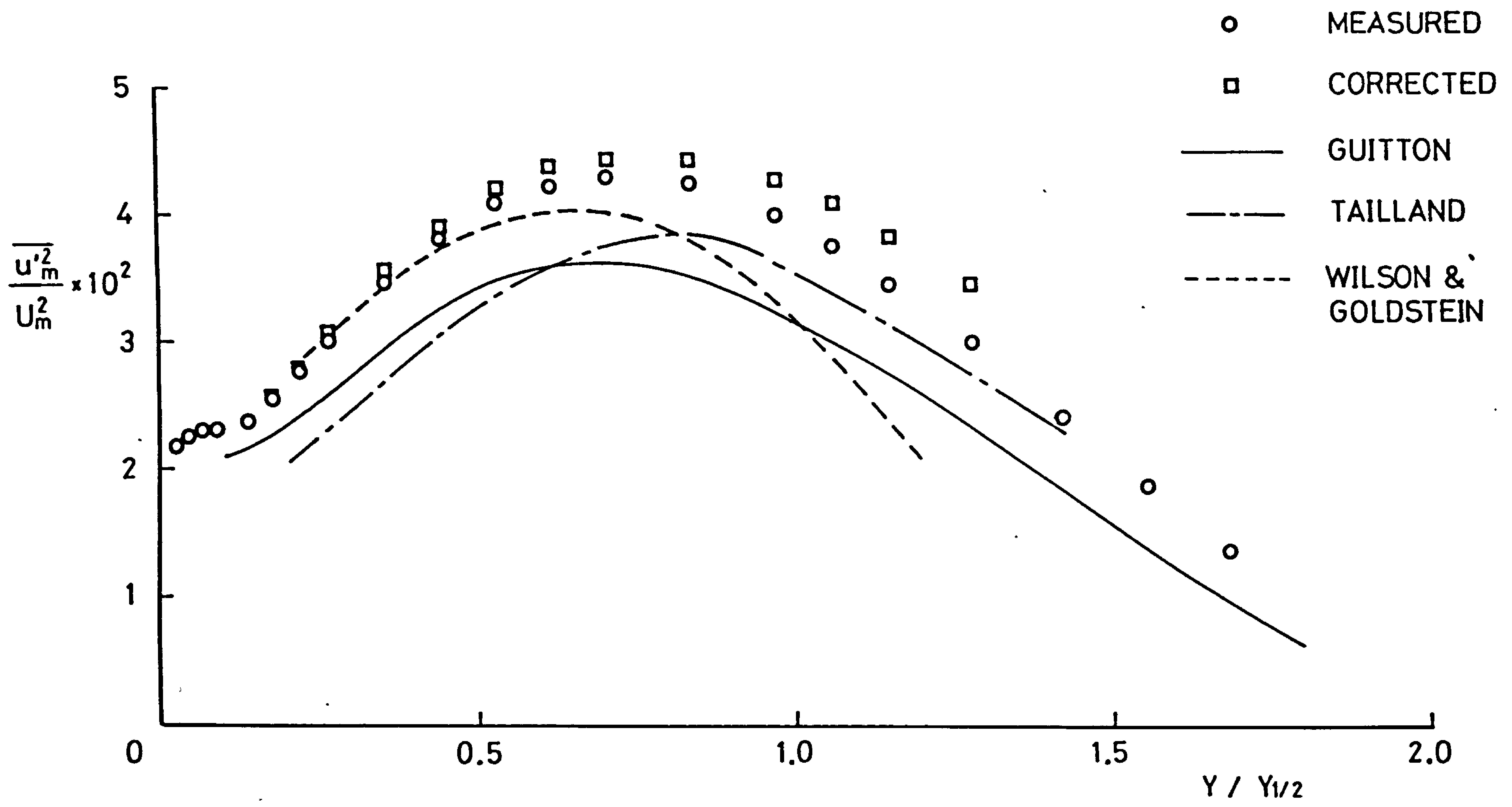

FIG. 4-13 TURBULENCE INTENSITY $\overline{u'^2}$ FOR PLANE WALL JETS

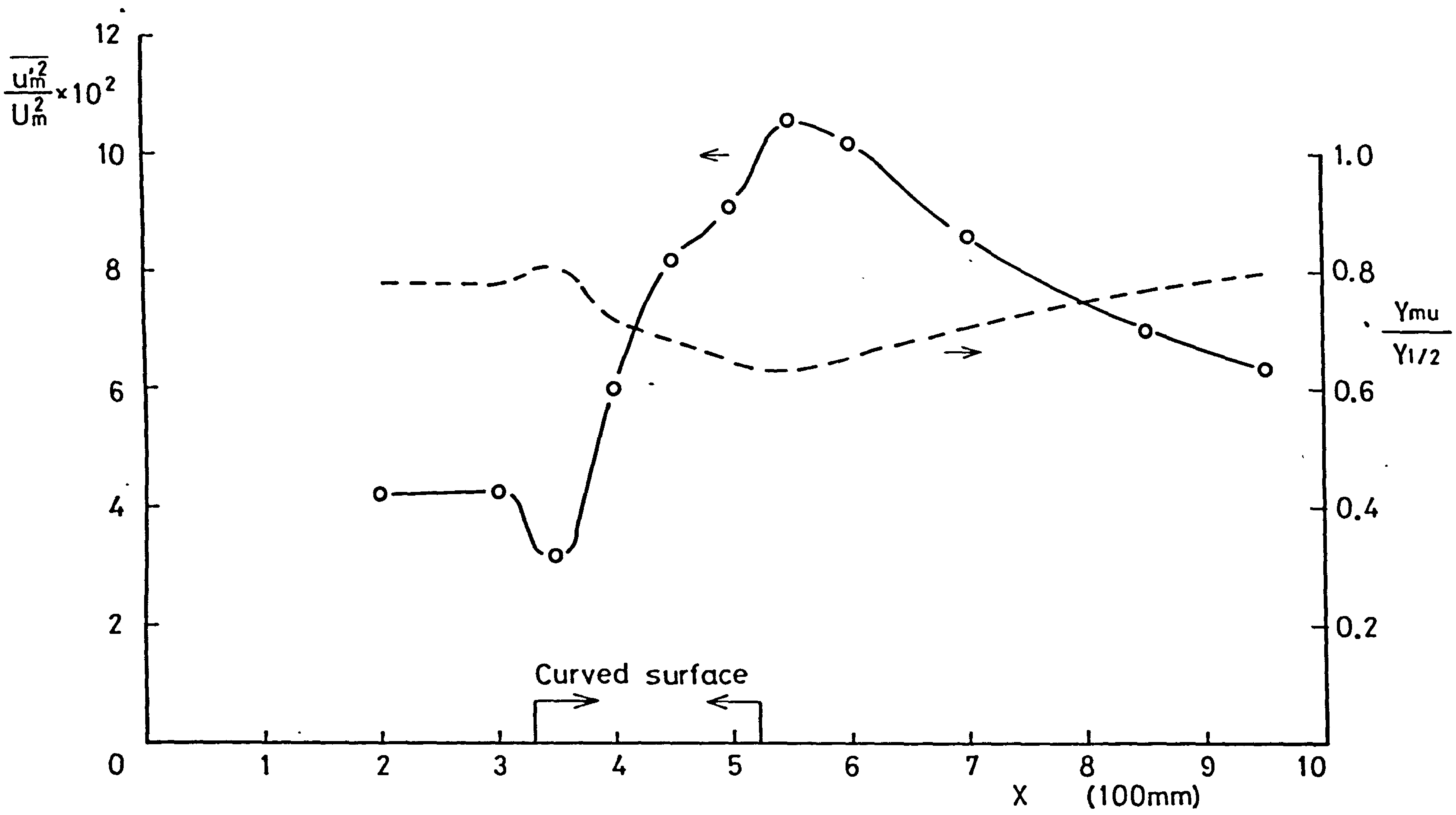

FIG. 4-14 DISTRIBUTION OF MAXIMUM TURBULENCE INTENSITY $\overline{u_m'^2}$ AND ITS POSITION

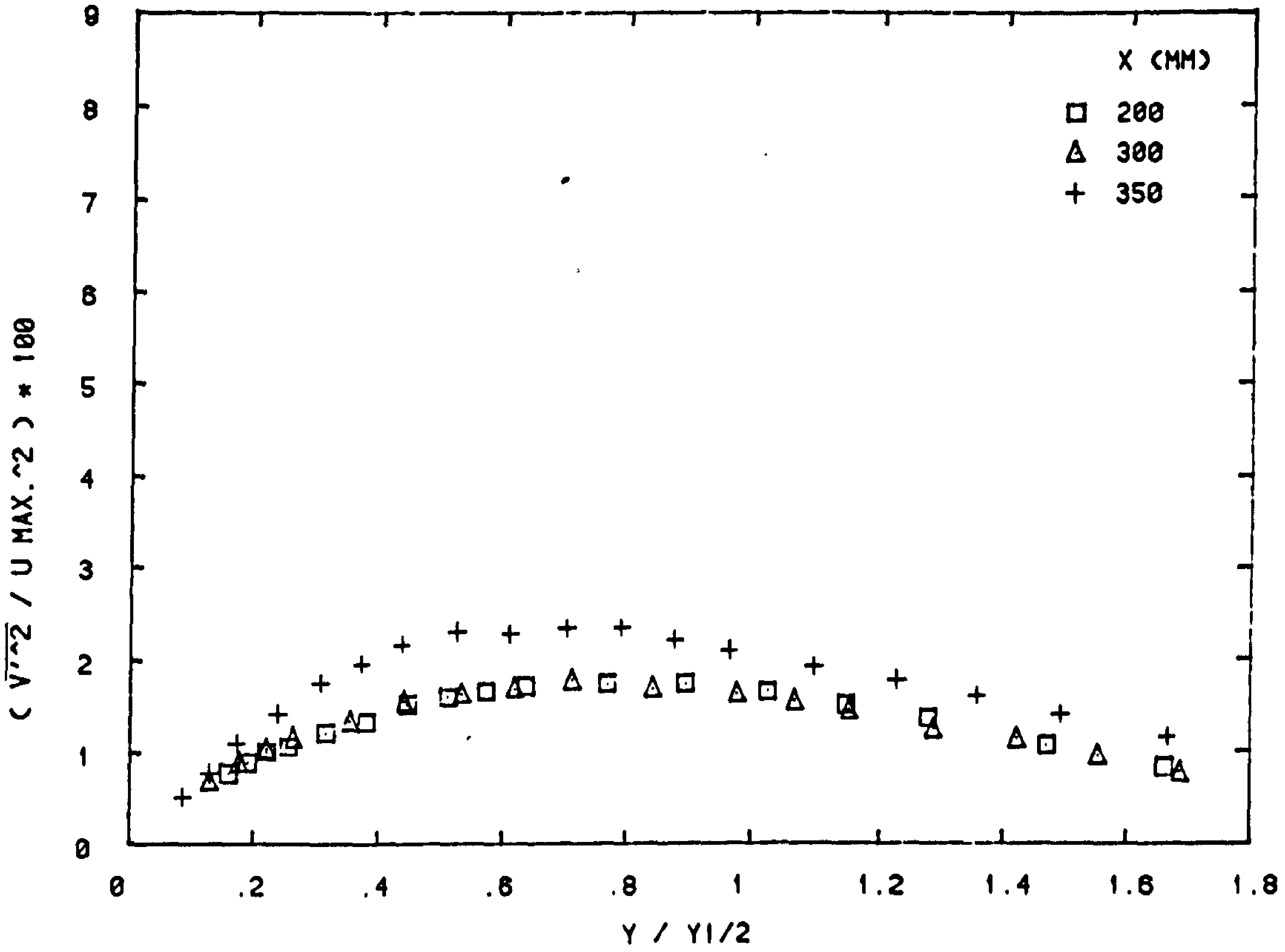

FIG. 4-15(A) TURBULENCE INTENSITY $\overline{V'^2}$ ACROSS THE JET

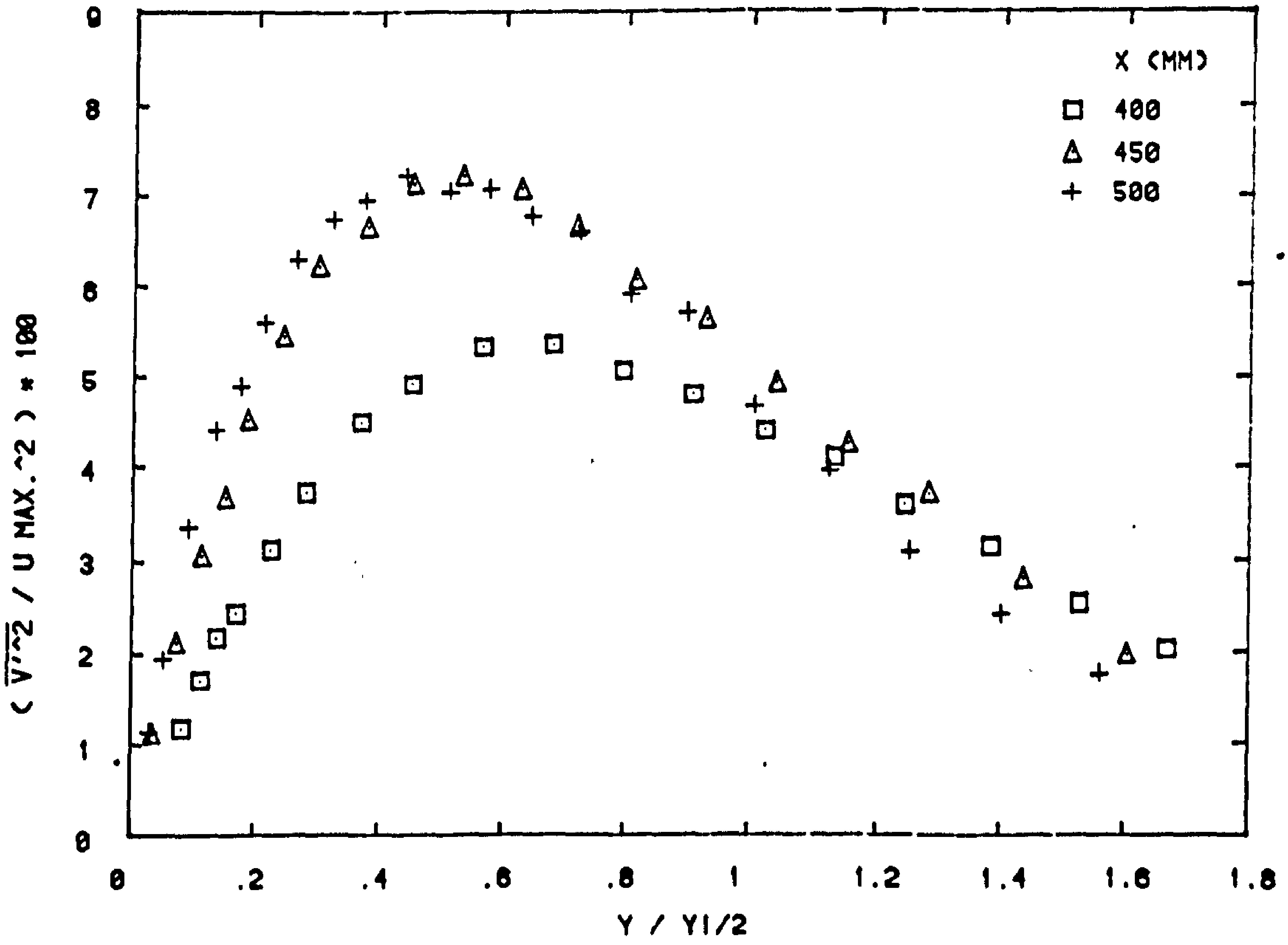

FIG. 4-15(B) TURBULENCE INTENCITY $\overline{V'^2}$ ACROSS THE JET

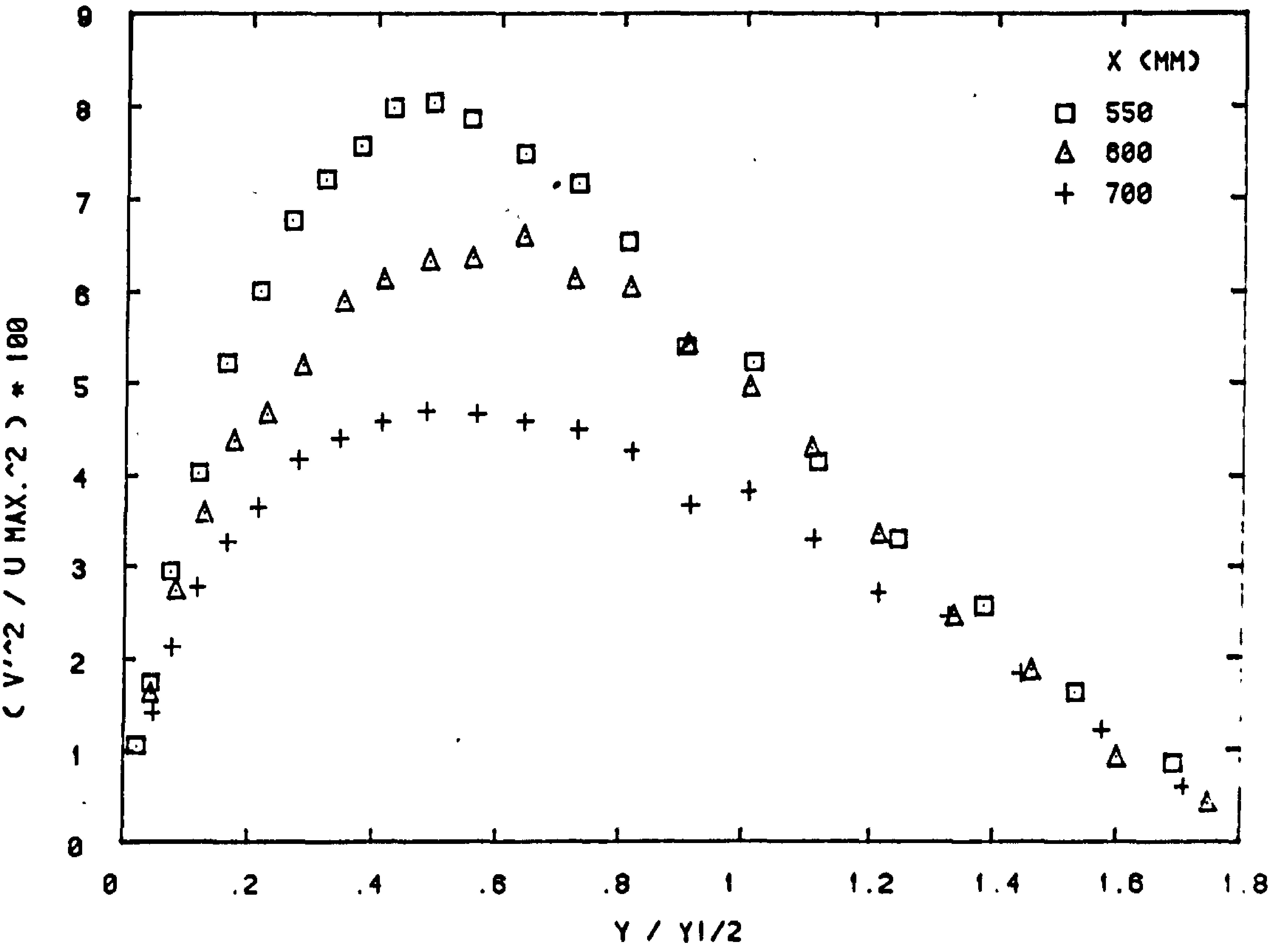

FIG. 4-15(C) TURBULENCE INTENSITY $\overline{V'^2}$ ACROSS THE JET

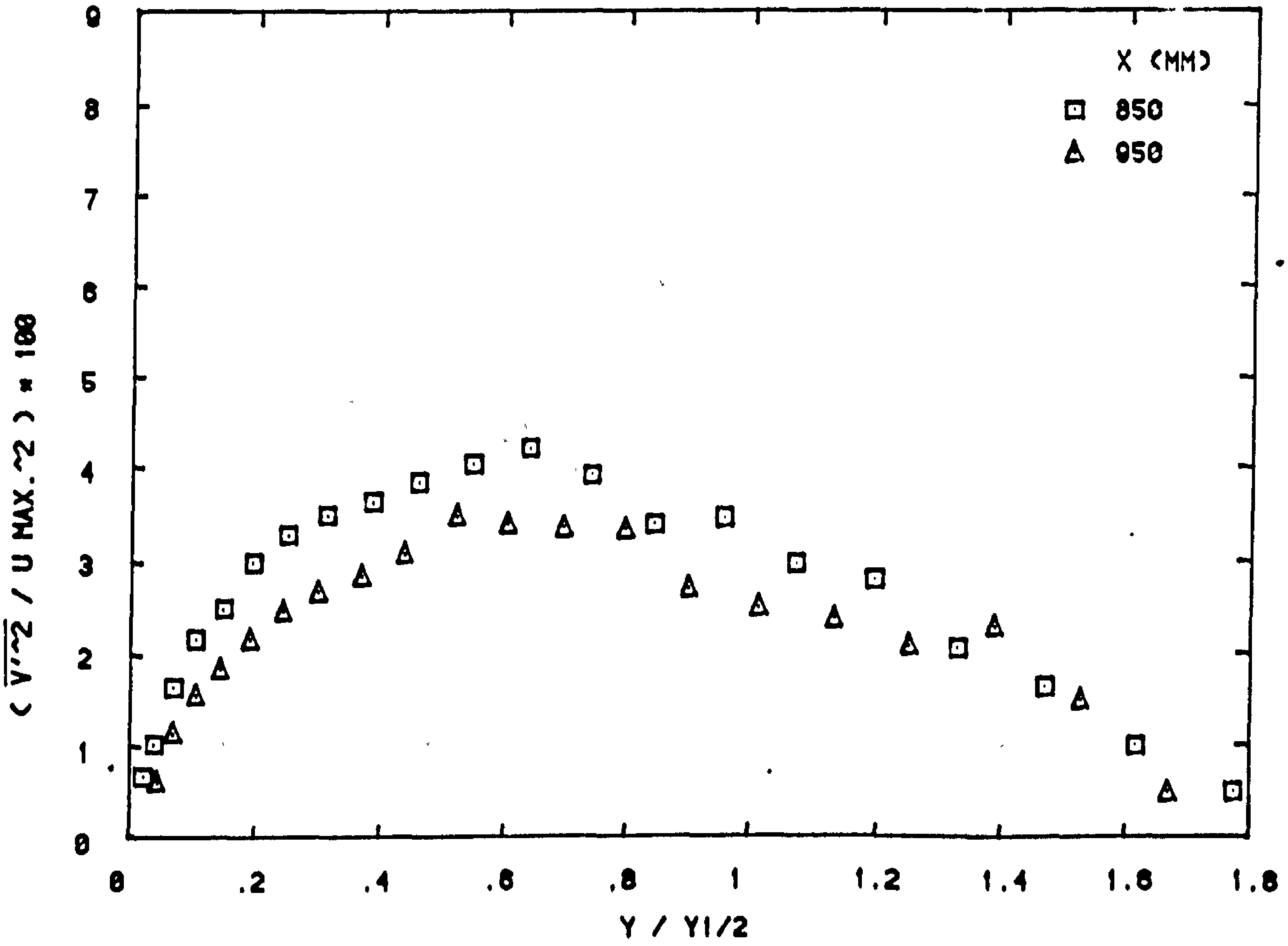

FIG. 4-15(D) TURBULENCE INTENSITY $\overline{V'^2}$ ACROSS THE JET

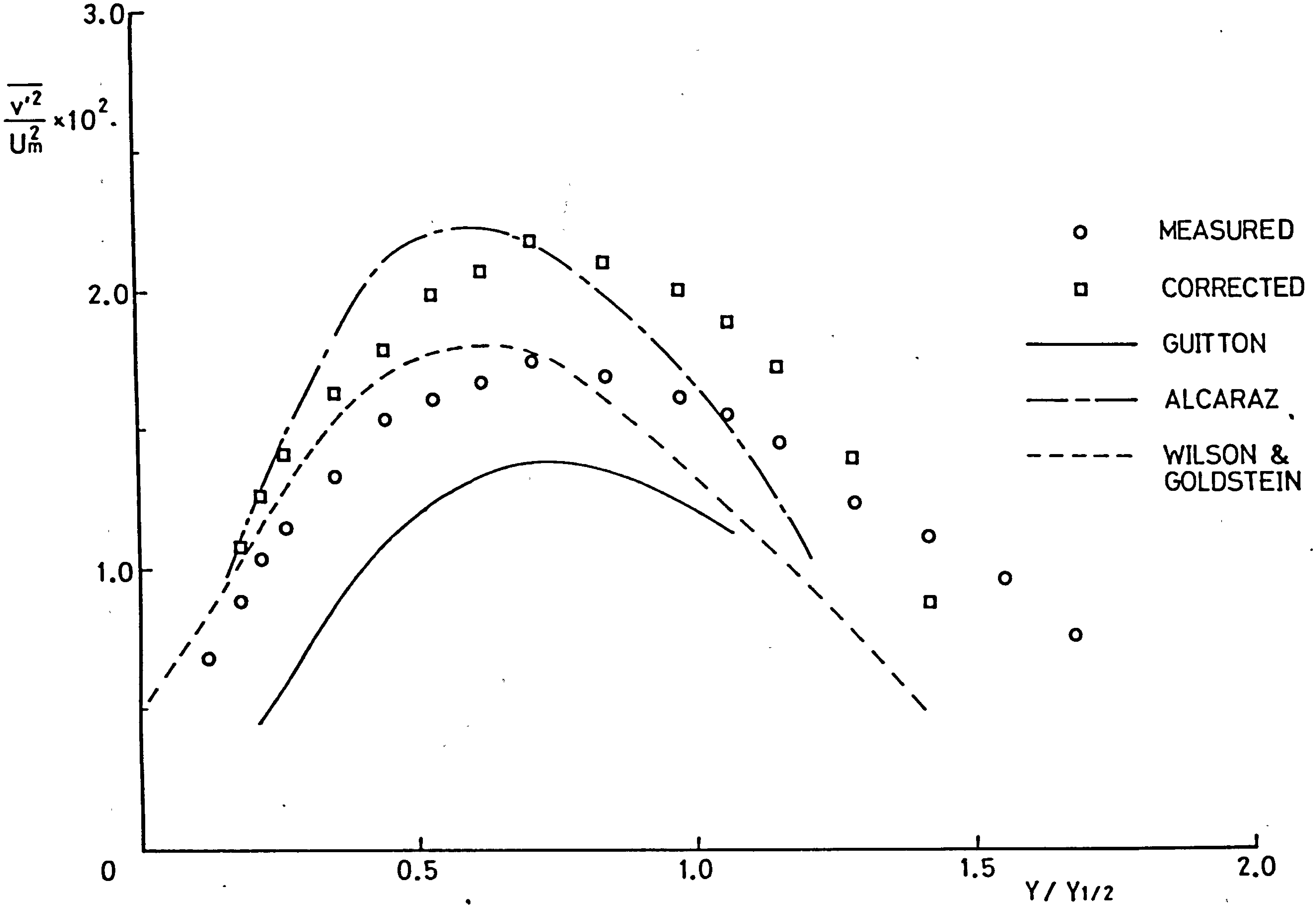

FIG. 4-16 TURBULENCE INTENSITY $\overline{v'^2}$ FOR PLANE WALL JETS

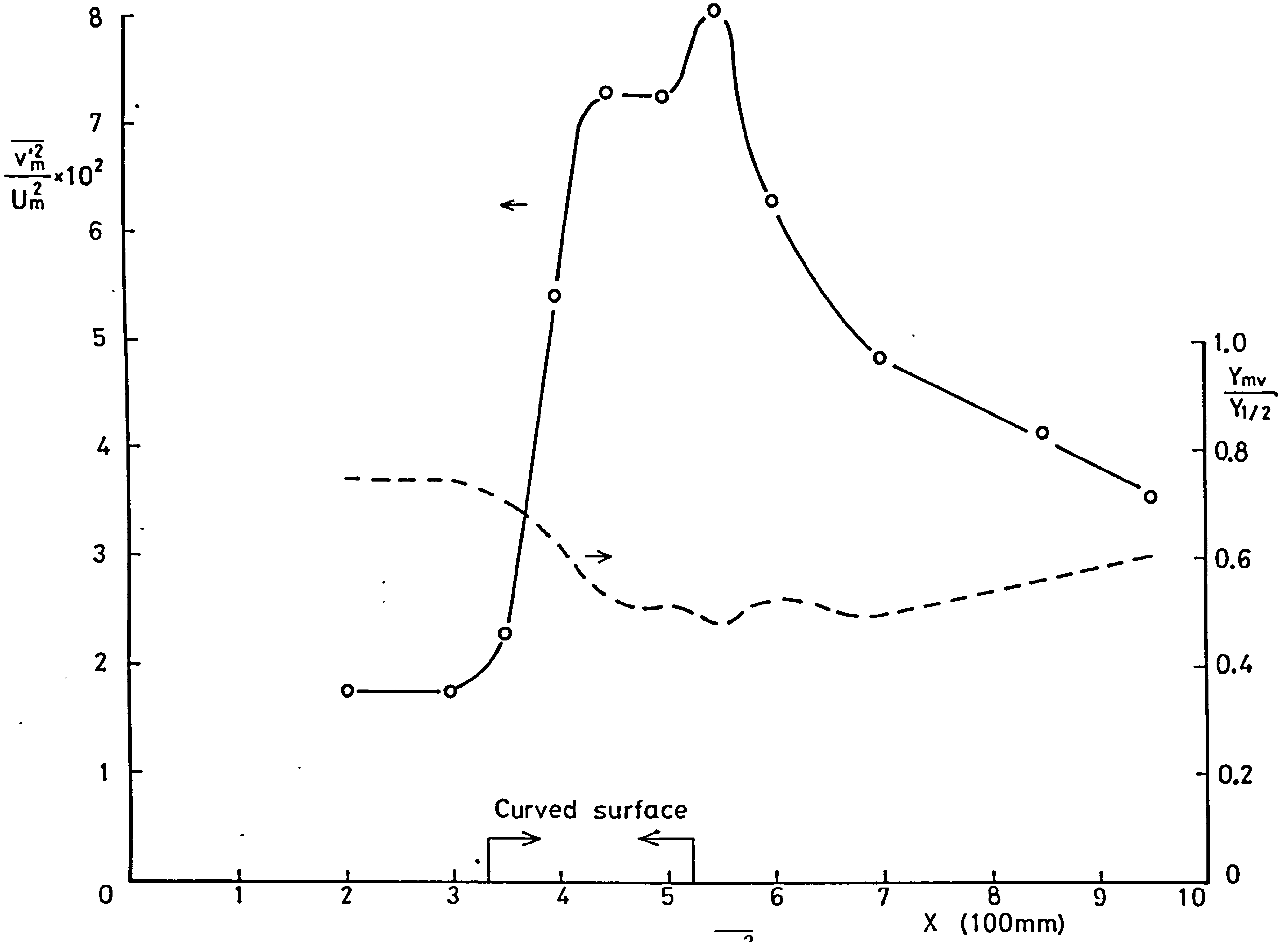

FIG. 4-17 DEVELOPMENT OF MAXIMUM TURBULENCE INTENSITY $\overline{v'^2_m}$ AND ITS POSITION

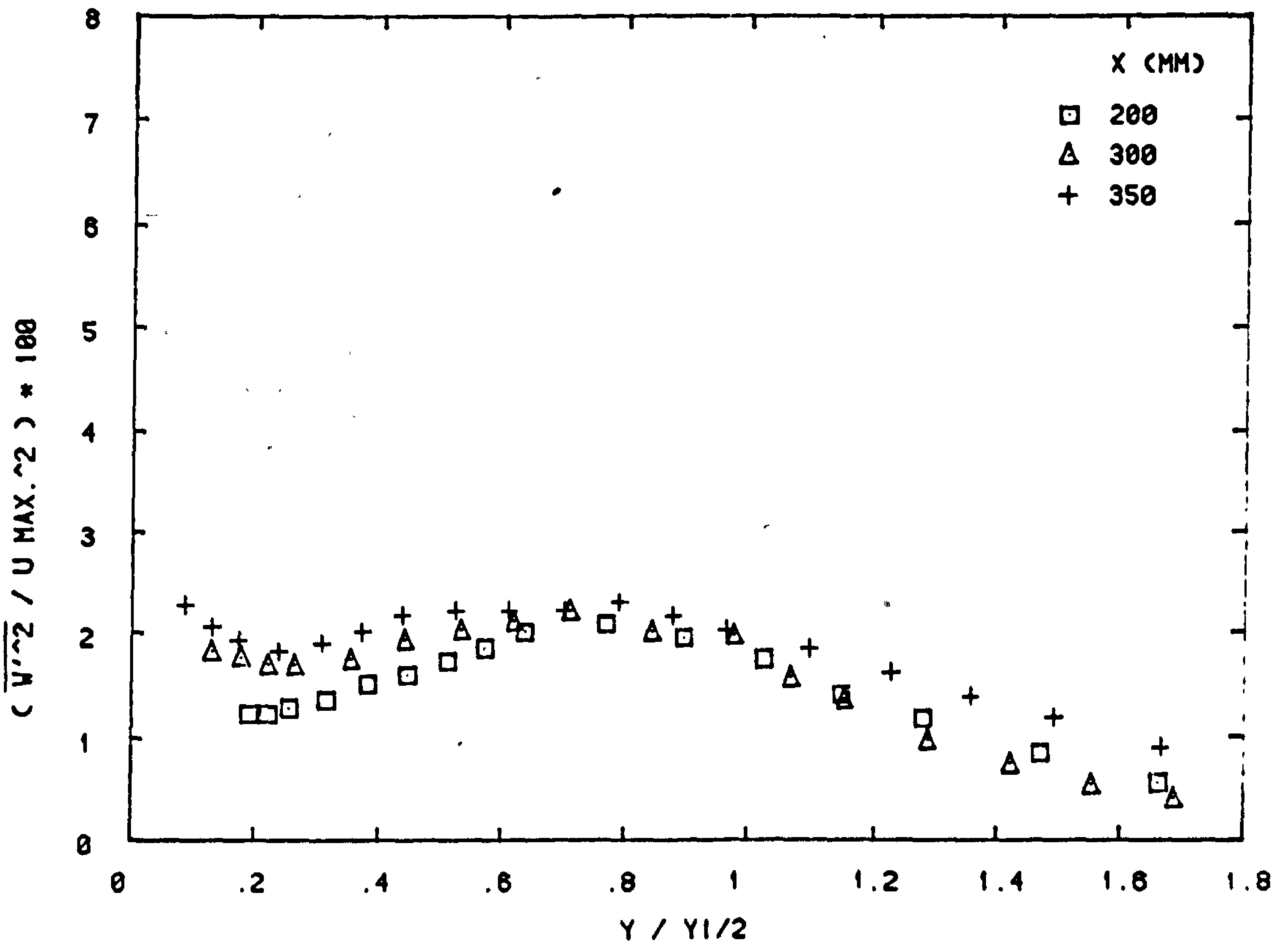

FIG. 4-18(A) TURBULENCE INTENSITY $\overline{W'^2}$ ACROSS THE JET

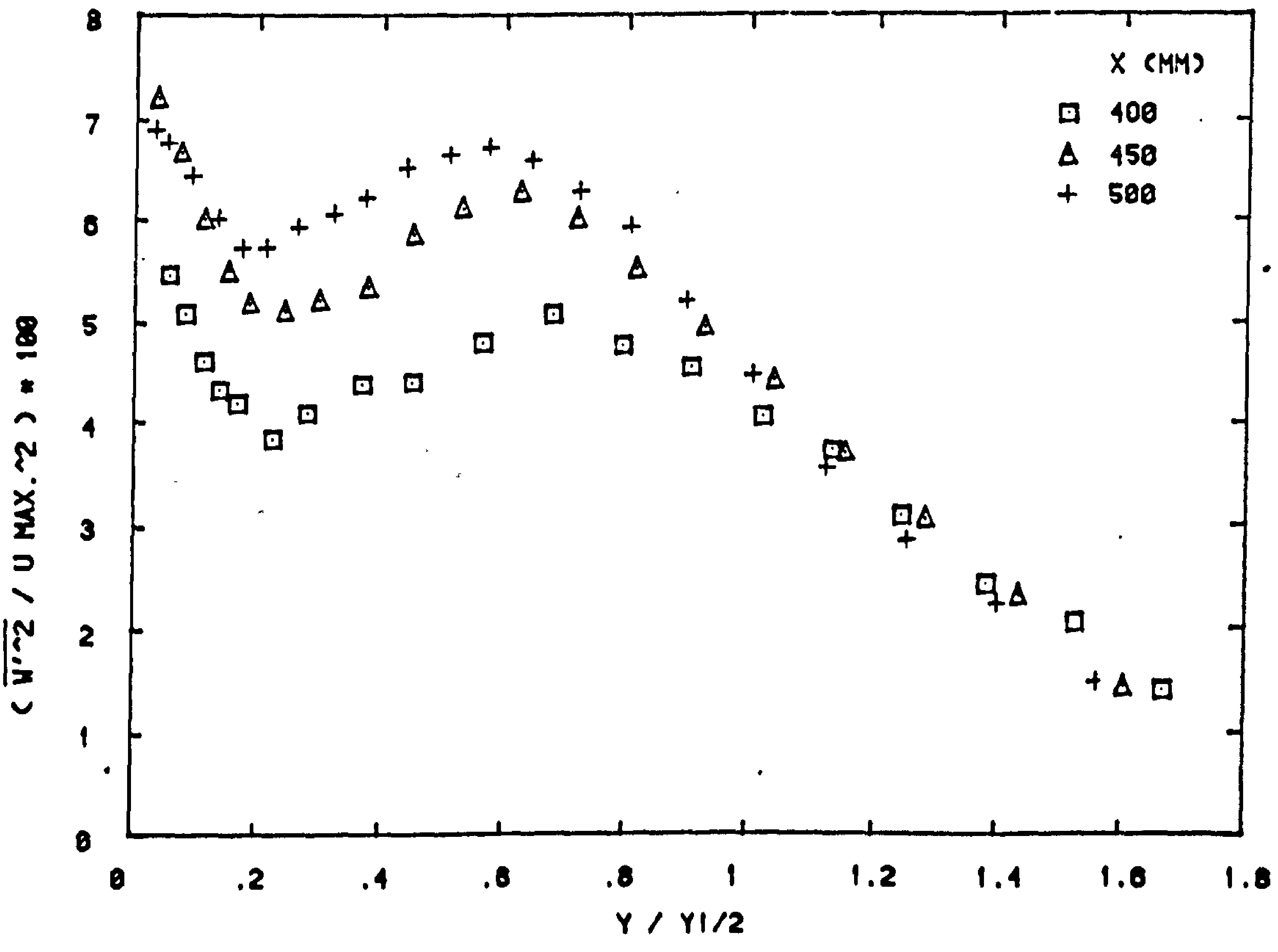

FIG. 4-18(B) TURBULENCE INTENSITY $\overline{W'^2}$ ACROSS THE JET

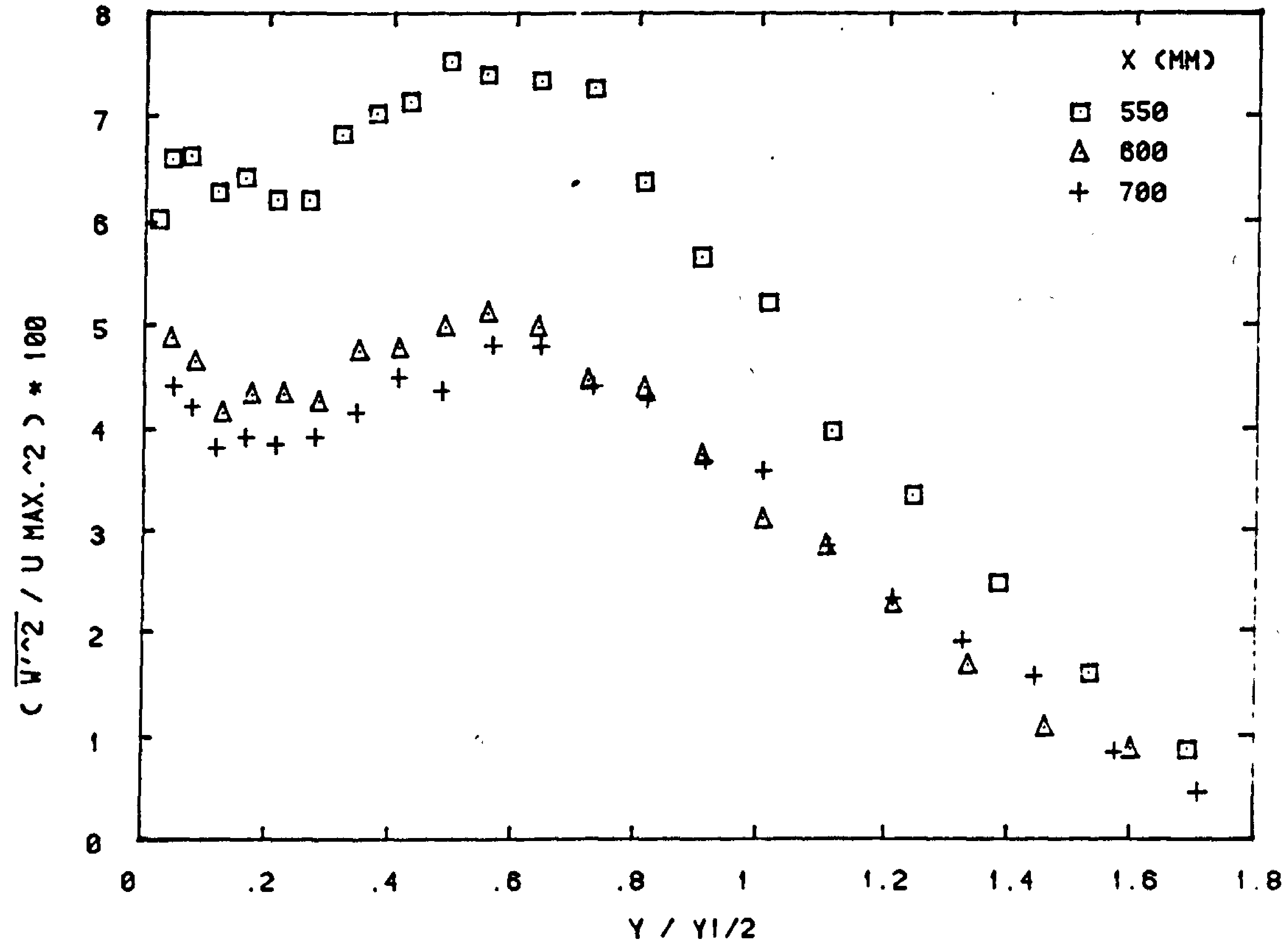

FIG. 4-18(C) TURBULENCE INTENSITY $\overline{W'^2}$ ACROSS THE JET

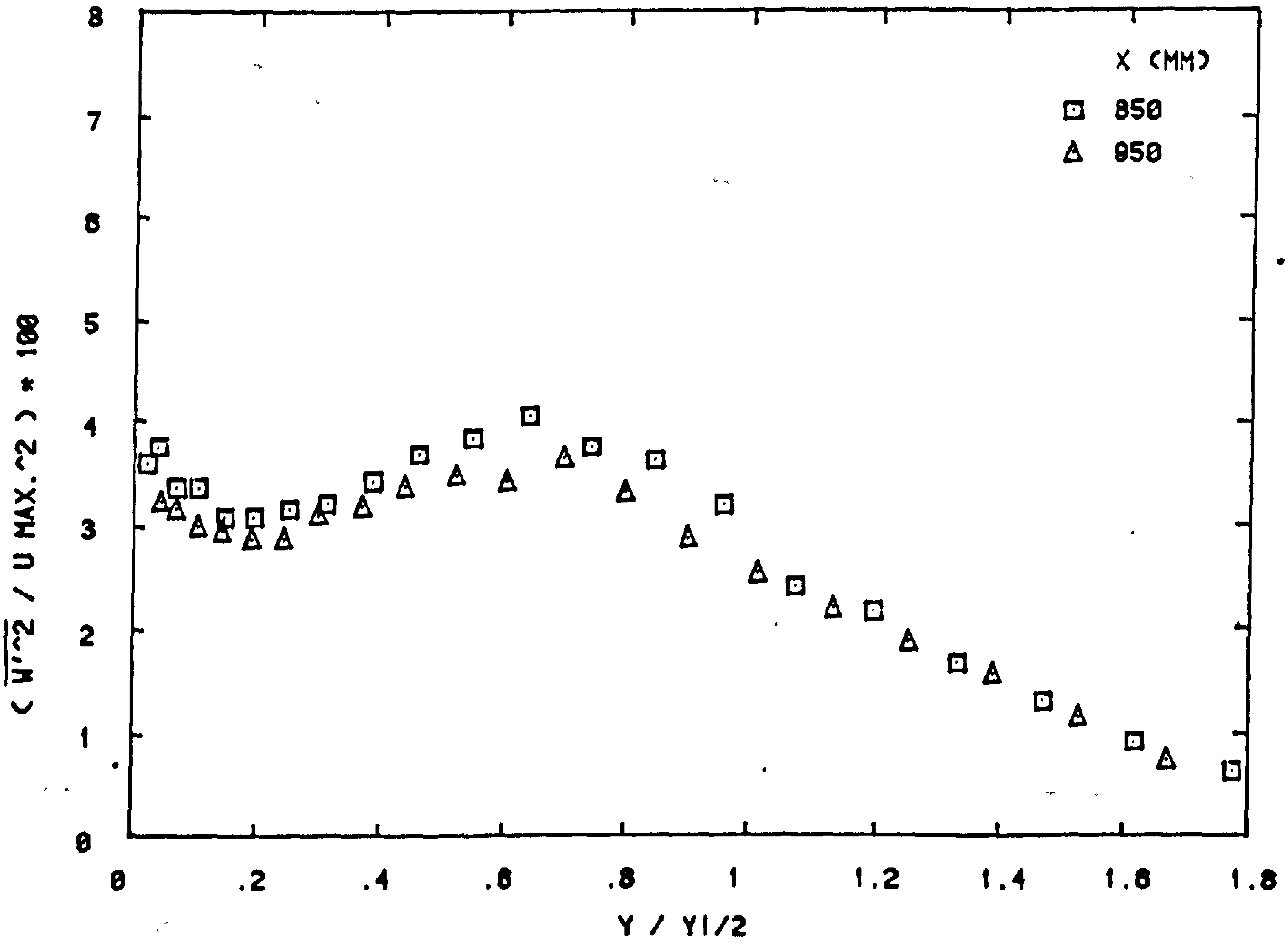

FIG. 4-18(D) TURBULENCE INTENSITY $\overline{W'^2}$ ACROSS THE JET

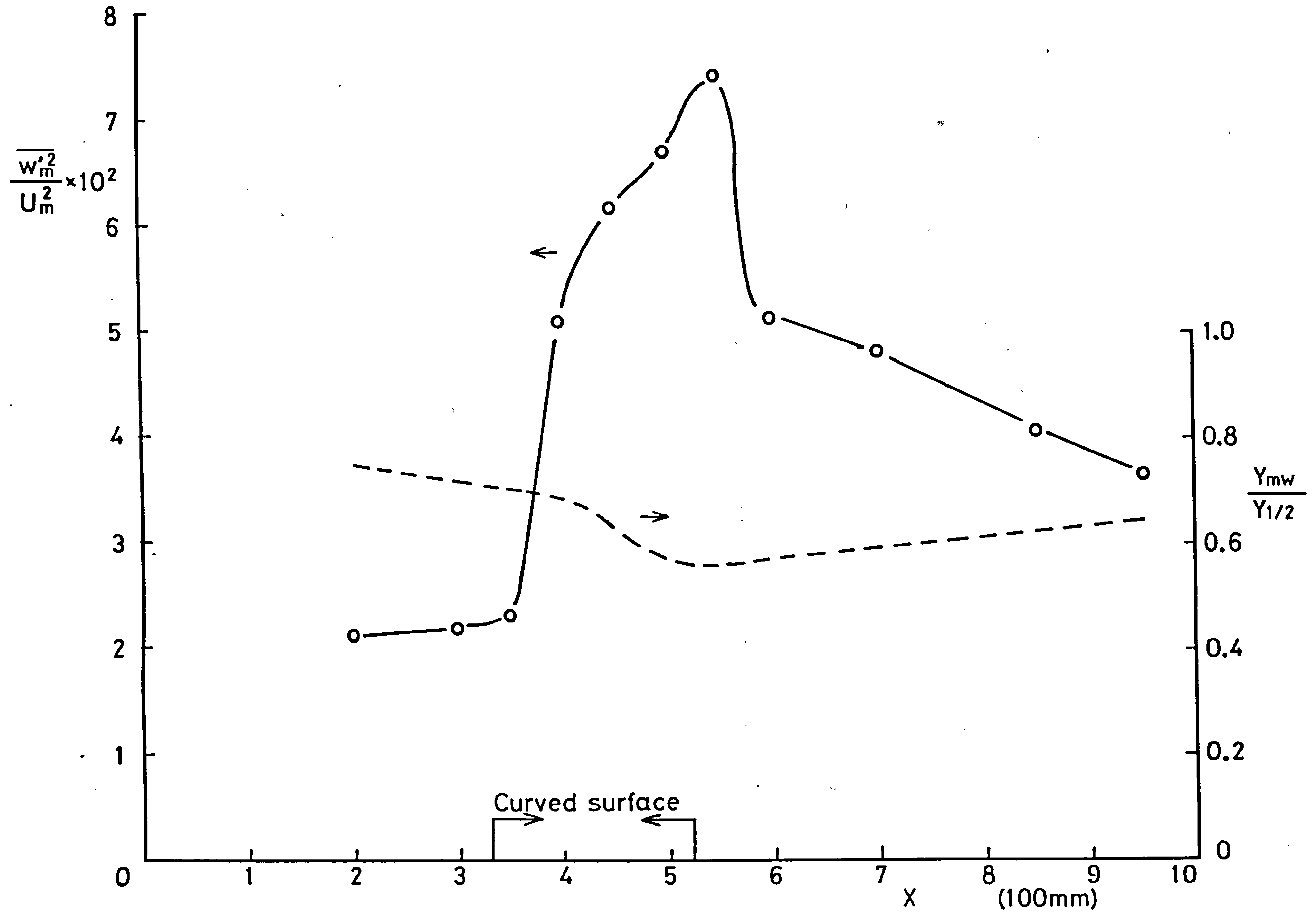

FIG. 4-19 DEVELOPMENT OF MAXIMUM TURBULENCE INTENSITY $\overline{w_m'^2}$ AND ITS POSITION

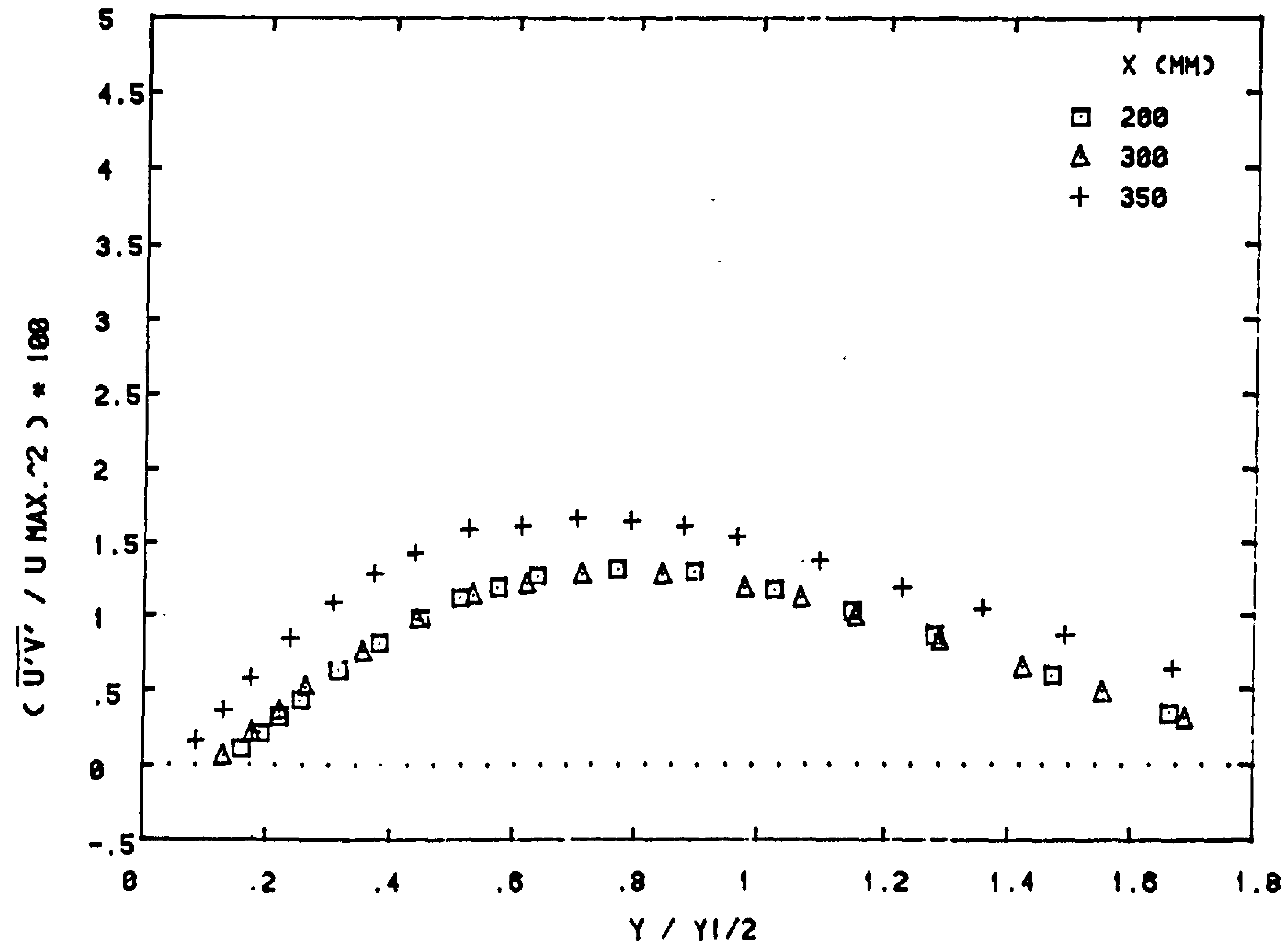

FIG. 4-20(A) TURBULENT SHEAR STRESS $\overline{U'V'}$ ACROSS THE JET

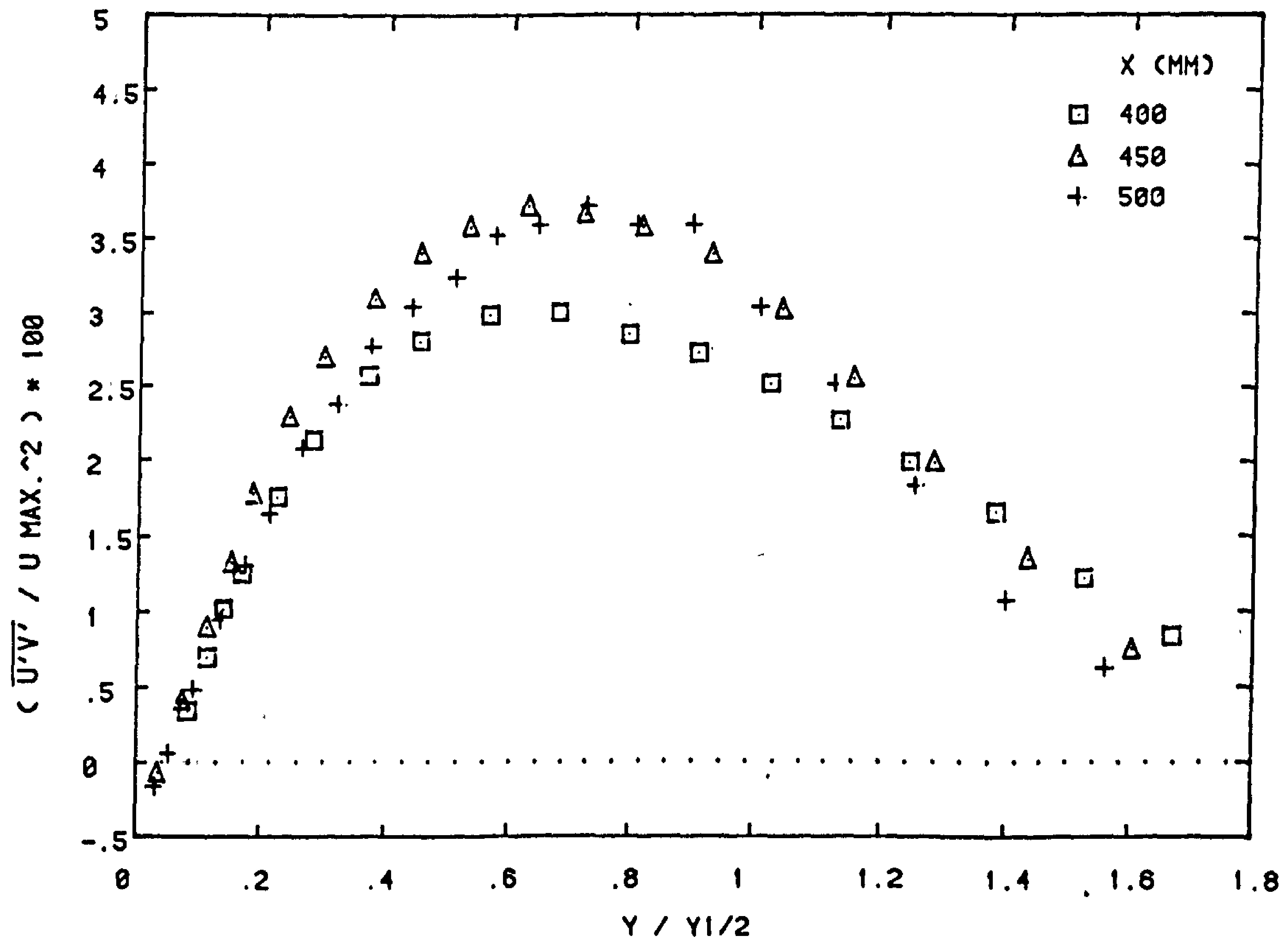

FIG. 4-20(B) TURBULENT SHEAR STRESS $\overline{U'V'}$ ACROSS THE JET

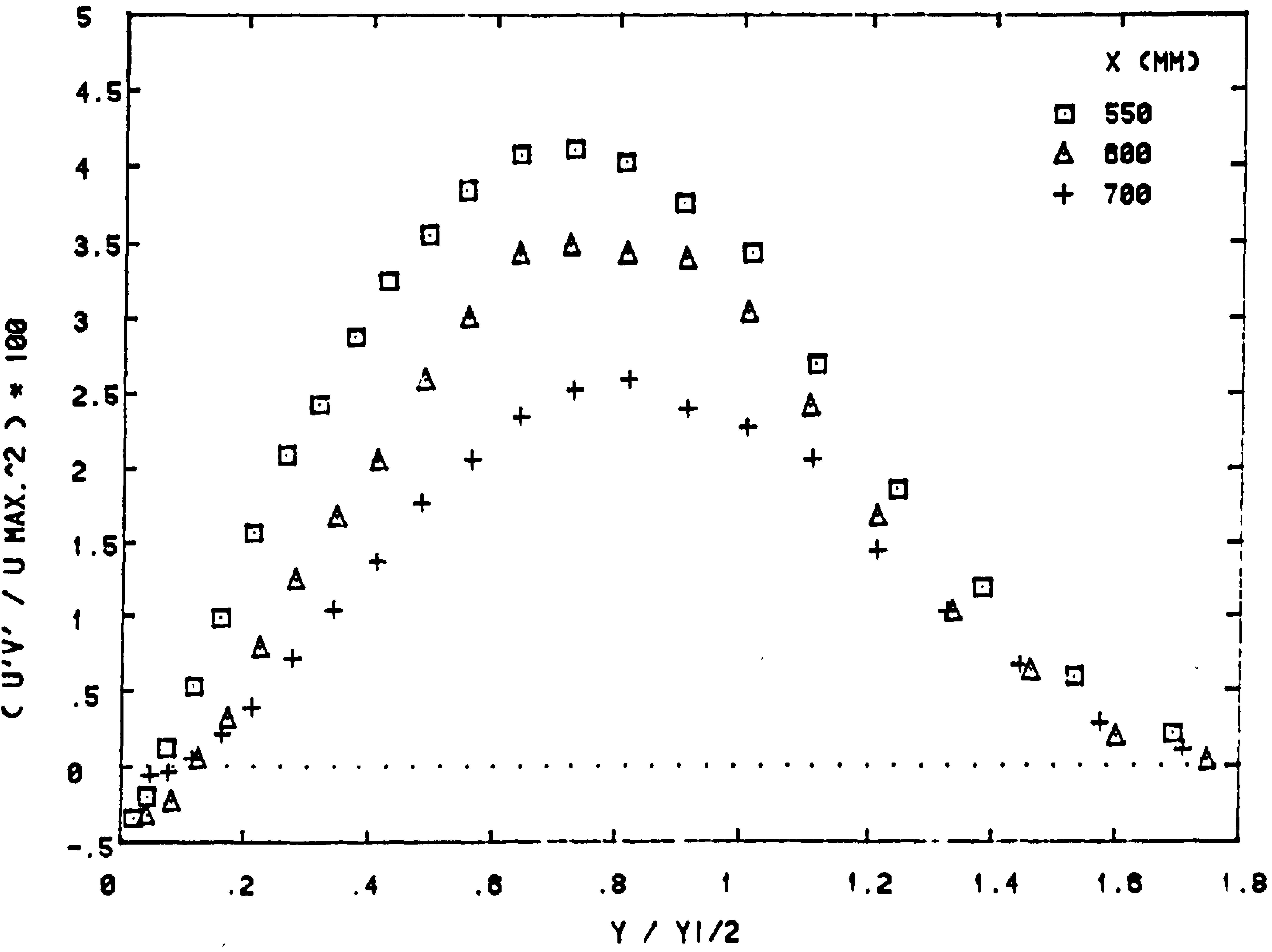

FIG. 4-20(C) TURBULENT SHEAR STRESS $\overline{U'V'}$ ACROSS THE JET

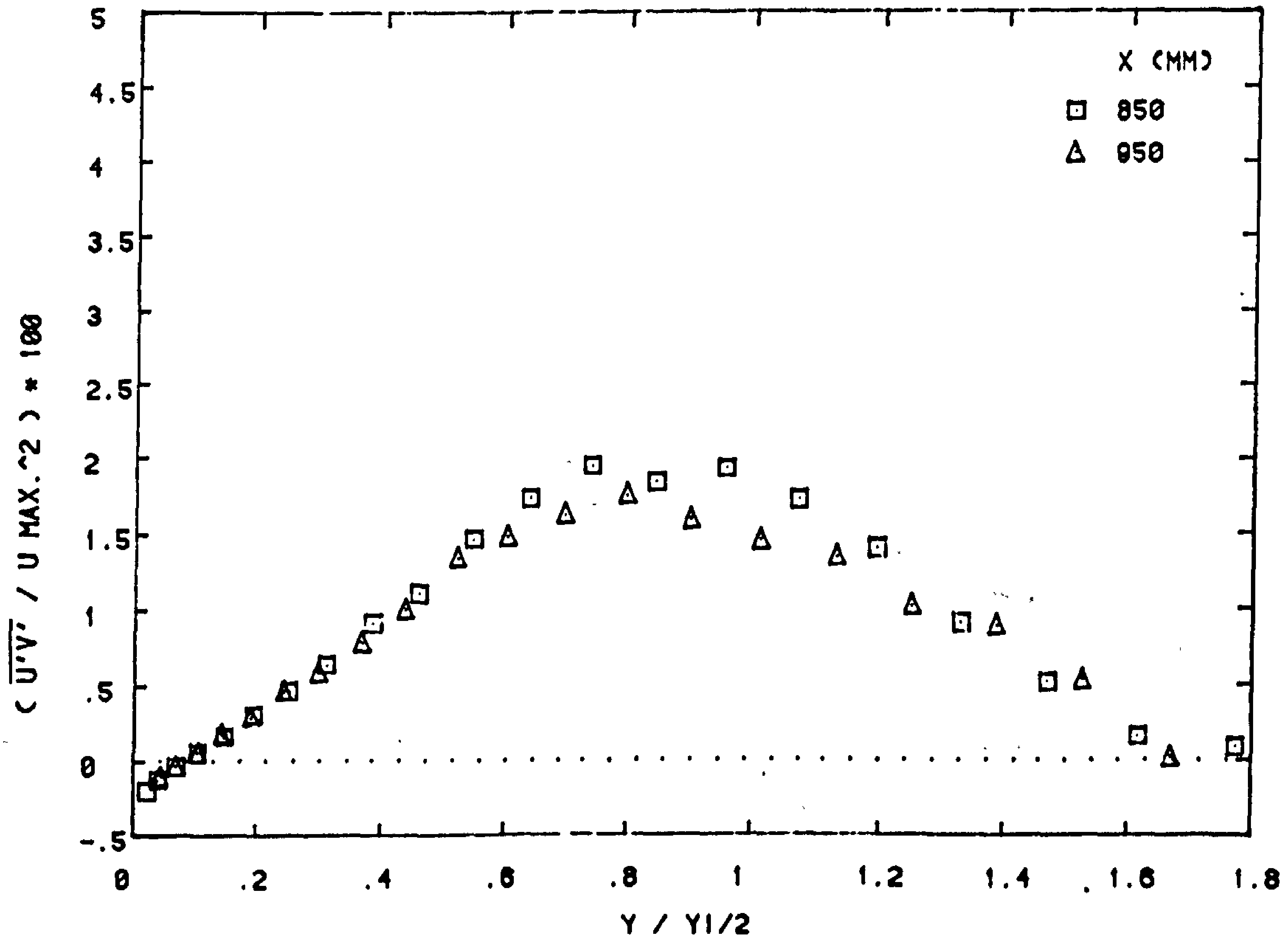

FIG. 4-20(D) TURBULENT SHEAR STRESS $\overline{U'V'}$ ACROSS THE JET

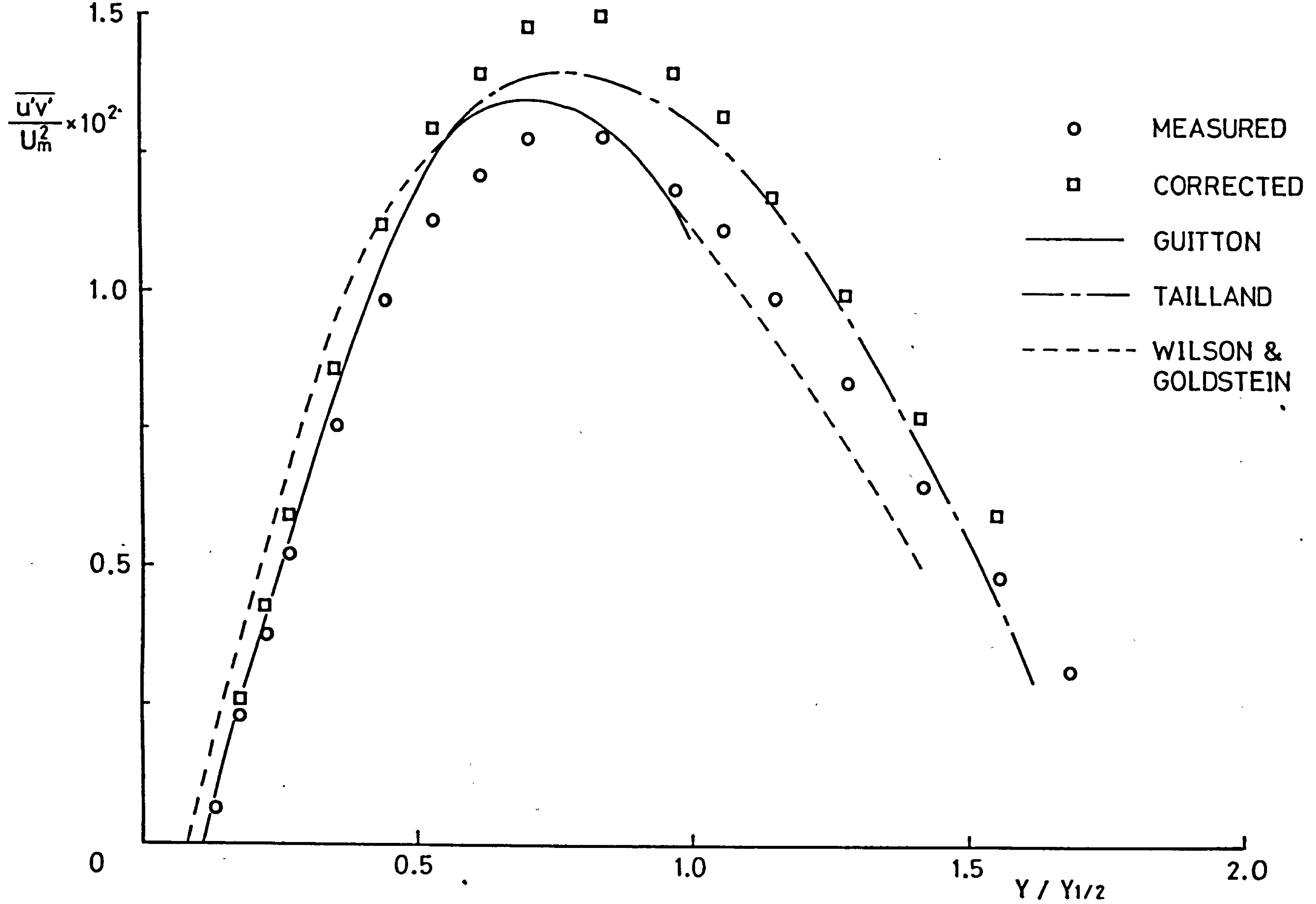

FIG. 4-21 TURBULENT SHEAR STRESS $\overline{u'v'}$ FOR PLANE WALL JETS

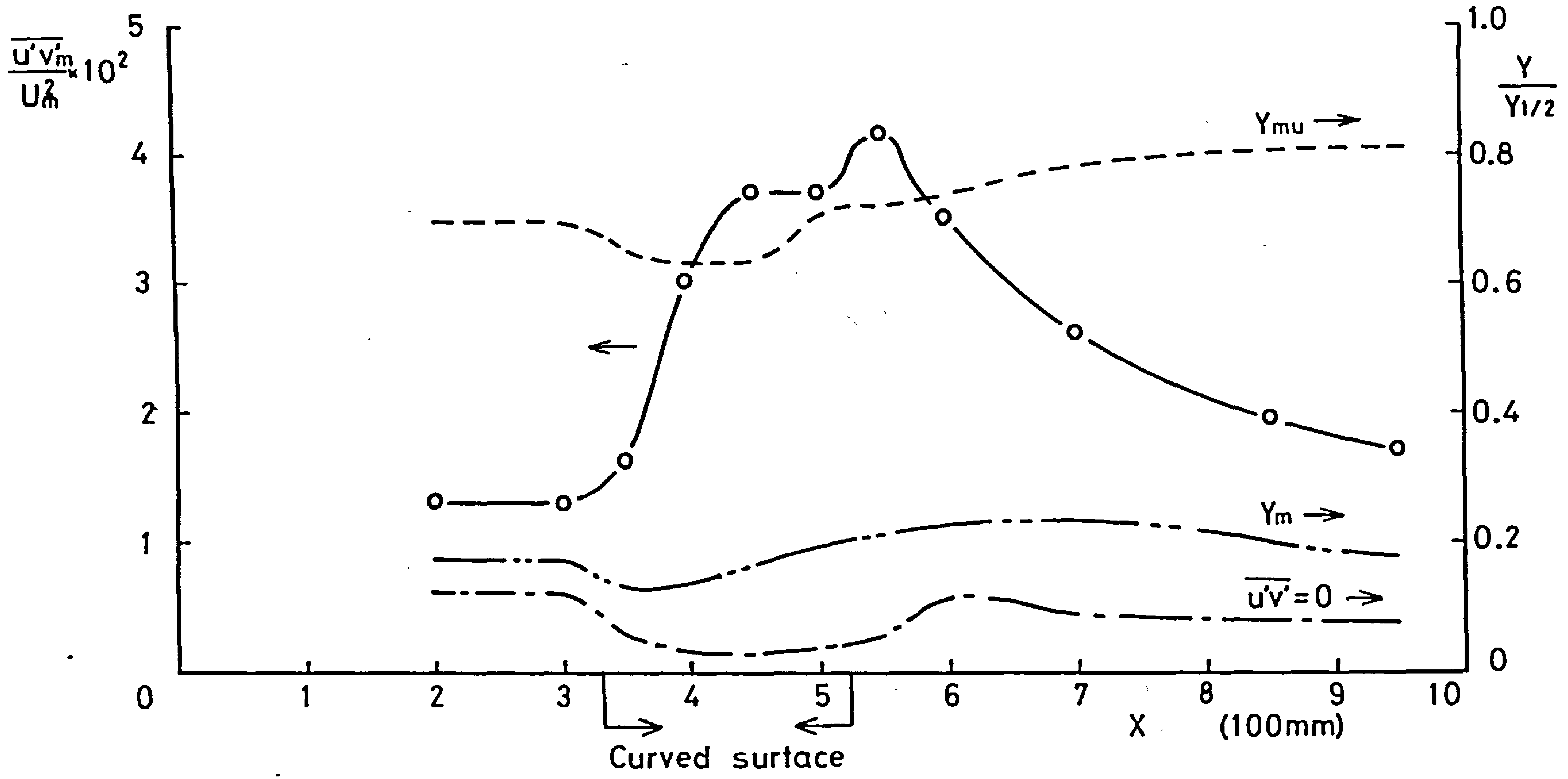

FIG. 4-22 DEVELOPMENT OF MAXIMUM TURBULENT SHEAR STRESS $\overline{u'v'}_m$, ITS POSITION AND POSITION OF $\overline{u'v'} = 0$

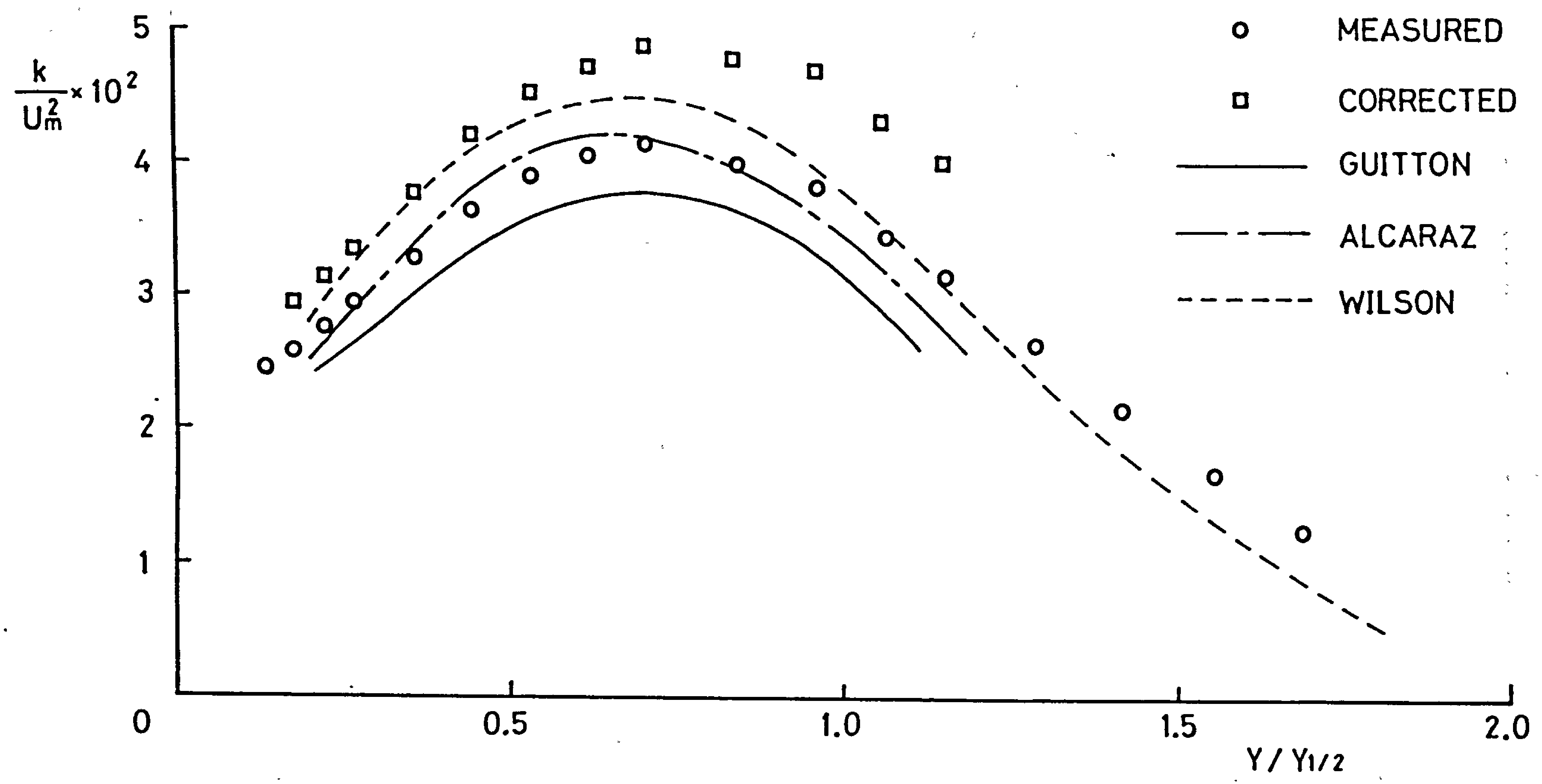

FIG. 4-23 TURBULENT KINETIC ENERGY k FOR PLANE WALL JETS

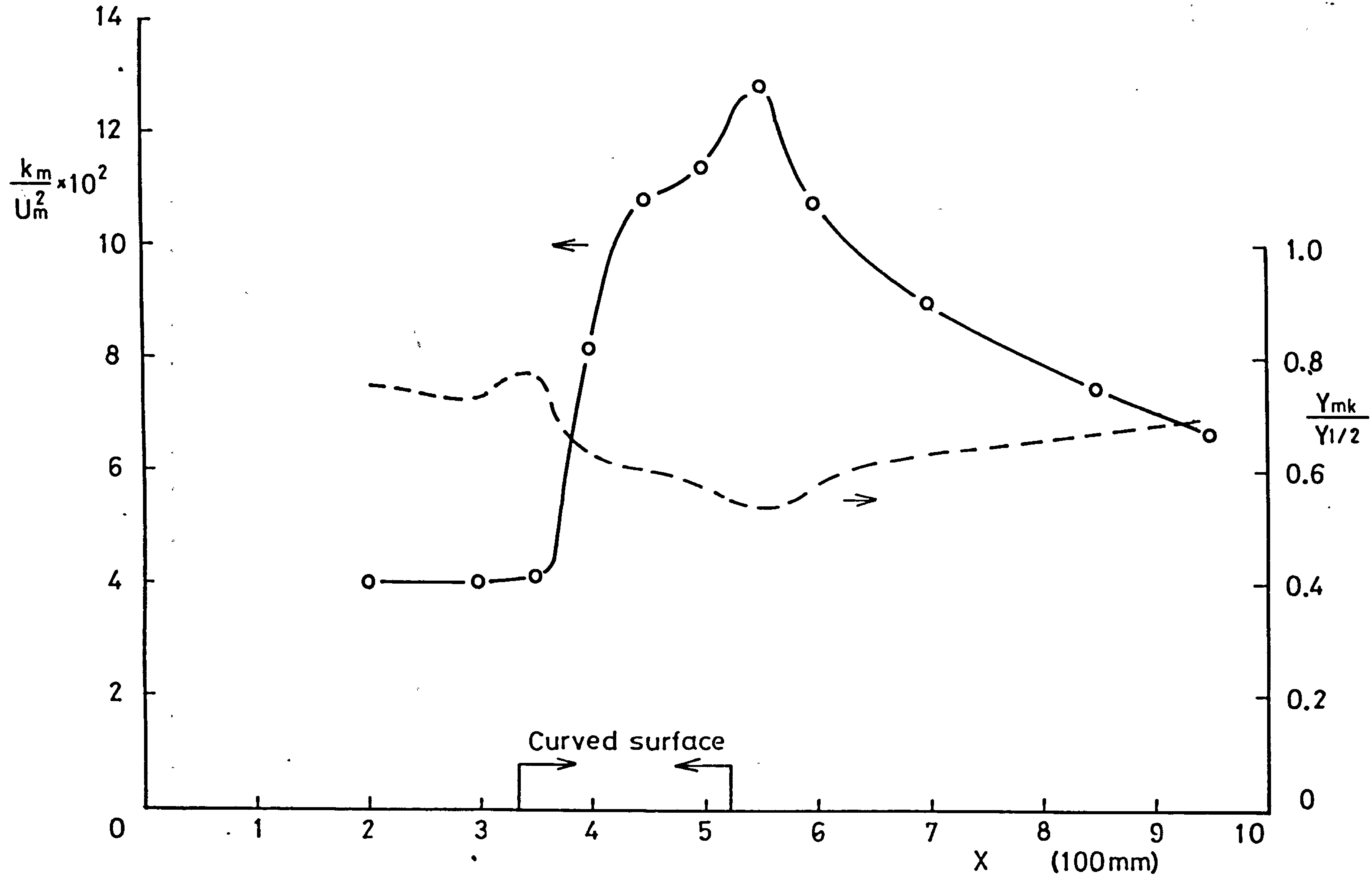

FIG. 4-24 DEVELOPMENT OF MAXIMUM TURBULENT KINETIC ENERGY k_m AND ITS POSITION

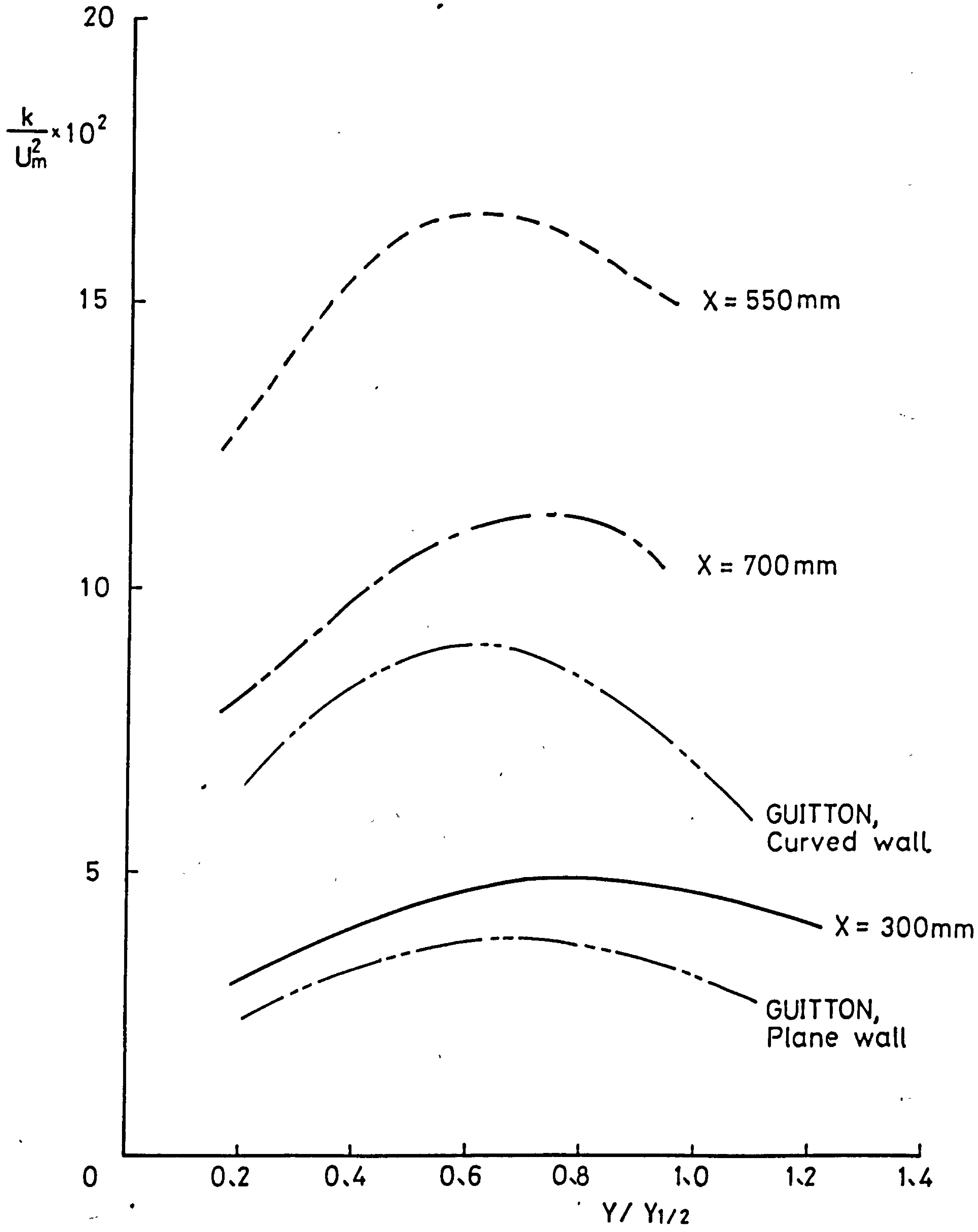

FIG. 4-25 TURBULENT KINETIC ENERGY k ACROSS THE JET, CORRECTED FOR HOT-WIRE'S DIRECTIONAL SENSITIVITY

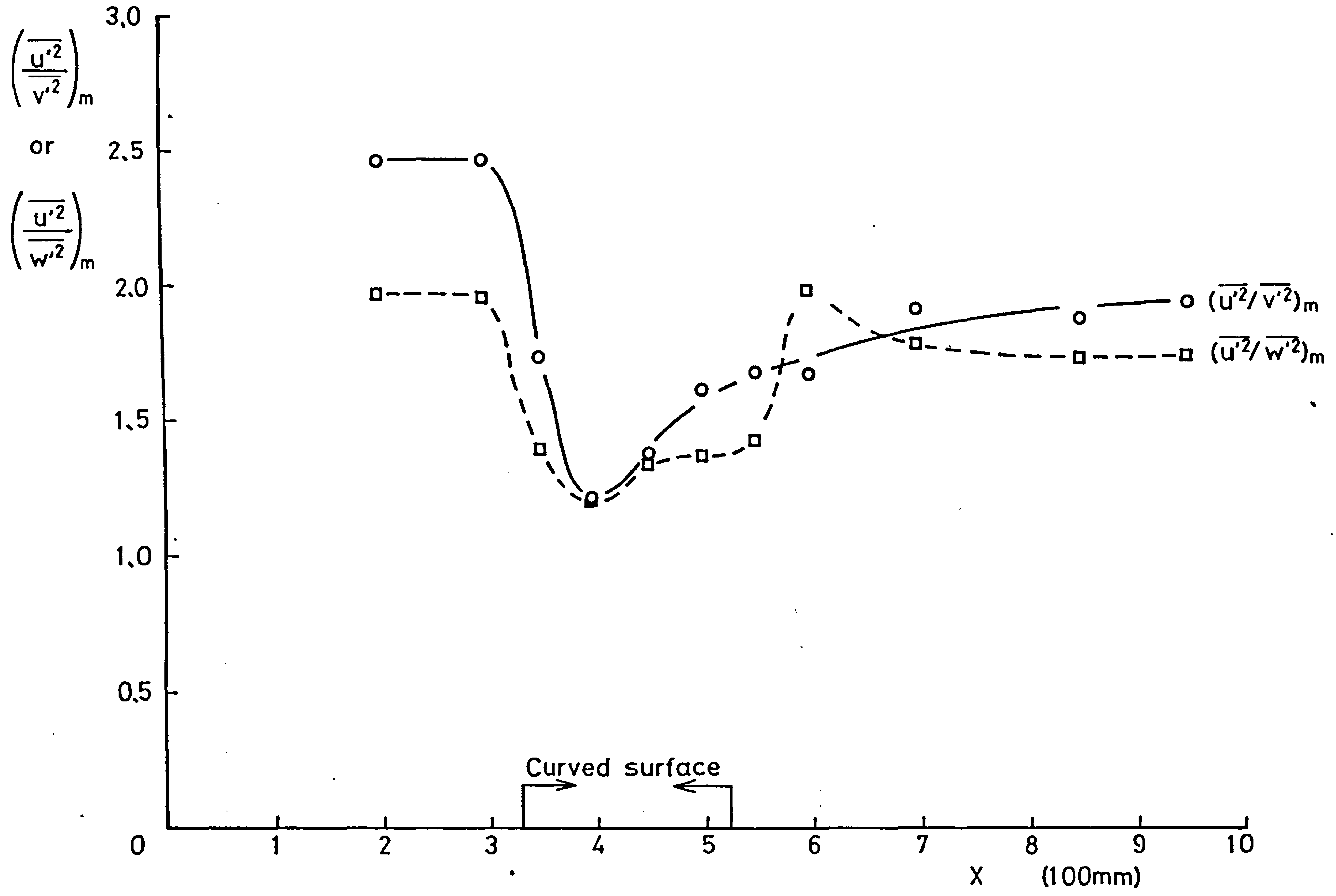

FIG. 4-26 DEVELOPMENT OF MAXIMUM RATIOS $(\overline{u'^2}/\overline{v'^2})_m$ AND $(\overline{u'^2}/\overline{w'^2})_m$

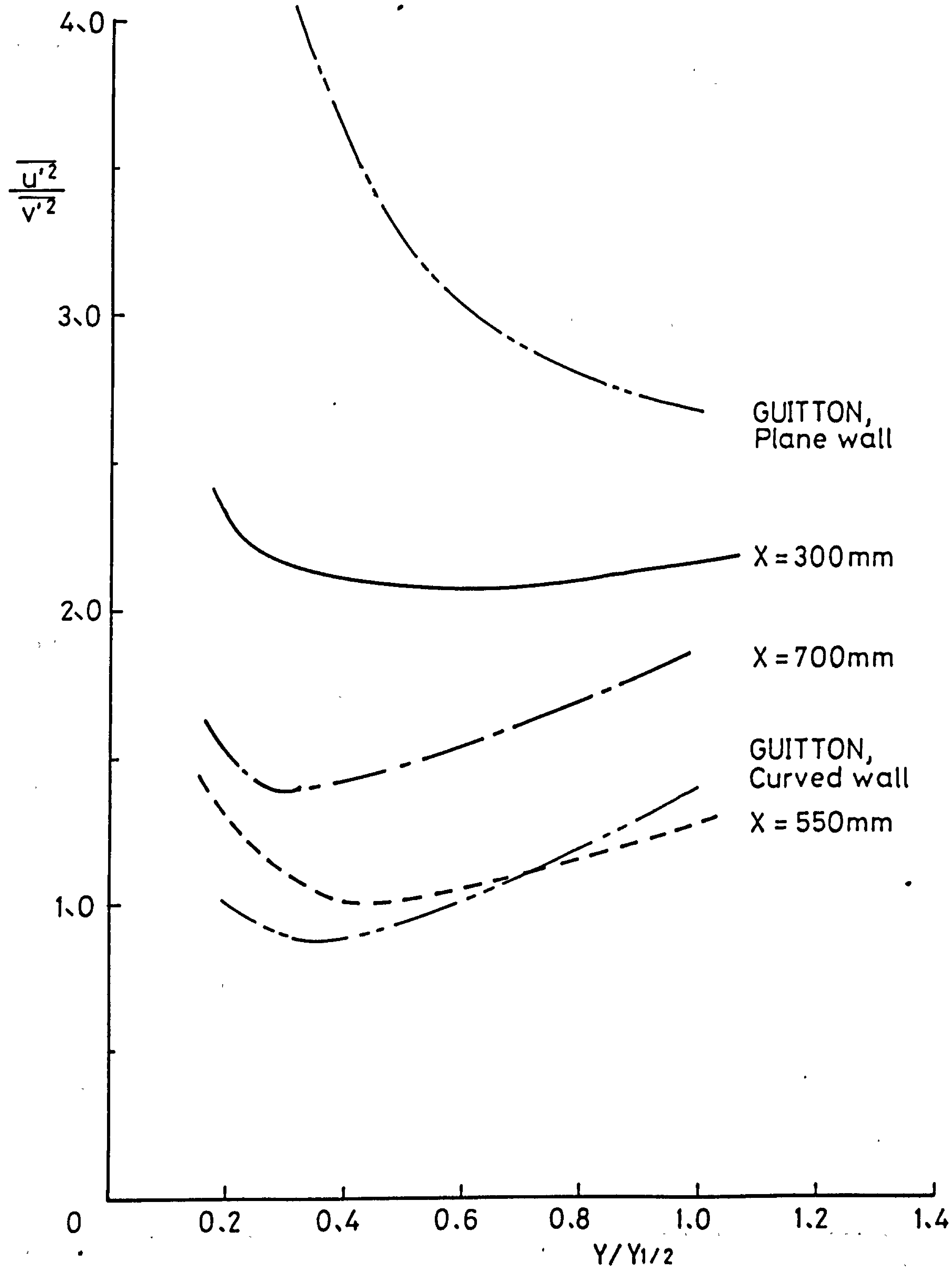

FIG. 4-27 RATIO $\overline{u'^2}/\overline{v'^2}$ ACROSS THE JET, CORRECTED FOR HOT-WIRE'S DIRECTIONAL SENSITIVITY

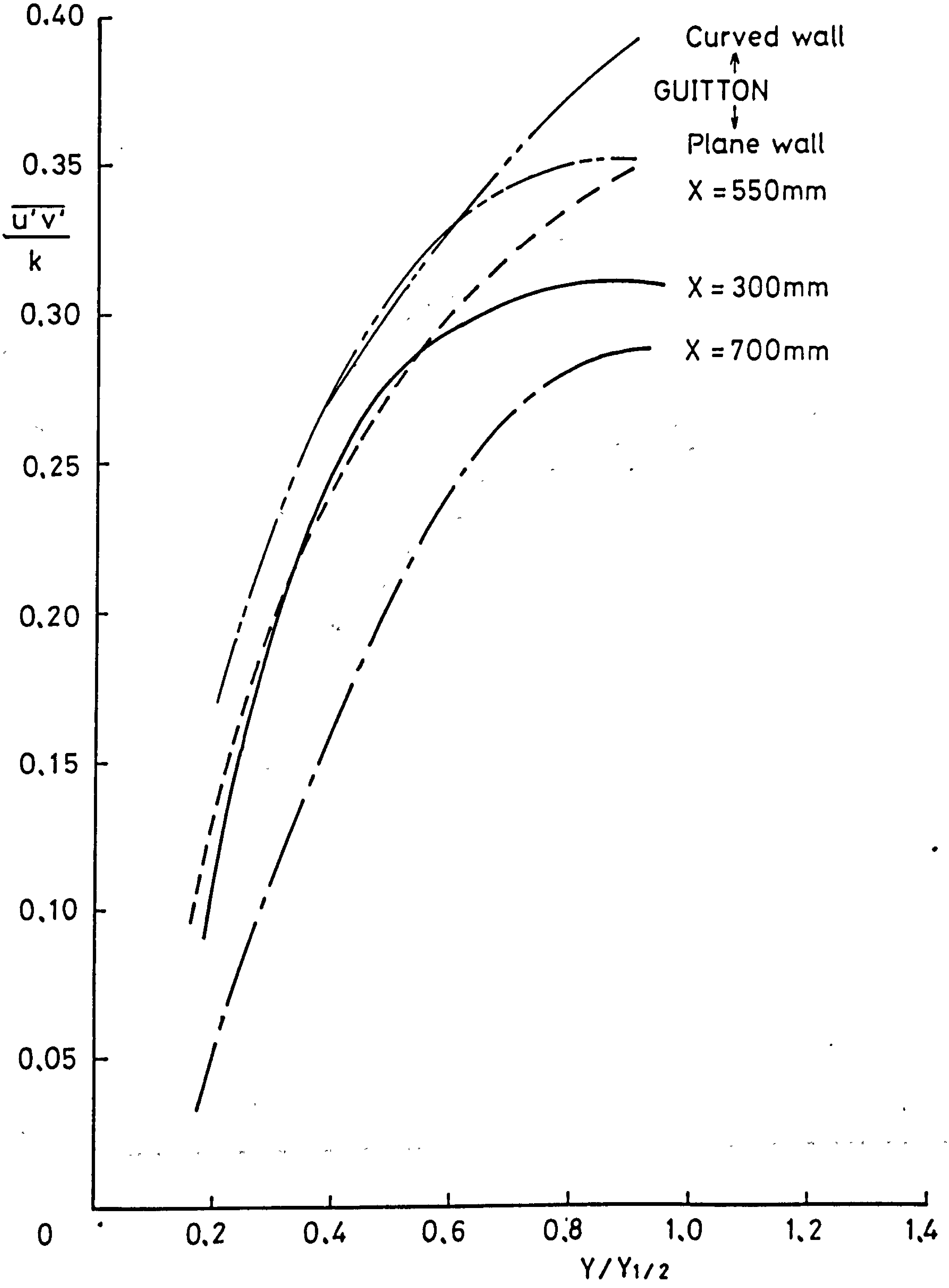

FIG. 4-28 RATIOS OF SHEAR STRESS TO KINETIC ENERGY $\overline{u'v'}/k$ ACROSS THE JET, CORRECTED FOR HOT-WIRE'S DIRECTIONAL SENSITIVITY

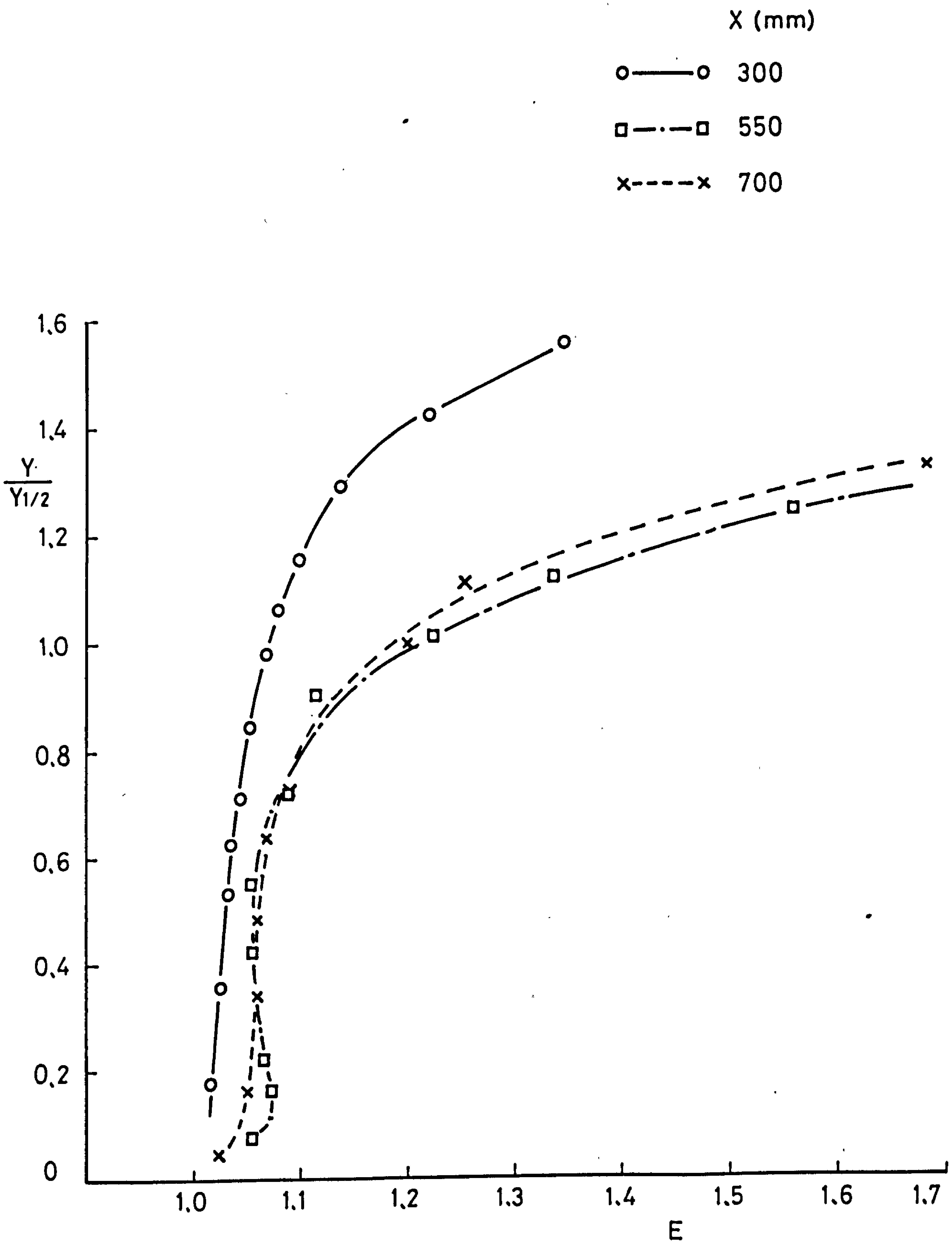

FIG. 4-29(A) HOT-WIRE'S DIRECTIONAL SENSITIVITY CORRECTION FACTOR E FOR $\overline{u'^2}$

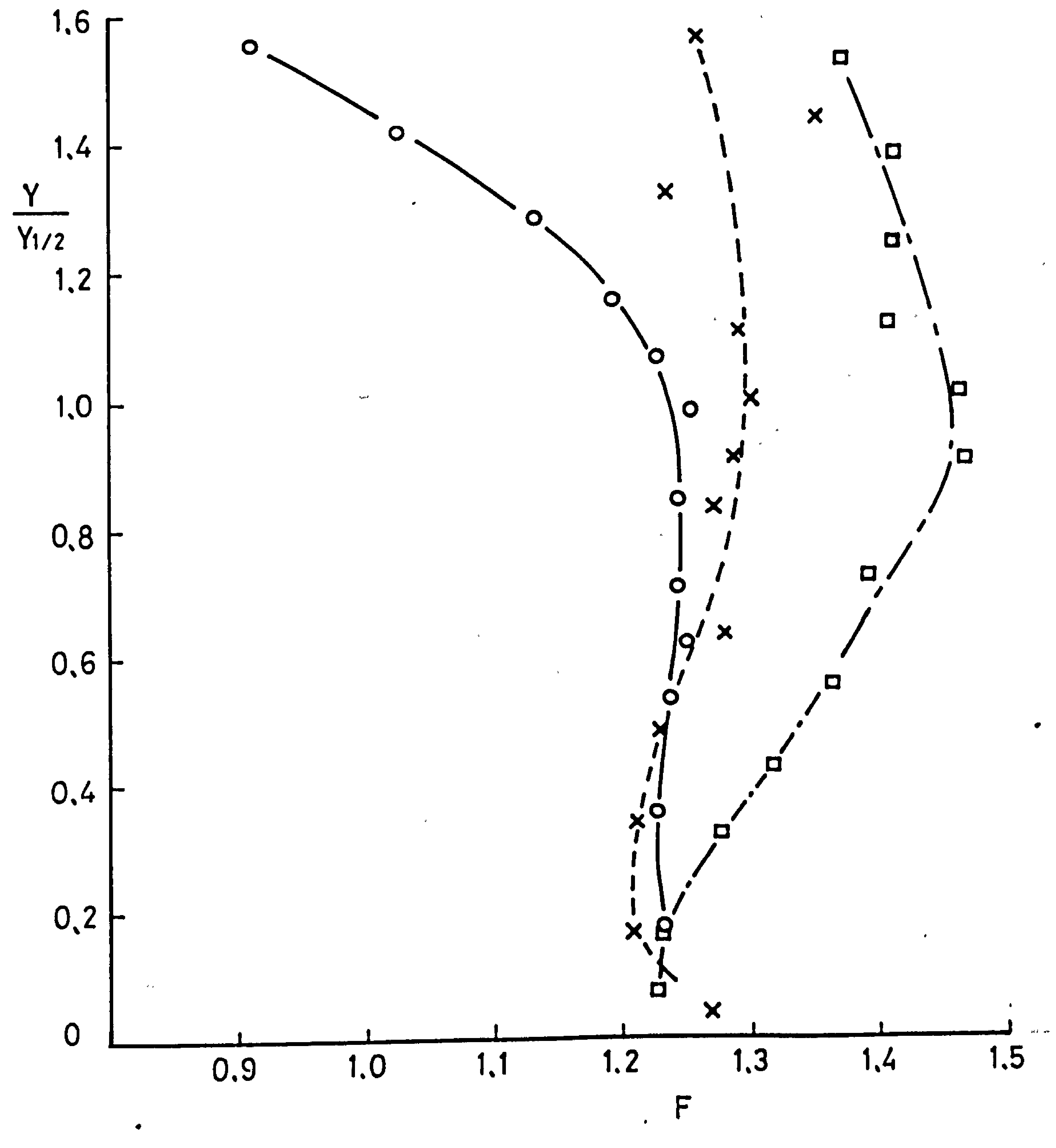

FIG. 4-29(B) HOT-WIRE'S DIRECTIONAL SENSITIVITY CORRECTION FACTOR F FOR $\overline{v'^2}$

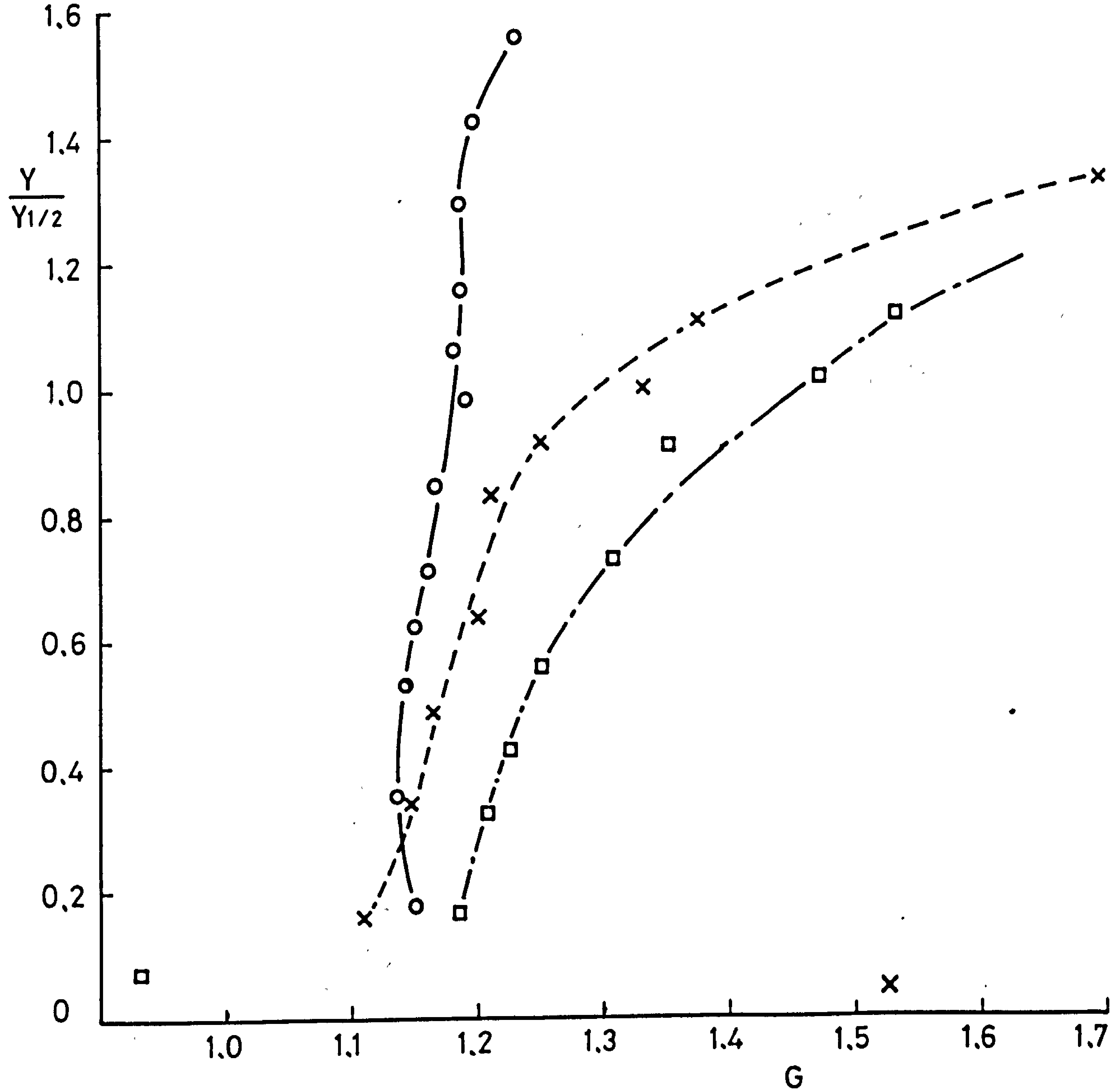

FIG. 4-29(C) HOT-WIRE'S DIRECTIONAL SENSITIVITY CORRECTION FACTOR G FOR $\overline{u'v'}$

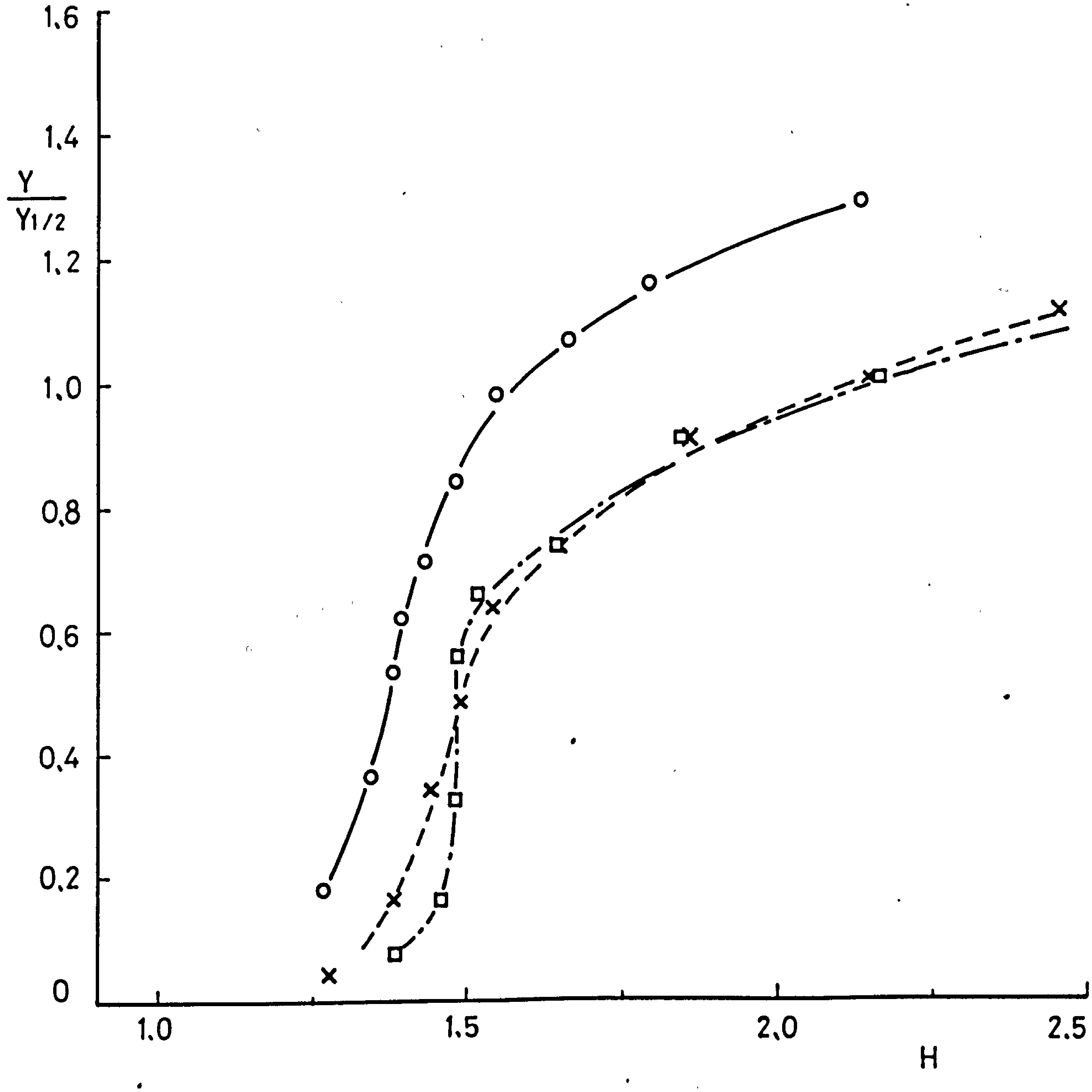

FIG. 4-29(D) HOT-WIRE'S DIRECTIONAL SENSITIVITY CORRECTION FACTOR H FOR $\overline{w'^2}$

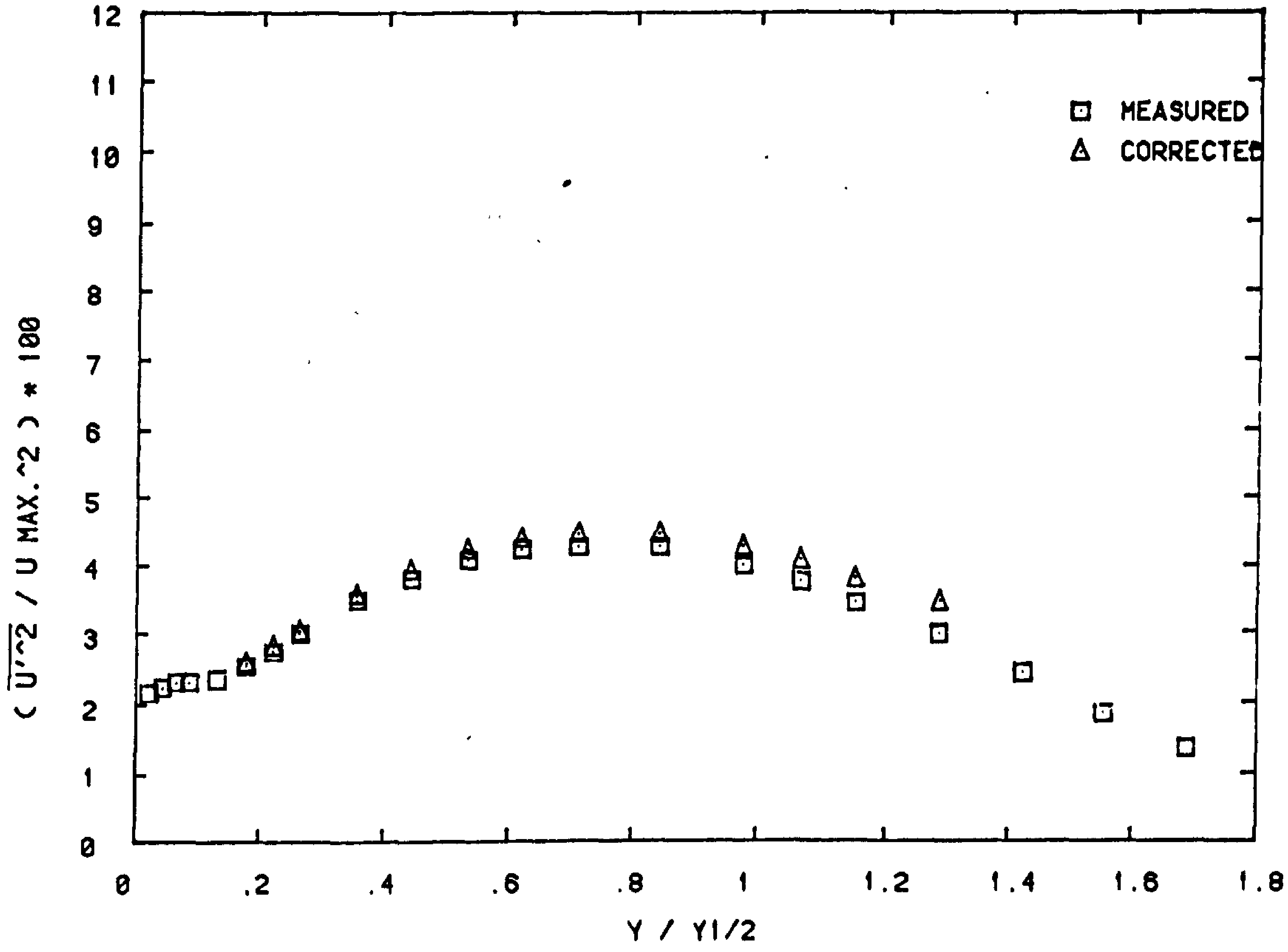

FIG. 4-30(A) TURBULENCE INTENSITY $\overline{U'^2}$ AND COERRECTED $\overline{U'^2}$ AT X=300

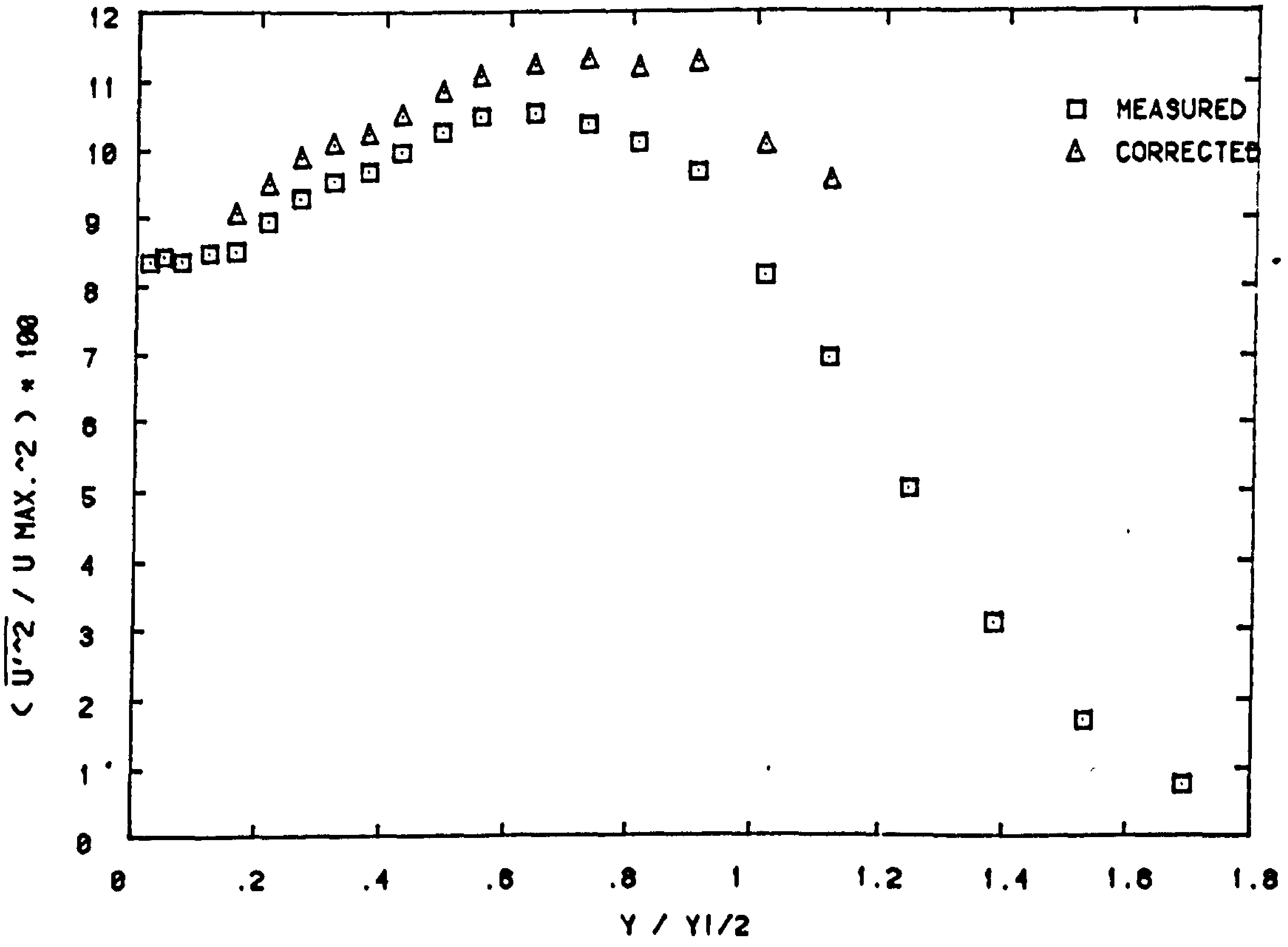

FIG. 4-30(B) TURBULENCE INTENSITY $\overline{U'^2}$ AND CORRECTED $\overline{U'^2}$ AT X=550

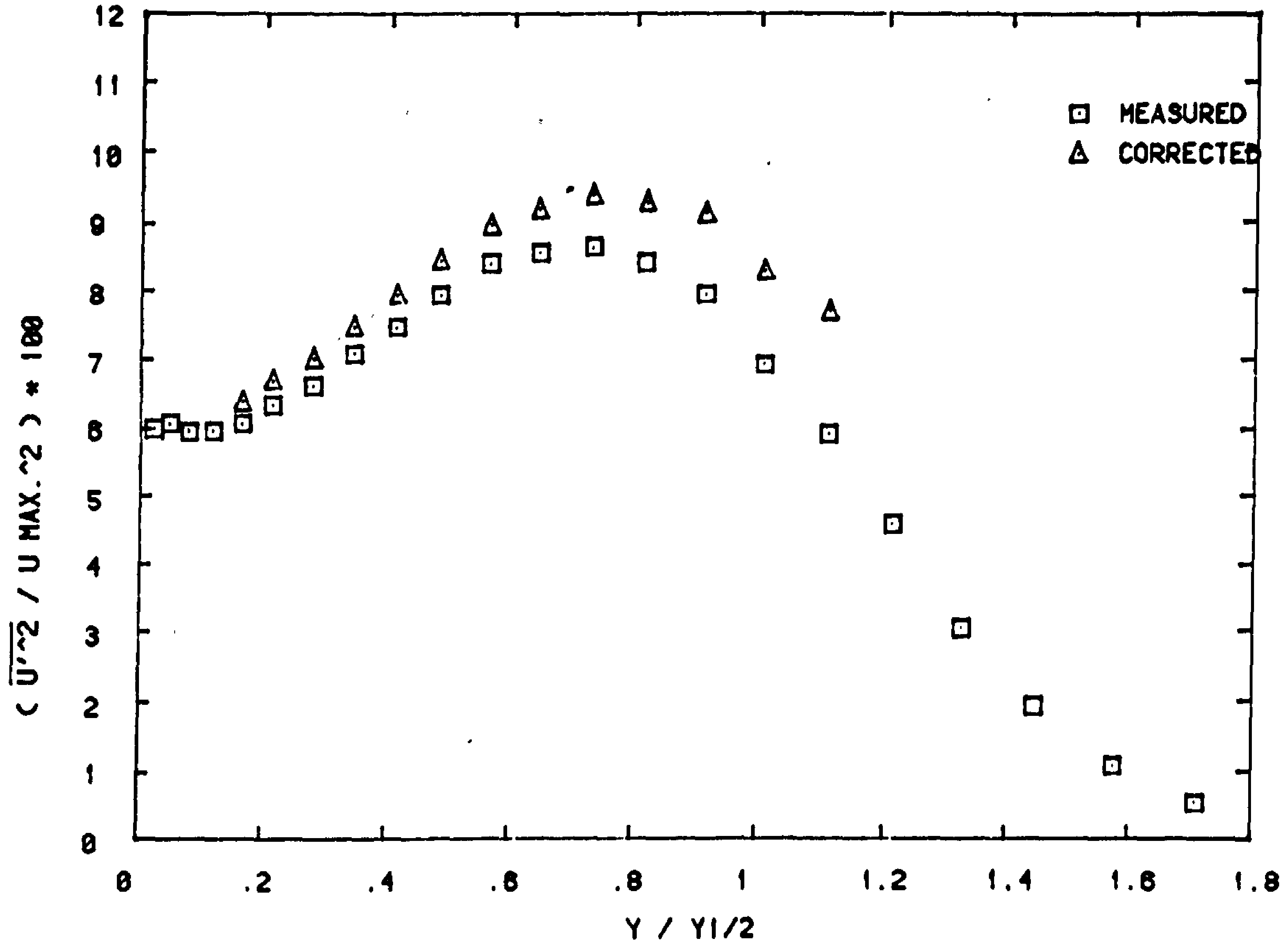

FIG. 4-30(C) TURBULENCE INTENSITY $\overline{U'^2}$ AND CORRECTED $\overline{U'^2}$ AT X=700

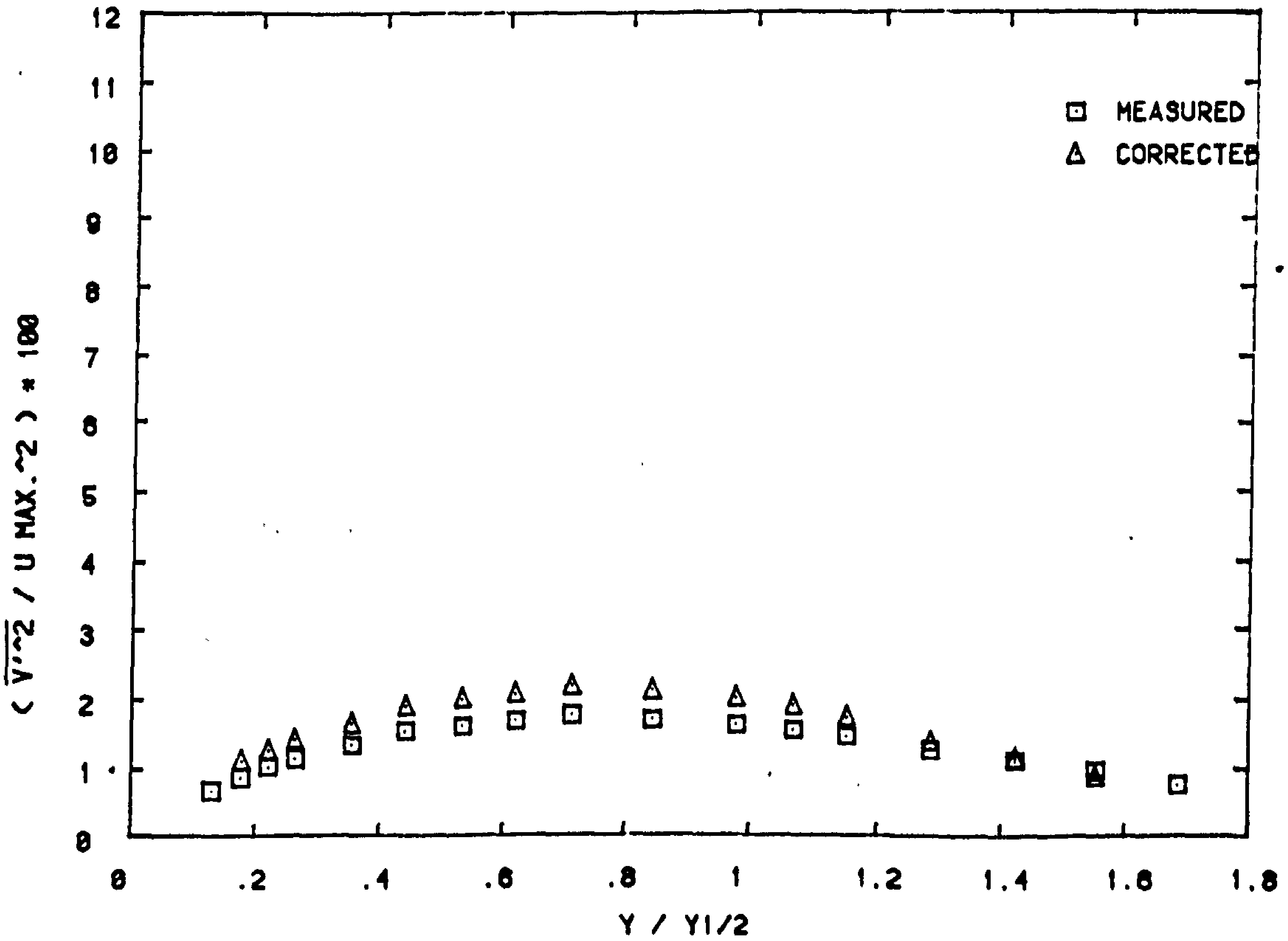

FIG. 4-31(A) TURBULENCE INTENSITY $\overline{V'^2}$ AND CORRECTED $\overline{V'^2}$ AT X=300

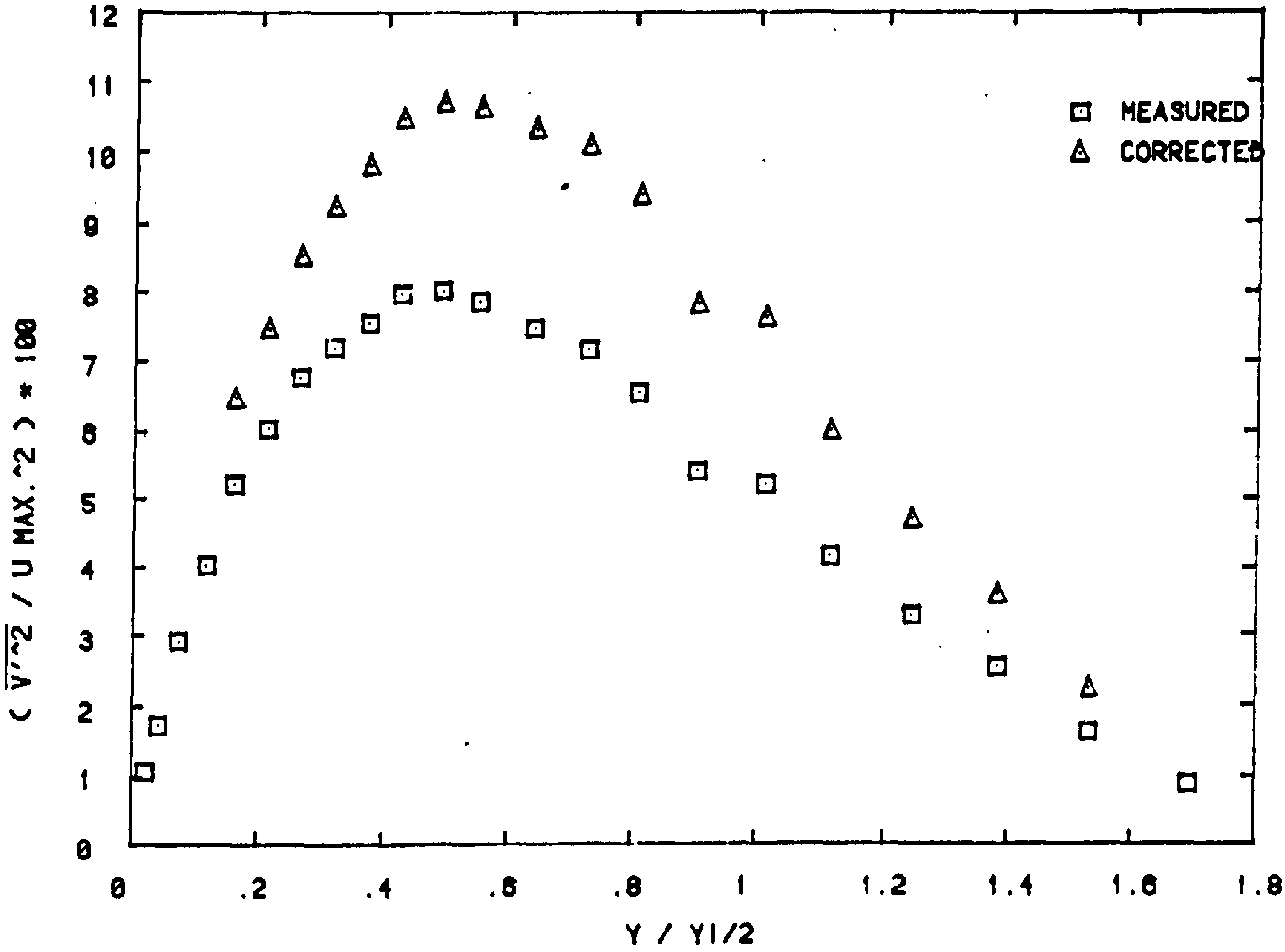

FIG. 4-31(B) TURBULENCE INTENSITY $\overline{V'^2}$ AND CORRECTED $\overline{V'^2}$ AT X=550

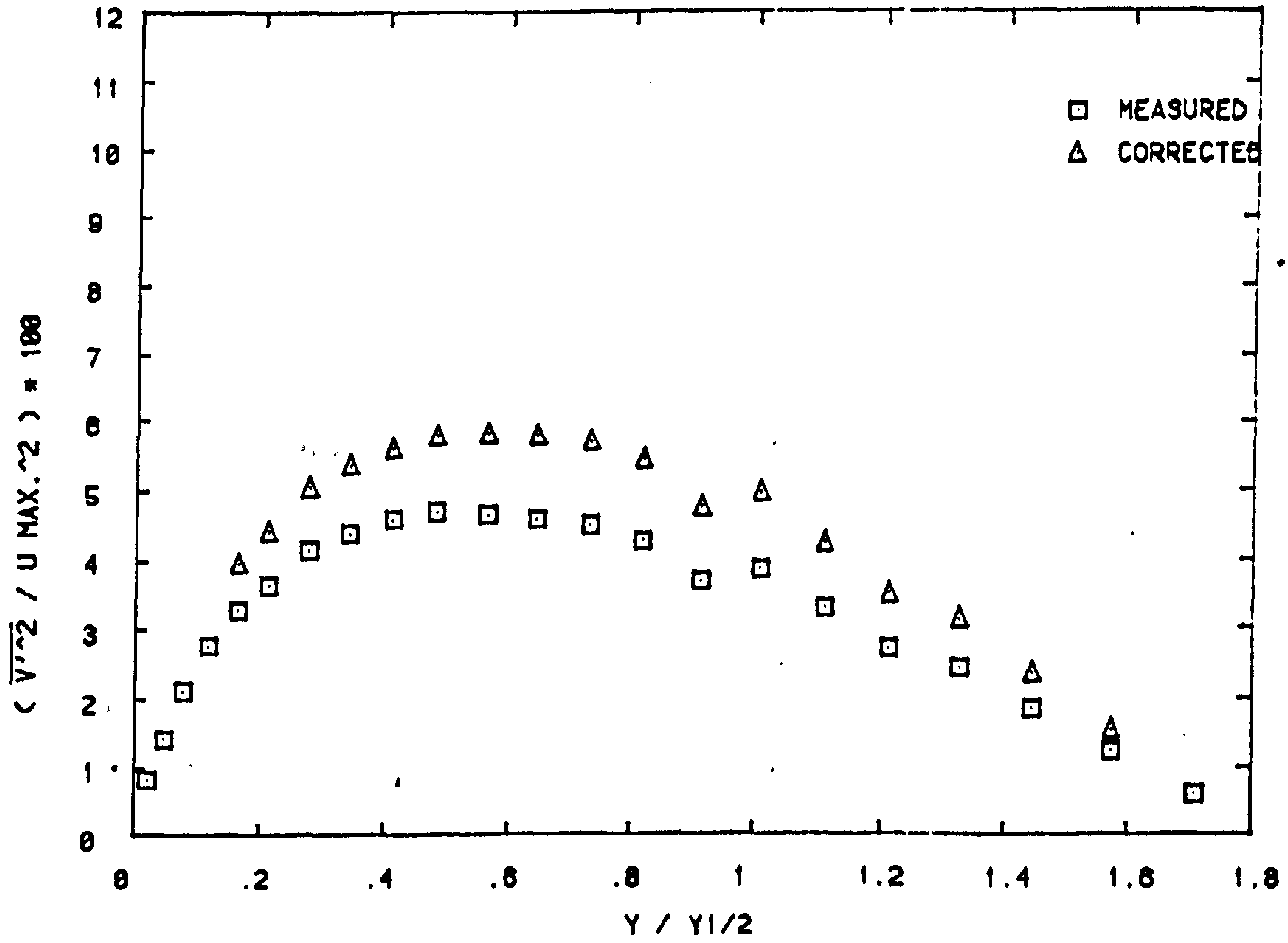

FIG. 4-31(C) TURBULENCE INTENSITY $\overline{V'^2}$ AND CORRECTED $\overline{V'^2}$ AT X=700

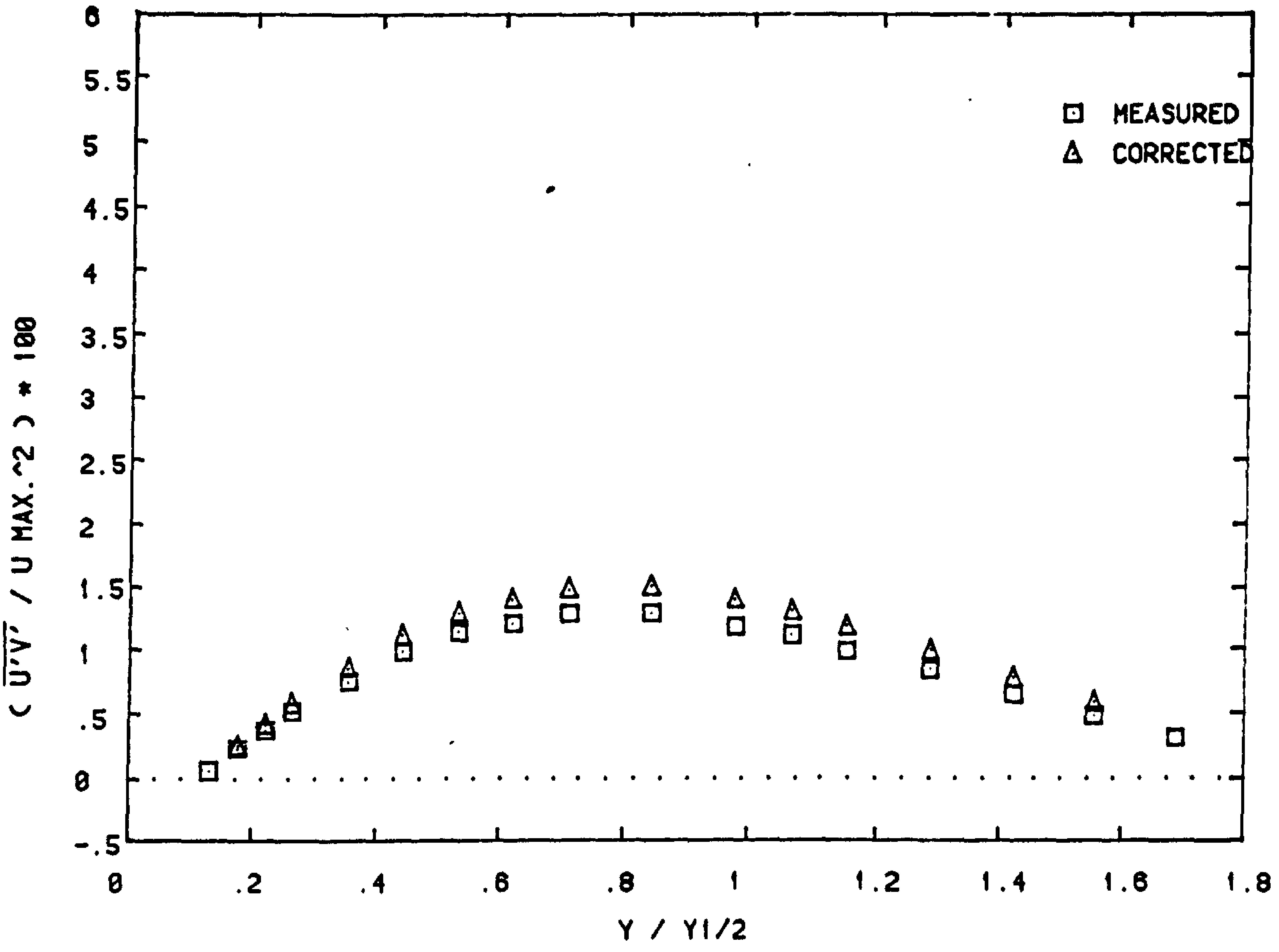

FIG.4-32(A) SHEAR STRESS $\overline{U'V'}$ AND CORRECTED $\overline{U'V'}$ AT X=300

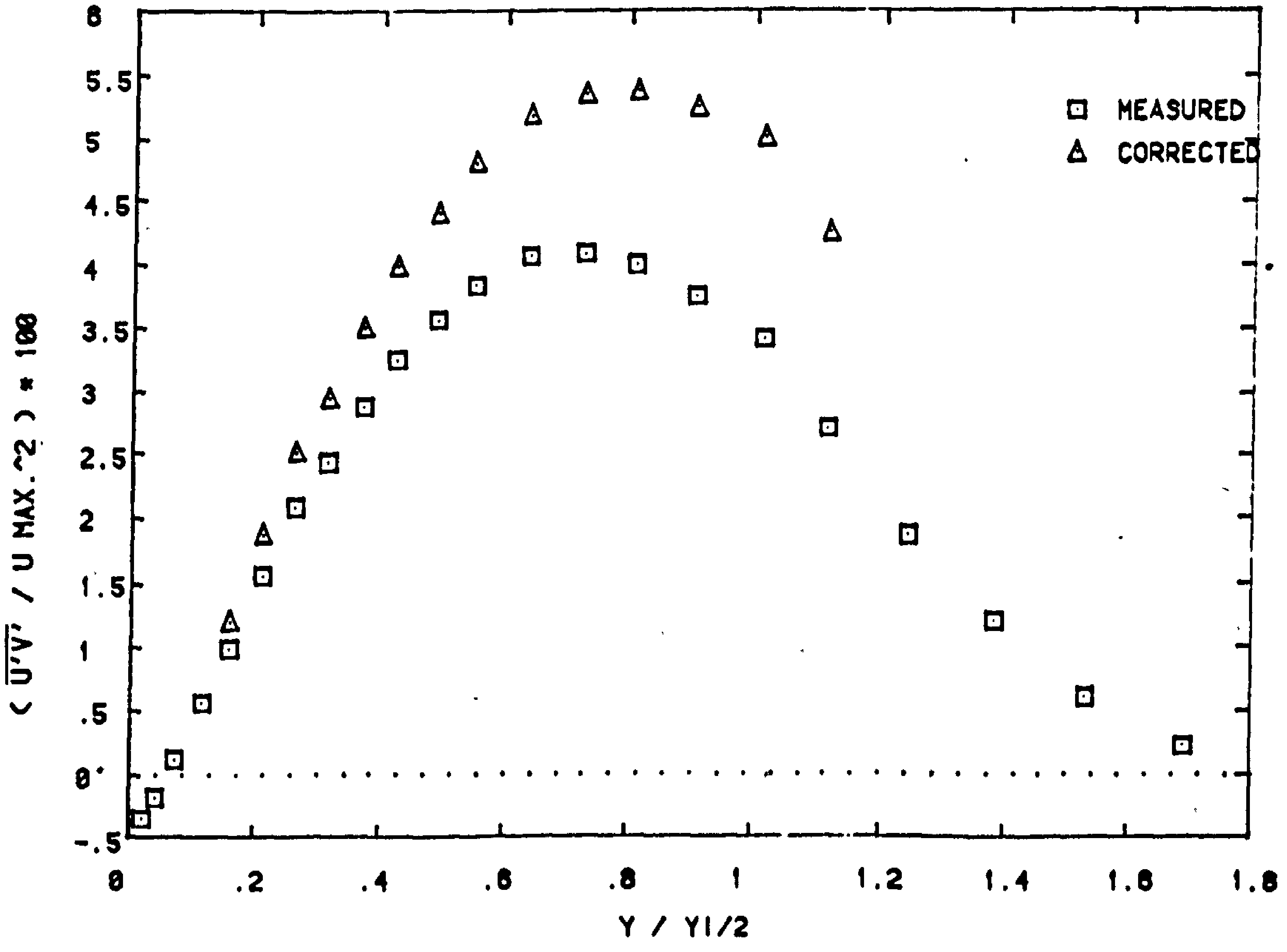

FIG. 4-32(B) SHEAR STRESS $\overline{U'V'}$ AND CORRECTED $\overline{U'V'}$ AT X=550

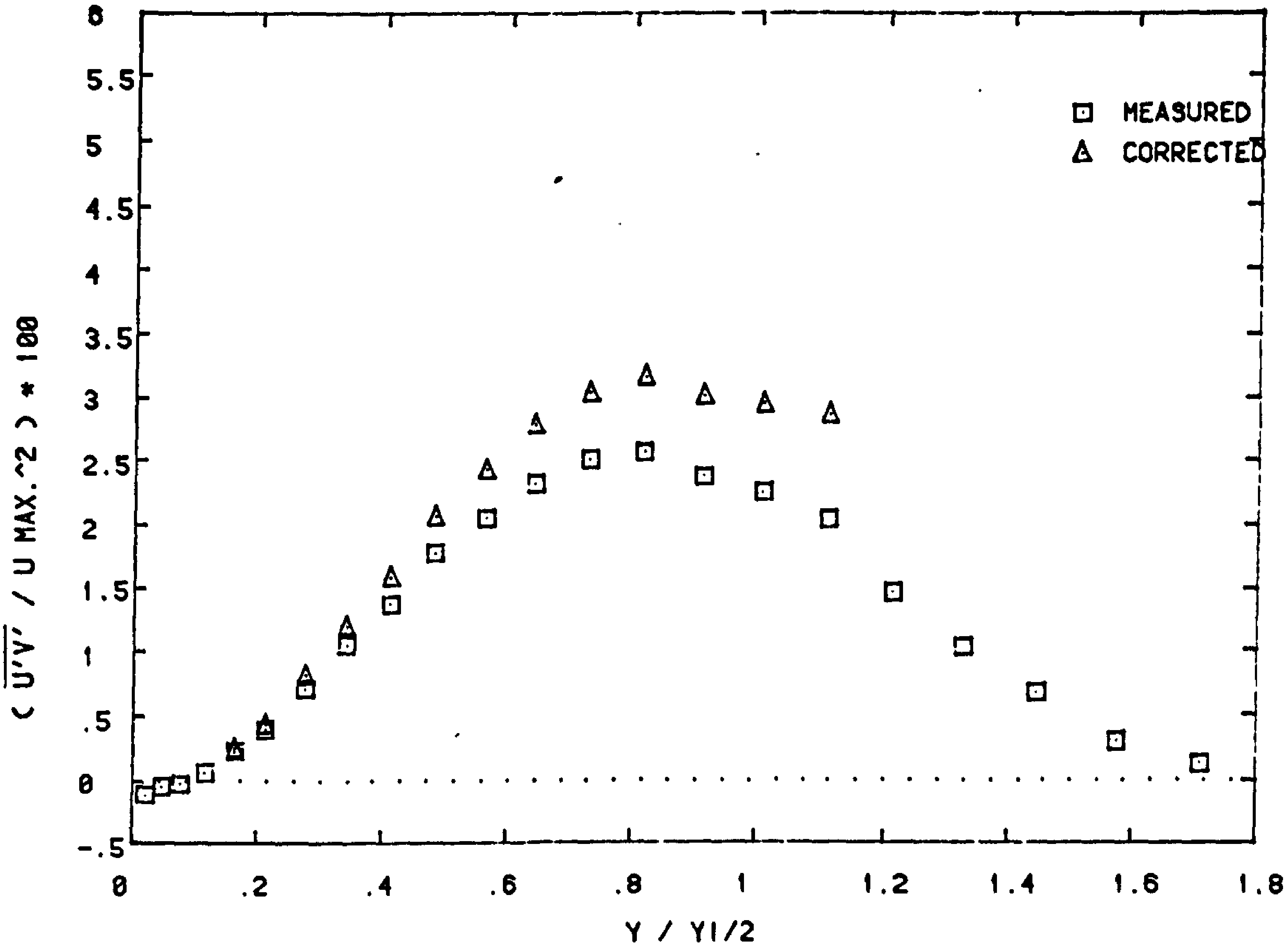

FIG. 4-32(C) SHEAR STRESS $\overline{U'V'}$ AND CORRECTED $\overline{U'V'}$ AT X=700

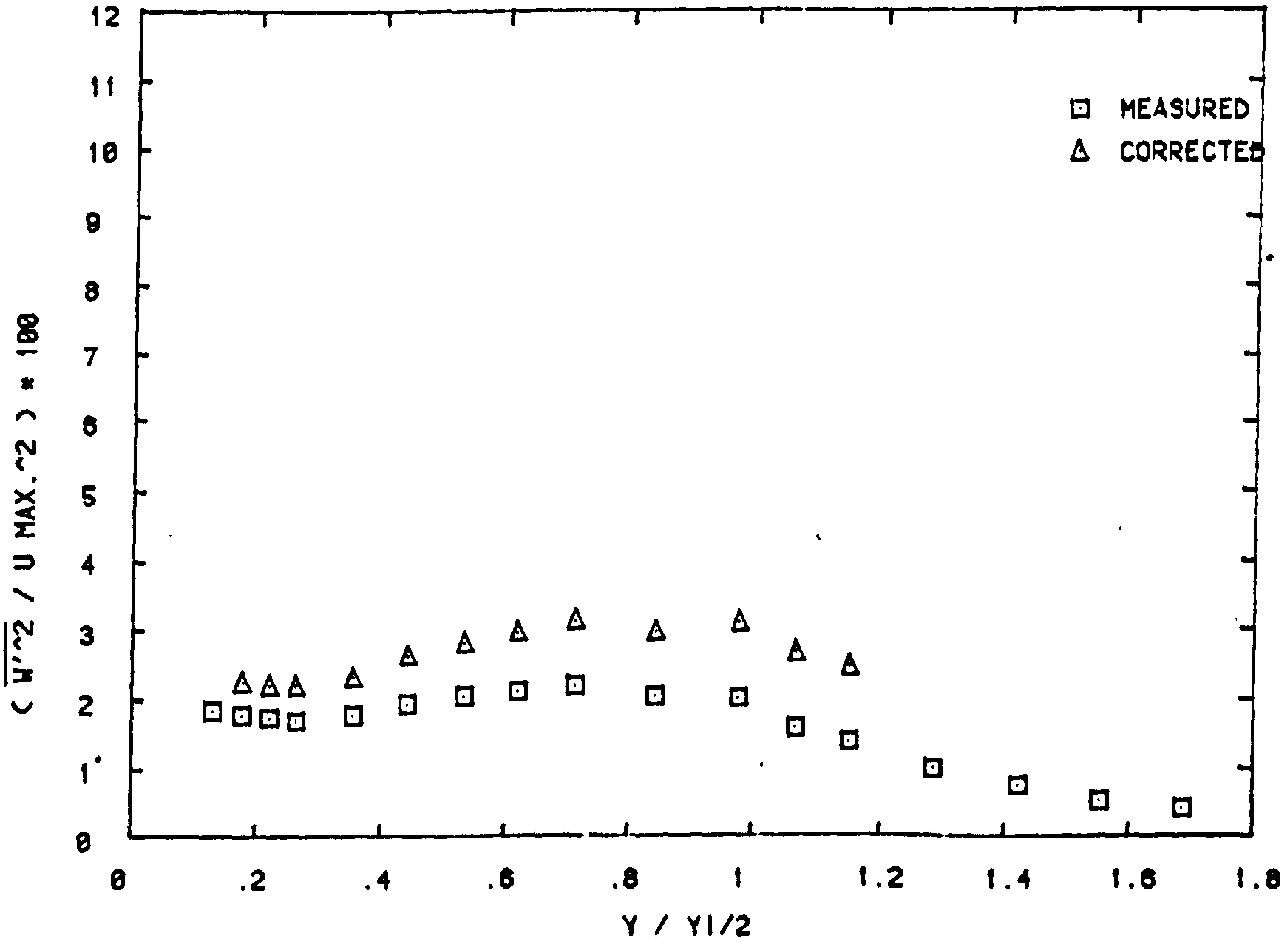

FIG. 4-33(A) TURBULENCE INTENSITY $\overline{W'^2}$ AND CORRECTED $\overline{W'^2}$ AT X=300

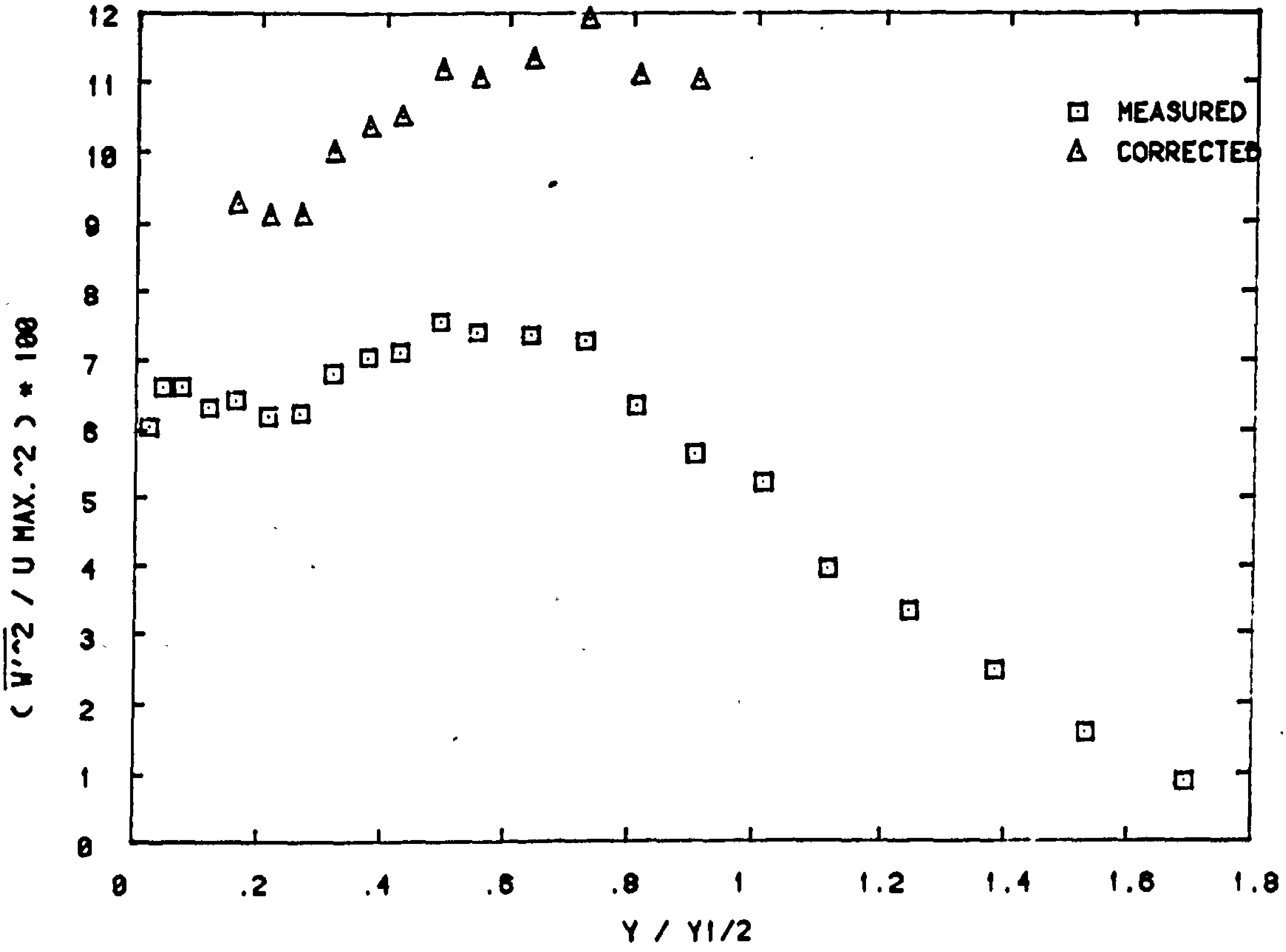

FIG. 4-33(B) TURBULENCE INTENSITY $\overline{W'^2}$ AND CORRECTED $\overline{W'^2}$ AT X=550

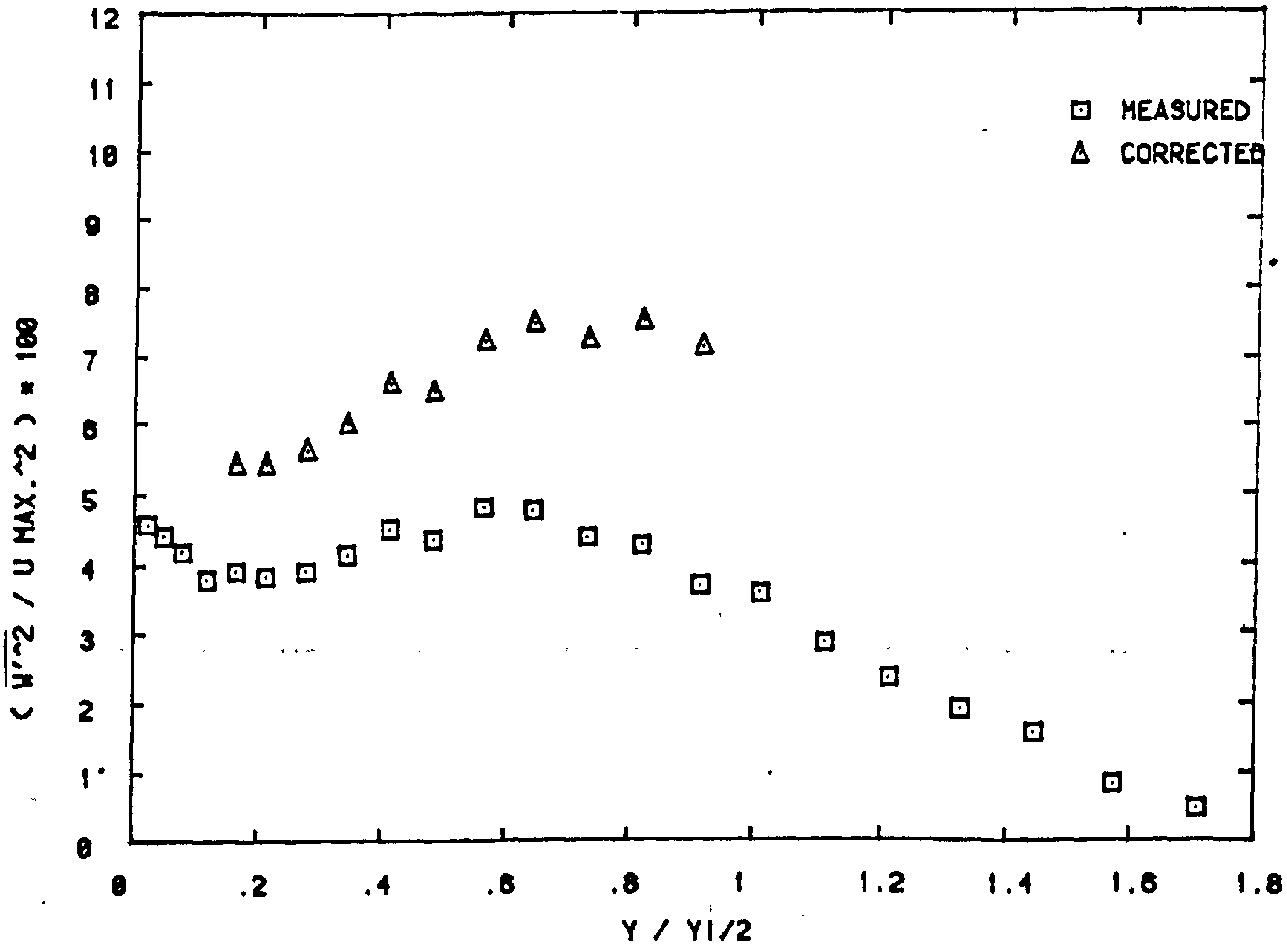

FIG. 4-33(C) TURBULENCE INTENSITY $\overline{W'^2}$ AND CORRECTED $\overline{W'^2}$ AT X=700

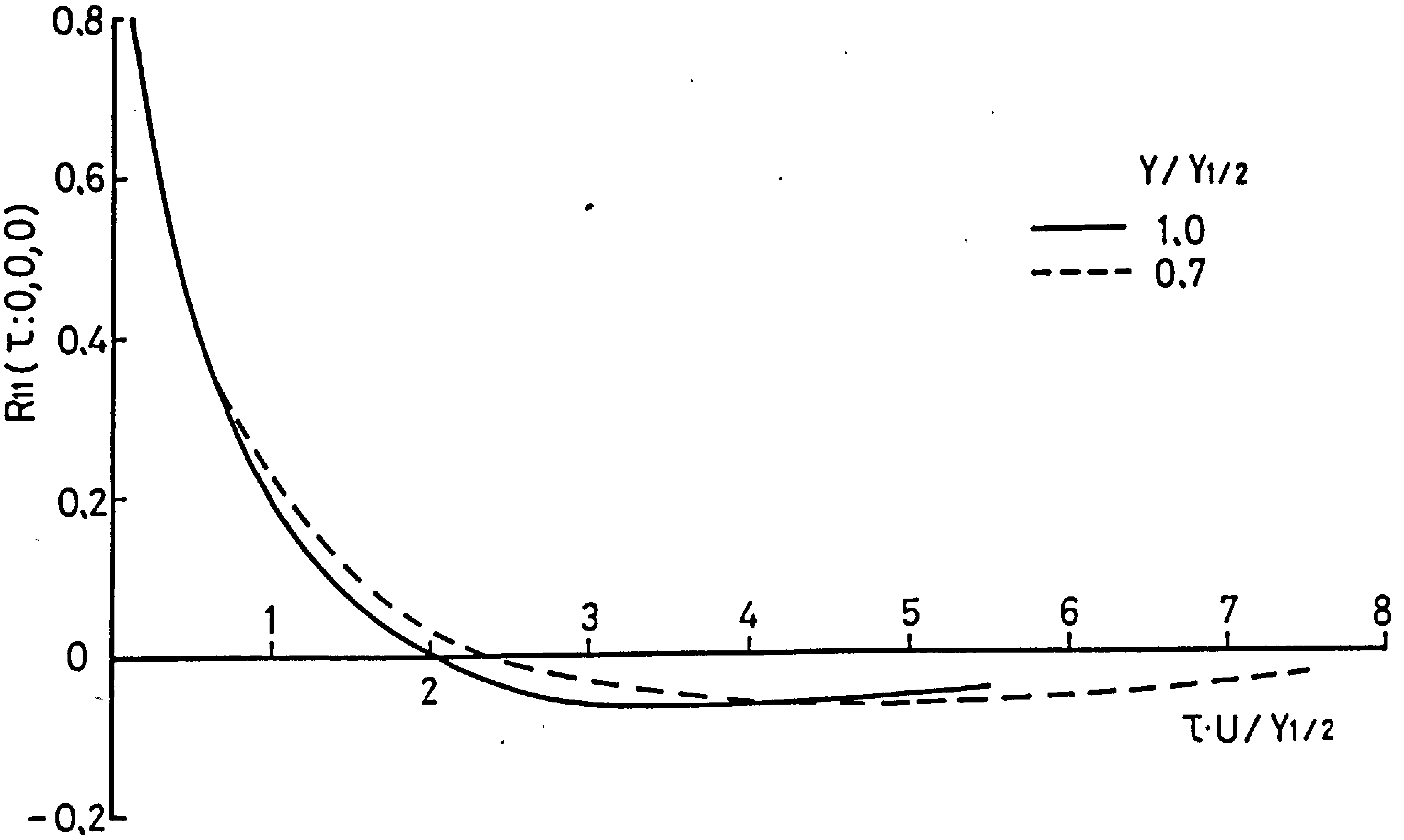

FIG. 4-34(A) $R_{11}(\tau:0,0,0)$ CORRELATIONS AT X=300mm

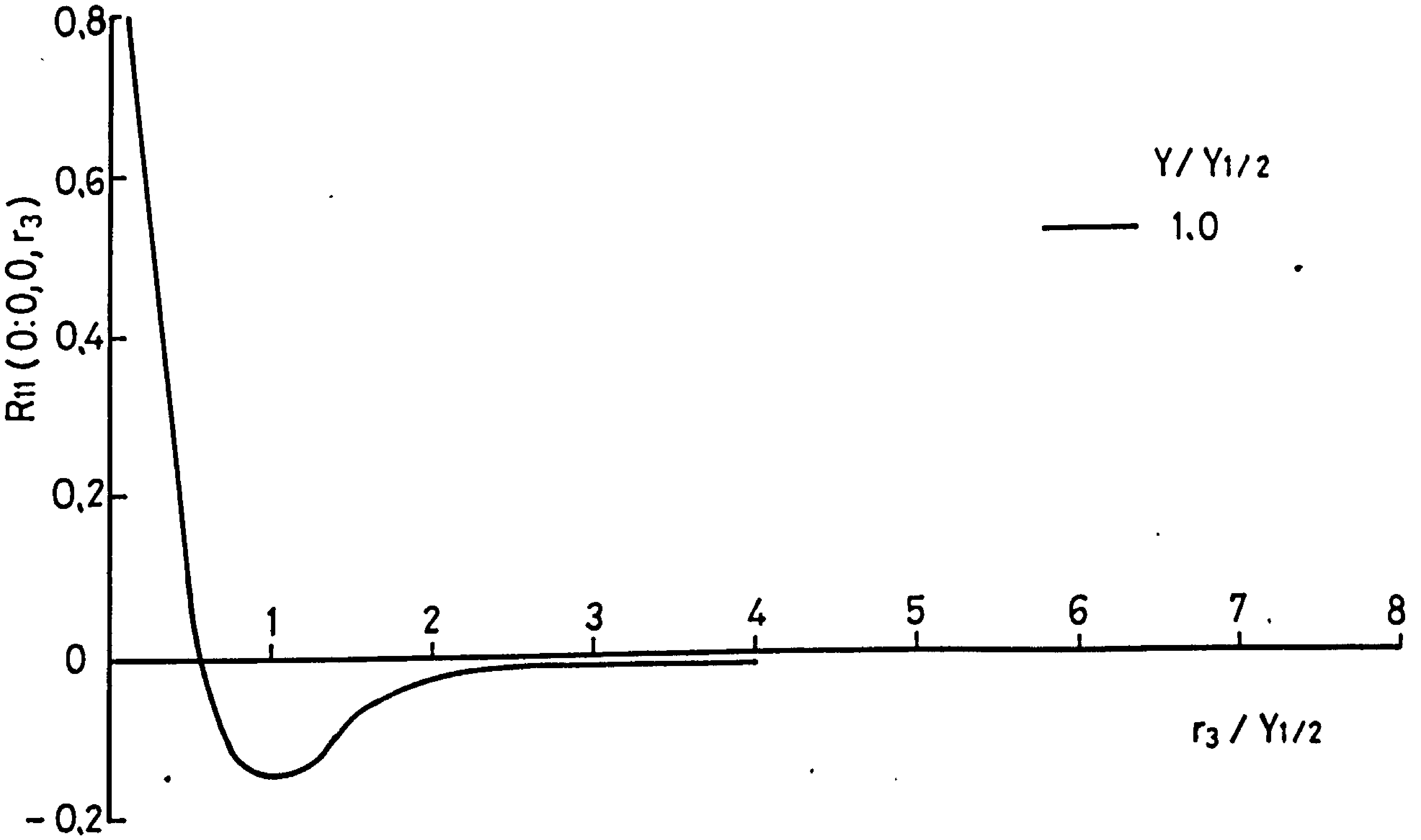

FIG. 4-34(B) $R_{11}(0:0,0,r_3)$ CORRELATION AT X=300mm

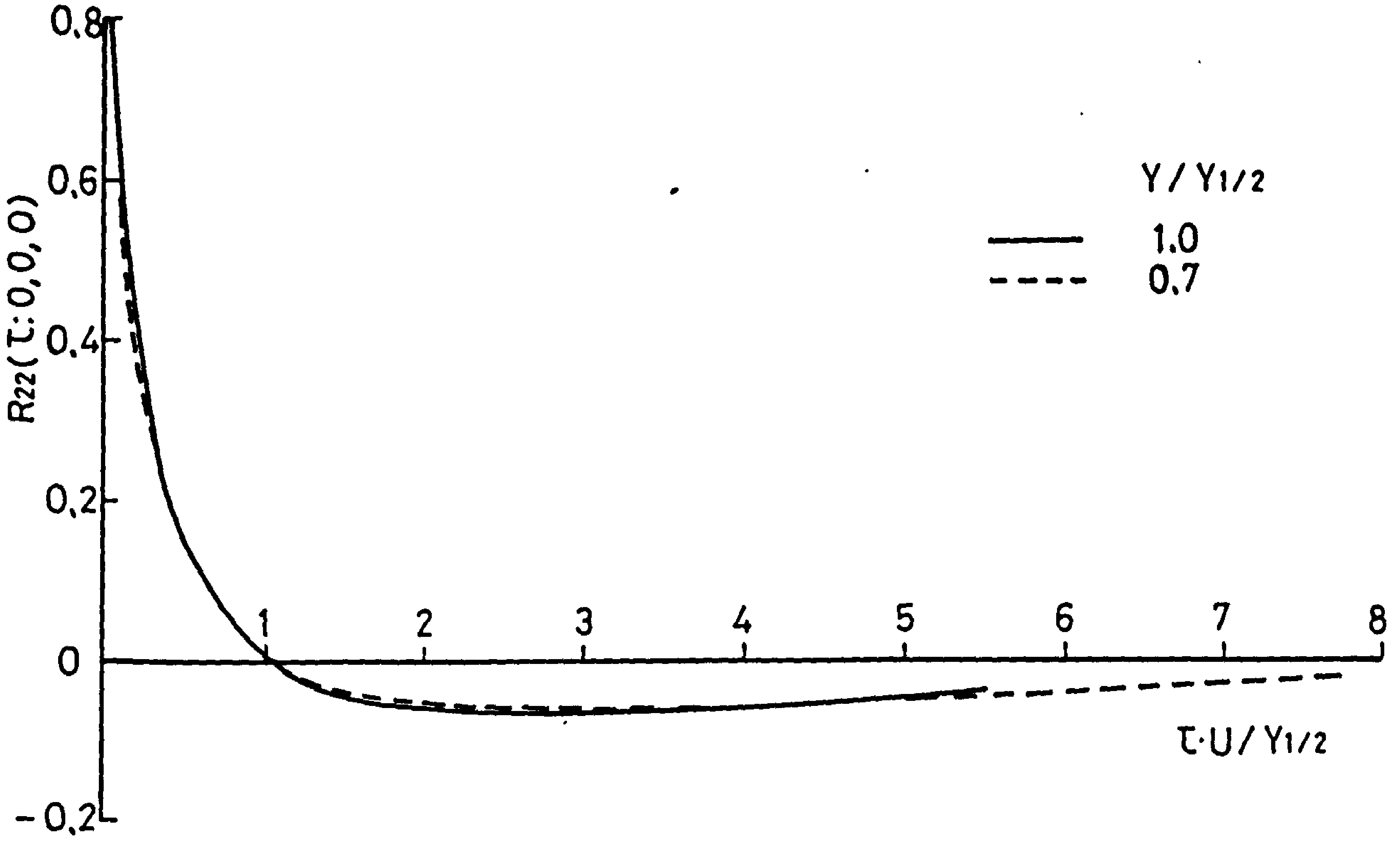

FIG. 4-34(C) $R_{22}(\tau:0,0,0)$ CORRELATIONS AT X=300mm

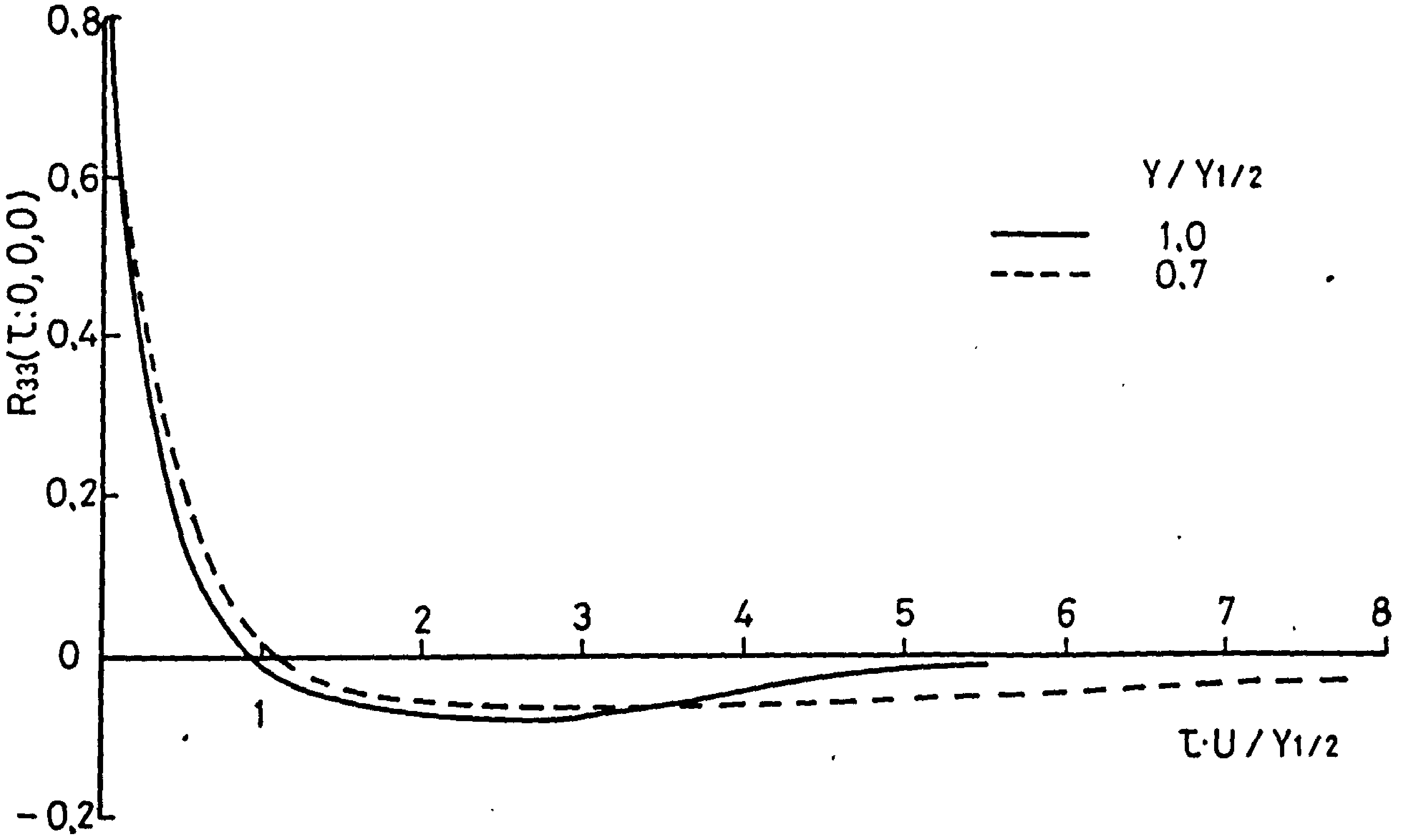

FIG. 4-34(D) $R_{33}(\tau:0,0,0)$ CORRELATIONS AT X=300mm

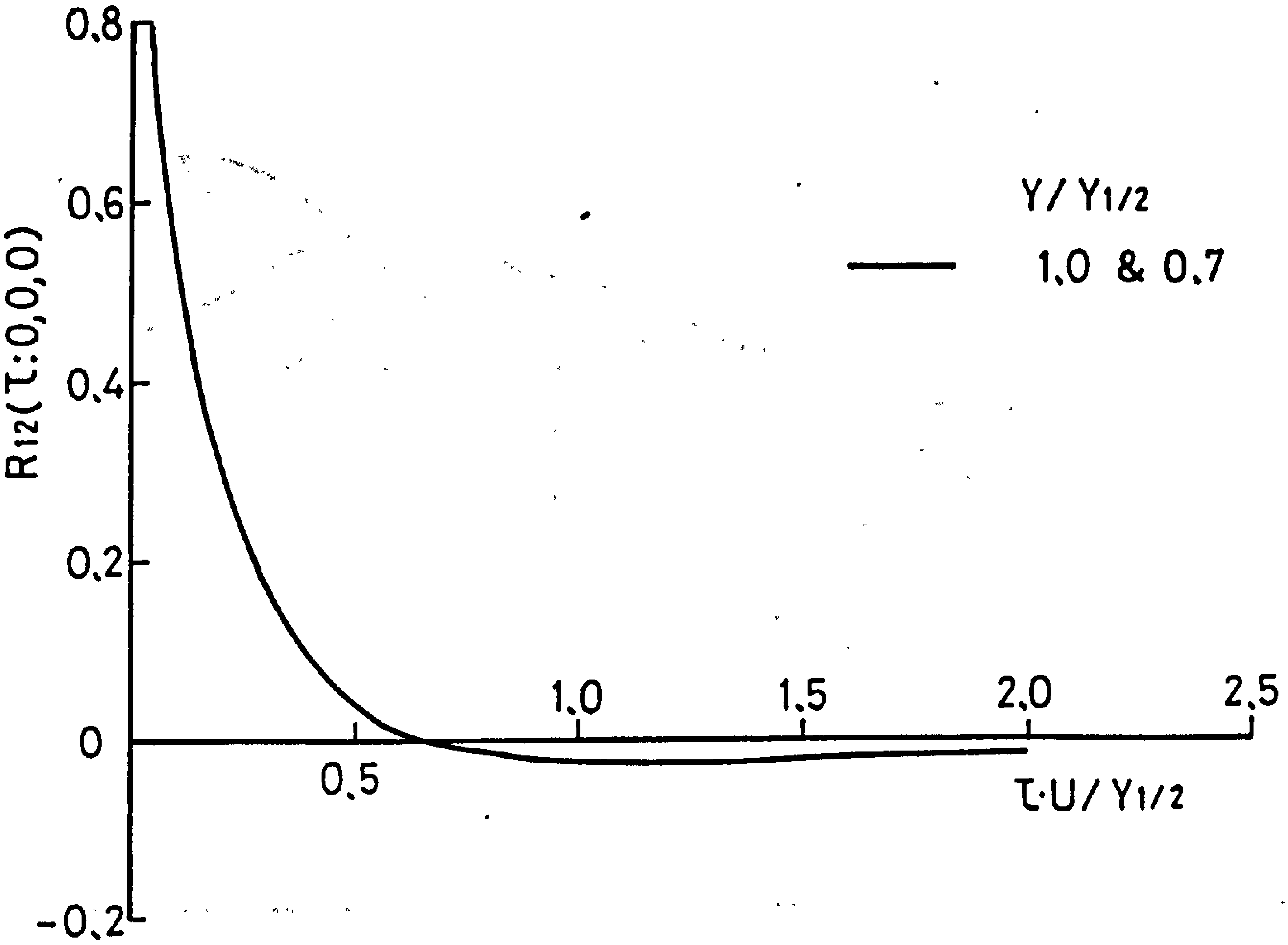

FIG. 4-35(A) $R_{12}(\tau{:}0,0,0)$ CORRELATIONS AT X=300mm

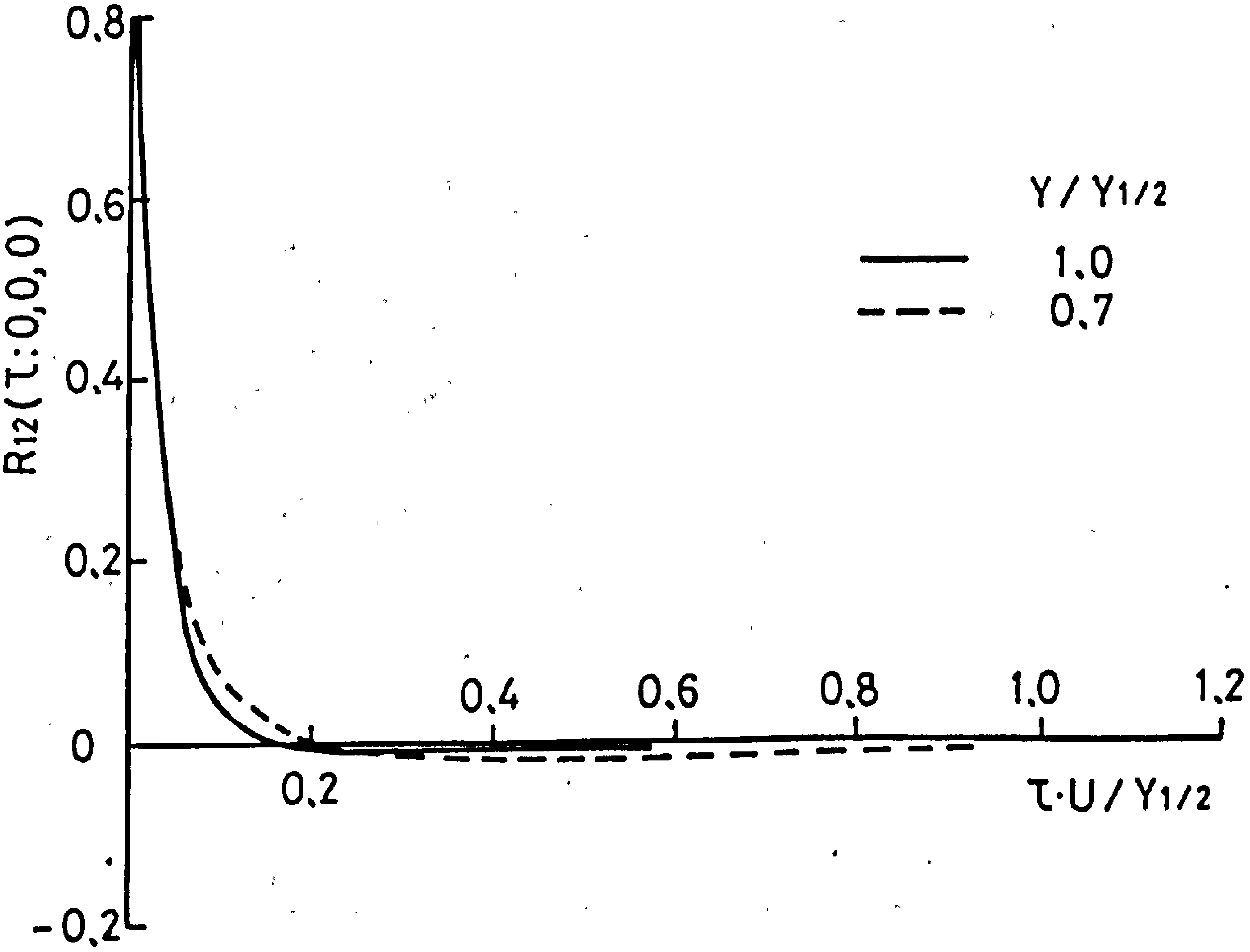

FIG. 4-35(B) $R_{12}(\tau{:}0,0,0)$ CORRELATIONS AT X=550mm

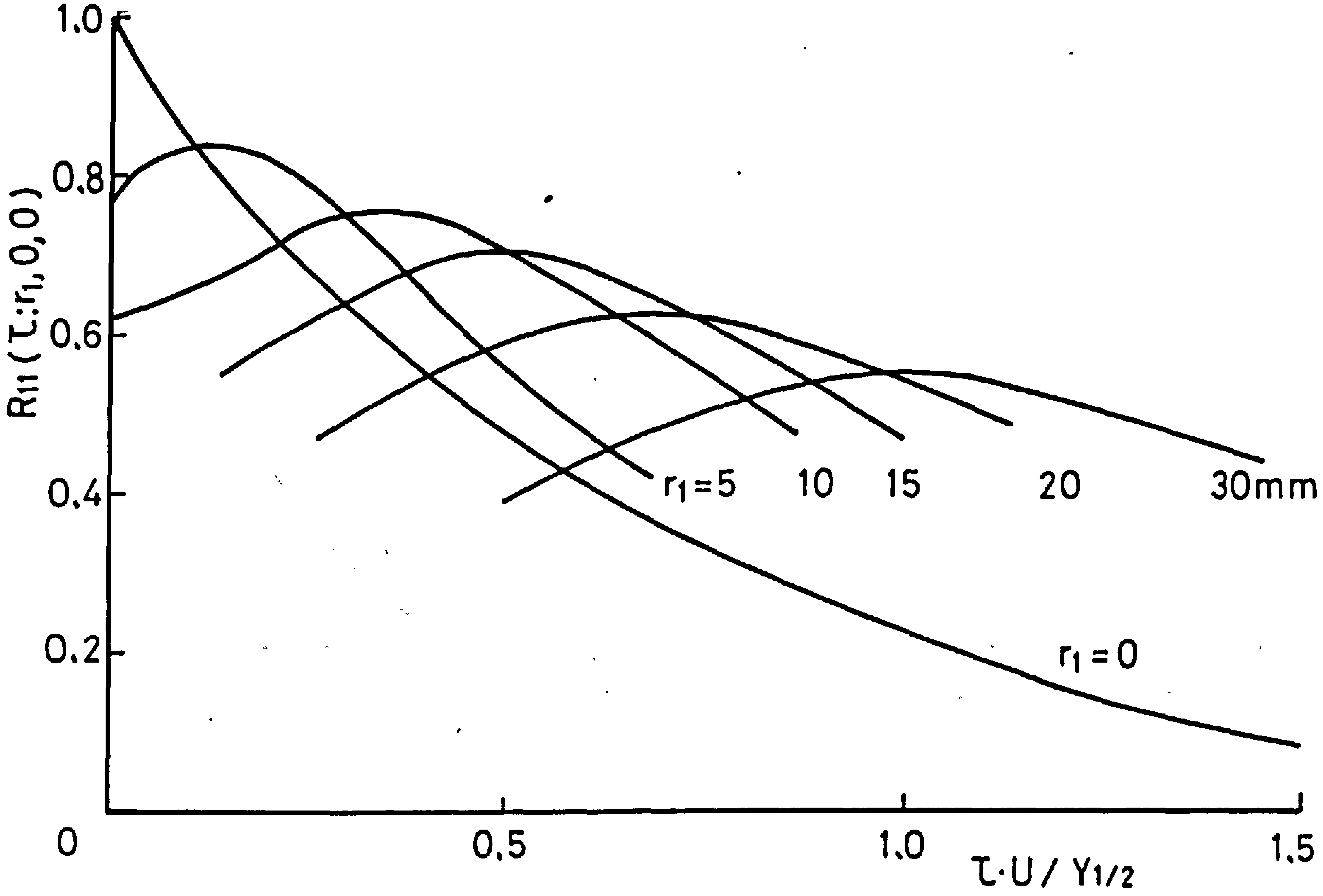

FIG. 4-36 SPACE-TIME CORRELATIONS AT X=300mm

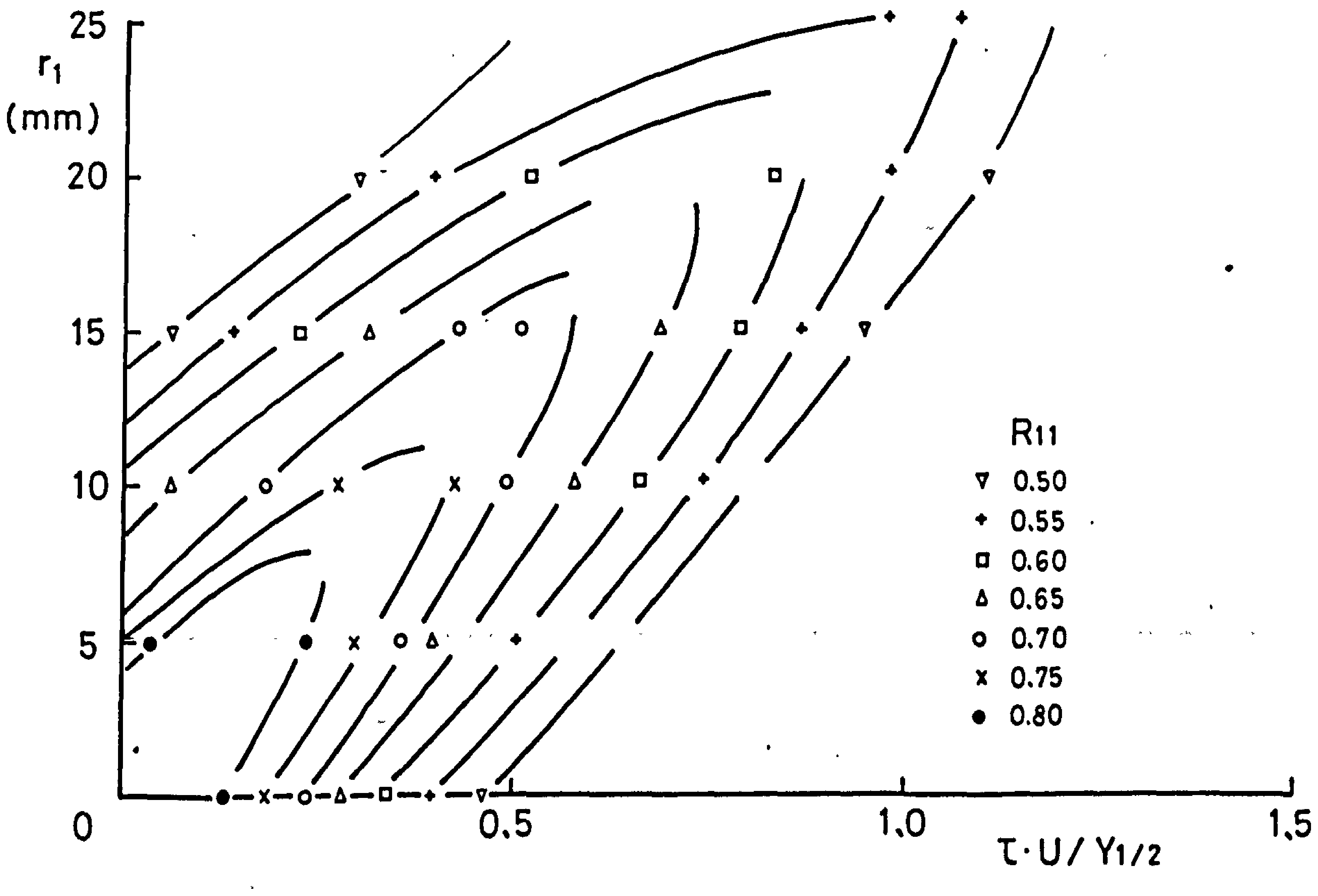

FIG. 4-37 ISO-CORRELATION CURVES AT X=300mm

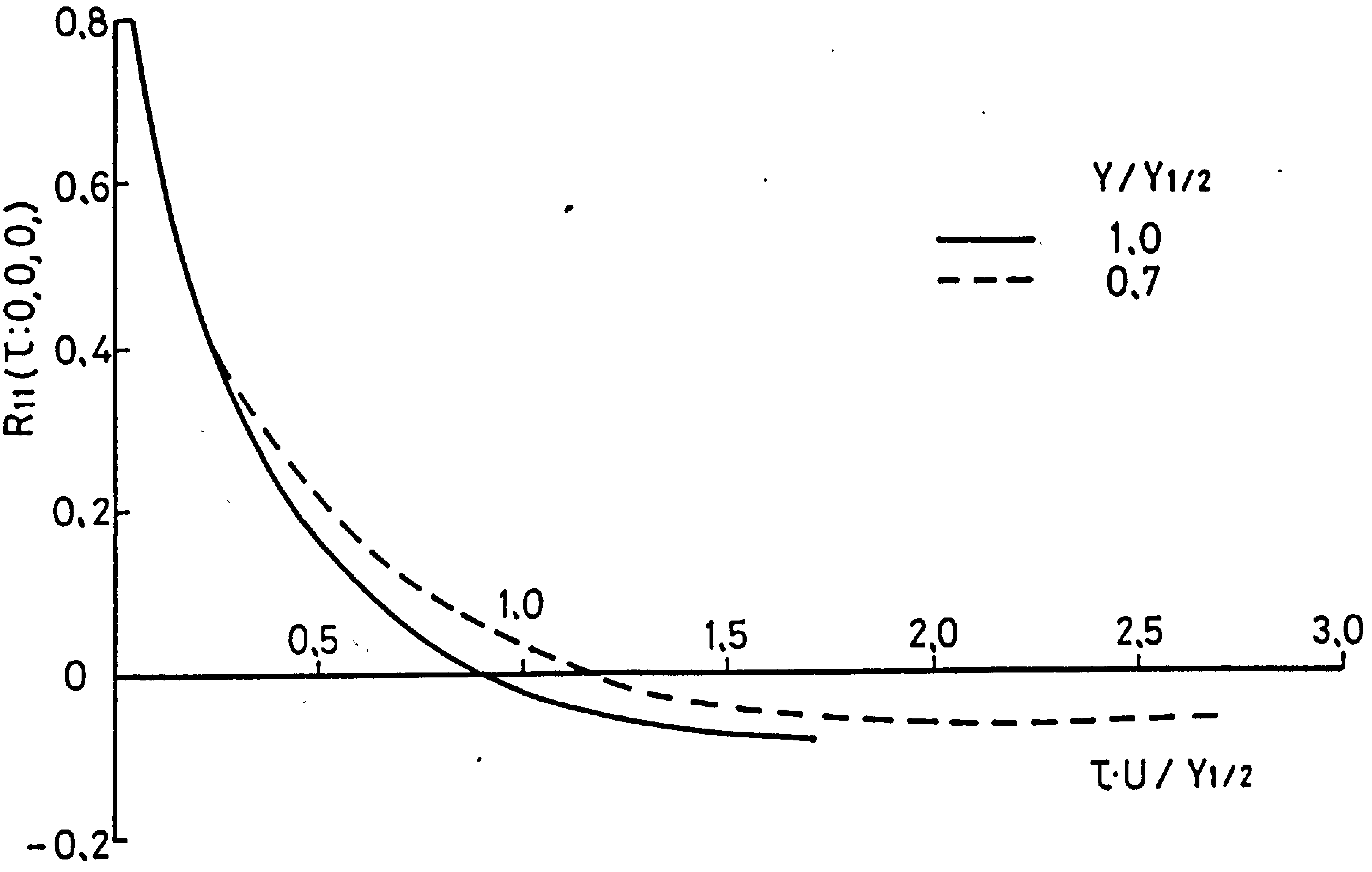

FIG. 4-38(A) $R_{11}(\tau:0,0,0)$ CORRELATIONS AT X=550mm

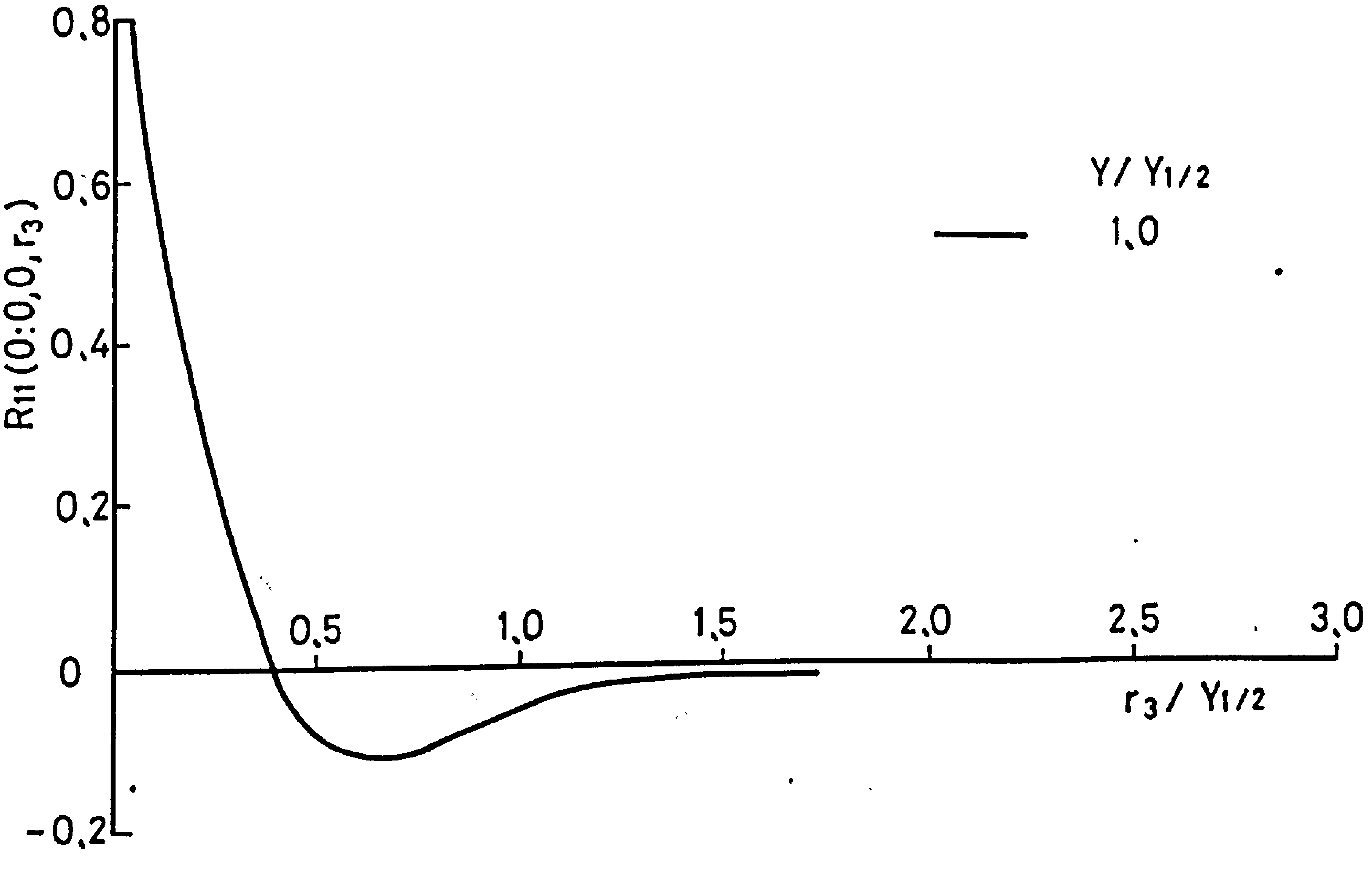

FIG. 4-38(B) $R_{11}(0:0,0,r_3)$ CORRELATION AT X=550mm

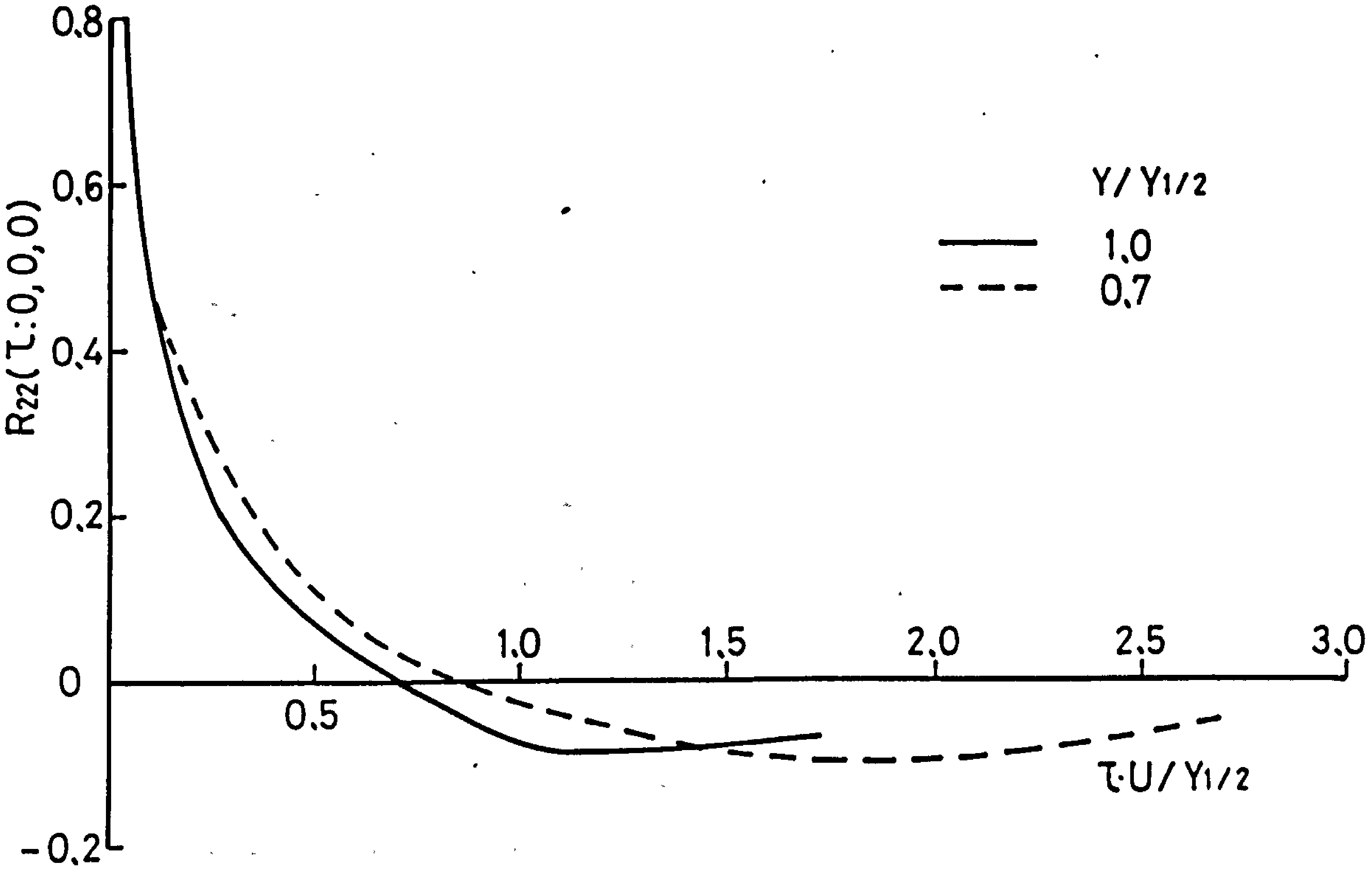

FIG. 4-38(C) R_{22}(τ:0,0,0) CORRELATIONS AT X=550mm

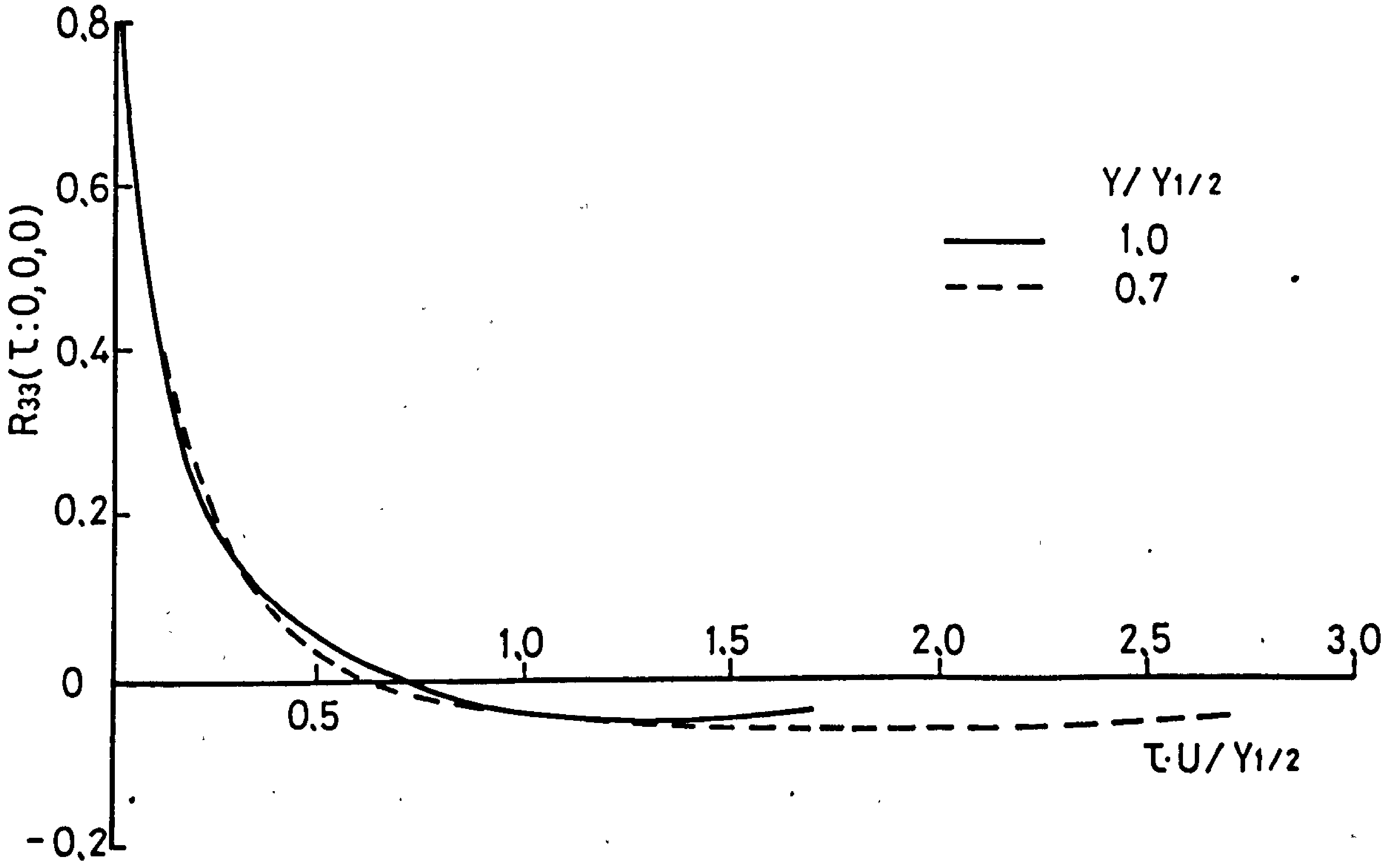

FIG. 4-38(D) R_{33}(τ:0,0,0) CORRELATIONS AT X=550mm

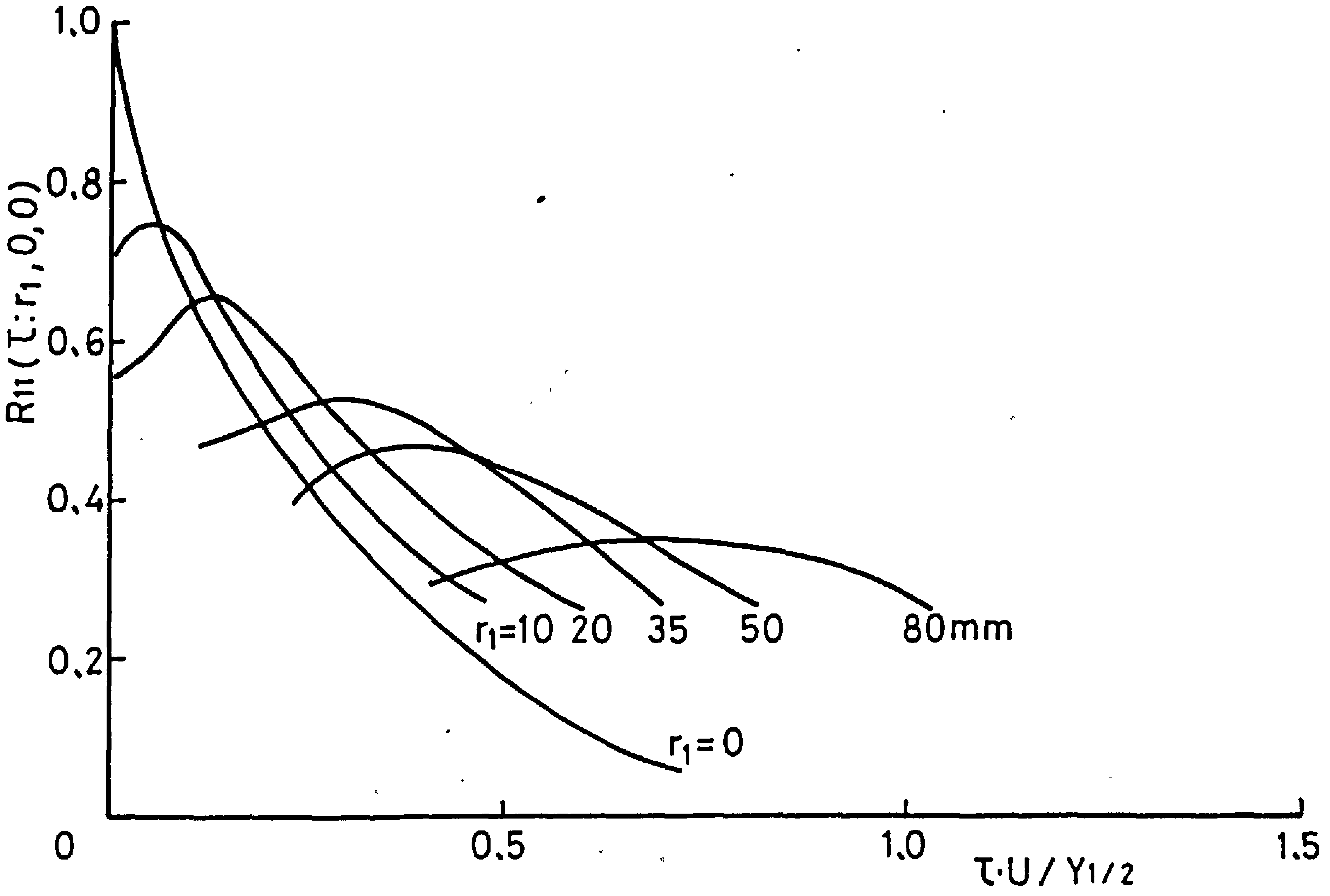

FIG. 4-39 SPACE-TIME CORRELATIONS AT X=550mm

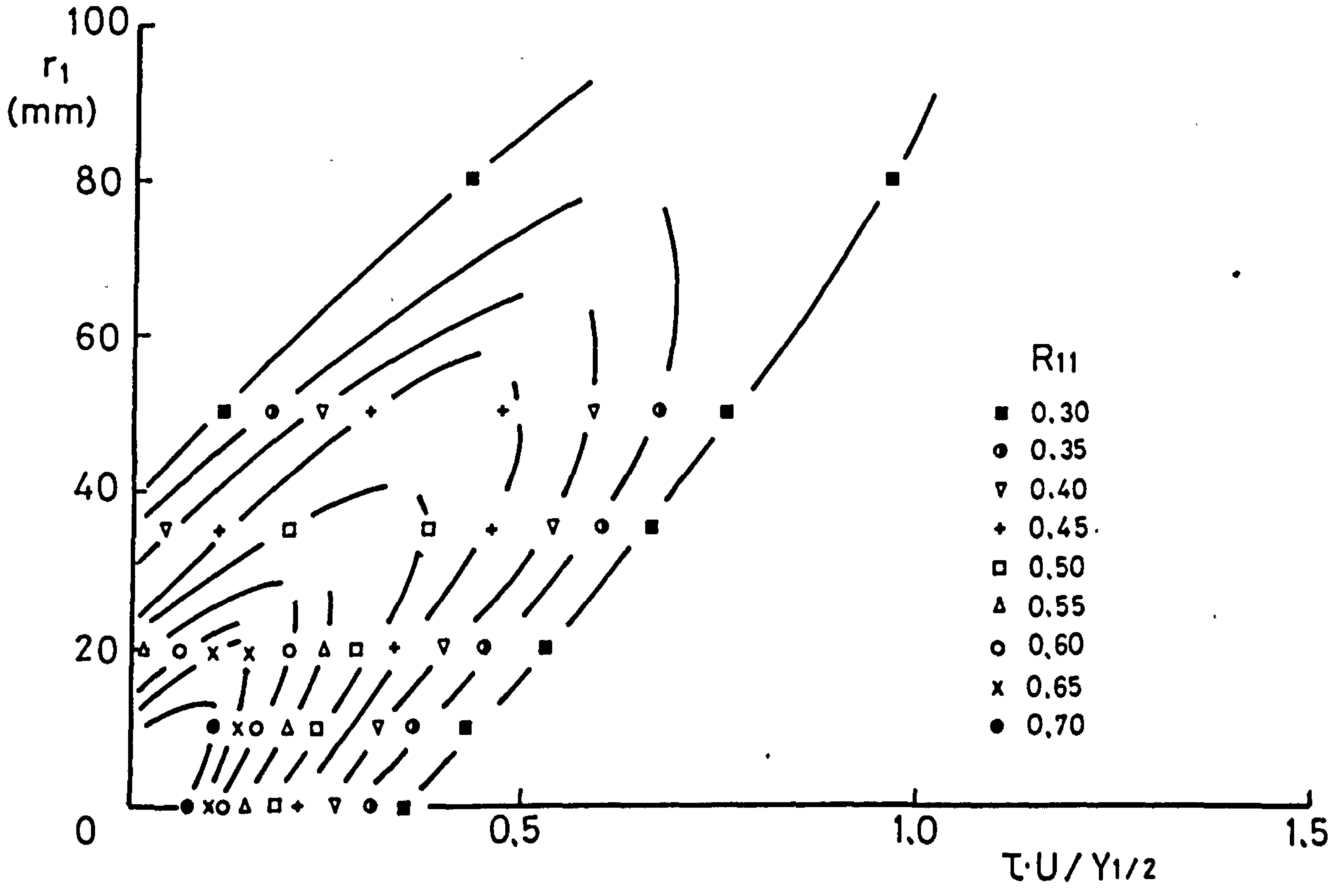

FIG. 4-40 ISO-CORRELATION CURVES AT X=550mm

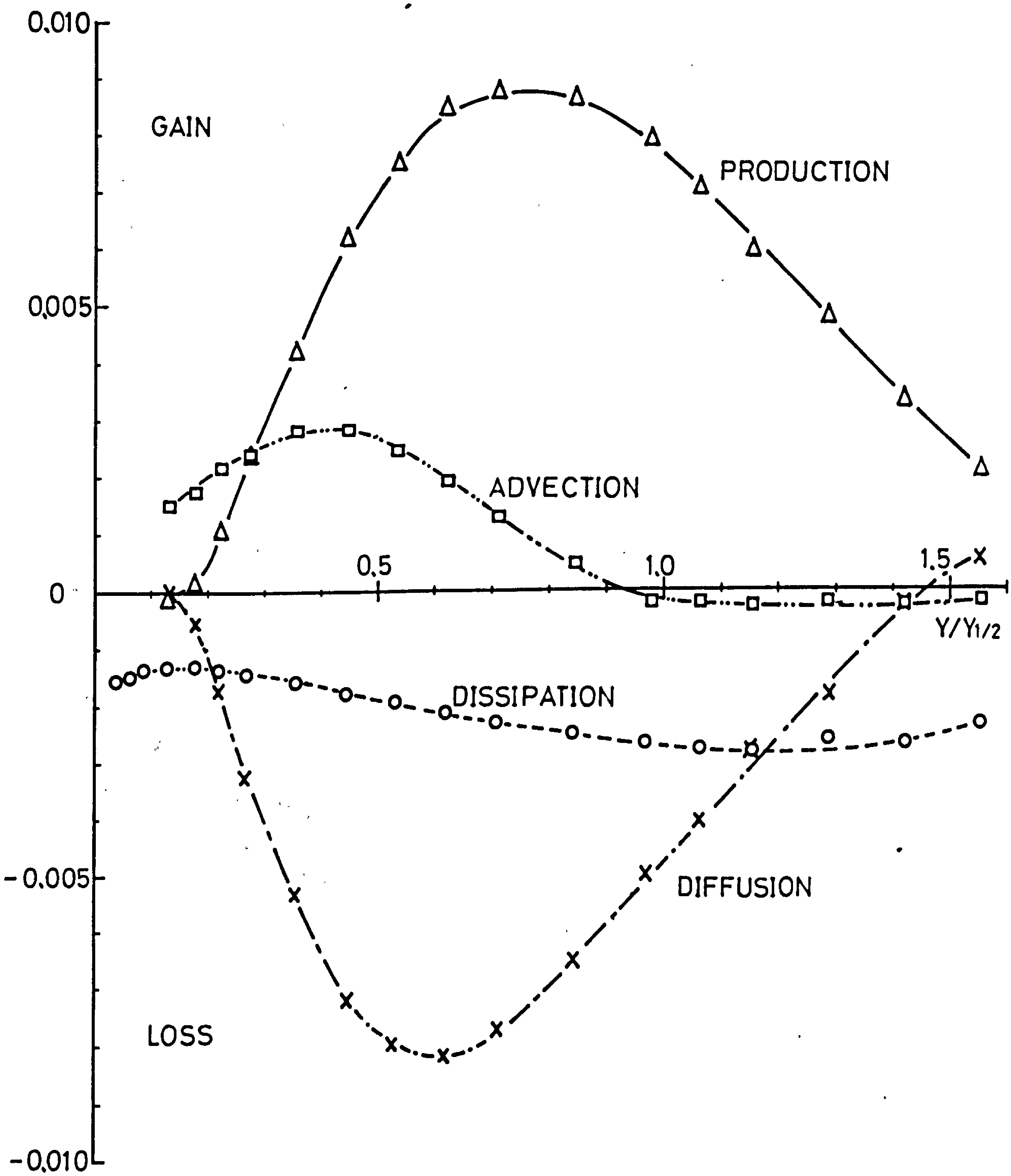

FIG. 4-41(A) TURBULENT KINETIC ENERGY BALANCE AT X=300mm

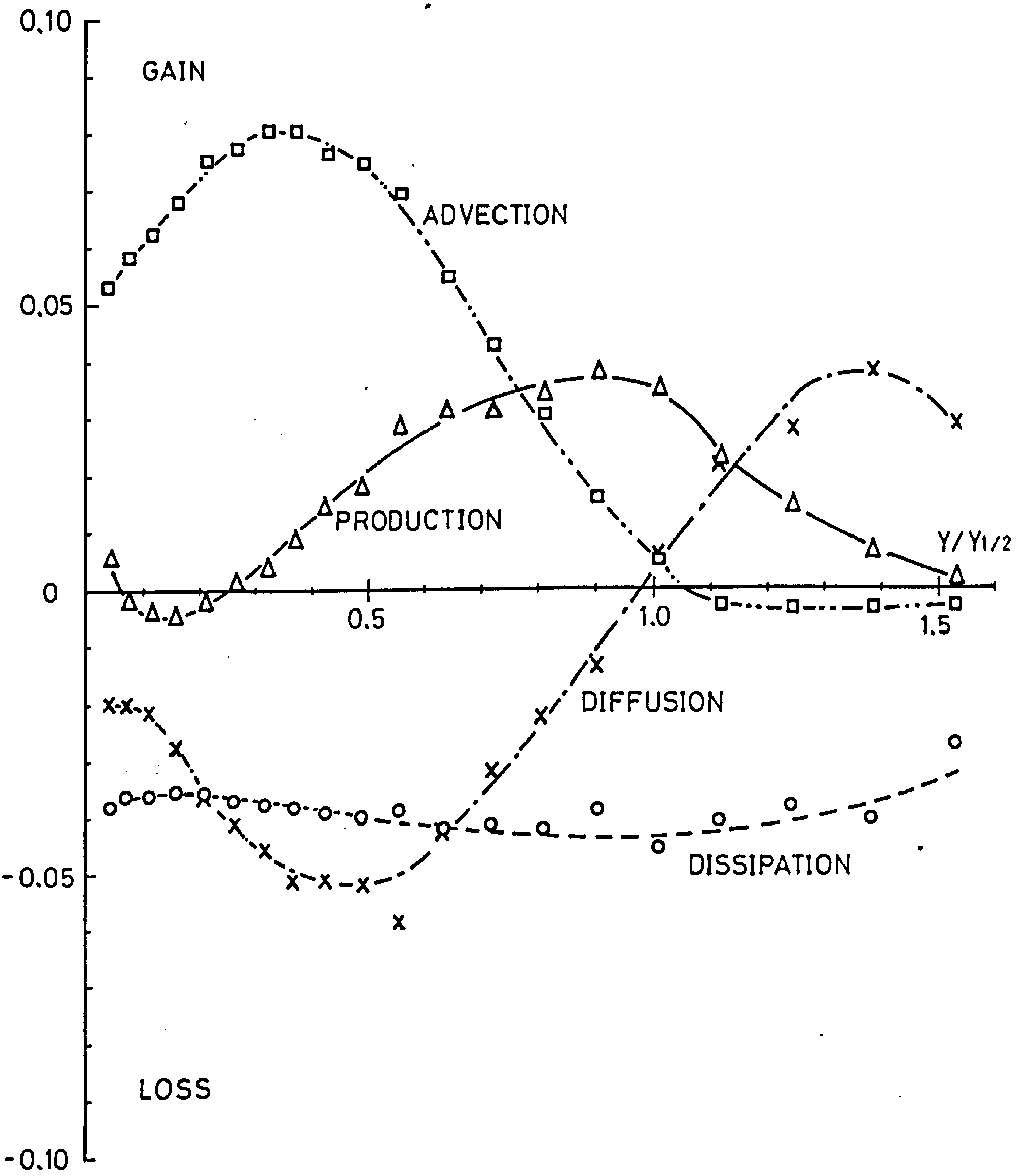

FIG. 4-41(B) TURBULENT KINETIC ENERGY BALANCE AT X=550mm

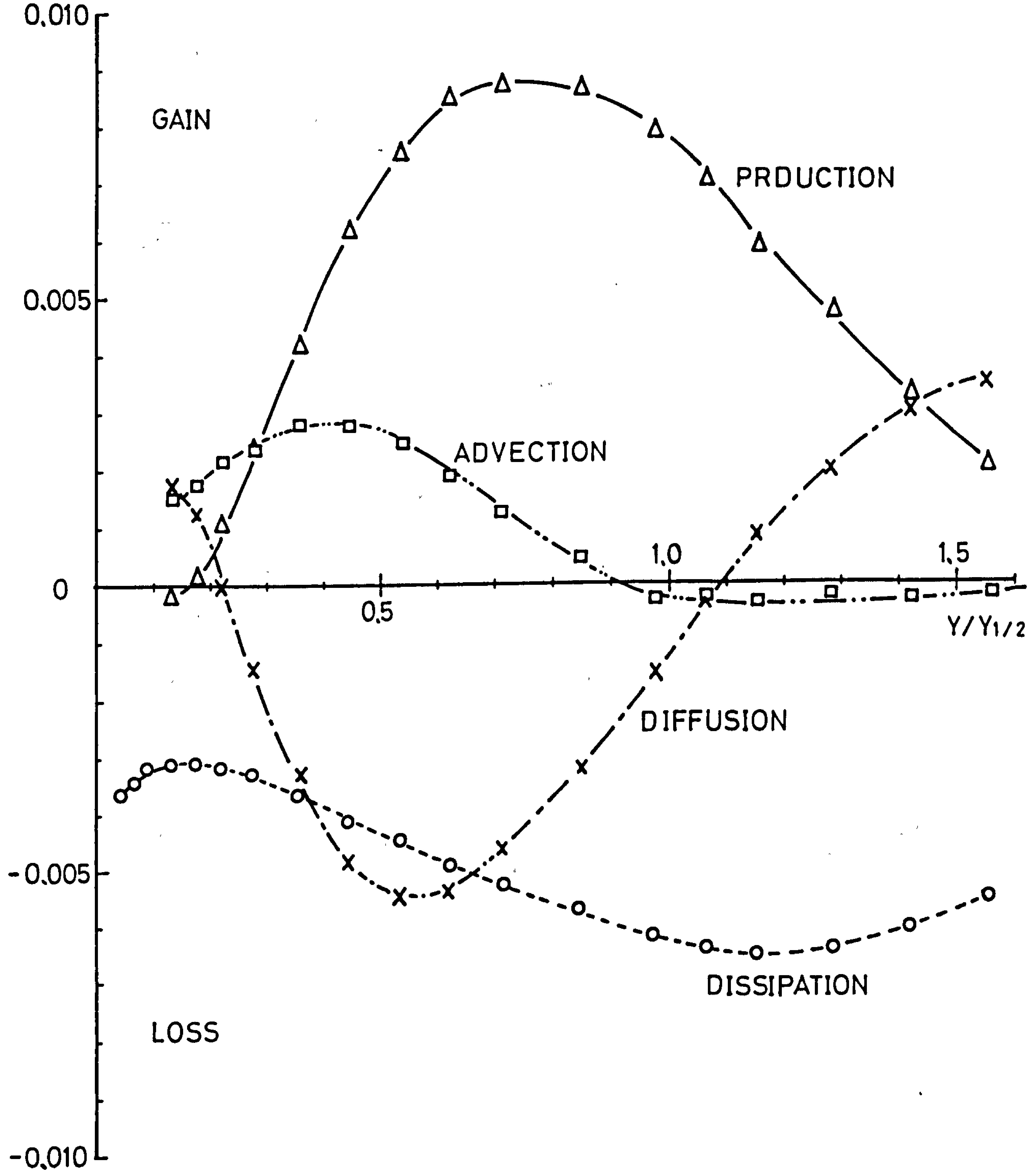

FIG. 4-42(A) CORRECTED TURBULENT KINETIC ENERGY BALANCE AT X=300mm

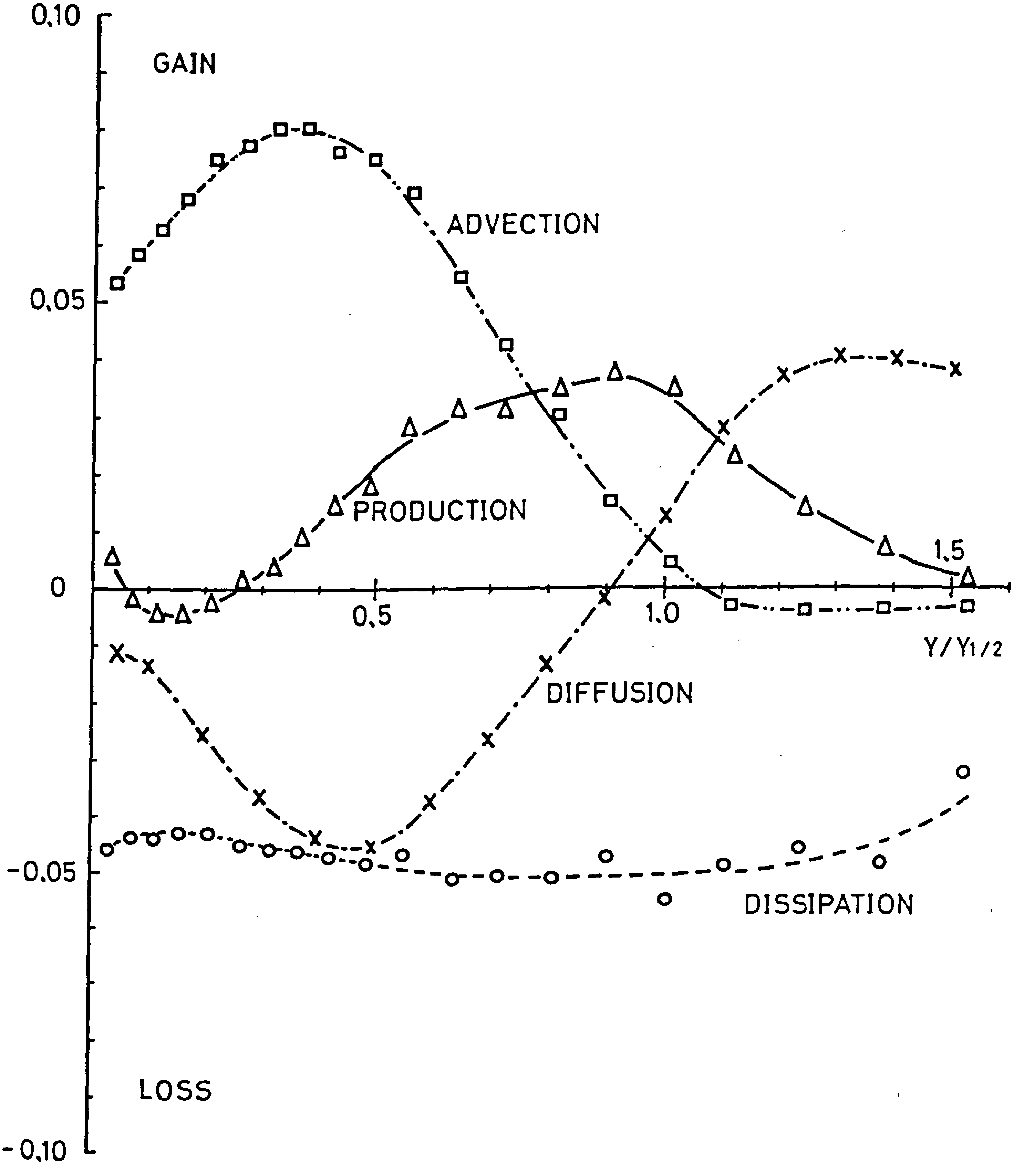

FIG. 4-42(B) CORRECTED TURBULENT KINETIC ENERGY BALANCE AT X=550mm

			X = 300mm					X = 550mm				
		$Y/Y_{\frac{1}{2}}$	$R_{11}(\tau)$	$R_{22}(\tau)$	$R_{33}(\tau)$	$R_{11}(r_3)$	$R_{12}(\tau)$	$R_{11}(\tau)$	$R_{22}(\tau)$	$R_{33}(\tau)$	$R_{11}(r_3)$	$R_{12}(\tau)$
$\tau.U/Y_{\frac{1}{2}}$ or $r/Y_{\frac{1}{2}}$	$R_{ij}=0$	1.0	2.10	1.00	1.00	0.55	0.60	0.90	0.75	0.68	0.40	0.18
		0.7	2.60	1.00	1.10	-	0.60	1.15	0.60	0.62	-	0.17
	$R_{ij}=\min$	1.0	3.5	3.0	2.5	1.0	1.4	2.0*	1.2	1.2	0.65	0.3*
		0.7	4.5	3.0	3.5	-	1.4	3.0*	1.8*	1.7	-	0.5*
$L=\int_0^\infty R_{ij}dr$	L (mm)	1.0	8.68	0	0.62	2.0	2.17	12.9	7.48	8.16	8.0	2.72
		0.7	7.85	-0.87	-0.87	-	2.18	15.4	3.71	2.12	-	2.12
	$L/Y_{\frac{1}{2}}$	1.0	0.386	0	0.028	0.089	0.096	0.137	0.080	0.087	0.085	0.028
		0.7	0.349	-0.039	-0.039	-	0.097	0.164	0.039	0.023	-	0.023
$R_{ij}=a\,e^{-r/L}-b$ or $R_{ij}=a(1-\frac{1}{2}\frac{r}{L})\,e^{-r/L}-b$	L	1.0	26.5	15.4	16.6	6.8	7.00	65.1	55.3	41.9	21.5	6.8
		0.7	30.5	15.3	17.3	-	7.00	71.7	34.7	42.5	-	10.2
	a	1.0	0.88	0.70	0.66	2.44	0.92	0.82	0.61	0.56	1.35	0.60
		0.7	0.84	0.65	0.68	-	0.92	0.72	0.66	0.56	-	0.48
	b	1.0	0.02	0.04	0.05	0.02	0.01	0.08	0.07	0.03	0.03	0
		0.7	0.02	0.04	0.04	-	0.01	0.04	0.03	0.04	-	0.01

*Points not clear

TABLE 4-1 Approximation of Correlations

CHAPTER 5

NUMERICAL COMPUTATIONS

CHAPTER 5 NUMERICAL COMPUTATION

5-1 Introduction

There have been a number of attempts to calculate wall jets. Glauert (1956) made a first theoretical analysis on wall jets and Newman (1961) made some theoretical approaches on curved wall jets. Sawyer (1962) and Guitton (1964) used integral methods to calculate wall jets and compared with their measurements. In these methods, either the eddy viscosity or the mixing length is adjusted to account for the curvature effect. Their results are generally in good agreement. More recently, differential methods have been applied to these flows since fast digital computers have made possible to use these methods. Patankar and Spalding (1967) carried out wall jet calculations with Prandtl's mixing length theory. They successfully predicted the growth rate of a plane wall jet in stagnant surroundings. However the constants in their ramp function had to be substantially changed to different cases e.g. a radial wall jet. The limitations of this hypothesis led to more complicated modelling. Two equation models have been widely used recently to calculate various flows. The $K - \epsilon$ model was used by Jones and Launder (1972) and Launder and Spalding (1974). The k-kL model was also used by Rodi and Spalding (1970) and Ng (1971) to calculate wall jets. These methods produced the results in good agreement with measured ones in wider range of flows than the mixing length hypothesis. However, the use of the eddy viscosity concept has a fundamental disadvantage on calculations of wall jets. With this concept, the shear stress has to vanish at the point where the velocity is maximum or velocity gradient on Y-axis is zero. This is not the case in wall jets which the points of zero shear stress are closer to the wall than the points where the velocity is maximum.

The first use of the Reynolds stress equation model to a wall jet was made by Hanjalic and Launder (1972). Irwin (1974) and Gibson and Youmis (1981) calculated the Irwin's (1973) equilibrium wall jet with the same type of models. Rodi, Celik, Demuren, Scheuerer, Shirani, Leschziner and Rastogi (1981) used a similar model but used an algebraic stress model which the convection and the diffusion are approximated by the corresponding transport of kinetic energy. The model used by Gibson and Younis (1981) has been used to calculate wall jets on moderate curved surface. Rodi et al. (1981) used their method to compute the wall jets on logarithmic spiral surfaces. These highly complex models gave much better agreements with measured results than the results obtained by eddy viscosity concept. The summary of computation of turbulent wall jets has been given by Launder and Rodi (1983).

Although the mixing length formula gives satisfactory results for engineering purposes in a wide range of calculations, it fails to predict the flow in the conditions where the flows become complicated, such as near separation. Bradshaw, Ferriss and Atwell (1967) used a new method using a differential equation for the turbulent shear stress which is derived from the turbulent kinetic energy equation with some empirical functions. The method does not employ the eddy viscosity concept, so that, the shear stress does not need to vanish at the point where velocity is maximum. This model is similar to the exact turbulent stress equation model but simpler because of the assumption that the turbulent energy k is specified by the shear stress. The original method was intended for boundary layer computation. The method was extended to compute many types of flows including compressible adiabatic, compressible heat transfer, unsteady flow, three dimensional flow etc. The application of the method is described by Bradshaw and Ferriss (1972). This method however cannot accept the condition which shear stress goes less than zero. For example a duct flow has a shear stress profile which changes its sign. Bradshaw, Dean and McEligot (1973) successfully applied this method to a symmetrical duct flow computation. They calculated a pair of boundary layers on each wall which have separate shear stress profiles but have a common velocity profile using the same empirical input as for the boundary layer. The method is discussed later in this chapter. This interaction hypothesis was used to calculate mixing layers, wakes and free jets by Morel and Torda (1974). They assumed that the flow which has a point where velocity is maximum may be considered to consist of several interacting layers. The empirical functions they have used were the same definition as boundary layer calculation, however, are much different values.

The present computation is based on Bradshaw - Ferris - Atwell method using Bradshaw, Dean and McEligot's interaction approach. We call them Bradshaw's method and Bradshaw's interaction approach respectively for convenience. We also call Bradshaw's boundary layer calculation program as the B-L program. The original of the present computer program was developed by Morel (1972) at Imperial College of Science and Technology in London. He developed a computer program for mixing layer, wake and free jet calculation with Bradshaw's method using Bradshaw's interaction approach. The wall jet program was developed after the development of free jet program however never been completed. The program was also developed before the final B-L program so that there are a number of differences in numerical procedures. Professor P. Bradshaw of Imperial College of Science and Technology has sent us Morel's wall jet program as well as the B-L program. The present computer program is based on both programs. The differences in both programs, limited information about the wall jet program and the incompleted wall jet program have made it necessary to carry out major modifications of the wall jet program. The details of Bradshaw's method and the B-L program are well documented by Bradshaw, Ferris and Atwell (1966, 1967). Ferris and Bradshaw (1966) and Bradshaw and Unsworth (1974). Also details of Bradshaw's interaction approach are given by Bradshaw, Dean and McEligot (1973) and the details for mixing layer, wake and jet calculation are given by Morel (1972) and Morel and Torda (1974). There is, however, no documentation for Morel's wall jet program.

5-2 Theory and Numerical Method

5-2-1 Equations

The present method has been developed for the boundary-layer calculation; therefore the equations are based on the boundary-layer approximation. The momentum equation for two-dimensional boundary-layers is

$$U \frac{\partial U}{\partial x} + V \frac{\partial U}{\partial Y} = - \frac{1}{\rho} \frac{dP}{dx} + \frac{\partial \tau}{\partial Y} \qquad (5\text{-}1)$$

where $\tau = -\rho \overline{u'v'}$.

The equation for continuity for incompressible flow is

$$\frac{\partial U}{\partial x} + \frac{\partial V}{\partial Y} = 0 \qquad (5\text{-}2)$$

It is commonly known that the shear stress τ in equation 5-1 makes the equations incomplete without further information - this is known as the closure problem. The present method uses the equation for the turbulent shear stress which was derived from the Navier-Stokes equations to close the equations.

The turbulent kinetic energy equation for a two-dimensional boundary layer is

$$\tfrac{1}{2}\rho\left(U\,\overline{\frac{\partial q^2}{\partial x}} + V\,\overline{\frac{\partial q^2}{\partial Y}}\right) - \tau\,\frac{\partial U}{\partial Y} + \frac{\partial}{\partial Y}\left(\overline{pv} + \tfrac{1}{2}\rho\,\overline{q^2 v}\right) + \rho\varepsilon = 0 \qquad (5\text{-}3)$$

where $q^2 = \overline{u'^2} + \overline{v'^2} + \overline{w'^2}$ and ε is viscous dissipation.
This is the equation for the rate of change of turbulent kinetic energy along a mean stream line. If we assume that the properties of turbulent energy at a given point X is specified by the shear stress profile, there are relations between the terms of equation 5-3 and the shear stress τ which can be simplified by introducing some empirical functions. The functions are

$$a_1 = \tau/\rho\,\overline{q^2} \qquad (5\text{-}4)$$

$$L = (\tau/\rho)^{3/2} / \varepsilon \qquad (5\text{-}5)$$

$$G = \left(\frac{\overline{pv'}}{\rho} + \tfrac{1}{2}\,\overline{q^2 v}\right) / \left(\frac{\tau_m}{\rho}\right)^{\frac{1}{2}} \frac{\tau}{\rho} \qquad (5\text{-}6)$$

where τ_m is the maximum stress at a given station X, a_1, L and G are functions of Y/δ. Here δ is the thickness of the layer. The definition of 5-4 shows that the shear stress is assumed to have a linear dependence on turbulent kinetic energy. The function L has the dimension of length and is similar to the dissipation length scale. However, L is not equal to the mixing length because in wall jets the terms of advection and diffusion in equation 5-3 are not negligible. The function G shows that the flux of diffusion of turbulent kinetic energy is assumed to be proportional to $(\overline{u'v'_m})^{\frac{1}{2}} \cdot \overline{u'v'}$. Then the equation for the turbulent transport becomes

$$U \frac{\partial}{\partial x} \left(\frac{\tau}{2a_1\rho}\right) + V \frac{\partial}{\partial Y} \left(\frac{\tau}{2a_1\rho}\right) - \frac{\tau}{\rho} \frac{\partial U}{\partial Y} + \left(\frac{\tau_m}{\rho}\right)^{\frac{1}{2}} \frac{\partial}{\partial Y} \left(G\frac{\tau}{\rho}\right) + \frac{(\tau/\rho)^{3/2}}{L} = 0 \tag{5-7}$$

Now the equations 5-1, 5-2 and 5-7 can be solved numerically for U, V and τ. The details of justifications of the assumptions and the method are given in Bradshaw's original paper (1967).

These equations are hyperbolic and therefore can be solved by the method of characteristics in which the partial differential equations are reduced to ordinary differential equations. The number of characteristic directions is the same as the number of equations. The angles γ between a characteristic and the X-axis are given by

$$\tan \gamma = \infty \tag{5-8}$$

$$\tan \gamma = \left[V + a_1 G \tau_m^{\frac{1}{2}} \pm (a_1^2 G^2 \tau_m + a_1 \tau)^{\frac{1}{2}}\right]/U \tag{5-9}$$

where we write τ for τ/p for simplicity and the same applies for the following descriptions.

The equation along the vertical characteristic is introduced by substituting equation 5-2 into equation 5-1

$$V \frac{dU}{dY} - U \frac{\partial V}{\partial Y} = U_e / \frac{dU_e}{dx} + \frac{d\tau}{dY} \qquad (5\text{-}10)$$

where U_e is the free stream velocity. The equation along the other two characteristics are

$$\tau \frac{dU}{ds} - \tfrac{1}{2}\left[G\tau_m^{\frac{1}{2}} \pm (G^2\tau_m + 2\tau/a_1)^{\frac{1}{2}} \right] \frac{d\tau}{ds}$$

$$= \frac{\tau}{U}\left\{ U_e \frac{dU_e}{dx} + a_1\left(\frac{\tau^{\frac{1}{2}}}{L} + \tau_m^{\frac{1}{2}} \frac{dG}{dY} \right)\left[G\tau_m^{\frac{1}{2}} \pm \left(G^2\tau_m + \frac{2\tau}{a_1}\right)^{\frac{1}{2}} \right]\right\} \frac{dx}{ds}$$

$$(5\text{-}11)$$

where s is measured along the characteristic and dx/ds is unity to the boundary layer approximation.

The method is based on the following approximations:

(1) The boundary layer approximation: e.g. there is no static pressure difference across the layer.

(2) Functions a_1, L and G change much more slowly than the change of τ and U in the streamwise direction so that they behave like coefficients rather than variables.

From the approximation (1) the equations are not valid for V > U. Also the angle of the ingoing characteristic at the outer edge of the layer can reach 90 deg. when V becomes large. Therefore the calculations for wall jets in stagnant surrounding or very small external stream can numerically fail at the edge where U = 0. The present calculation is intended for a wall jet in still air. However, the calculation with small external stream can represent the tendencies of wall jet in still air. It is possible to overcome the numerical difficulties with some special treatment at the edge. Nevertheless it is more practical to carry out the calculations with small external stream. The velocity of the external stream will be discussed in the later section.

5-2-2 Interaction approach

The method for calculating boundary layers cannot accept a change of sign in the shear stress distribution. This is another restriction for this method. However Bradshaw, Dean and McEligot (1973) successfully calculated interacting symmetrical flow in a duct. This is done by calculating two separate boundary layers on each wall having two separate shear stress profiles but with a common velocity profile. The shear stress of a duct flow changes its sign alternately so that the shear stress of one layer has an intermittency region. The width of this intermittent region is restricted by the negative energy production experienced by positively sheared fluid entering a region of negative velocity gradient. This property of the interaction makes the superposition of both shear stresses quite plausible. Thus the positively and negatively sheared regions can be at the same place but not at the same time. The only information given from one layer to another is through the mean velocity profile. The each 'simple' layer has the shear stress profile which does not change sign.

This interaction concept does not require the restriction that the shear stress has to vanish at the point where the velocity is maximum. This is an important advantage for wall jet computation because the points where the shear stress is zero do not coincide with the points where velocity is maximum.

This concept has also been successfully used for mixing layer, wake and free jet calculations by Morel and Torda (1974). They used the same interaction concept and demonstrated that this approach is a workable concept.

The shear stresses are obtained from two equations and then simply added together. The transport equation 5-9 becomes

$$U \frac{\partial}{\partial x}\left(\frac{\tau^+}{2a_1}\right) + V \frac{\partial}{\partial Y}\left(\frac{\tau^+}{2a_1}\right) - \tau^+ \frac{\partial U}{\partial Y} + |\tau_m^+|^{\frac{1}{2}} \frac{\partial}{\partial Y}(G\tau^+) - \frac{\tau^+|\tau^+|^{\frac{1}{2}}}{L} = 0 \tag{5-12}$$

$$U \frac{\partial}{\partial x}\left(\frac{\tau^-}{2a_1}\right) + V \frac{\partial}{\partial Y}\left(\frac{\tau^-}{2a_1}\right) - \tau^- \frac{\partial U}{\partial Y} + |\tau_m^-|^{\frac{1}{2}} \frac{\partial}{\partial Y}(G\tau^-) - \frac{\tau^-|\tau^-|^{\frac{1}{2}}}{L} = 0 \tag{5-13}$$

The momentum equation 5-1 becomes

$$U \frac{\partial U}{\partial x} + V \frac{\partial U}{\partial Y} = -\frac{1}{\rho}\frac{dp}{dx} + \frac{\partial \tau^-}{\partial Y} + \frac{\partial \tau^+}{\partial Y} \tag{5-14}$$

The present calculation is the combination of a boundary layer and a two-dimensional free jet. They will be regarded as Layer 1 and Layer 2 respectively. The interaction approach is the same method used by Bradshaw, et al (1973) and Morel and Torda (1974). The details of the method are given in their reports. The present calculations are concerned with two layers; however, according to this theory three or more layers can be calculated. For example, a wall jet or a blown boundary layer in adverse pressure gradient has points where the velocity is a maximum and a minimum. In this case three simple layers could represent the whole layer. However, the present calculation is a new attempt because all the previous computations with this interaction approach have been made with two layers of the same type so the present calculation is concerned with two layers.

5-2-3 Empirical functions

The values of the functions a_1, L and G are critical for the accuracy of the calculation method. These are fairly universal for boundary layer calculations. In fact, Bradshaw et al (1973) used exactly the same empirical functions for their calculation of duct flows as for boundary layers. The only difference was in the definition of the thickness of the layer. The usual boundary layer thickness is defined as the distance from the wall to the point where $U/U_e = 0.995$. They introduced a new length scale for the duct flow which is the distance from the wall to the point where $\tau/\tau_m = 0.05$. It is more consistent for a complicated layer and Morel and Torda (1974) followed this procedure. The empirical functions for the boundary layer were obtained from the experimental kinetic energy balances and the shear stress profiles. Then the functions were adjusted to give the best agreement of mean flow predictions with experiment. In the present calculations these values were used for Layer 1 computations. Although it is possible to alter these functions the values used for Layer 1 were not changed because the change of values of the functions for Layer 2 is much more effective than for Layer 1 since Layer 2 is much thicker than Layer 1.

The functions are defined to be

$$a_1 = 0.15$$

$$L/\delta_1 = f_1(Y/\delta_1)$$

$$G = (\tau_m/U_m^2)^{\frac{1}{2}} f_2(Y/\delta_1)$$

where δ_1 is the thickness of Layer 1.

The functions which were used by Morel and Torda (1974) for mixing layers, wakes and jets were not universal. The present calculation for Layer 2 is a free jet calculation so that only their free jet calculation values are concerned. They used the same definition for the functions as for a boundary layer. These are

$$a_1 = 0.15$$

$$L/\delta_2 = f_3(Y/\delta_2)$$

$$G = (\tau_m/U_m^2)^{\frac{1}{2}} f_4(Y/\delta_2)$$

They reported that the functions, particularly G, are dependent on the spreading ratio of the layer $d\delta_2/dX$. The spreading ratio for the present case, the growth rate of jet, is only 0.017. The growth rate of wall jets is much smaller than free jets because the presence of the wall restricts the spread of flow. Therefore function G for $d\delta_2/dX = 0$ was used for the calculation. The value of a_1 is not far from the experimental results when the data is not corrected for hot-wire's directional sensitivity. A constant value of a_1 is used throughout the calculation. The functions L and G which are calculated from the experimental kinetic energy balance are far from their functions used by Morel. The most notable difference is that the function L is not constant across the layer, as is assumed by Morel and Torda. They also used the function L which was calculated by a length scale equation. Both results were reported to be very close. The sensitivity of calculations to L is the most important, although G and a_1 are more important than is the case for a boundary layer.

Several types of profiles of the function L have been tested in the present calculations, including Morel and Torda's free jet profile. Morel and Torda also reported that the position where the function G = 0 was an important factor and they fixed this position with respect to the position of the shear stress maximum. Several tests have been made to find the effect of the various distances between the positions where G = 0 and the shear stress is maximum. The effects were found to be very small for the present case, so that the distance has been fixed at $0.09\delta_2$, which is the same as for the case of a free jet. Both functions G obtained from the experiment and Morel and Torda's have been tested.

There are two types of experimental results which have been discussed in the previous chapter. One is the data corrected to balance out the diffusion term across the layer and the other is not corrected. In the case of the function L both types of data were used to calculate function L. However in the case of the function G, the function calculated from the corrected kinetic energy balance is somewhat unrealistic so that this function has not been used. For the calculations which have been carried out with various functions L and G, all other conditions have been kept the same.

The functions which are calculated from experimental results are functions of $Y/Y_{\frac{1}{2}}$ rather than Y/δ_2. This is because the present calculations are made only for a plane wall jet in which the flow is self-preserving. Therefore it is best to fix these functions with respect to the normalized Y direction rather than the shear stress with δ_2. L and G functions are based on Y/δ_2 have also been tried but without success. These will be discussed later in this chapter.

The functions L and G which are calculated from the experimental kinetic energy balance and those used by Morel and Torda are shown in Fig. 5-1(A) and (B) respectively. In Fig. 5-1(A) the function L is calculated from the corrected and the function G is from the uncorrected kinetic energy balance.

5-2-4 Boundary conditions

The wall boundary conditions for Layer 1 are the same as Bradshaw et al (1967). The boundary conditions are $U = 0$, $V = 0$ and $\tau = \tau_w$. We assumed that the first mesh point in Layer 1 is calculated by the conditions at the wall and the shear stress gradient by the logarithmic law of the wall

$$\frac{U}{U_\tau} = \frac{1}{k}\left(\ln\frac{U_\tau Y}{\nu}\right) + B \qquad (5\text{-}14)$$

where k and B are constants. U_τ is the friction velocity. The first mesh point is the first mesh point outside the viscous sub-layer and satisfies $U_\tau Y/\nu > 40$ so that the logarithmic law of the wall should be valid. This requirement was not used by Bradshaw et al (1967) because they found this led to numerical instability and inaccuracy at low Reynolds numbers. In the case of the wall jet calculation, however, Layer 1 is thin compared with the thickness of the jet. If this condition is not satisfied, the first few points can be within the sub-layer. If the interval of mesh is large enough for the first mesh point to be outside of the sub-layer, the number of mesh points can be too few and lead to a large error. Therefore all the calculations have been made with this restriction. There are a number of reports concerned with the values of logarithmic law constants. The most common values are $k = 0.41$ and $B = 5.2$. These values have been used by Bradshaw et al (1967) for their boundary layer calculations with success. Some different values have been tested which will be discussed later.

The outer boundary conditions for Layer 1 are $U = U_m$ and $\tau = 0$, and these are easy to satisfy numerically. The inner boundary conditions for Layer 2 are not those of a free boundary if the layer extends into the first mesh point because of the existence of the surface. In this case further extension of the layer is stopped but the same conditions apply. The conditions are $U = 0$ and $\tau = 0$. The conditions for the outer edge of Layer 2 are $U = U_e$ and $\tau = 0$.

As has been discussed in the previous section, the present method cannot calculate jets in still air. In order to obtain results close to those for a wall jet in still air, the following outer stream velocity was chosen. A wall jet with an external stream can only be self-preserving when the ratio U_m/U_e is constant. U_e should be small enough compared with U_m to minimise the external stream effect. The boundary layer approximation, on the other hand, cannot accept a situation in which V is greater than U. Morel (1972) recommended that $U_e = 0.05U_m$. Tests have been carried out with $U_e = 0.05U_m$ and $U_e = 0.025U_m$. The difference was found to be negligible. Therefore, for the present calculations $U_e = 0.05U_m$ was chosen. U_e was calculated using the experimental results along the X direction.

5-2-5 Initial conditions

Two separate profiles of shear stress are required to start the calculation. The mean velocity profile is derived from the experimental results at X = 200mm. The outer edge of the profile is adjusted to satisfy the condition $U_e = 0.05U_m$. The choice for input profile of shear stress for the outer part of Layer 2 is also straight forward. The profile outside the point of maximum velocity is derived from the experimental results. The shear stress profile from the experimental data inside the maximum velocity point is changed to decay exponentially to zero at Y = 0. This is the input profile for Layer 2 which is called τ_2. The input profile for layer 1 is calculated from the experimental profile τ_{tot} and the profile for Layer 2 τ_2.

$$\tau_2 = \tau_{tot} - \tau_1$$

Both input profiles are shown in Fig. 5-2. If the boundary conditions and the method are correct, the calculated flow should settle to an equilibrium type so that the initial conditions are not as critical as the boundary conditions.

In order to decide on the initial skin friction coefficient C_f various approximations have been tested. The final choice was the value from Bradshaw's (1960) approximation

$$C_f = 0.0315 \left(\frac{U_m Y_m}{\nu}\right)^{-0.182} \tag{5-15}$$

The value of $C_f = 0.0628$ at $X = 200$mm was used for the initial input throughout the calculations.

5-2-6 Numerical method

Equations 5-2 and 5-11 can be written in finite difference approximation form. The equations for the outgoing characteristic α and ingoing characteristic β are

$$\tau_\alpha(U-U_{2c}) - \tfrac{1}{2}\sigma_\alpha(\tau - \tau_{2c}) = \Delta X\frac{\tau_\alpha}{U_\alpha}\left[U_e\frac{dU_e}{dx} + \frac{a_1}{\delta}\left(\frac{\sqrt{\tau_\alpha}}{L_\alpha} + G'_\alpha\tau_m^{\frac{1}{2}}\right)\sigma_\alpha \right]$$

$$\tau_\beta(U-U_{1c}) - \tfrac{1}{2}\sigma_\beta(\tau-\tau_{1c}) = \Delta X\frac{\tau_\beta}{U_\beta}\left[U_e\frac{dU_e}{dx} + \frac{a_1}{\delta}\left(\frac{\sqrt{\tau_\beta}}{L_\beta} + G'_\beta\tau_m^{\frac{1}{2}}\right)\sigma_\beta \right] \tag{5-16}$$

where $\sigma_\alpha = G_\alpha\tau_m^{\frac{1}{2}} + \left[G_\alpha^2\tau_m + (2\tau_\alpha/a_1) \right]^{\frac{1}{2}}$ and

$$\sigma_\beta = G_\beta\tau_m^{\frac{1}{2}} + \left[G_\beta^2\tau_m + (2\tau_\beta/a_1) \right]^{\frac{1}{2}} .$$

and U_{1c} and U_{2c} are the values of U at either end of the characteristic segments. The suffixes α and β represent average values on the characteristic as distinct from end values. Now the equation 5-16 is solved for U and τ. The values of V are calculated along the vertical characteristic.

The X step ΔX has to be chosen subject to a stability condition. This is

$$(\Delta X/\Delta Y) \tan \alpha_m < 1.0$$

where ΔY is the Y step and α_m is the maximum value of the characteristic angle in the layer at a given station X.

The thickness of Layer 1 is much smaller than that of Layer 2. If there are enough points to satisfy the stability and the accuracy of conditions for Layer 1, there will be too many points to cover Layer 2. This leads to an excessive C.P.U. memory and time to calculate is thus not practical. In order to provide a reasonable number of mesh points for each layer, a variable interval mesh system was introduced. The mesh interval starts as fine as $0.004Y\frac{1}{2}$ and gradually increases towards the outer edge to $0.07Y\frac{1}{2}$ initially. The number of mesh points for the initial profiles are 32 points for Layer 1 and 89 points for Layer 2.

The flow chart of the computer program is shown in Fig. 5-3. The program has been written in such a way that the flow chart is very similar to that for the B-L program.

5-3 Results and discussions

5-3-1 Preliminary tests

The computer program to calculate wall jets, we call it the wall jet program, consists of calculations of two separate layers as has been discussed in the last section. The calculation starts from Layer 1 (which is the boundary layer calculation) and then calculates Layer 2. It is therefore possible to run the part to calculate Layer 1 only. This part of the program was written in the same way as the B-L program so that it should produce the identical result or at least an almost identical result. If there is a large discrepancy between the two results, there must be an error in the program or simply a mistake in the coding. Two programs were run with the identical input data. Many of the routines in the wall jet program are commonly used to calculate both layers. It is therefore a useful way to check the whole program. The data used for these tests were AFOSR-IFP-STANFORD Conference data 1300 and 1400. 1300 is the accelerating boundary layer flow data of Ludwieg and Tillman. 1400 is the data for the boundary layer with no pressure gradient of Wieghardt. The initial momentum thickness, Reynolds number Ue θ/ν , C_f and the value of Ue along X axis are the main input data to start the B-L program. The initial velocity and the shear stress profiles are generated by the built-in synthetic routine. This routine uses Cole's logarithmic law with cosine wake velocity profiles and a mixing length assumption for shear stress profiles. The details are given by Bradshaw and Unsworth (1974). The generated velocity and shear stress profiles were used to start the wall jet program. The details of the test cases of the B-L program have been already given by Bradshaw et al (1967). The purpose of this test is to eliminate all the possible errors from the wall jet program. The results from the B-L program and the wall jet program were almost identical after a debugging process.

The tests for the wall jet program were carried out with various parameters. All the tests are calculations of an equilibrium plane wall jet in a slow moving stream. The conditions of the flow are the same as the experimental conditions except for the presence of an external stream. The calculations were started from X = 200mm, where the jet is fully developed, to X = 650mm. The parameters changed in preliminary tests are the initial skin friction coefficicent C_f, logarithmic law constants K and B, the levels of the functions a_1, L and G. All the comparisons are made with the results of TEST 1. The parameters are tabulated in Table 5-1. The results of TEST 1 to TEST 11 are shown in Figs. 5-4 to 8. The comment 'ESTIMATED' means the values are estimated from the experimental results for an equilibrium plane wall jet.

TEST 1 shows results which are typical of the calculations for all the test cases. The distance between the maximum velocity U_m and the wall Y_m is larger than that of the experiments. The velocity profile is generally fuller and continues to be more full along the X direction. The profile does not reach an equilibrium state. The value of Y_m from the experiments is approximately $0.18Y_{\frac{1}{2}}$. The case of TEST 1, $Y_m = 0.22Y_{\frac{1}{2}}$ at X = 300mm and $0.3Y_{\frac{1}{2}}$ at X = 600mm. The outermost part of the profile, i.e. $Y > Y_{\frac{1}{2}}$, is in agreement with the experimental profile. The maximum shear stress τ_m increases along the X direction. The measured τ_m along X axis however, stays constant because the flow is self-preserving. The shear stress is over-estimated at the inner part of the jet, which is $Y < Y_m$. The position of $\tau = 0$, therefore, is closer to the surface than that of measured one. The position of τ_m is also closer to the surface. The decay of the shear stress at the outer part of the profile is slower than that of the experimental profile. The growth rate of the jet is lower than the measured rate. The growth is not linear and the rate of $dY_{\frac{1}{2}}/dX$ is approximately 0.062 between X = 450 and 650mm compared with 0.069 for the measured value. The discrepancy is 4.3%. However the actual value $Y_{\frac{1}{2}}$ at X = 650mm is 8.4% lower than that of the experiment. The maximum velocity decay is also slower than that of the experiments. The normalized velocity decay gradient $d(U_J^2/U_m^2)/d(X/b)$ where U_J is the initial slot velocity and b is the slot width, is 0.057 between X = 450 and 650mm compared with the measured value of 0.078.

The difference is 27%. Both calculated and the experimental results are linear. The skin friction coefficient has not been measured experimentally so that the estimated values from equation 5-15 were used for comparisons. The decay of C_f along X axis does not settle until approximately X = 450mm. This point is about 170 X steps from the start of the calculation. After this point C_f decays much quicker than the estimated C_f decay.

TEST 2 and 3 were calculated with initial C_f plus and minus 0.001 respectively from the value used for TEST 1. There is almost no difference in both cases except for some small differences at the early stage of the calculations.

TEST 4 and 5 were made with two sets of logarithmic law constants. The constants used in TEST 1 are k = 0.41 and B = 5.2. These values were changed to k = 0.44 and B = 7.8 for TEST 4 which were presented by Kanemoto (1974). k = 0.555 and A = B.0 were used for TEST 5 which were suggested by Alcaraz et al. (1977). TEST 4 shows slightly slower rate of decay than the case of TEST 1. The rate of decay of C_f in the case of TEST 5 is the same as TEST 1. The values of C_f at X = 650mm are 0.00474, 0.00408 and 0.00461 for TEST 1, 4 and 5 respectively. There is almost no difference in the velocity profiles and the shear stress profiles in those three tests. It is interesting to note that the logarithmic law constants have only a minor effect on the results except, naturally, on C_f. This indicates that effect of Layer 1 on the jet is small compared with the effect of Layer 2. The changes of parameters, therefore, are centred on Layer 2 only. The conditions of Layer 1 are to be fixed with those of TEST 1 for all the rest of the computations.

TEST 6 and 7 were calculated with the shift in the value of a_1 plus and minus 10% respectively. There is only a small difference in the velocity profiles from that of TEST 1. The difference in the maximum velocity decay and C_f decay in the X-direction are also small. The values of $Y\frac{1}{2}$ at X = 650mm of TEST 6 and 7 are approximately ± 2% of the value of TEST 1. The development of the maximum shear stress τ_m shows the same tendency. τ_m of TEST 6 grows faster than that of TEST 1 and the opposite is true for TEST 7.

TEST 8 and 9 are the tests with plus and minus 25% in the level of the function L respectively. The value of L/δ for TEST 1, i.e. Morel and Torda's, is constant and equal to 0.09 across the layer and at both edges of the layer the value decreases to zero exponentially. The change in the function L is the most significant factor in every respect. The growth rate of jet of TEST 8 is rather strongly non-linear. At X = 500mm and onwards the growth rate becomes higher than that for the experiment. The case of TEST 9, on the other hand, the rate is nearly linear and much lower than that of TEST 1. The maximum velocity of TEST 8 lies between the decays of the experiments and TEST 1. The decay in TEST 9 is much slower than that of TEST 1. The growth rate of jet and the maximum velocity decay are clearly in favour of TEST 8. The comparisons of the decay of C_f and the development of τ_m along X axis have however an opposite tendency. The gradient of the C_f decay of TEST 9 is much closer to that of Bradshaw's approximation. Nevertheless the value at X = 650mm is approximately 15% lower than that of the estimated value. The value of C_f of TEST 8 is far lower than that for any of the tests and the rate of decay is also much higher. The value of τ_m of TEST 9 along the X direction increases slowly compared with the increase of TEST 1, but the level is 21% lower than the initial value of X = 650mm.

In the case of TEST 8, τ_m rapidly increases and reaches a value 83% higher than the initial value at X = 650mm. The velocity profiles of TEST 1, 8 and 9 are generally similar at X = 300mm. At X = 650mm there are some differences. The higher level of the function L produces a fuller velocity profile. The profile of TEST 8 is much fuller than that of TEST 1. The profile of TEST 9 is, this time, thinner than for TEST 1 but still fuller than the experimental profile. As the result Y_m becomes large with the larger value of L/δ. The shape of shear stress profiles are generally similar but there are significant differences in the magnitudes of shear stresses.

TEST 10 and 11 were carried out with changes in the level of the function G. The value of Morel and Torda's function G was used but multiplied by factors 1.25 and 0.75 for TEST 10 and 11 respectively. The case of TEST 11, the computation failed numerically at approximately X = 600mm. The results of TEST 10 are not much different from the results of TEST 1 except for the decay of C_f. The rate of decay is roughly the same as of TEST 1 but the level is much lower. The shear stress of TEST 10 at outer part of the profile decays slower than that of TEST 1.

The results of TEST 1 to 12 are summarised as follows:-

(1) Layer 1 does not have as strong an influence as Layer 2. This is the consequence of the interaction approach. Layer 1 is much thinner than Layer 2 and the mutual influence can only be transferred through the velocity profile. Thus the effect of Layer 1 on the whole jet cannot be large.

(2) Functions a_1 and G are not as critical to the development as

the function L. The increase in either function understandably produces a higher level of shear stress. As a result it leads to a higher growth rate of the jet and a quicker decay of maximum velocity.

(3) A change in the value of the function L is the most significant to the results.

(4) Shifts in the levels of the function a_1, L or G produce changes in the shear stress levels. However the shapes of the shear stress and the velocity profiles stay nearly unchanged.

(5) Changes of the levels of any function do not produce better agreement to the experimental results in any of the comparisons. For example, the growth rate of jet and the maximum velocity decay of TEST 8 is closest to the experiments among the tests however the development of τ_m and C_f are the farthest.

The tests indicate that the best functions to bring the calculated results close to the measured results are the functions L and G. It is also clear that resutls are the more sensitive to the values of the function L. For all the test cases the velocity profiles stayed almost unchanged. This suggests that the assumption of constant L/δ across the layer may not be valid for wall jets. This is understandable because of the presence of a solid wall just next to Layer 2. The value of Y_m for all the cases are larger than that which has been measured. The shape of the shear stress profile is also unchanged. These suggest that the shapes of the velocity profiles and the shear stress profiles are not determined by the change of values of the empirical functions. This is another support to the idea that the assumption of constant L/δ across the layer is no longer valid for wall jets.

It is therefore concluded that further tests with various shapes of the empirical functions L and G are required.

5-3-2 Further tests

It became clear that the functions L and G are the critical factors for the calculations. Further tests have been carried out with various shapes of the function L and with the experimentally obtained function G. The table of tests are shown in Table 5-2. This time we call the tests WJTESTs.

WJTEST 1 same as TEST 1. This example is used for comparisons as it has been used in the previous section.

WJTEST 2. Morel and Torda's function G for free jet was used. The function L is defined as

$Y < 0.225Y_{\frac{1}{2}}$, $\quad L/Y_{\frac{1}{2}} = 0.41Y/Y_{\frac{1}{2}}$,

$Y > 0.225Y_{\frac{1}{2}}$, $\quad L/Y_{\frac{1}{2}} = 0.09$

WJTEST 3. Morel and Torda's function G. The function L was calculated from the uncorrected measured dissipation.

WJTEST 4. Same as WJTEST 3 but the function L is shifted $0.03Y_{\frac{1}{2}}$ in Y direction towards the surface. This is to examine the sensitivity of the function in Y direction.

WJTEST 5 same as WJTEST 4 but with the shift increased to 0.06Y½.

WJTEST 6. The function G was calculated from the corrected experimental diffusion. The function L was calculated from the uncorrected measured dissipation.

WJTEST 7. Same as WJTEST 6 but both functions are shifted 0.06Y½ in the Y direction towards the surface.

Some other tests have also been carried out.

(1) Morel and Torda's function G. The uncorrected experimental function L for the inner side of the flow within the point where L is maximum. L stays constant for the outer layer.

(2) Same as (1) but L is shifted 0.06Y½ towards the surface.

(3) Morel and Torda's function G. L is calculated from the corrected experimental dissipation.

(4) Both functions L and G are calculated from the corrected experimental energy balance.

These tests have numerically failed during the computations. The results of WJTEST 2 to 7 are shown in Figs. 5-9 to 12.

WJTEST 2 is to examine the applicability of the mixing length to Layer 2. However the defined function L is not equal to the mixing length because even in the region close to the surface, unlike the case of boundary layer, advection and diffusion are not negligible. It is therefore expected that both functions L and G work together in the region close to the surface and the function L is not as simple as $L = 0.41Y$. The result of WJTEST 2 is remarkably similar to the result of WJTEST 1 which is shown in Fig. 5-13. The change in the function L near the surface does not effect most of the properties of the flow in Layer 2. This indicates that the effect of the presence of the surface on the function L is large and it looks as though the function L outside $0.225Y_{\frac{1}{2}}$ is affected.

WJTEST 3 is the test to examine how the experimentally obtained function L works in the present computation. It must be mentioned that L is calculated from the uncorrected measured dissipation which is from the experiment on the wall jet, not Layer 2. Therefore no effects from the interaction of two layers are accounted for in this function.

The growth rate of the jet of WJTEST 3 is lower than that of WJTEST 1, but is linear. The rate is 26% lower than that of experiments and 23% below the value of WJTEST 1. The decay of maximum velocity is also slower than for WJTEST 1. The normalized rate of decay $d(U_j^2/U_m^2)/d(X/b)$ is 44% and 23% lower than those of the experiments and of WJTEST 1 respectively. The rate of decay of skin friction C_f is in good agreement with that of Bradshaw's approximation. The value of C_f at X = 650mm is however 7% lower.

There are remarkable differences in the velocity profiles from thos of WJTEST 1 which are shown together with the shear stress profiles in Fig. 5-14. The profiles are highly distorted. The profiles of velocity at X = 300 and 600mm agree well except at the inner and outside of the jet. The points where velocity is maximum become closer to the wall at X = 600mm than that of X = 300mm. The profiles have a sharp peak at U_m. The velocity at the outer edge of the jet, i.e. Y > Y½, decay quicker than those of the experiments and WJTEST 1. The shear stress profiles are also notably different from those of WJTEST 1. The profile at X = 300mm is rather different from the others, but it is thought that at X = 300mm the calculation has not settled to an equilibrium state. The profiles of shear stress are in better agreement with that of experiments than with the profile of WJTEST 1. The position of $\tau = 0$ is very close to the position of the measured profile. The shear stress at the outside of the jet, i.e. Y >Y½, however, decays slightly faster than that of the experiments. The level of τ_m decreases very slowly along X direction but the value is 22.7% lower than the experimental value of X = 650mm. The introduction of the experimentally calculated function L demonstrates the effects in the results.

WJTEST 4 is to examine the effect of the shift of function L towards the surface. The amount of shift is only 0.03Y½, however it is large enough to make a noticeable change in the velocity profile. The growth rate of the jet and the rate of maximum velocity decay are slightly improved from those of WJTEST 3. The rate of C_f decay stays the same but the value of C_f at X = 650mm is only 4% from the experimental value, compared with 7% in the case of WJTEST 3. The velocity profile is somewhere between those of WJTEST 1 and 3 which is shown in Fig. 5-15. A large dent on the profile just outside of U_m of WJTEST 3 has almost disappeared, however a hollow in the profile between 0.4Y½ < Y < Y½ is larger than that for WJTEST 3. The outer edge of the profile is still under-estimated. The shear stress profile at X = 600mm is similar to that of WJTEST 3. The profile is, however, slightly shifted inwards as is the position of $\tau = 0$. The level of τ_m is higher than that of

WJTEST 3 but still 13.6% lower than the measured τ_m. τ_m along the X-axis is almost unchanged after X = 350mm.

WJTEST 5 is the test with a further L shift. The growth rate of the jet is the same as that of WJTEST 4. The rate of maximum velocity decay is again slightly improved from that of WJTEST 4. The decay of C_f stays almost the same as for WJTEST 4. Again there are changes in the velocity profile and the shear stress profile which are shown in Fig. 5-16. The velocity profile at X = 600mm is in good agreement with that of the experiments in the inner region i.e. $Y<Y_m$ of the jet. The velocity in the region $Y_m < Y < Y_{\frac{1}{2}}$ is over-estimated. The quick decay of the velocity at the outer edge of the jet is similar to that found in WJTEST 3 and 4. The shear stress profiles are almost unchanged. The level of τ_m at X = 650mm is even higher than that of WJTEST 4 and is only 6.8% lower than that of the experiments. τ_m slightly increases along the X direction.

WJTEST 6 has the input functions L and G both calculated from the experimental kinetic energy balance. The effect of adding the experimental function G is small on the growth rate of jet. However the computation failed numerically after X = 600mm so that the result of X = 650mm is excluded from the general consideration of the results. The values used for comparisons are the estimated values for this particular test case, from the results of X = 200 to 600mm. The rate of maximum velocity decay becomes a little worse than that of WJTEST 1. It is however slightly better than WJTEST 3. The decay of C_f is almost the same as that of WJTEST 3. The velocity profile is again highly distorted. The shape of the profile around U_m is even sharper than those of WJTEST 3, 4 and 5. There is a large dent in the profile at middle of the jet which is shown in Fig. 5-17. The faster decay of velocity at the outer edge of the jet of WJTEST 3, 4 and 5 is much closer to the experimental results but still under-estimates the decay of τ_m along the X axis. At X = 600mm, τ_m is 33.3% lower than the measured value. The shape of the shear stress profile looks different from the measured profile, however, the rate of decay of shear stress at the outermost part of the jet, i.e. $Y > 1.2Y\frac{1}{2}$, agrees well with the experiment. The position of $\tau = 0$ gives the best agreement with the experiment of all the calculated results.

WJTEST 7 is the last one in the present series of numerical tests. It is to examine the effect of the shift of both functions L and G in Y direction towards the surface. The amount of the shift is $0.06Y\frac{1}{2}$. The growth rate of the jet stays the same as for WJTEST 6, but the value of $Y\frac{1}{2}$ at X = 600mm is slightly higher. The rate of maximum velocity decay is a little worse than that of WJTEST 6, but again the value of U_m at X = 600mm is slightly better. The velocity profile is generally similar to that of WJTEST 6; however, the large dent shown in the profile of WJTEST 6 becomes smaller which is shown in Fig. 5-18. The value of τ_m at X = 600mm is 19.7% lower than that measured. τ_m decays very slightly along the X axis. The shear stress profile is in very good agreement with that measured.

5-3-3 Discussion of the results

The results of WJTEST 1 to 7 clearly show the effect of the functions L and G, particularly of L. The results are tabulated together with the experimental results in Table 5-3. Some of the experimental values such as C_f, U_m and $Y\frac{1}{2}$ are estimated from the measured values.

The growth rates of the jet are taken from the results between X = 450 and 650mm, because all the calculated growths are not linear. The growth rates should be examined with the values of $Y\frac{1}{2}$ at X = 650mm. If only the growth rate is concerned, WJTEST 1 and 2 are the best match to the measured value. However, it is clear from the preliminary tests that the increase in levels of functions a_1, L and G produce higher rates of growth so that it is too early to conclude that the functions used for WJTEST 1 and 2 are the best. The same can be said for the maximum velocity decay. The decay and the rate of decay of WJTEST 1 and 2 are the closest to the measured values. These values can also be moved by adjusting the levels of functions a_1, L and G. The normalized rate of maximum velocity decay gives a clearer picture of the difference between the measured and calculated rates. The rates of WJTEST 3, 4, 5 and 7 are not linear. The introduction of the experimental function L produces results which are little worse than the case of WJTEST 1 for the growth rate of the jet. The addition of the experimental function G makes the rate slightly better. The shift of functions in the Y direction also brings the rates little better. The introduction of the experimental L also makes the maximum velocity decay worse than the case of WJTEST 1. The addition of the experimental G again makes the decay a little better.

The skin friction coefficients C_f plotted against the X co-ordinate shows the improvement made by the introduction of the experimental functions L on the rate of decay of C_f. The values of C_f at X = 650mm are however a few percent lower than those of the experiments. The addition of the experimental G makes the development of C_f a little worse. Although the difference in velocity profile is small when the experimental G is used, there is a clear difference in C_f. The change in the diffusion factor G affects the region close to the wall through the velocity profile of Layer 1. In the cases of WJTEST 1 and 3 the velocity profiles close to the wall are different, so that it is expected that there should be different developments in C_f. The rate of decay of C_f can also be adjusted by shifting the levels of the functions. However the actual value at X = 650mm is much lower than those of WJTEST 1 to 7.

The value of the maximum shear stress τ_m along the X axis should stay constant because the flow is self-preserving. At least when the calculation has settled the value of τ_m should stay at a certain level. This requirement is not satisfied by shifting the levels of the functions except for the case of the function L minus 25% i.e. TEST 9. The growth rate of the jet and the maximum velocity decay of TEST 9 are however far from those of other tests. It suggests that the dissipation for this particular calculation across Layer 2 is so high that the development of the shear stress is hardly possible. There is a remarkable improvement in the development of τ_m along the X axis when the experimental functions are introduced. τ_m along the X axis does not change much particularly in the cases of WJTEST 3, 4 and 7. The shift of the function L in the Y direction also affects the development of τ_m.

The velocity profile is not sensitive to the shift of the levels of the functions. The introduction of the experimental function L changes the velocity profile remarkably. The velocity profile is highly distorted and very sensitive to the shift of the function in the Y direction. It is clear that the inner half of the profile of the function L is critical to the velocity profile. The outer part of the profile i.e. $Y > Y\frac{1}{2}$, is not sensitive to the shift of the function L. The quicker decay of the velocity in this region compared with that measured is thought to be caused by the outer half of the function L profile. The use of the experimental function G brings the profile of this region closer to that of the experiments. This indicates that the diffusion at this region plays an important role. The addition of the experimental G also changes the profile at $Y_m < Y < Y\frac{1}{2}$. This is another indication that the diffusion at the middle of the jet is not negligible, as was seen with the kinetic energy balance. The innermost region, however, stays almost the same with or without the use of the experimental G. The diffusion in this area therefore may not be as important as the dissipation. This is supported by consideration of the energy balance close to a wall, e.g. that of a boundary layer in which diffusion is very small.

The shear stress profile is also in favour of the experimental functions L and G. The shift of the levels of the functions only changes the magnitude of the shear stress profile. The introduction of the experimental function L produces a shear stress profile much closer to the measured profile than those of TEST1 to 11. The over-estimated shear stress in the innter region of the jet shown in TEST 1 to 11 and WJTEST 1 has disappeared. In the outer region of the flow, the slower decay of shear stress compared with those of the experiments is also corrected. The decay in this region is rather faster than that of the experiments. The shift of the function in the Y direction slightly shifts the shear stress profile in the same direction. The position of $\tau = 0$ also changes with the shift of the function in the Y direction. The position of $\tau = 0$ however may be affected by the solution of Layer 1. The use of the experimental function G produces smaller changes to the shear stress profiles than is the case with the introduction of the experimental L. The shear stress profile in the outer part of the jet i.e. $Y > Y_{\frac{1}{2}}$ agrees well with that of the measured profile. The magnitudes of the shear stress are generally lower than the measured stress. The shift of both functions in the Y direction mainly affects the magnitude of the shear stress at down-stream stations. The level of τ_m stays the same and there is a little change in the shear stress profile.

The results of these tests are summarized below:

(1) The effect of the external stream is minimal.

(2) The functions L and G used by Morel and Torda for the free jet produced the closest growth rate of the jet and maximum velocity decay among WJTESTs to those measured. The velocity and the shear stress profiles do not agree with those of the experiments.

(3) Layer 1 plays a rather minor role in the calculation.

(4) The function L in Layer 2 is the most effective parameter in the calculation but the effect of the function G is not negligible.

(5) The shifts in the levels of functions do not alter the profiles of velocity and shear stress.

(6) The introduction of the experimentally obtained function L produces the better agreement with experimental results for the shear stress profiles. However the growth rate of the jet, the maximum velocity decay and particularly the velocity profile become poorer.

(7) The velocity profile is very sensitive to a shift of the function L in the Y direction.

(8) The addition of the experimentally obtained function G produces even better agreement with measured results for the shear stress profile. Although the velocity profile in the outer part of the flow is improved, the profile is distorted.

The function L used for WJTEST 3 to 7 is calculated from the experimental kinetic energy balance which has not been corrected to balance out the diffusion across the flow. The function G used for WJTEST 6 and 7, on the other hand, is calculated from the corrected energy balance. Although the two functions were calculated from different origins, they produce shear stress profiles in good agreement with the measured profile. This indicates that the shapes of these functions are basically the right ones. The disagreement in the velocity profiles and the shear stress profiles with Morel and Torda's functions suggests that the interaction of two different types of layers is more complex than that of two similar layers. A wall jet has a thin Layer 1 which is assumed to be a boundary layer and a thick Layer 2 which is assumed to be a free jet. The inner edge of Layer 2 is close to a solid wall so that Layer 2 may not be thought as a simple free jet. Bradshaw's interaction approach is therefore a workable concept; however, the interaction of wall jet is not as simple as the cases of duct flow, mixing layer, wake and free jet flows.

There are still some disagreements between the results of WJTEST 6 and 7, i.e. the experimental L and G, and those of the experiments. The sensitivity of the shift of the function L in the Y direction on the results suggests that fine adjustments of both functions may be able to produce an optimum result in agreement with the experiments. The agreement between the calculated and the measured shear stress profiles with both experimental functions is evidence that the assumptions made in this method and Bradshaw's method itself are also valid.

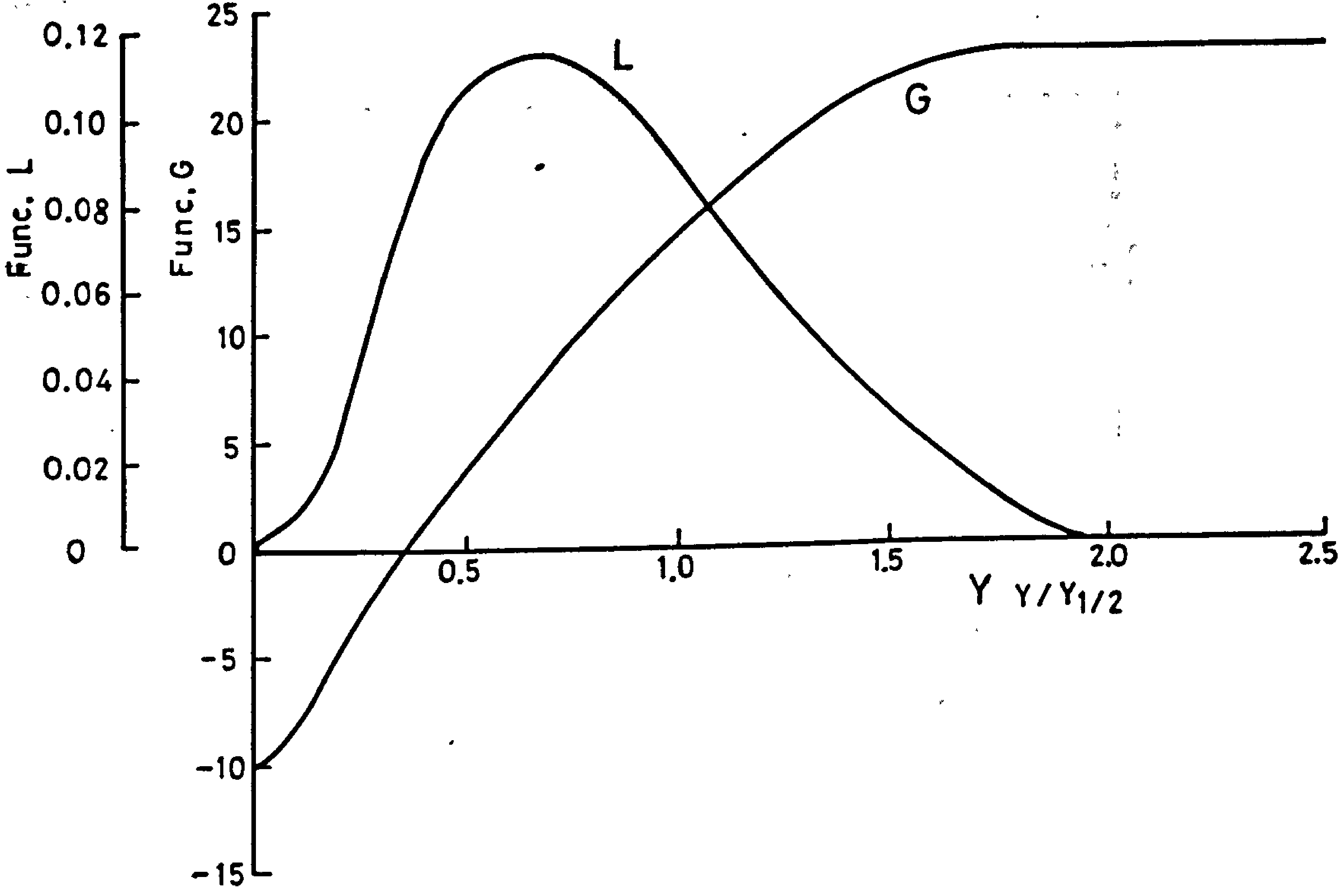

FIG. 5-1(A) EMPIRICAL FUNCTIONS CALCULATED FROM MEASURED KINETIC ENERGY BALANCE

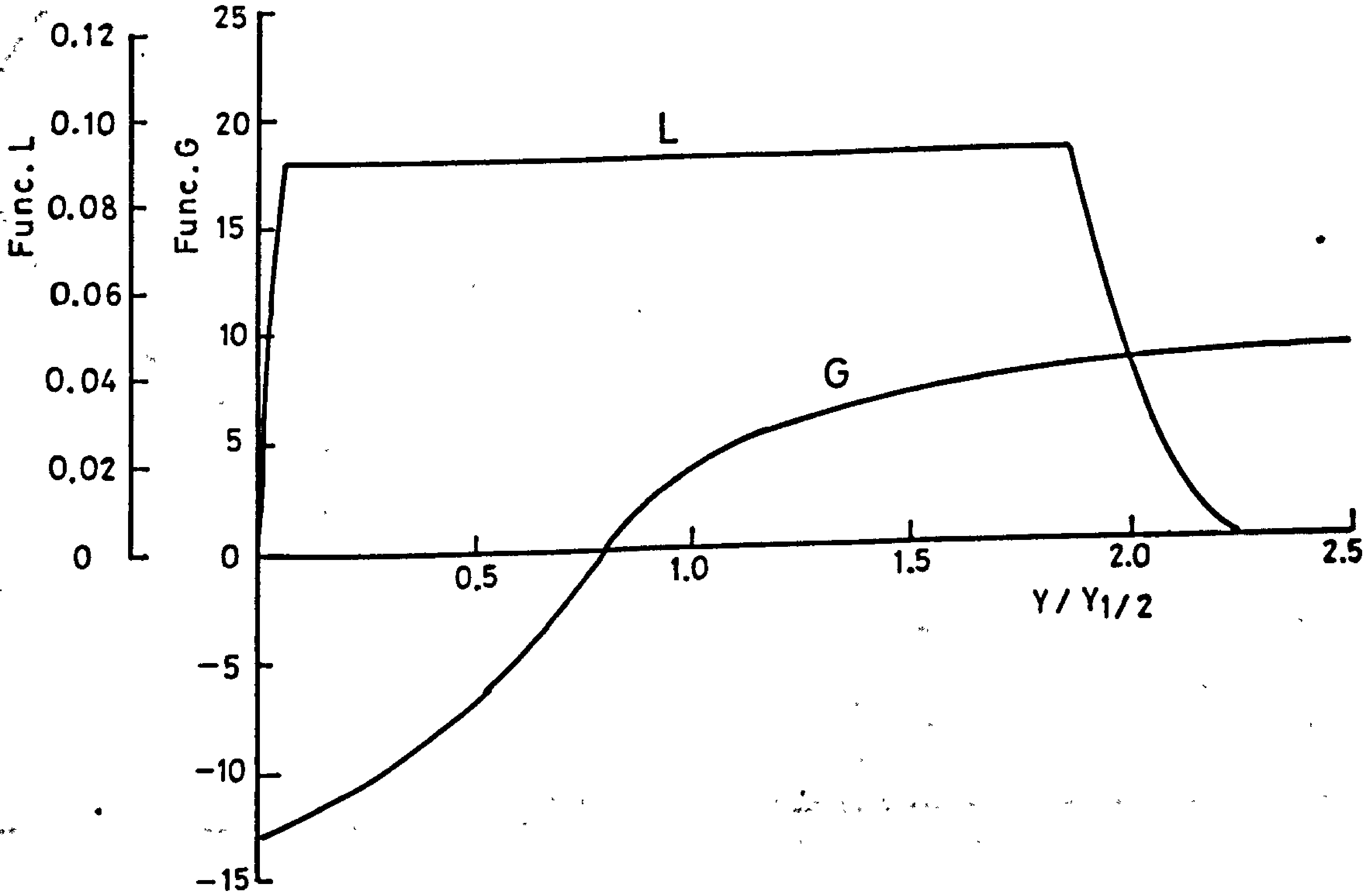

FIG. 5-1(B) EMPIRICAL FUNCTIONS USED BY MOREL AND TORDA FOR THEIR FREE JET CALCULATIONS

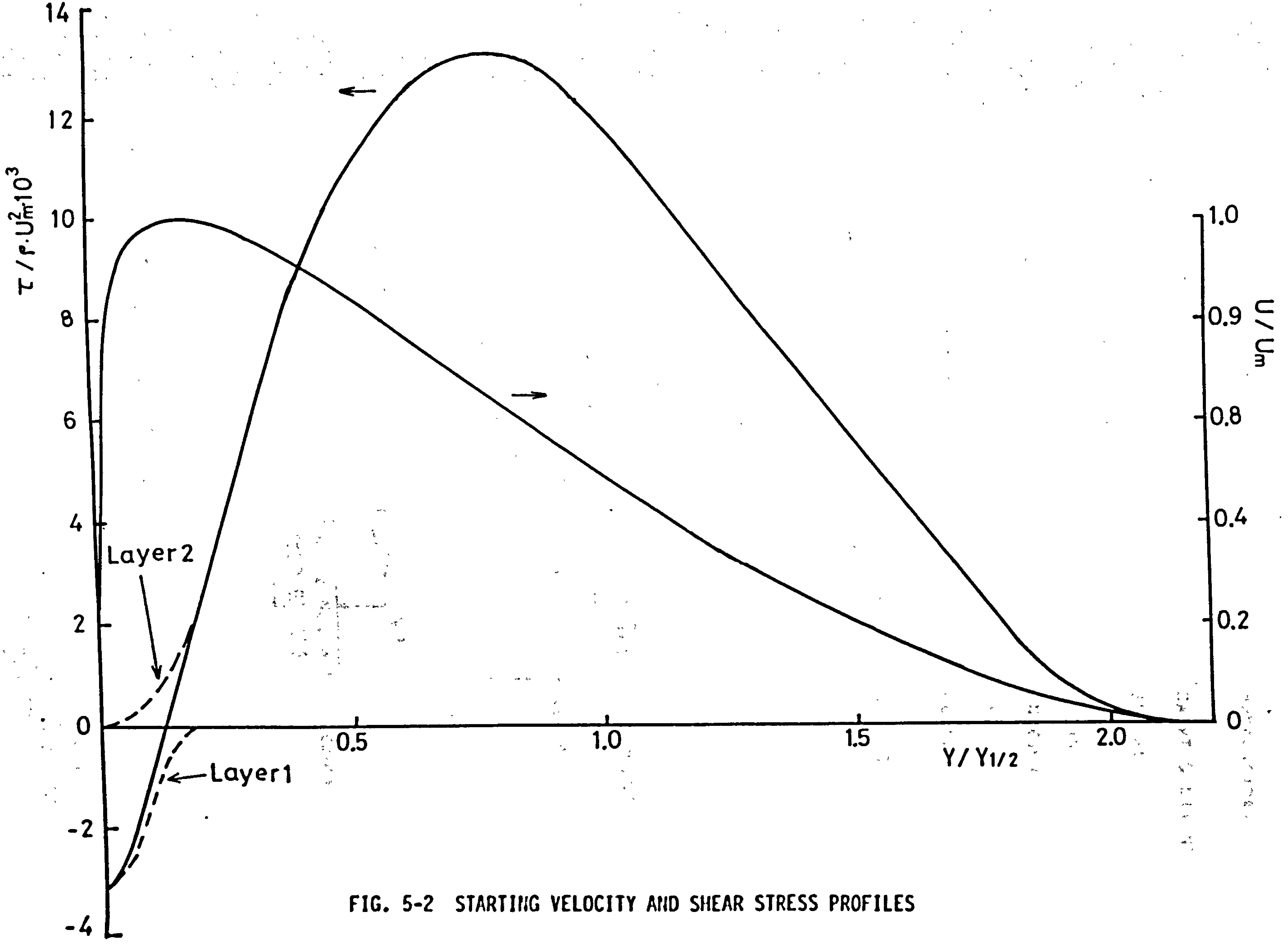

FIG. 5-2 STARTING VELOCITY AND SHEAR STRESS PROFILES

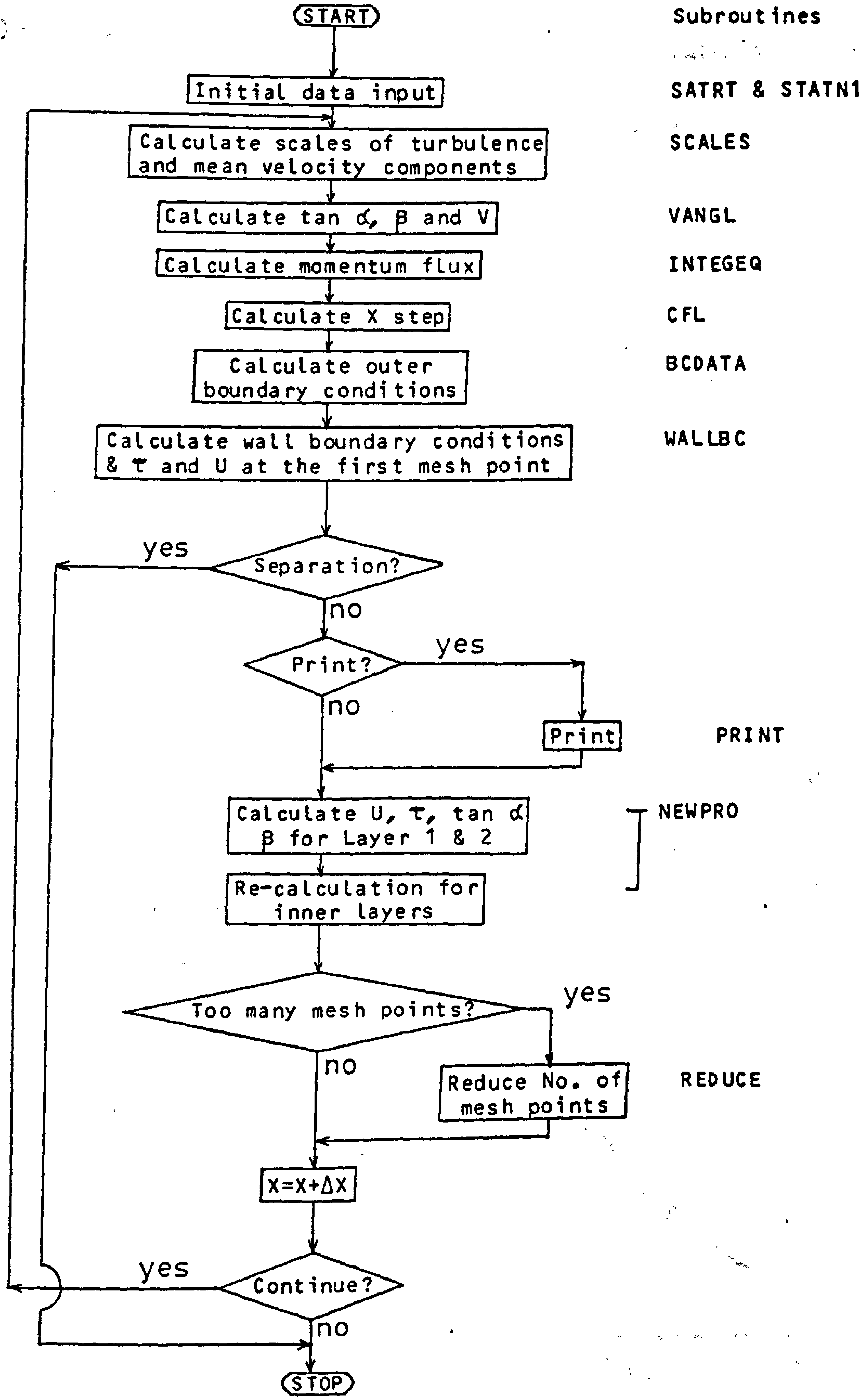

FIG. 5-3 FLOW CHART OF COMPUTER PROGRAM

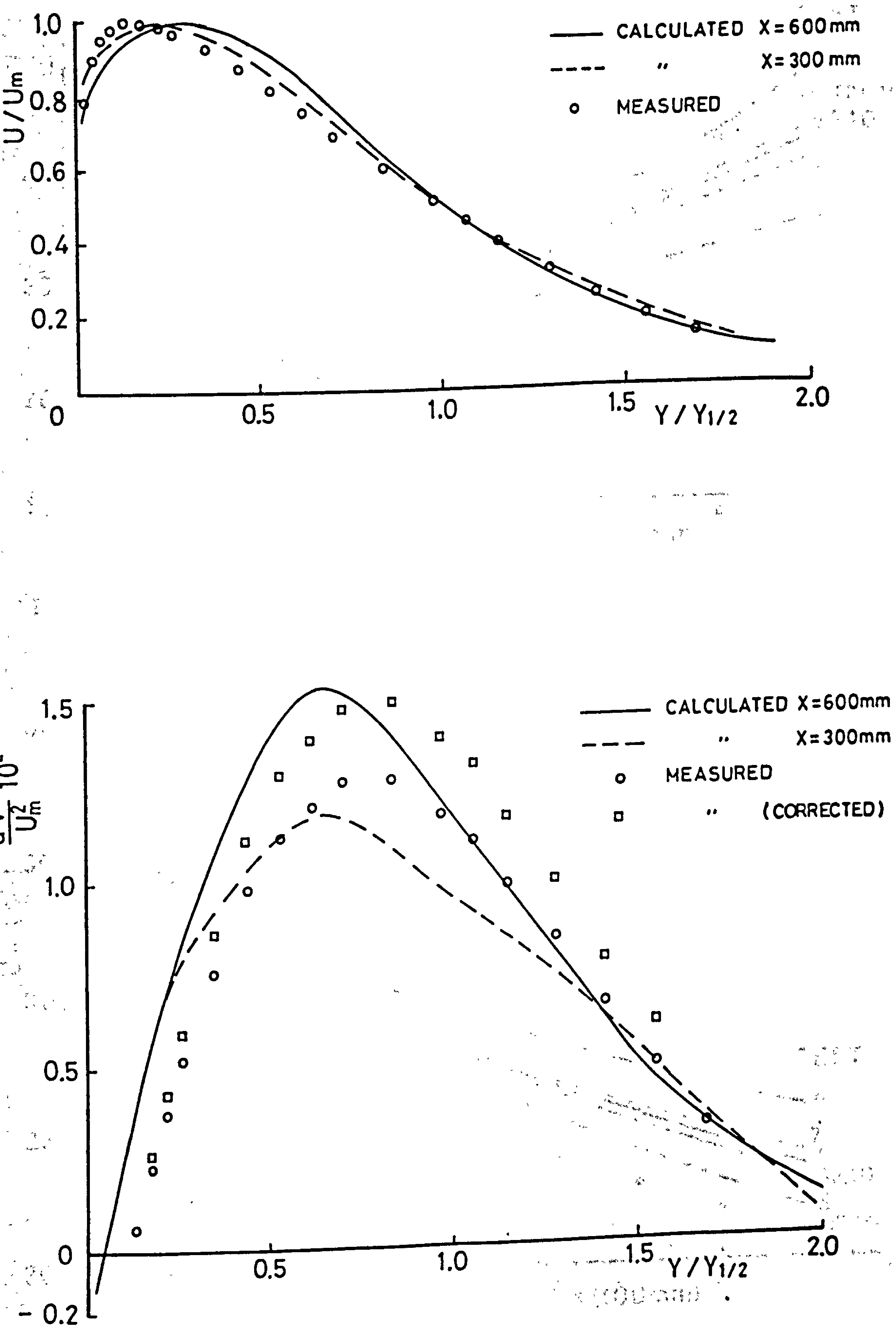

FIG. 5-4 TEST 1 / WJTEST 1 VELOCITY AND SHEAR STRESS PROFILES

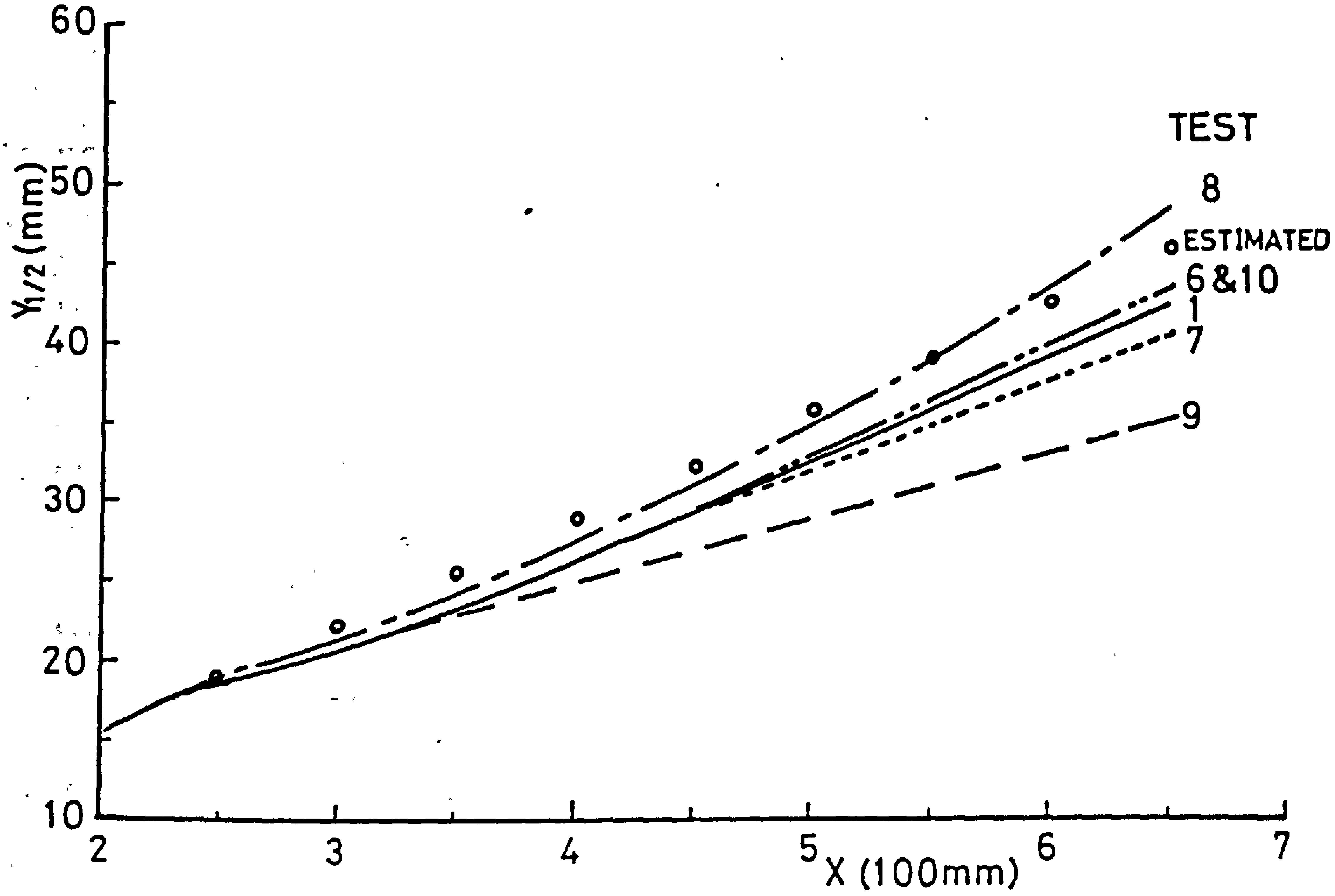

FIG. 5-5 GROWTH OF JET WIDTH, PRELIMINARY TESTS

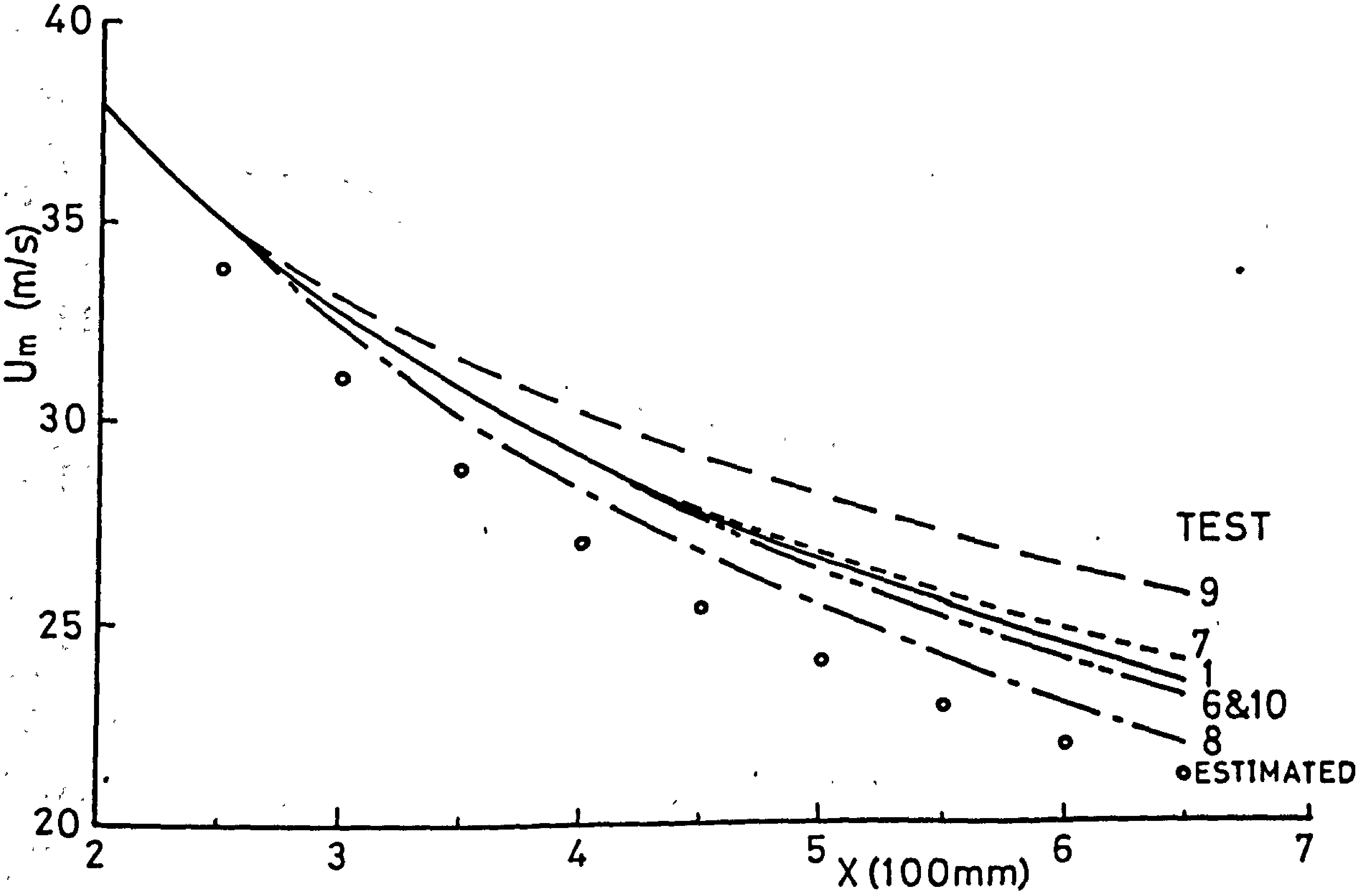

FIG. 5-6 MAXIMUM VELOCITY DECAY, PRELIMINARY TESTS

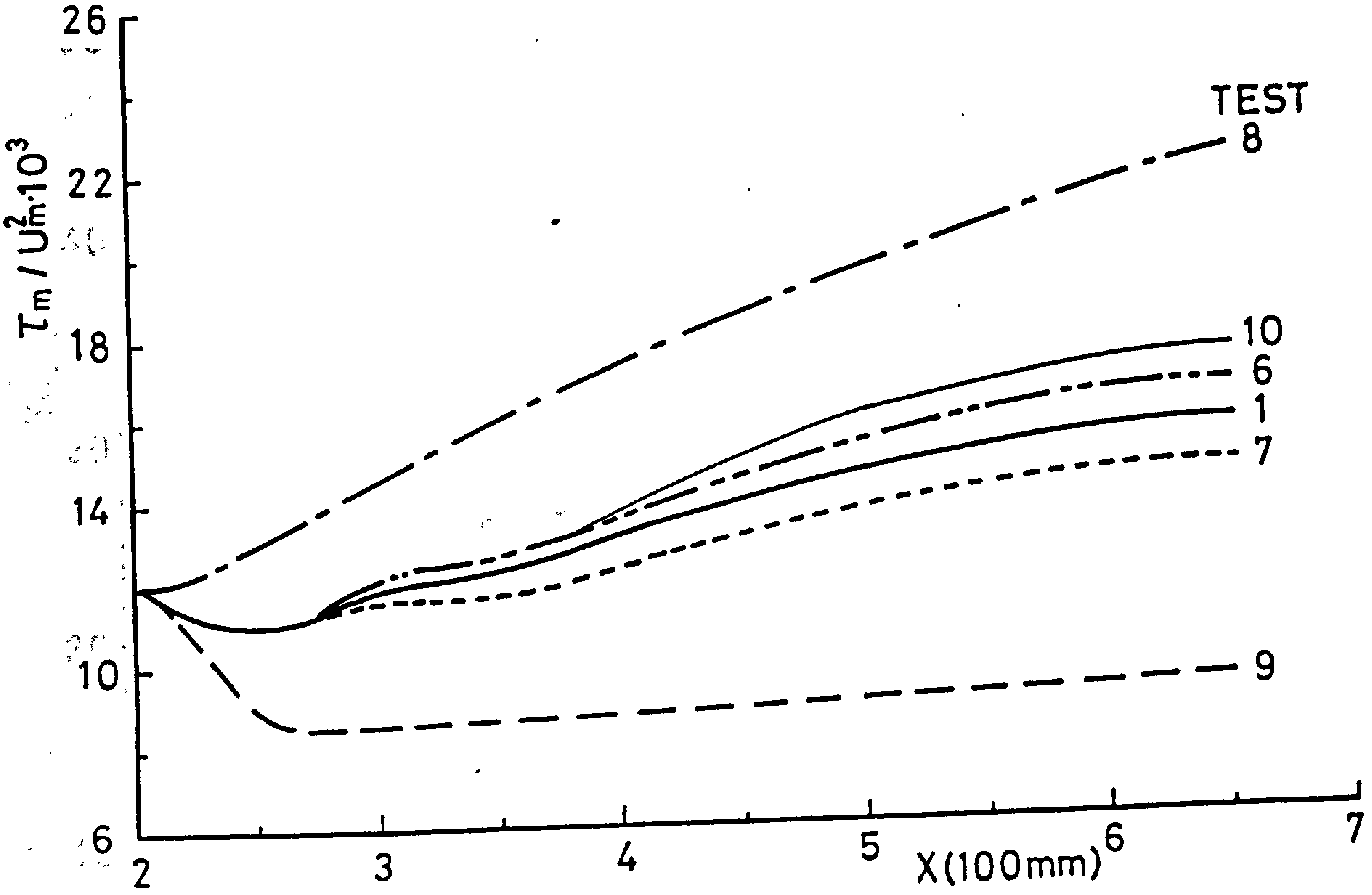

FIG. 5-7 DEVELOPMENT OF MAXIMUM SHEAR STRESS, PRELIMINARY TESTS

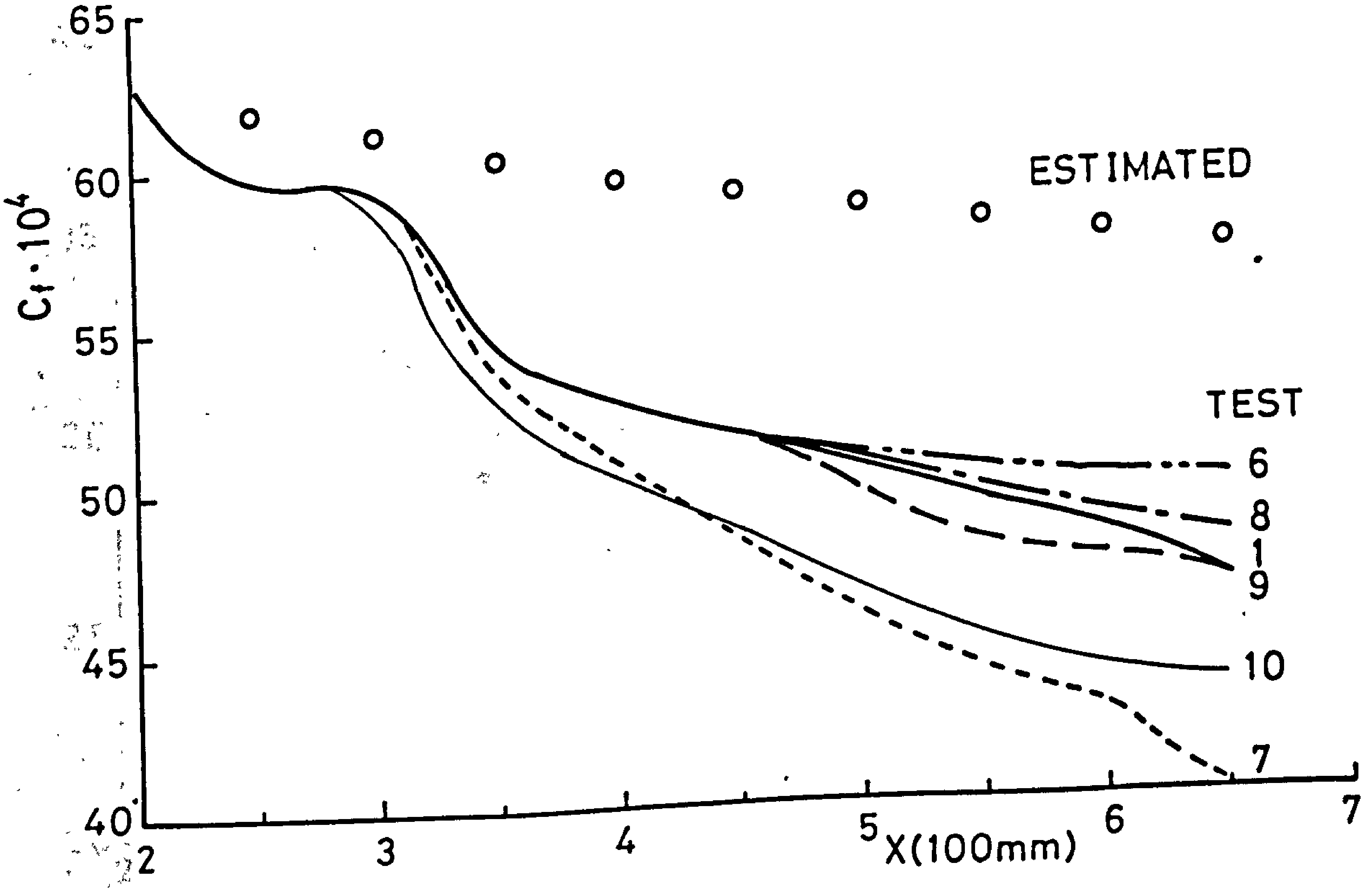

FIG. 5-8 DEVELOPMENT OF SKIN FRICTION COEFFICIENT, PRELIMINARY TESTS

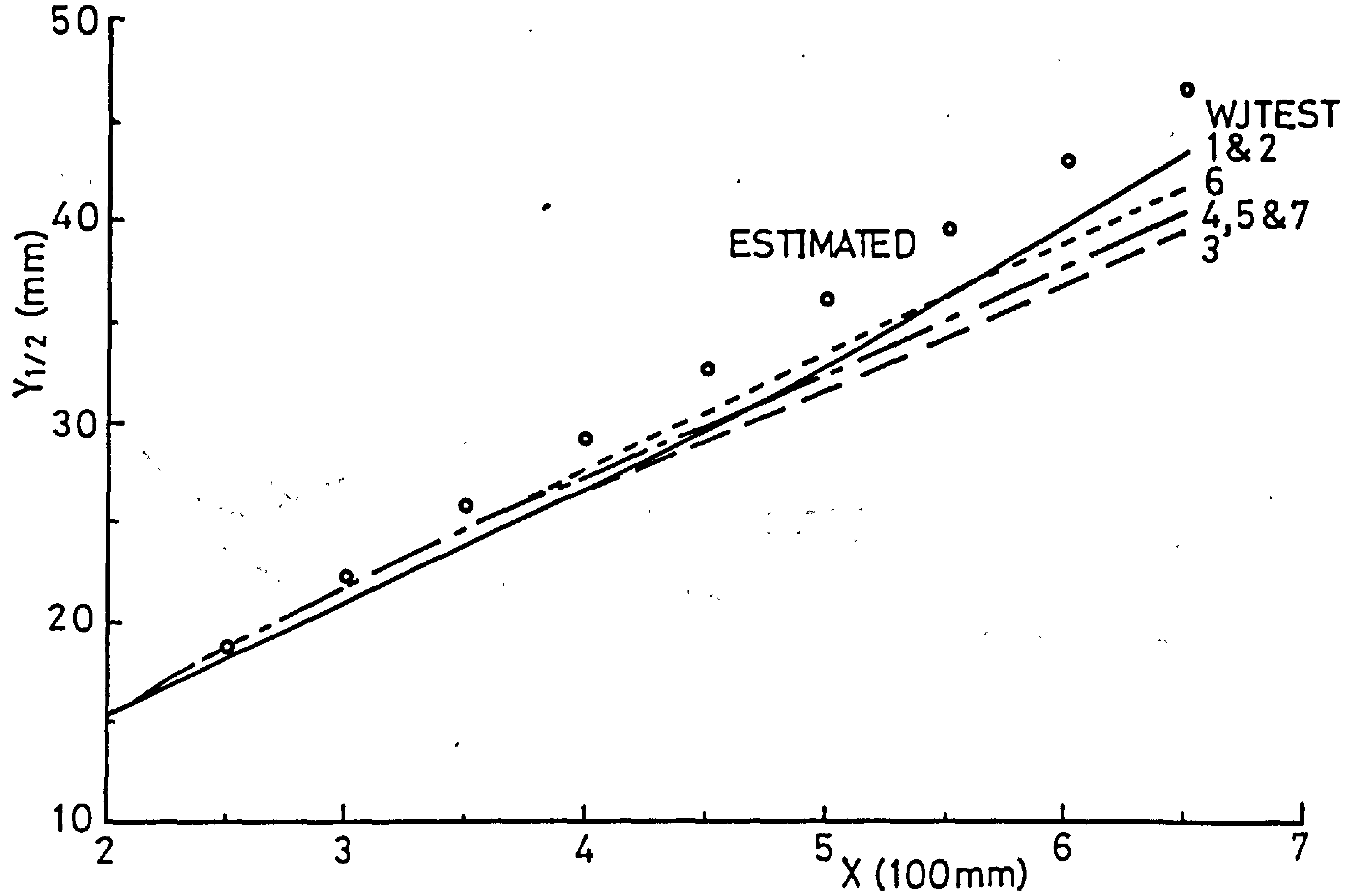

FIG. 5-9 GROWTH OF JET WIDTH

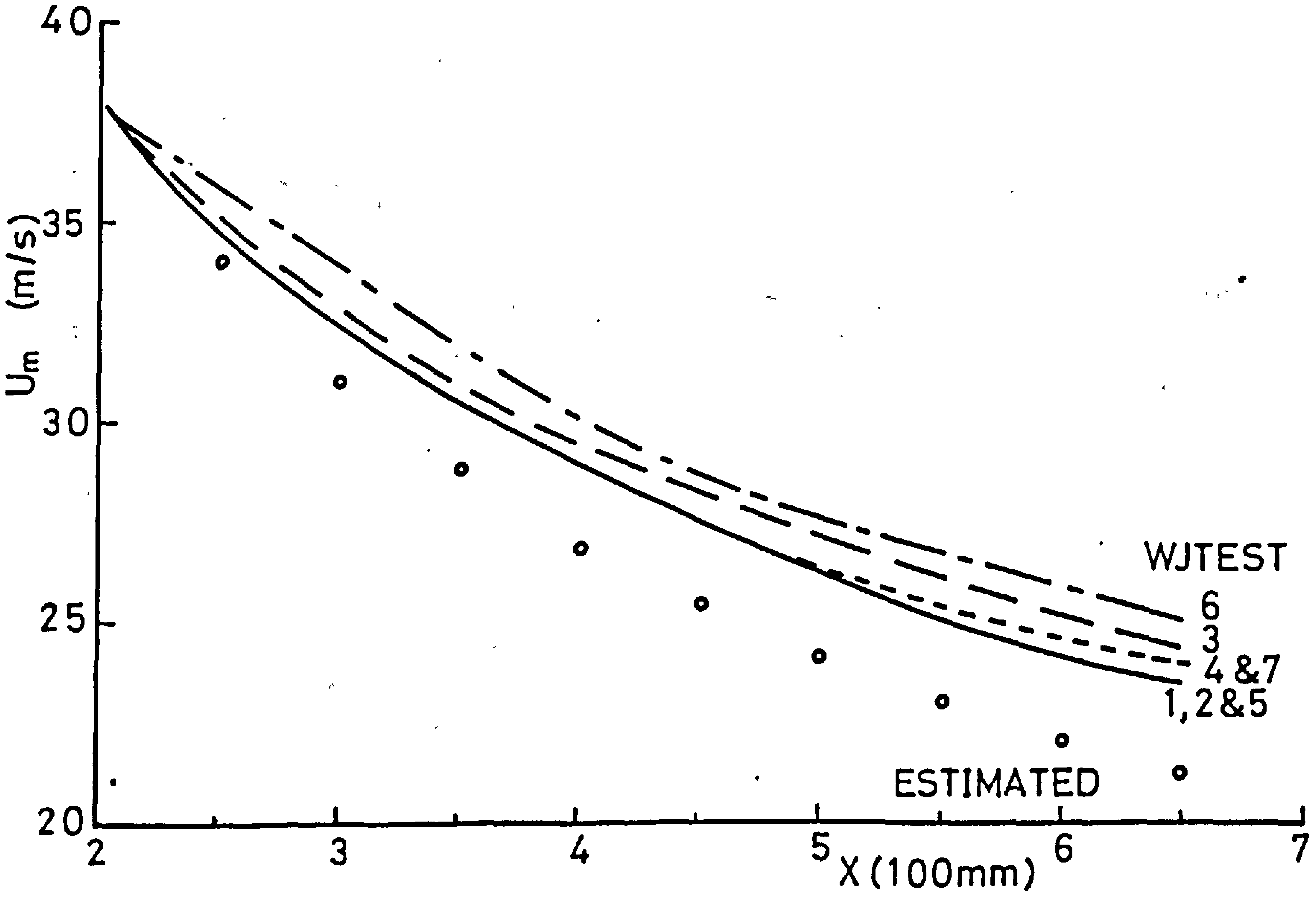

FIG. 5-10 MAXIMUM VELOCITY DECAY

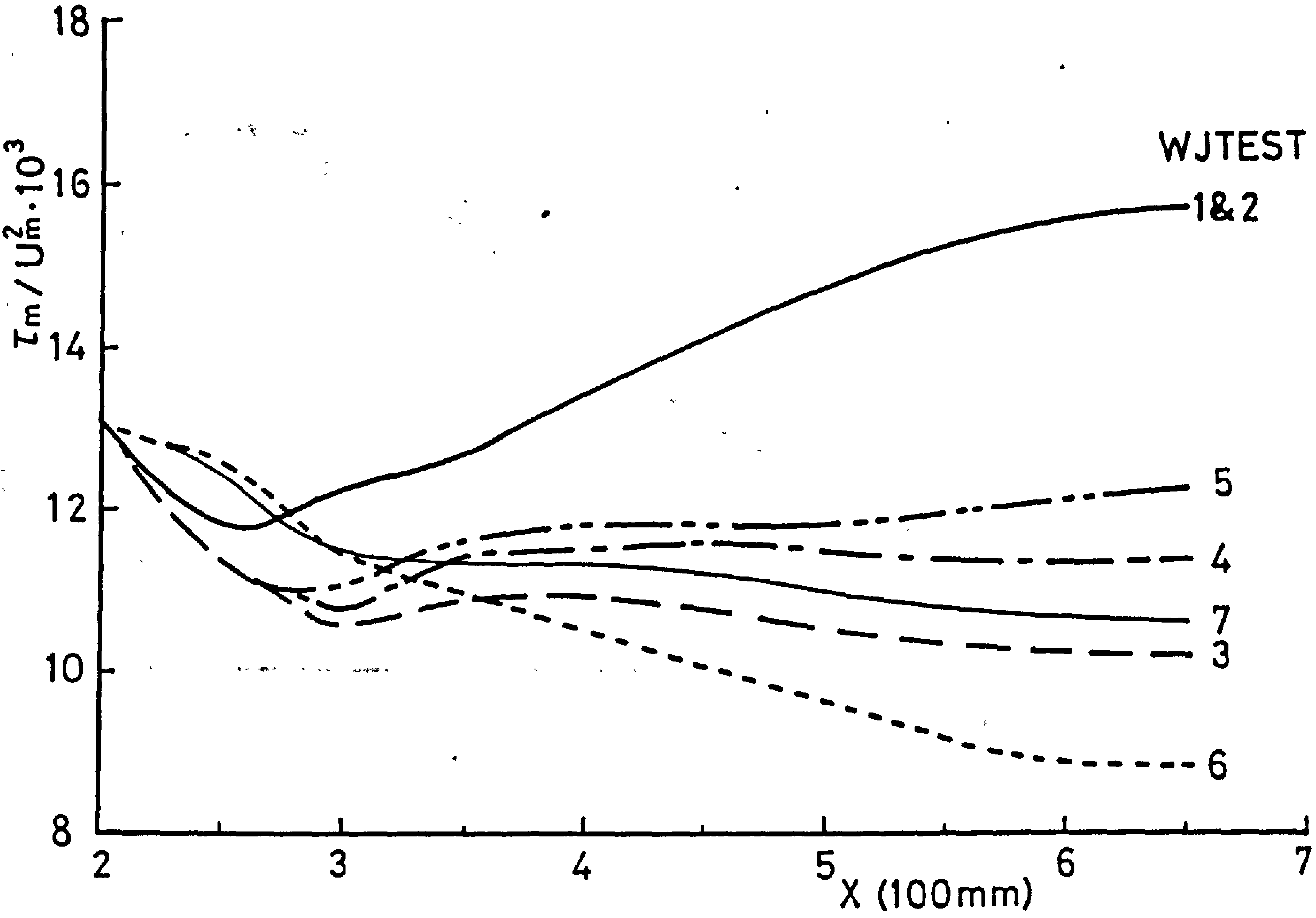

FIG. 5-11 DEVELOPMENT OF MAXIMUM SHEAR STRESS

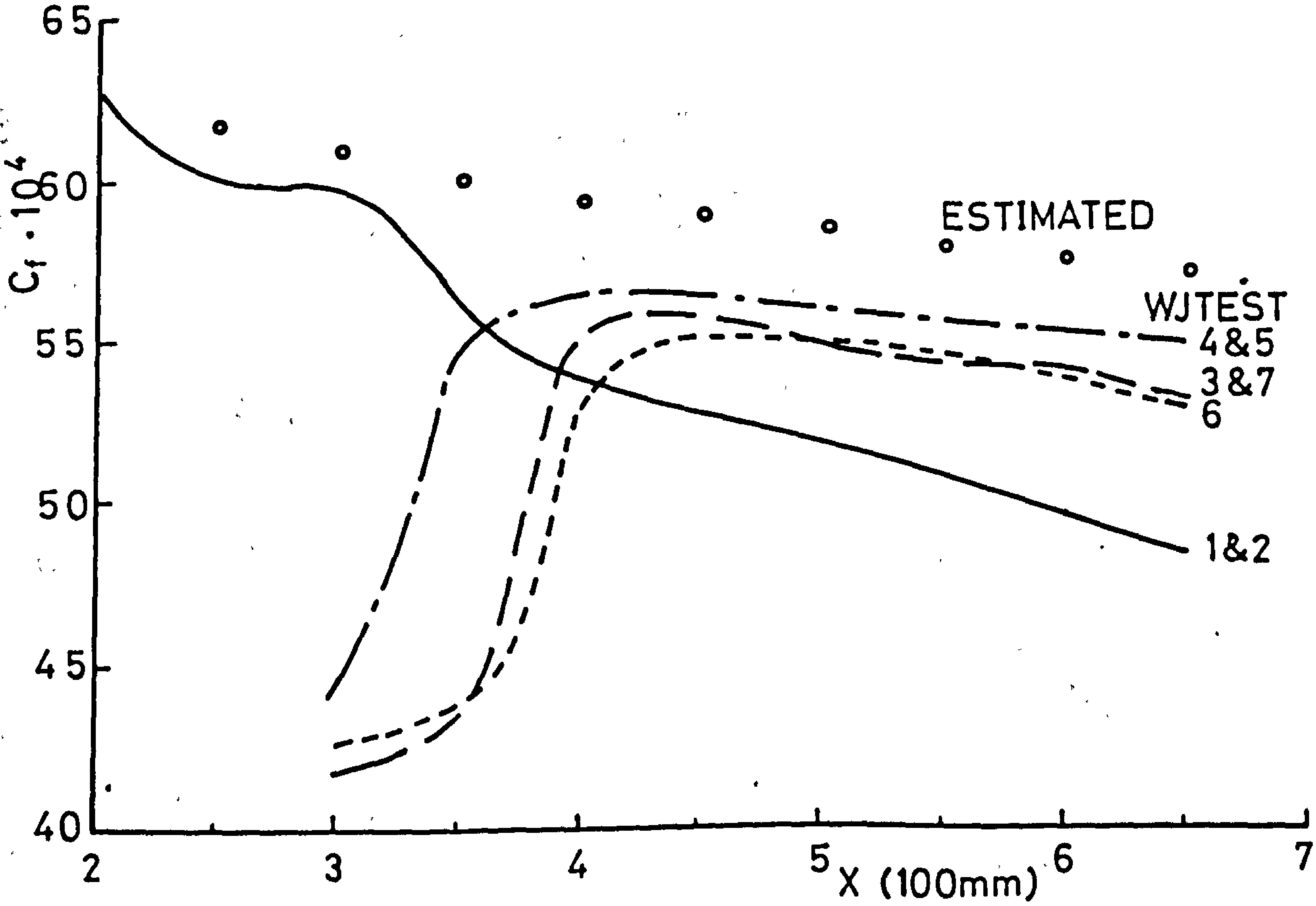

FIG. 5-12 DEVELOPMENT OF SKIN FRICTION COEFFICIENT

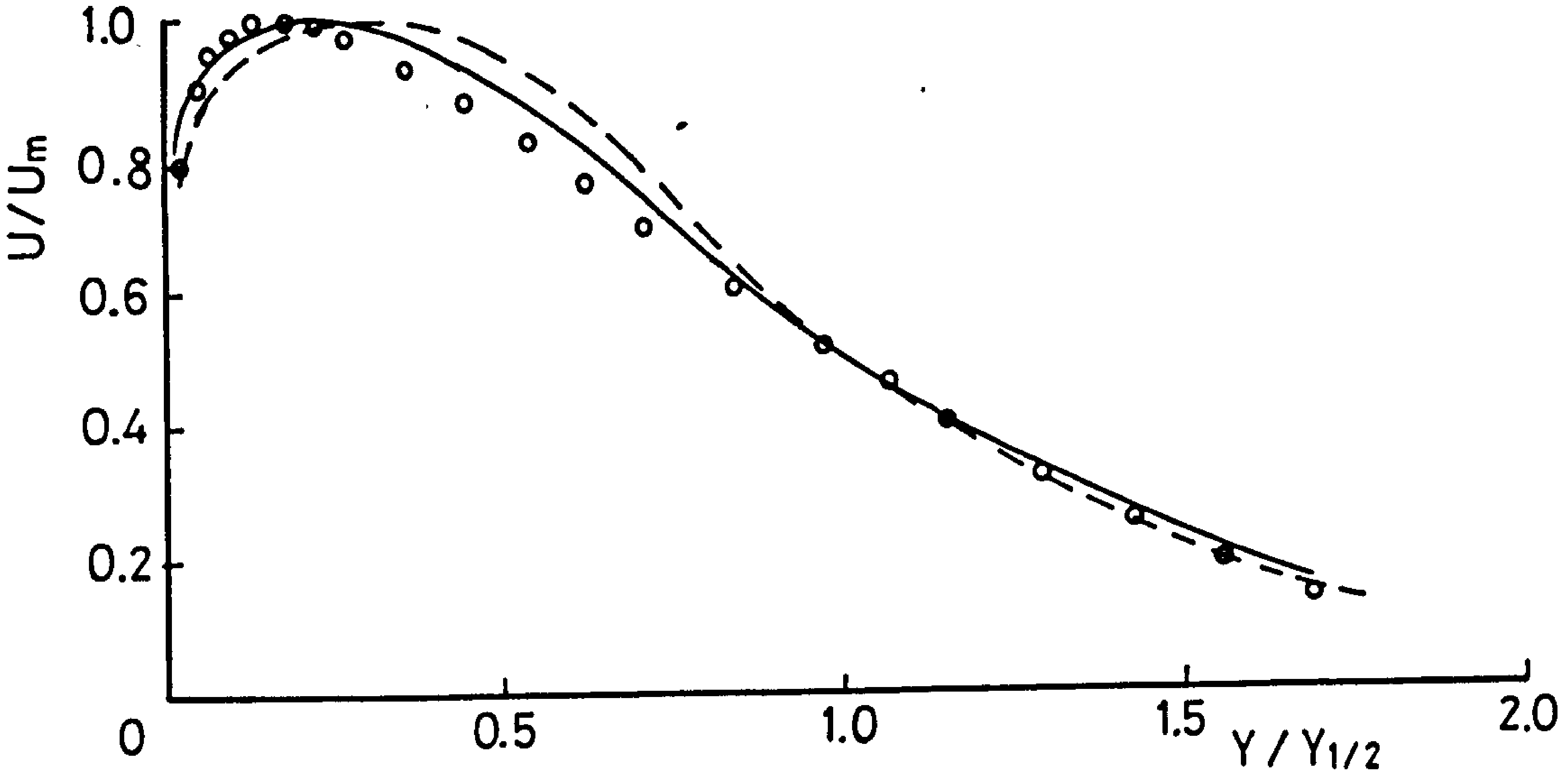

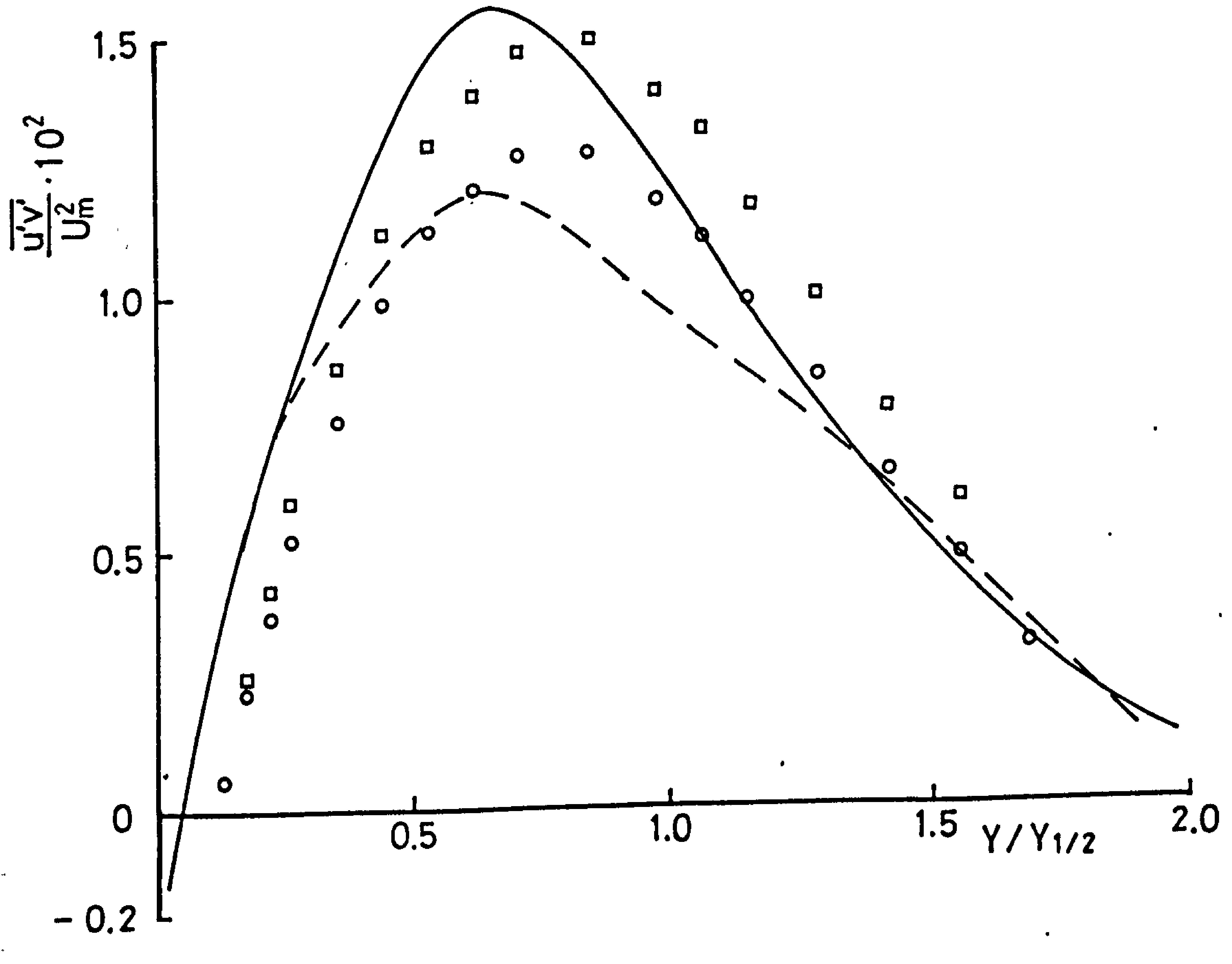

FIG. 5-13 WJTEST 2 VELOCITY AND SHEAR STRESS PROFILES

KEY TO SYMBOLS SEE FIG. 5-4

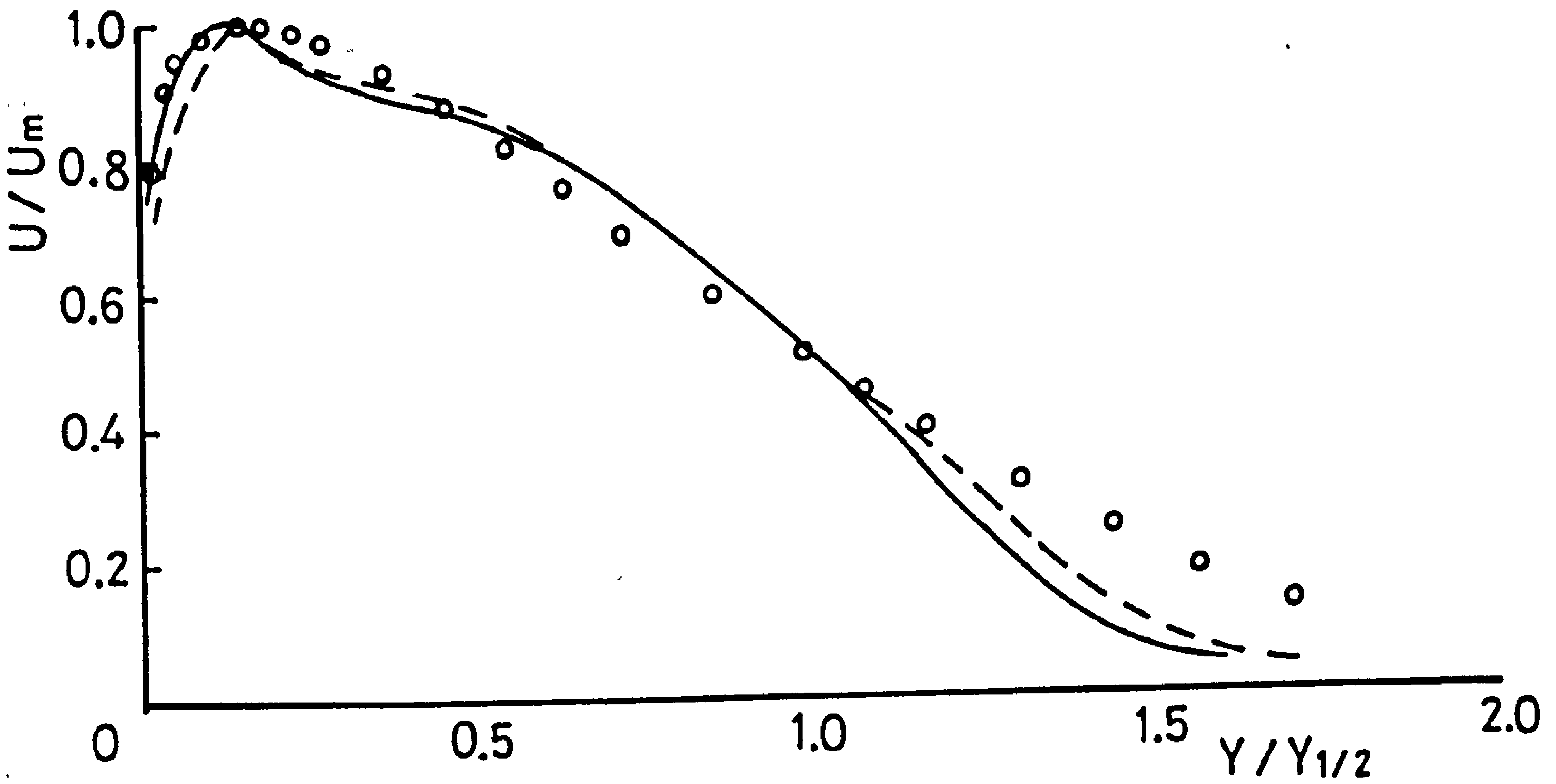

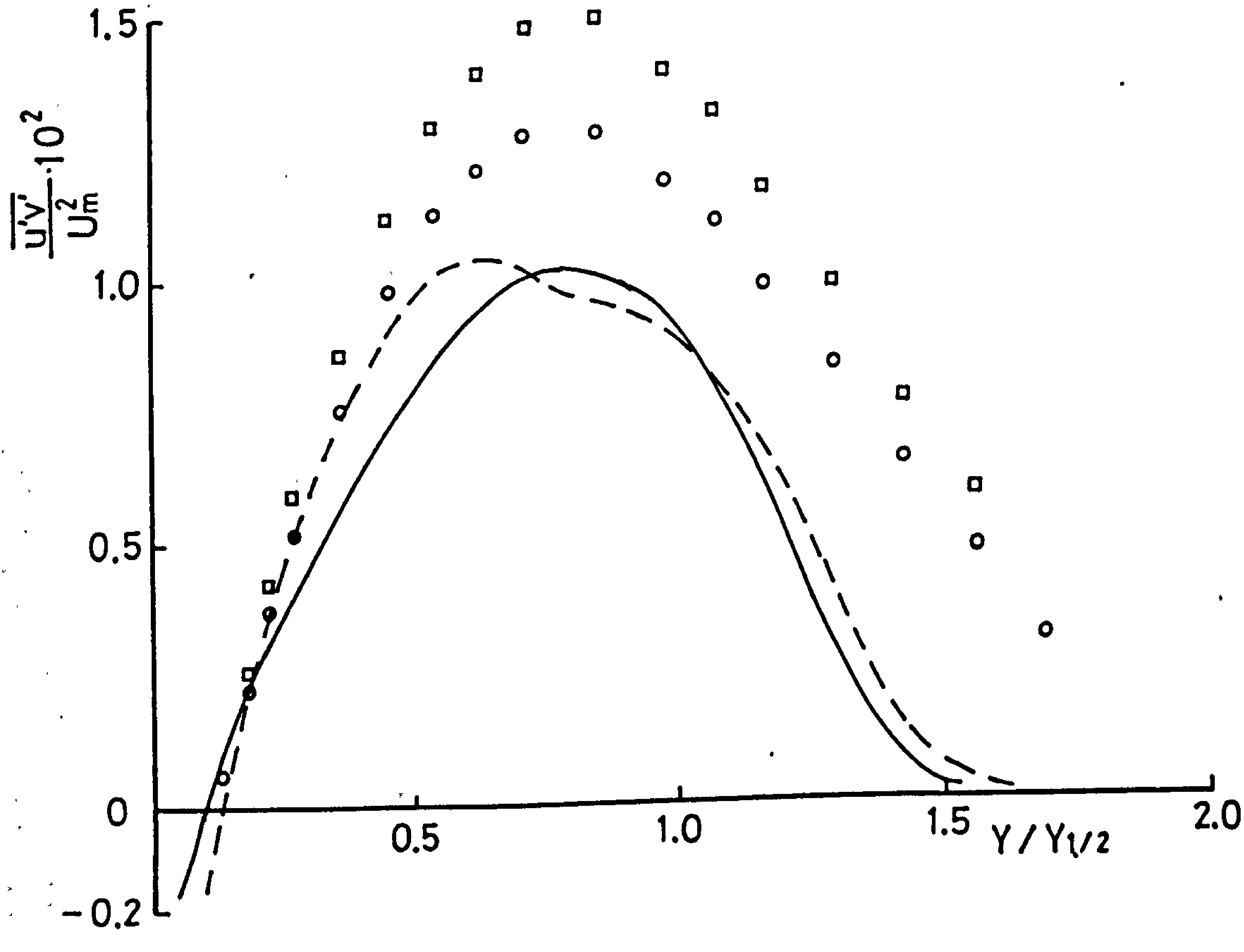

FIG. 5-14 WJTEST 3 VELOCITY AND SHEAR STRESS PROFILES

KEY TO SYMBOLS SEE FIG. 5-4

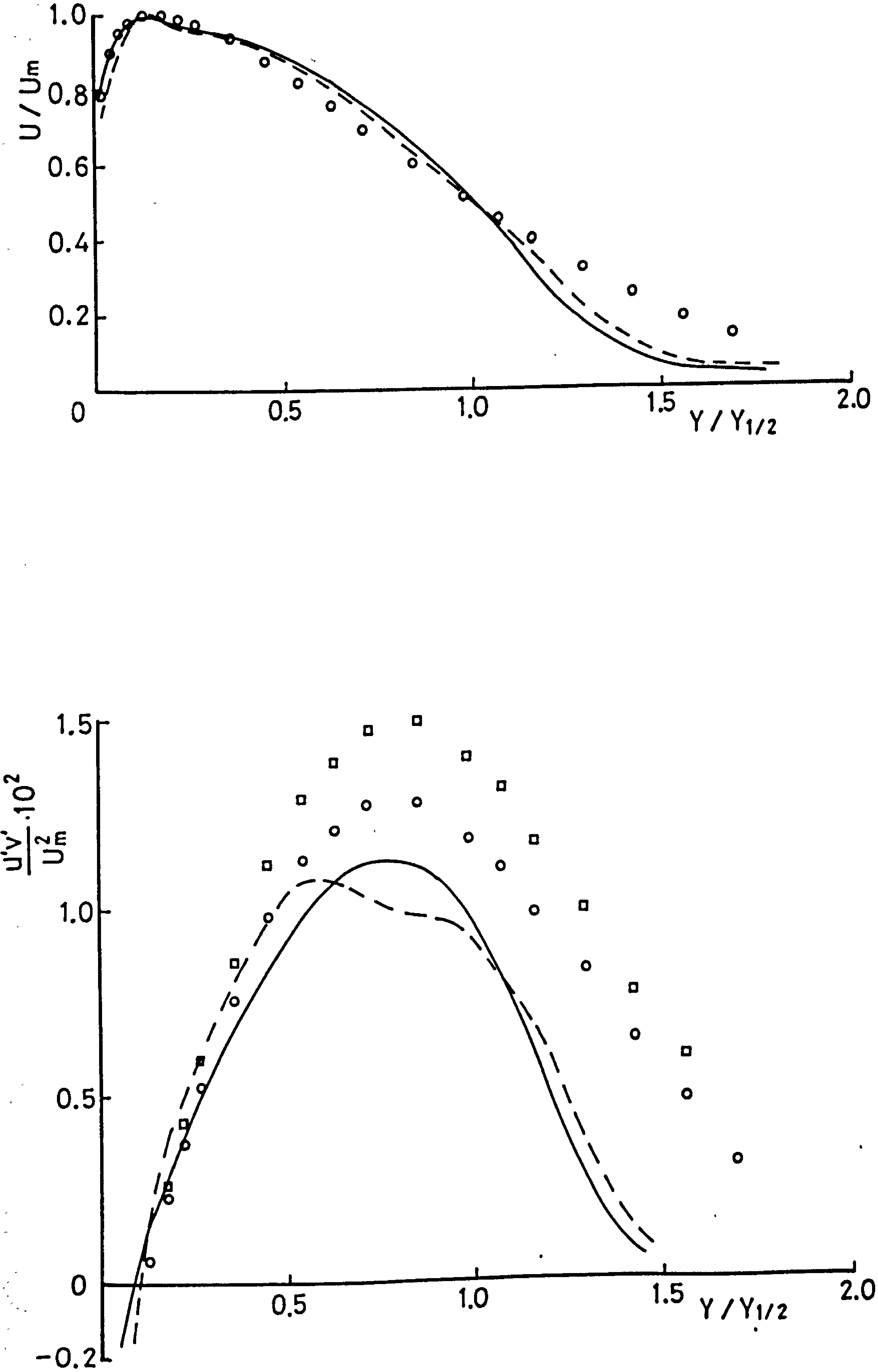

FIG. 5-15 WJTEST 4 VELOCITY AND SHEAR STRESS PROFILES

KEY TO SYMBOLS SEE FIG. 5-4

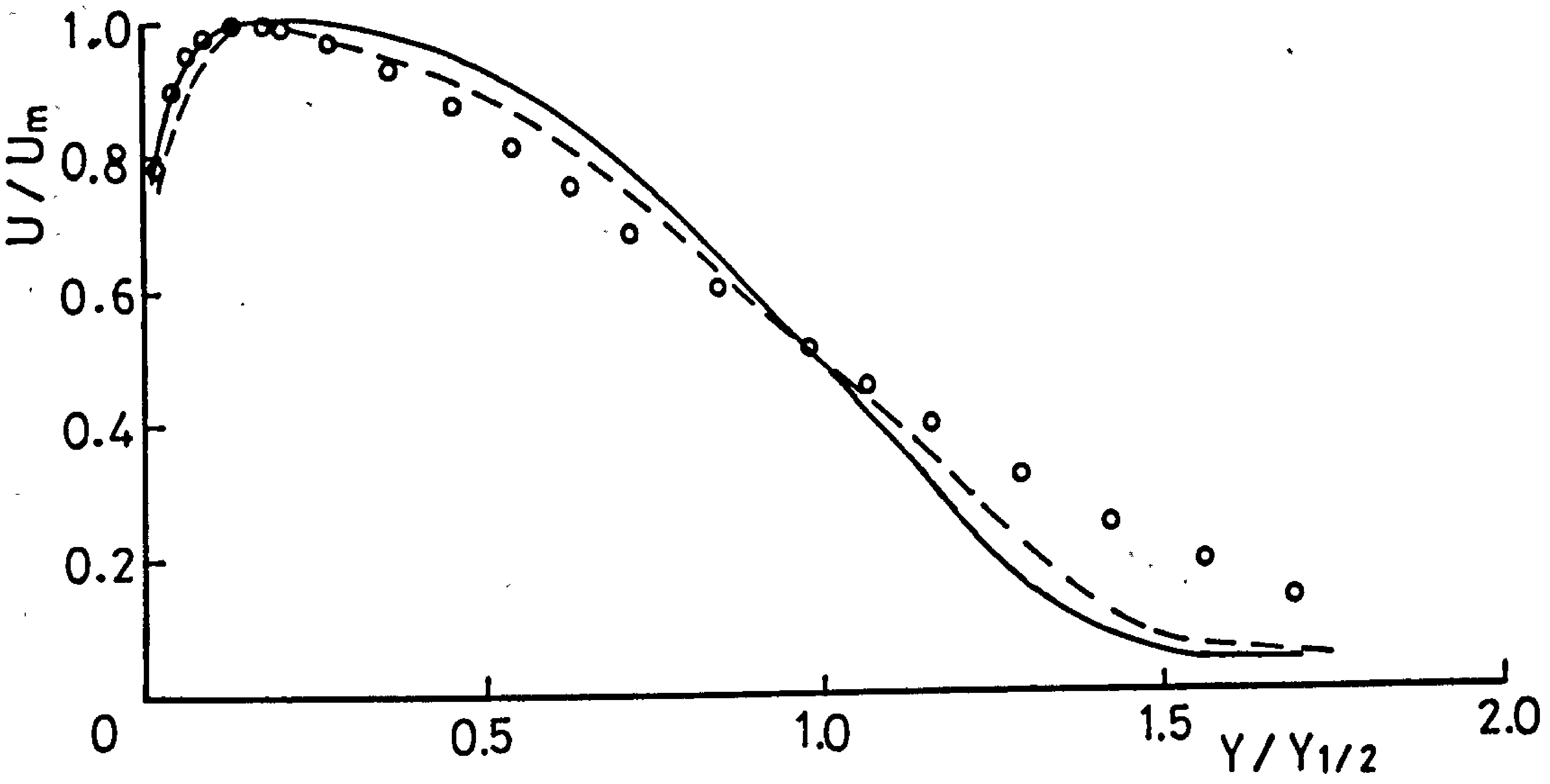

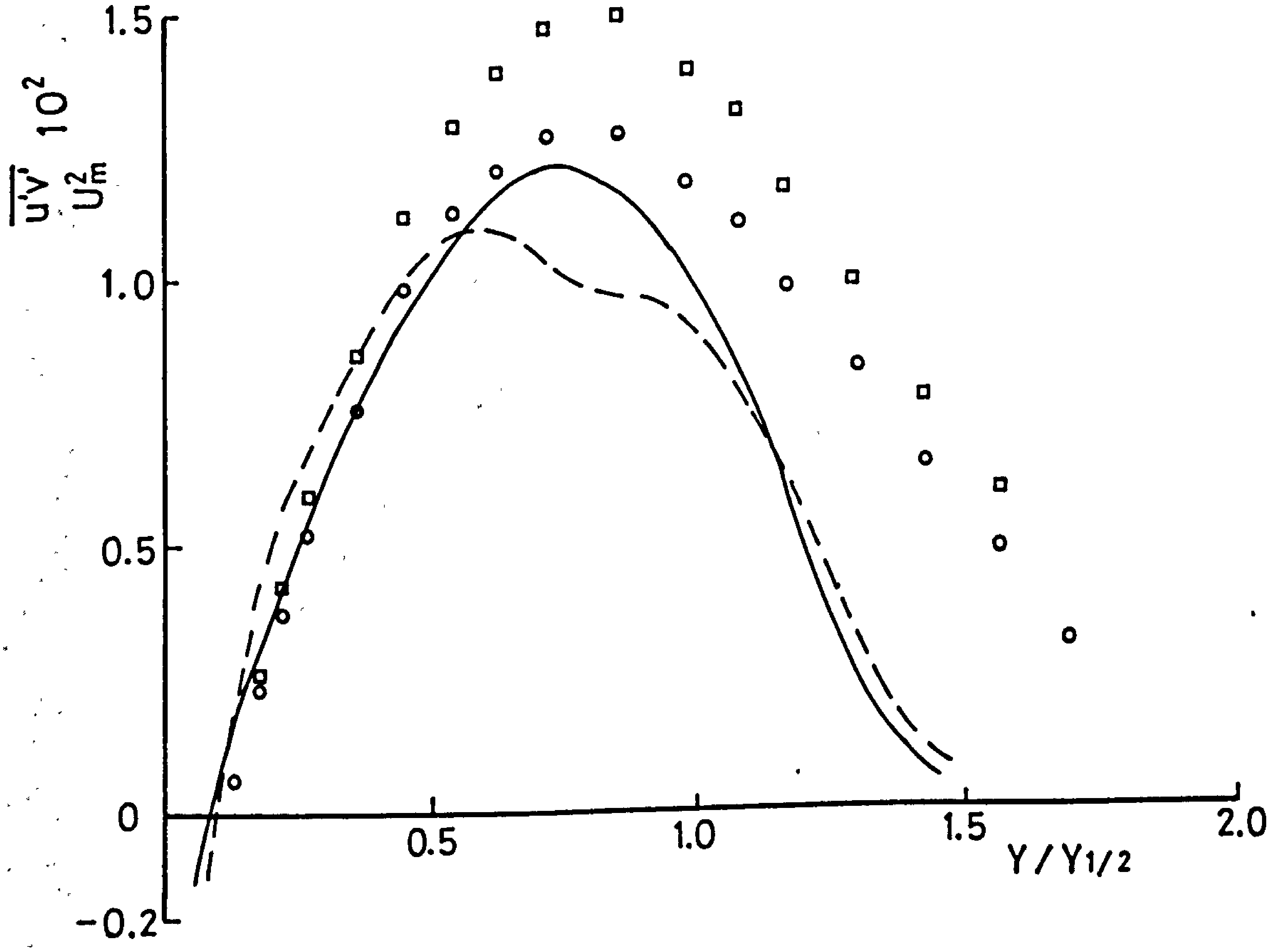

FIG. 5-16 WJTEST 5 VELOCITY AND SHEAR STRESS PROFILES

KEY TO SYMBOLS SEE FIG. 5-4

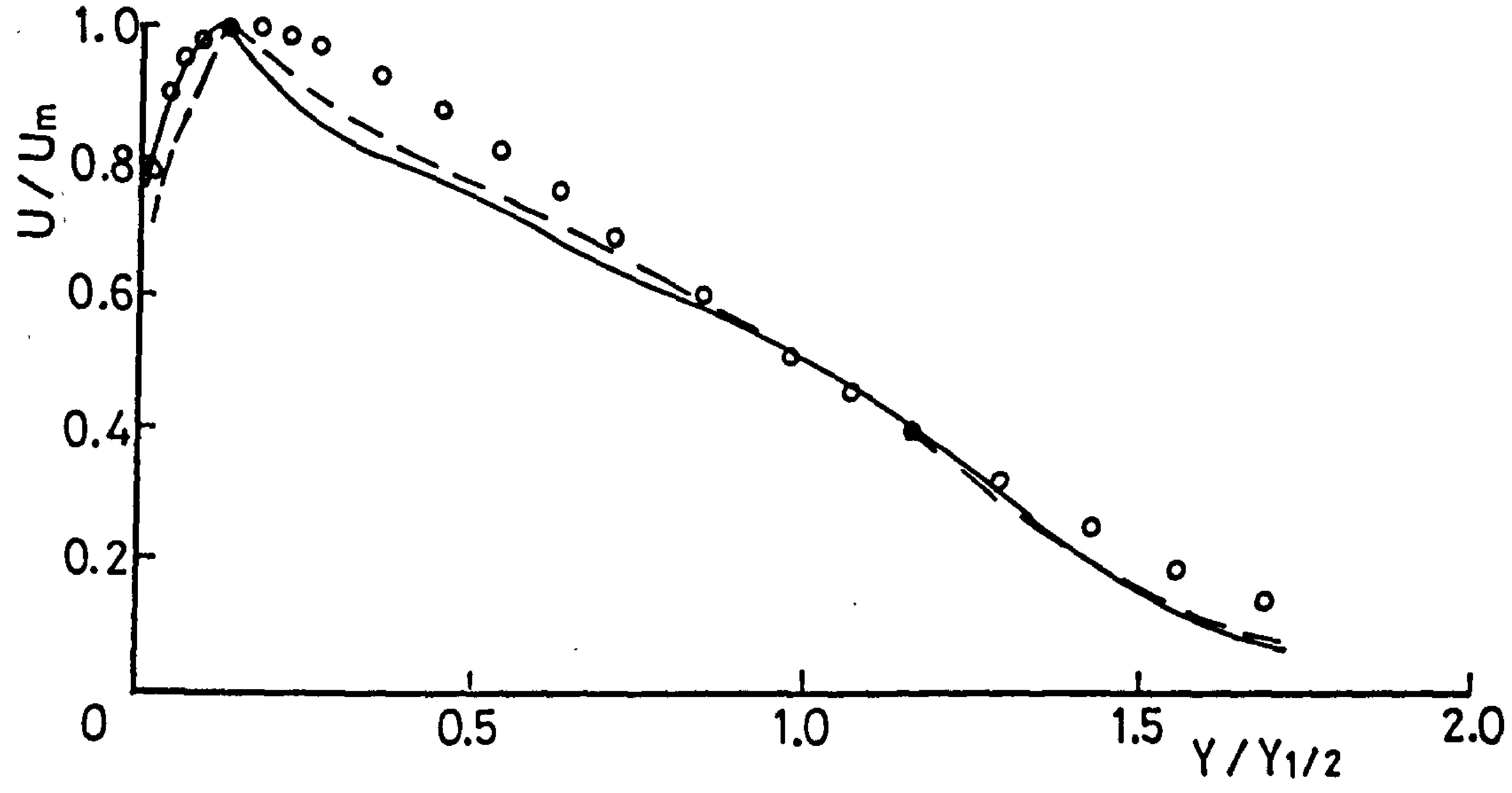

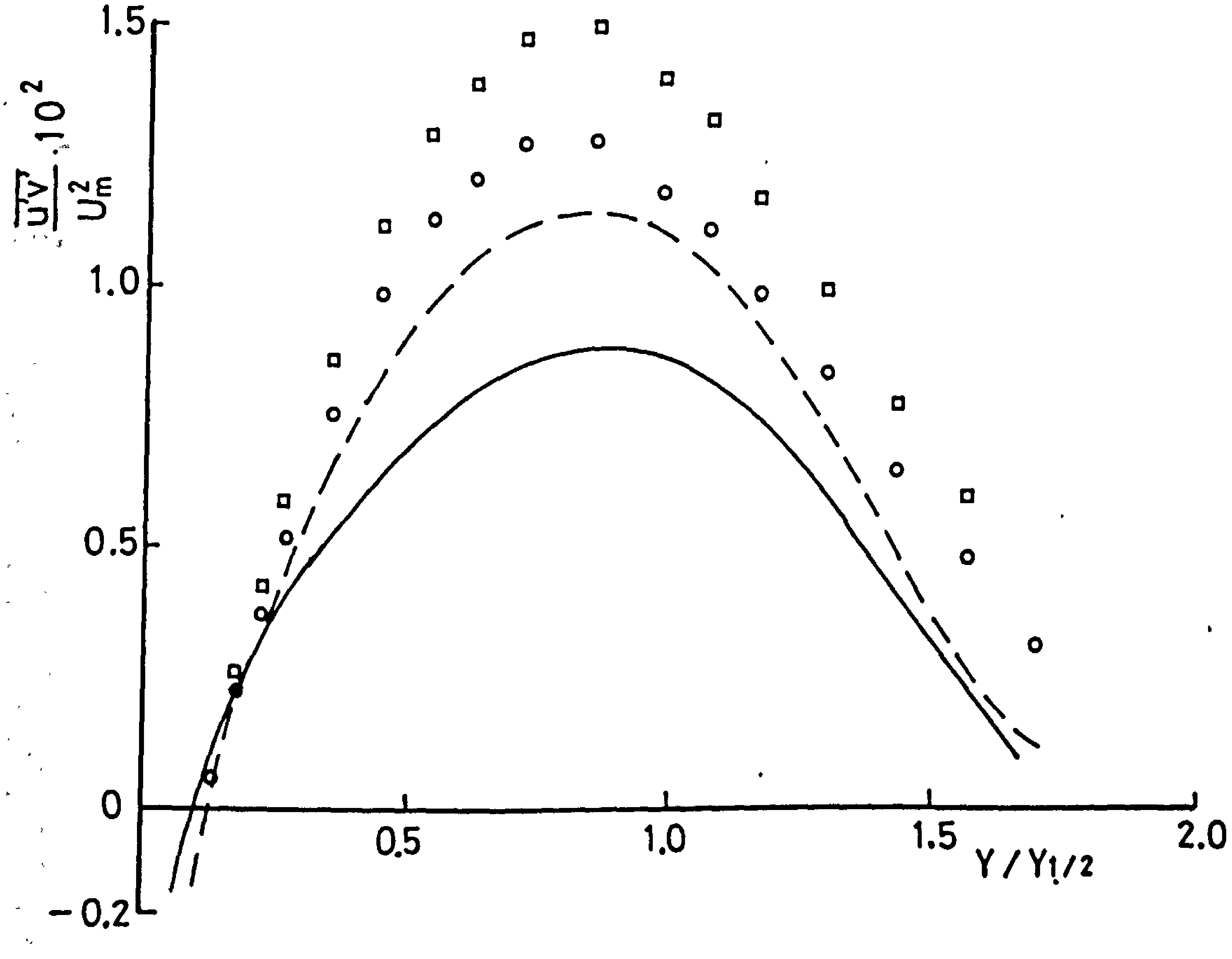

FIG. 5-17 WJTEST 6 VELOCITY AND SHEAR STRESS PROFILES

KEY TO SYMBOLS SEE FIG. 5-4

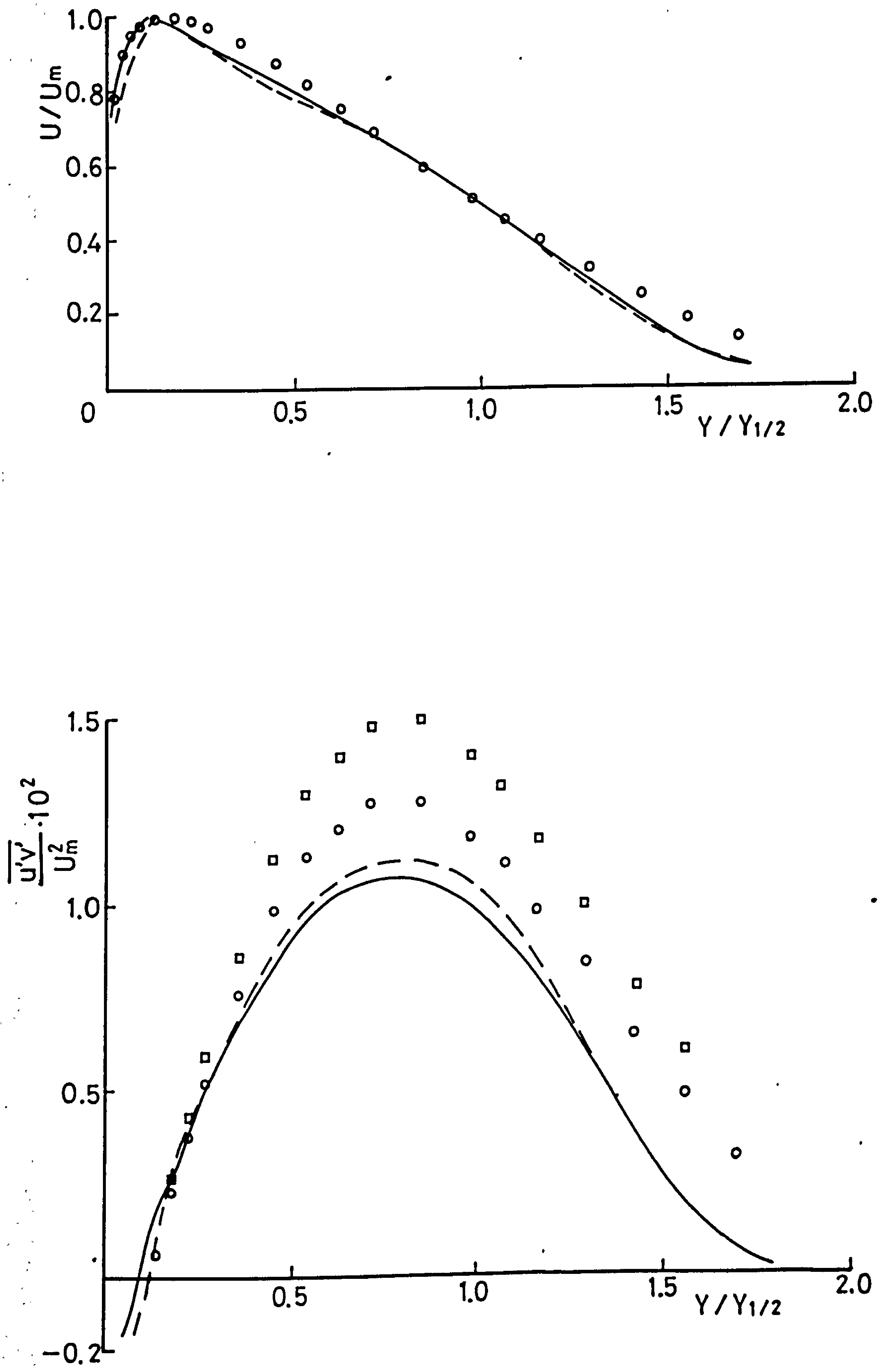

FIG. 5-18 WJTEST 7 VELOCITY AND SHEAR STRESS PROFILES

KEY TO SYMBOLS SEE FIG. 5-4

	Initial	Log. low constants		a_1	L/δ	G
	C_f	K	B			
TEST 1	0.00628	0.41	5.2	0.15	0.09*	*
TEST 2	0.0728	"	"	"	"	"
TEST 3	0.00528	"	"	"	"	"
TEST 4	0.0628	0.44	7.8	"	"	"
TEST 5	"	0.555	8.0	"	"	"
TEST 6	"	0.41	5.2	0.165	"	"
TEST 7	"	"	"	0.135	"	"
TEST 8	"	"	"	0.15	0.1125	"
TEST 9	"	"	"	"	0.0675	"
TEST 10	"	"	"	"	0.09*	+25%
TEST 11	"	"	"	"	"	-25%

TABLE 5-1 Parameters of TEST 1 to 11

*From Morel and Torda

	FUNCTION L	SHIFT	FUNCTION G	SHIFT
WJTEST 1	$Y \quad 0.225Y^{\frac{1}{2}} \quad L = 0.4Y$ $Y \quad 0.225Y^{\frac{1}{2}} \quad L = 0.09Y^{\frac{1}{2}}$	0	Morel & Torda free jet	0
WJTEST 2	From non-corrected energy balance	0	"	0
WJTEST 3	"	0	"	0
WJTEST 4	"	$0.003Y^{\frac{1}{2}}$	"	0
WJTEST 5	"	$0.006Y^{\frac{1}{2}}$	"	0
WJTEST 6	"	0	From corrected energy balance	0
WJTEST 7	"	$0.006Y^{\frac{1}{2}}$	"	$0.06Y^{\frac{1}{2}}$

TABLE 5-2 Functions of WJTEST 1 to 7

	X = 450 ~ 650mm	Values at X = 650mm						
	$\frac{dY_{\frac{1}{2}}}{dx}$	C_f	τ_m/U_m^2	Position of $\tau_m (Y/Y_{\frac{1}{2}})$	Position of $\tau=0 (Y/Y_{\frac{1}{2}})$	Position of $U_m (Y/Y_{\frac{1}{2}})$	Y_m (mm)	U_m (m/s)
Estimated from the measured values	0.069	0.00572	0.0132	0.79	0.115	0.18	46.5	21.2
WJTEST 1	0.066 (-4,3%)	0.00474 (-17.1%)	0.0157 (+18.9%)	0.65	0.045	0.30	42.6 (-8.4%)	23.8 (+12.3%)
WJTEST 2	0.066 (-4.3%)	0.00491 (-14.2%)	0.0157 (+18.9%)	0.67	0.050	0.30	43.3 (-6.9%)	23.4 (+10.4%)
WJTEST 3	0.051 (-26%)	0.00532 (-7.0%)	0.0102 (-22.7%)	0.77	0.095	0.12	39.5 (-15.1%)	24.8 (+17.0%)
WJTEST 4	0.053 (-23%)	0.00549 (-4.0%)	0.0114 (-13.6%)	0.76	0.090	0.12	40.4 (-13.1%)	23.9 (+12.7%)
WJTEST 5	0.053 (-23%)	0.00550 (-3.8%)	0.0123 (-6.8%)	0.76	0.090	0.20	40.3 (-13.3%)	23.5 (+10.8%)
WJTEST 6	0.053 (-23%)	0.00412 (-28.0%)	0.0088 (-33.3%)	0.83	0.100	0.11	40.7 (-12.5%)	25.0 (+17.9%)
WJTEST 7	0.053 (-23%)	0.00545 (-4.7%)	0.0106 (-19.7%)	0.78	0.085	0.11	41.4 (-11.0%)	24.0 (+14.2%)

TABLE 5-3 Results of WJTEST 1 to 7 and comparison with measured values ( ) Difference in % from the measured value

CHAPTER 6

CONCLUDING REMARKS AND RECOMMENDATIONS FOR FUTHER WORK

CHAPTER 6 CONCLUDING REMARKS AND RECOMMENDATIONS FOR FURTHER WORK

6-1 Concluding remarks

(1) A large amount of attention has been paid to establish a good quality flow which was mainly concerned with obtaining good two-dimensionality, and to obtain better accuracy in the measurements with the hot-wire anemometer system. The mean velocity components U and V and the turbulence stresses $\overline{u'^2}$, $\overline{v'^2}$, $\overline{w'^2}$ and $\overline{u'v'}$ have been measured. In addition, correlation and dissipation measurements have been made.

(2) The jet on the first plane surface is nearly self-preserving after X = 200mm i.e. X/b = 31.5. The growth rate of the jet is linear and is given by $dY\frac{1}{2}/dX = 0.069$. This value is slightly lower than that reported by Launder and Rodi (1981). The velocity profile is in good agreement with those measured by other investigators. There is a large scatter in the normal and shear stresses profiles among those previously reported. However, these profiles are reasonably in agreement with those of present measurements.

(3) At the first measured station on the curved surface i.e. X = 350mm, there is a considerable change in the flow. The maximum flow velocity increases and this produces the reduced turbulence intensity in the longitudinal direction. The growth of jet stays the same as on the plane surface. Other stresses $\overline{v'^2}$, $\overline{w'^2}$ and $\overline{u'v'}$ increase at this station.

(4) On the curved surface, the flow does not reach an equilibrium

state, nevertheless the mean velocity components show some sign of an equilibrium state. The growth rate is 0.39 which is much larger than that on plane surface. The rate becomes linear again until at just downstream at the end of the curved surface i.e. X = 550mm. The velocity profile becomes fuller than that on the plane surface. The levels of the stresses $\overline{u'^2}$, $\overline{v'^2}$, $\overline{w'^2}$ and $\overline{u'v'}$ increase, particularly $\overline{v'^2}$, until X = 550mm and their profiles keep changing their shapes throughout on the curved surface.

(5) At the beginning of the second surface, the change is not as immediate as is the case at the beginning of the curved surface. The growth rate of the jet becomes nearly linear and reaches almost the same rate as on the first plane surface. The velocity profile, however, still changes slightly. The levels of stresses $\overline{u'^2}$, $\overline{v'^2}$, $\overline{w'^2}$ and $\overline{u'v'}$ decrease gradually till the end of the surface. This flow also does not settle to an equilibrium state.

(6) The corrections for directional sensitivity on hot-wires are not negligible in a high turbulence intensity flow and they have been applied to the stress measurements. The levels of the corrections are particularly high at X = 550mm due to the high intensity turbulence. The correction involved the higher order correlations so that $\overline{u'v'^2}$ and $\overline{u'w'^2}$ measurements have been made.

(7) . The correlations indicate that there are mixing jet type motions of the type which were reported by Bradshaw et al (1964). The jet motions exist in the X-Y plane at middle to outer part of the

jet and are inclined. At X = 550mm the size of the motions is relatively smaller than those on the plane surface. However the relative size in the Z direction does not change, the motions are not as strong as those in a round jet. The range of the eddy size stays unchanged on both the plane surface and at the end of the curved surface, however, the normalized integral scale $L_f/Y_{\frac{1}{2}}$ is larger on the plane surface.

(8) The additional dissipation measurements enable the evaluation of the terms of the turbulent kinetic energy balance equation except for the diffusion term. This term has been obtained by difference. The energy balances, which have been corrected to balance out the diffusion across the flow, have also been evaluated because of some uncertainties in the dissipation measurements. The balances on the first plane surface and the end of the curved surface are generally in reasonable agreement. The levels of terms are, however, much higher at X = 550mm than those on the first plane surface.

(9) The Bradshaw-Ferriss-Atwell method has been used together with the interaction approach, which was introduced by Bradshaw et al. (1973), in order to calculate a wall jet on plane surface. The empirical functions used on the outer layer were calculated from the measured energy balances. The results have been compared with those calculated with Morel and Torda's (1974) functions for a free jet.

(10) The results, particularly for the velocity profile, are very sensitive to the empirical function L. The use of the empirical

functions for free jets produced a fuller velocity profile and rather different shear stress profile when compared with those of experiments.

(11) The results with the functions calculated from the measured energy balance produces a rather distorted velocity profile but the shear stress profile is in good agreement with those measured. The velocity profile is very sensitive to a shift of the function L in the Y direction, so that it may be possible to adjust the function to obtain an optimum velocity profile.

(12) The good agreement between the measured and the calculated shear stress profile indicates that the present method and the assumptions made are valid. However, the interaction between layers in wall jets is not as simple as those of duct flows, mixing layers, wakes and free jets so that a special treatment of empirical functions is necessary.

6-2 Recommendations for further work

(1) The present experiments have been carried out with a single slot Reynolds number = 2.54×10^4. It has been reported that there is a shift in the development of the growth of the jet with different slot Reynolds numbers. The identical measurements with various Reynolds numbers would be interesting in order to observe the effects of Reynolds number change on the flow.

(2) The turbulence quantities did not settle to an equilibrium state on the curved and the second plane surfaces. It may be useful to

carry out measurements with a mild curvature parameter e.g. $k = 2/3$, or longer second plane surface. This may provide enough evidence to observe the cause of the non-equilibrium state on the surfaces. The cause has been suggested as being three-dimensional effects or the fact that the surfaces are too short.

(3) In order to carry out the above measurements and/or further measurements, it is recommended to develop an on-line data acquisition system. The output signals from C.T.A and the signal to indicate the current position of the hot-wire could be converted to digital signals and are fed into a computer. The linearization of the C.T.A. signals could be done in the computer so that it eliminates the rather complex and awkward linearizer operation. It may take some time to develop such a system and the software. However in order to collect and process much more data than has been obtained in the present measurements, it will eventually save a considerable amount of time.

(4) More correlations such as $R_{11}(0:0,r_2,0)$ and $R_{22}(0:0,0,r_3)$ would make it possible to draw more detailed conclusions covering the large eddy structures of turbulence. The use of the conditional sampling technique is even better. The coherent structures in the flow can be understood better with this technique. The conditional sampling, however, requires the computer controlled data acquisition system.

(5) There are advantages and disadvantages in each method to correct a hot-wire's directional sensitivity in highly turbulent flows.

The comparisons between the results of various methods may help to evaluate the accuracy of the present method.

(6) The use of an electrostatic filter and a large capacity flow temperature control system are essential if hot-wires are used for mean flow velocity measurements. The effect of wire contamination by small dust particles, which are difficult to remove with fabric filters, is large. The change in flow temperature also affects in the accuracy of the hot-wire measurements.

(7) It seems to be possible to adjust the empirical functions in the calculations to obtain a velocity profile close to the measured profile. Having established the empirical functions for a plane wall jet, the further calculation for a curved wall jet should be carried out.

REFERENCES

References

Acrivlellis, M.
Finding the spatial flow field by means of hot-wire anemometry.
DISA Information, No.22, p21, 1977.

Acrivlellis, M.
An improved method for determining the flow field of multi-dimensional flows of any turbulence intensity.
DISA Information, No. 23, p11, 1978.

Acrivlellis, M.
Flow field dependence on hot-wire probe cooling law and probe adjustment.
DISA Information, No.23, p17, 1978.

Alcaraz, E., Charnay, G. and Mathieu, J.
Measurements in a wall jet over a convex surface.
Physics of Fluids, Vol.20, No.2, p203, 1977.

Bakke, P.
An experimental investigation of a wall jet.
Journal of Fluid Mechanics, Vol.2m p467, 1957.

Bartenwerfer, M.
Remarks on hot-wire anemometry using "squared signals",
DISA Information, No.24, 1979.

Bradbury, L.J.S.
The structure of a self-preserving turbulent plane jet.
Journal of Fluid Mechanics, Vol.23, p31, 1965.

Bradshaw, P. and Gee, M.T.
Turbulent wall jets with and without an external stream.
Aeronautical Research Council, R & M 3252, 1960.

Bradshaw, P., Ferriss, D.H. and Johnson, R.F.
Turbulence in the noise-producing region of a circular jet.
Journal of Fluid Mechanics, Vol.19, p591, 1964.

Bradshaw, P., Ferriss, D.H. and Atwell, N.P.
Calculation of boundary later development using the turbulence energy equation.
N.P.L. Aero. Report 1182, 1966.
also Journal of Fluid Mechanics, Vol.28, p593, 1967.

Bradshaw, P.
An introduction to turbulence and its measurement.
Pergamon Press, Oxford, 1971.

Bradshaw, P., and Ferris, D.H.
Application of a general method of calculating turbulent shear layers.
Trans. ASME, Journal of Fluids Engineering, Vol. 94, p.345, 1972.

Bradshaw, P.
Effects of streamline curvature on turbulent flow.
AGARDograph, No. 169, 1973.

Bradshaw, P., Dean, R.B. and McEligot, D.M.
Calculation of interacting turbulent shear layers: Duct flow,
Trans. ASME, Journal of Fluids Engineering, P.214, June, 1973.

Bradshaw, P. and Unsworth, K.
An improved FORTRAN program for the Bradshaw-Ferris-Atwell method of calculating turbulent shear layers.
Imperial College Aero. Report, 74-02, Imperial College of Science and Technology, London, 1974.
Reprinted with minor revisions, Nov., 1980.

Bradshaw, P.
Introduction to the section on "coherent structures",
Turbulent shear flow 2.
Edited by Bradbury, L.J.S., Durst, F., Launder, B.E.,
Schmidt, F.W. and Whitelaw, J.H.
Springer-Verlag, Berlin, p.259, 1980.

Brown, G.L. and Roshko, A.
On density effects and large structures in turbulent mixing layers.
Journal of Fluid Mechanics, Vol.64, p.775, 1974.

Champagne, F.H., Sleicher, C.A. and Wehrmann, O.H.
Turbulence measurements with inclined hot-wires.
Part. 1, Heat transfer experiments with inclined hot-wire.
Journal of Fluid Mechanics, Vol.28, p.153, 1967.

Champagne F.H. and Sleicher, C.A.
Turbulence measirements with inclined hot-wires.
Part 2, Hot-wire response equations.
Journal of Fluid Mechanics, Vol.28, p.177, 1967.

Coanda, H.
Procédé de propulsion dans un fluide.
Brenet Invent. Gr. Cl.2, No. 762688, République Française, 1932.

Crow, S.C. and Champagne, F.H.
Orderly structure in jet turbulence.
Journal of Fluid Mechanics, Vol.48, p.547, 1971.

Davis, P.O.A.L. and Yule, A.J.
Coherent structures in turbulence.
Journal of Fluid Mechanics, Vol. 69, p.513, 1975.

DISA
Instruction manual for 55M system with 55M10 C.T.A.
Standard bridge.

DISA
Instruction and service manual for type 55D10 Linearizer.

DISA
Instruction and service manual for type 55D35 R.M.S. Voltmeter.

DISA
Instruction manual for type 52B25 Turbulence processor.

DISA
Instruction manual for type 55D70 Analog Correlator.

DISA
Instruction for the T.C.A. system.

DISA
Instruction manual for type 55A06 Random signal indicator and correlator.

DISA
Instruction manual for type 55D41 calibration unit.

Fekete, G. I.
Coanda flow in a two-dimensional wall jet on the outside of a circular cylinder.
Mech. Eng. Dept. Report, No. 63-11, McGill University, 1963.

Ferriss, D.H. and Bradshaw, P.
A computer program for the calculation of boundary-layer development using the turbulent eneregy equation.
N.P.L. Aero. Report 1195, 1966.

Förthmann, E.
Über turbulente Strahlausbreitung.
Ingenieur-Archiv, Vol. 5, p.42, 1934.

Gibson, M.M. and Younis, P.A.
Calculation of a turbulent wall jet on a curved wall with a Reynolds stress model of turbulence.
Proc. 3rd. Symposium on turbulent shear flows, Davis, Calif. 1981.

Giles, J.A., Hays, A.P. and Sawyer, R.A.
Turbulent wall jets on logarithmic spiral surfaces.
Aeronautical Quarterly, Vol. 17, p.201, 1966.

Gilmore, D.C.
The probe interference effect of hot-wire anenometers.
Mech. Eng. Dept., TN67-3, McGill University, 1967.

Glauert, M.B.
The wall jet.
Journal of Fluid Mechanics, Vol. 1, p.625, 1956.

Grant, H.L.
The large eddies of turbulent motion.
Journal of Fluid Mechanics, Vol. 4, p.149, 1958.

Guitton, D.E.
Two-dimensional turbulent wall jets over curved surfaces.
Mech. Eng. Dept., Report, No. 64-7, McGill University, 1964.

Guitton, D.E.
Correction of hot-wire data for high intensity turbulence, logitudinal cooling and probe interference.
Mech. Eng. Dept., Report, No. 68-6, McGill University, 1968.

Guitton, D.E.
Some contributions to the study of equilibrium and non-equilibrium wall jets over curved surfaces.
PhD. thesis, Mech. Eng. Dept., McGill University, 1970.

Guitton, D.E.
The effect of high intensity turbulence on the response of a hot-wire.
Canadian Aeronautics and Space Institute Transactions, Vol. 7, No. 2, 1974.

Guitton, D.E. and Newman, B.G.
Self-preserving wall jets over convex surfaces.
Journal of Fluid Mechanics, Vol. 81, p.155, 1977.

Hanjalic, K. and Launder, B.E.
A Reynolds stress model of turbulence and its application to thin shear flows.
Journal of Fluid Mechanics, Vol. 52, p.609, 1972.

Heskestad, G.
Hot-wire measurements in a plane turbulent jet.
Trans. ASME, Journal of Applied Mechanics, Vol. 32, p.721, 1965.

Hinze, J.O.
Turbulence.
2nd Edition, McGraw Hill, New York, 1975.

Irwin, H.P.A.H.
Measurements in a self-preserving wall jet in a positive pressure gradient.
Journal of Fluid Mechanics, Vol. 61, p33, 1973.

Irwin, H.P.A.H.
Measurements in blown boundary layers and their prediction by Reynolds stress modelling.
PhD. thesis, McGill University, 1974.

Jerome, F.E., Guitton, D.E. and Patel, R.P.
Experimental study of the thermal wake interference between closely spaced wires of a X-type hot-wire probe.
Aeronautical Quarterly, Vol.22, p.119, 1971.

Jones, W.P. and Launder, B.E.
Prediction of laminarization with a two-equation model of turbulence.
International Journal of Heat and Mass Transfer, Vol. 15, p.301, 1972.

Jørgensen, F.E.
Directional Sensitivity of wire and fiber-film probes,
DISA Information, No.11, p.31, 1971.

Kanemoto, K.
Investigation of turbulent wall jets over logarithmic spiral surfaces. Part 1: Development of jets and similarity of velocity profile. Part 2: Properties of flow near wall.
Bulletin of the Japan Society of Mechanical Engineers, Vol 17, No. 105, p.335, 1974.

Kobayashi, R. and Fujosawa, N.
Curvature effects on two-dimensional turbulent wall jets.
Ingenieur Archiv. Vol.53, p.409, 1983.

Launder, B.E. and Spalding, D.B.
The numerical computation of turbulent flows.
Computer Methods in Applied Mechanics and Engineering, Vol. 3, p.269, 1974.

Launder, B.E. and Rodi, W.
The turbulent wall jet.
Progress in Aerospace Science, Vol. 19, p.81, 1981.

Launder, B.E. and Rodi, W.
The turbulent wall jet - measurements and modeling.
Annual Review of Fluid Mechanics, Vol. 15, p.429, 1983.

Lim, E.H.
Spatial variation of velocity profile and turbulence structure in turbulent internal flows.
PhD. thesis, Salford University, 1980.

Martinez-val, R., Jimenez, J. and Rebollo, M.
Sensor contamination effect in hot-wire anemometry in air.
DISA Information, No. 27, p.12, 1982.

Morel, T.
Calculation of the free turbulent mixing. Interaction approach.
PhD. thesis, Illinois Institute of Technology, Chicago, Ill, 1972.

Morel, T. and Torda, T.P.
Calculation of free turbulent mixing by the interaction approach.
AIAA Journal, Vol. 12, No. 4, p.533, 1974.

Morrow, T.B.
Effects of dirt accumulation on hot-wire and hot-film sensors.
Fluid dynamic measurements in the industrial and medical environments, Edited by Cockrell, D.J.,
Leicester University Press, Vol. 1, p.122, 1972.

Nakaguchi, H.
Jet along a curved wall.
Dept. of Aeronautics, University of Tokyo, R & M No. 4, 1961.

Newman, B.G.
The deflexion of plane jets by adjacent boundaries - Coanda effect.
Boundary layer and flow control, Edited by Lachmann, G.V.,
Pergamon Press, Oxford, Vol. 1, p.232, 1961.

Ng. K.H.
Prediction of turbulent boundary layer development using a two equation model of turbulence.
PhD. Thesis, University of London, 1971.

Patankar, S.V. and Spalding, D.B.
Heat and Mass transfer in Boundary Layers.
Morgan-Grampian, London, 1967.

Patel, R.P.
Self-preserving, two-dimensional turbulent jets in a moving stream.
M. Eng. Thesis, Mech. Eng. Dept., McGill University, 1962.

Perry, A.E.
Hot-wire anemometry.
Clarendon Press, Oxford, 1982.

Reynolds, O.
Suspension of a ball by a jet of fluid.
Proceedings of the Literary and Philosophical Society of Manchester, Vol. 9, No. 13, p.133, 1870.

Rodi, W. and Spalding, D.B.
A two-parameter model of turbulence and its application to free jets.
Waerme-Stoffuebertrag, 3, 85, 1970.

Rodi, W.
A new method of analysing hot-wire signals in highly turbulent flow, and its evaluation in a round jet.
DISA Information, No. 17, p.9, 1975.

Rodi, W., Celik, I., Demuren, A.O., Scheuerer, G., Shirani, E., Leschziner, M.A. and Rastogi, A.K.
Calculations for the 1980/81 AFOSR-HTTM-Stanford Conference on complex turbulent flows.
University of Karlsruhe Report, SFB80/T/199, 1981.

Rose, W.G.
Some corrections to the linearized response of a constant temperature hot-wire anemometer operated in a low speed flow.
Trans. ASME, Journal of Applied Mechanics, Vol. 29, p.554, 1962.

Sawyer, R.A.
Two-dimensional turbulent jets with adjacent boundaries.
PhD. thesis, Cambridge University, 1962.

Sawyer, R.A.
The growth of two and three-dimensional turbulent wall jets on curved surfaces.
Internal Report, Salford University, FM/13/72, 1973.

Simpson, L.
Two-dimensional turbulent wall jets.
B.Sc Project Report, Aero and Mech. Eng., Salford University, 1970.

Tailland, A. and Mathieu, J.
Jet Pariétal.
Journal de Mécanique, Vol. 6, p. 103, 1967.

Tailland, A.
Contribution à l'etude d'un jet plan dirigé tangentiellement à une paroi plane.
Thèse de Docteur es Sciences, University Claude Bernard, Lyon, 1970.

Townsend, A.A.
The structure of turbulent shear flow.
Cambridge University Press, 1st. Edition, 1956.
2nd Edition, 1975.

Townsend, A.A.
Entrainment and the structure of turbulent flow.
Journal of Fluid Mechanics, Vol. 41, p.13, 1970.

Verhoff, A.
Steady and pulsating two-dimensional turbulent wall jets in a uniform stream.
Princeton University Report, No. 723, 1970.

Wille, R. and Fernholz, H.
Report on the first European Mechanics Colloquium on the Coanda effect.
Journal of Fluid Mechanics, Vol. 23, p.801, 1965.

Wilson, D.J.
An experimental investigation of the mean velocity, temperature and turbulence fields in plane and curved two-dimensional wall jets: Coanda effect.
PhD. Thesis, Mech. Eng. Dept. University of Minnesota, 1970.

Wilson, D.J. and Goldstein, R.J.
Turbulent wall jets with cylindrical streamwise surface curvature.
Trans. ASME, Journal of Fluids Engineering, Vol. 98, p.550, 1976.

Wyatt, L.A.
A technique for clearning hot-wires used in anemometry.
Journal of Scientific Instruments, Vol. 30, p.13, 1953.

Wygnanski, I. and Fiedler, H.
Some measurements in the self-preserving jet.
Journal of Fluid Mechanics, Vol. 38, p.577, 1969.

Wygnanski, I. and Fiedler, H.
The two-dimensional mixing region.
Journal of Fluid Mechanics, Vol. 41, p.327, 1970.

Young, T.
Outlines of experiments and inquiries, respecting sound and light.
Lecture to the Royal Society on 16 Jan. 1800.
(See the dawn of aerodynamics by Pritchard, J.L.,
Journal of Royal Aeronautical Society, Vol. 61, p.157, 1957.)